

Department of Chemical and Process Engineering

**Production and characterisation of  
poly(vinyl chloride) (PVC) hollow  
fibre membranes for gas separation  
applications**

Alexandra Costa

PhD Chemical and Process Engineering

2017



---

This thesis is the result of the author's original research. It has been composed by the author and has not been previously submitted for examination which has led to the award of a degree.

The copyright of this thesis belongs to the author under the terms of the United Kingdom Copyright Acts as qualified by University of Strathclyde Regulation 3.50. Due acknowledgement must always be made of the use of any material contained in, or derived from, this thesis.

Signed:

---

Date:

---



# Acknowledgements

First, I would like to thank my supervisors, Simon Shilton and Vitor Magueijo, for the opportunity to develop this work. The advice and guidance you both gave me during these three years were fundamental to getting here. Thank you for all the motivation and support, even when the results were not as expected and, more importantly, for all the knowledge I acquired from you.

Thanks to all the staff in the department for making these three years a great experience in so many different levels and for making me feel welcome since the first day of this adventure. A special thanks to Joy Leckie for being an inspiration and for providing amazing outreach opportunities that certainly had a positive impact in my personal and professional growth. I will never forget our amazing dance moves and all the laughs we had together!

To all the good friends I made in Glasgow (specially in the University), thank you all for your support. Thank you for all the friendship and for moments of fun we had together. I am sure that some of you will be friends for life. A special thanks to Martin for all the helpful discussions we had about this work.

A big thanks to the *Portuguese Crew* I met in Glasgow - Carla, Pedro, Miguel, Sofia e Nicolau - obrigada pelo vosso carinho e amizade!

---

Um agradecimento muito especial para a minha tia Paula Martins. Obrigada por todo o apoio e por teres sempre acreditado em mim. Certamente nunca tinha chegado até aqui sem a tua ajuda.

Obrigada ao meu namorado Miguel Pinto por me ter acompanhado em grande parte deste caminho. Obrigada por todo o teu apoio, amor e dedicação.

A todos os meus amigos e família em Portugal, que nunca deixaram que a distância fosse o caminho para o esquecimento. Obrigada por estarem sempre presentes.

Patrícia Ferreira, *amori*, muito obrigada por tudo. Sabes que para mim és como uma irmã, que mesmo distante, faz questão de estar sempre presente.

Ruben Rosário, obrigada por esta longa amizade e por todo o apoio nesta caminhada. Obrigada por todos os momentos de parvoeira ao longo destes 14 anos. Que estejamos cá para contar muitos mais.

Jóni Silva e Ruben Jesus, obrigada pela preocupação, pelo apoio e amizade.

A todos, um grande obrigada!

# Conference Presentations

## Conference Oral Presentations

Alexandra Costa, V. M. Magueijo, S. J. Shilton, *Rheological Profile of PVC Solutions for Gas Separation Hollow Fibre Membrane Production*, Chemical and Process Engineering Department Celebration Event, University of Strathclyde, Glasgow (December 2015)

## Conference Poster Presentations

Alexandra Costa, V. M. Magueijo, S. J. Shilton, *Production and characterization of hollow fibre membranes for oxygen/ozone gas separation*, Research Presentation Day, University of Strathclyde, Glasgow (June 2015)

Alexandra Costa, V. M. Magueijo, S. J. Shilton, *Rheological Profile of PVC Solutions for Gas Separation Hollow Fibre Membrane Production*, EMS Summer School, Bertinoro, Italy (June 2016)

Alexandra Costa, V. M. Magueijo, S. J. Shilton, *Rheological Profile of PVC Solutions for Gas Separation Hollow Fibre Membrane Production*, Nanomaterials for Technology: Theory meets Experiment Workshop, University of Strathclyde, Glasgow (June 2016)

Alexandra Costa, V. M. Magueijo, S. J. Shilton, *Rheological Profile of PVC Solutions for Gas Separation Hollow Fibre Membrane Production*, Research Presentation Day, University of Strathclyde, Glasgow (June 2016)



# Abstract

The present work was focused in the development of polyvinylchloride (PVC) hollow fibre membranes suitable for gas separation applications using the dry/wet phase inversion technique.

The first part of this work involved the preparation of quaternary polymer solutions containing polyvinylchloride (PVC), dimethylacetamide (DMAc), tetrahydrofuran (THF) and ethanol (EtOH) to study their phase inversion properties. Different solutions, with different compositions, were prepared and a visual evaluation was made in order to understand the properties of the ternary phase diagram for this system and the possible location of the binodal boundary that separates the one phase homogeneous region from the two phase region (non-homogeneous). For all the solutions prepared, there was one composition that is suggested to be inside the non-homogeneous region, thus indicating the potential position of the binodal curve in the region studied.

During the spinning process, a polymer solution is subjected to shear stresses and deformation; therefore, the rheology of the quaternary PVC solutions was studied in detail. Oscillatory, creep and recovery and flow experiments were performed to fully characterize these solutions. Temperature and composition showed to have a big influence in the viscoelastic properties of the solutions investigated. The preparation of the solution used to spin the hollow fibre membranes followed a different procedure due to a larger quantity of solution needed and a different "ageing" time. Because of that, a rheological evaluation of this solution was also carried out and the effect of procedural differences on the viscoelastic properties

---

of the spinning solution was analysed.

After the rheological studies, different spinning conditions were established to better understand the impact of the solutions' rheology features on the final performance of the PVC hollow fibre membranes. Spinning dope temperature, dope extrusion rate and external bath temperature were the parameters studied. The design of the experiments was done using the *Taguchi* method and a set of nine experiments with different experimental conditions were performed. Gas permeation results obtained for the different membranes showed poor selectivities, even after the two coating cycles. The analysis of variance (*ANOVA*) showed that the external bath temperature was the parameter that most contributed to the variability of the results.

Scanning electron microscopy surface images revealed defects in the membranes surface (tearing). However, the *Knudsen* selectivity obtained for the uncoated membranes and the significant decline in the gas permeation through the membrane after coating cycles suggests that the fractures are not the main reason for the poor selectivities obtained.

Mass transfer and resistance models available in the literature were used to predict the active layers thickness and the surface porosity of the membranes. Mass transfer model predicts thick active layers if high temperatures are used and is in accordance with the values obtained by the resistance modelling that also predict the existence of thick active layers with high surface porosity. The high surface porosity obtained is suggested to be due to the incomplete coalescence of the polymer nodules during the formation of the active layer in the dry gap and is pointed out as the possible reason for the poor selectivities.

# Introduction

This thesis focuses on the development of gas separation membranes suitable for oxygen/ozone separation. Effective ozone separation membranes would have a major impact on industrial applications such as water treatment, effluent processing, bleaching and sterilization. The ozone production is an expensive process due to the large amounts of oxygen wastage during the process. A way to improve the economics of the process is the separation of the non-reacted oxygen from the generated ozone and its recycle back to the reactor. This would make ozone technology as a more attractive alternative to more conventional chemical processes.

Polyvinyl chloride (PVC) appears as a good candidate for oxygen/ozone gas separation due to its ozone resistance properties. Also, its low price and excellent physical and chemical properties make this polymer competitive when comparing with more expensive ones.

Hollow fibre membranes are very attractive for gas separation applications due to its advantages when compared with flat sheet membranes. However, the technology necessary to manufacture and develop hollow fibre membranes for gas separation is challenging on a number of fronts. The equipment is difficult to operate, the experimental techniques are demanding and the underlying principles of membrane formation are multidisciplinary.

In this work, a number of different aspects related with hollow fibre membrane fabrication will be addressed. Rheological and mass transfer factors were already found as very important in the manufacture of membranes by forced convection spinning and will be intensively studied in this work.

---

This work aims to produce novel gas separation hollow fibre membranes from PVC, an ozone resistant polymer.

The objectives of this work include:

- Preparation of multi-component PVC solutions with different concentrations to get information about the system's ternary diagram;
- Rheological characterisation of the prepared multi-component PVC solutions;
- Establish the hollow fibre membrane spinning conditions based on the results obtained in the rheological tests using the *Taguchi* approach;
- Characterisation of the prepared membranes in terms of gas permeation and relation of the results with the operational conditions;
- Characterisation of the prepared membranes using surface imaging spectroscopy;
- Predict membrane properties based on the operational conditions using a mass transfer based model;
- Characterisation of the prepared membranes using the resistance model.

# Contents

<b>Acknowledgements</b>	<b>v</b>
<b>Conference Presentations</b>	<b>vii</b>
<b>Abstract</b>	<b>ix</b>
<b>Introduction</b>	<b>xi</b>
<b>List of Figures</b>	<b>xvii</b>
<b>List of Tables</b>	<b>xxv</b>
<b>1 Background</b>	<b>3</b>
1.1 Ozone Production and Applications . . . . .	3
1.2 Polyvinylchloride . . . . .	4
1.2.1 Structure and Properties . . . . .	4
1.2.2 PVC as a Novel Material for Membrane Fabrication . . . . .	6
1.2.3 PVC Solution Properties . . . . .	7
1.3 Separation Processes . . . . .	10
1.3.1 Advantages, Disadvantages and Challenges of Using Membranes in Separation Processes . . . . .	12
1.3.2 Membrane Technology . . . . .	14
1.3.2.1 Membrane Structures and Geometries . . . . .	14
1.3.2.1.1 Membrane Structures . . . . .	16
1.3.2.1.2 Flat Sheet Membranes . . . . .	18
1.3.2.1.3 Hollow Fibre Membranes . . . . .	19
1.3.2.2 Membrane Materials . . . . .	20
1.3.2.3 Membranes for Gas Separation . . . . .	20
1.3.2.4 Gas Transport Mechanisms Through a Membrane . . . . .	22
1.3.2.4.1 Solution-Diffusion . . . . .	23
1.3.2.4.2 <i>Knudsen</i> Diffusion and Viscous Flow . . . . .	24
1.3.2.5 Production of Hollow Fibre Membranes for Gas Separation . . . . .	27
1.4 Phase Inversion Mechanisms in Membrane Formation . . . . .	29

---

1.4.1	Ternary Phase Diagrams . . . . .	29
1.4.2	Skin Formation Mechanisms and Techniques . . . . .	32
1.4.3	Prediction of Polymer Ternary Diagrams . . . . .	40
1.4.3.1	<i>Flory-Huggins</i> Model . . . . .	41
1.5	Rheology of Polymer Solutions . . . . .	46
1.5.1	Importance of Rheology in Membrane Spinning . . . . .	46
1.5.2	Concepts of Polymer Solution Rheology . . . . .	48
1.5.2.1	Viscoelasticity . . . . .	54
1.5.2.1.1	Oscillatory Rheology . . . . .	55
1.5.2.1.2	Mechanical Models to Describe Viscoelastic Materials . . . . .	59
1.5.2.1.3	Creep and Recovery Tests . . . . .	62
1.5.3	Rheology of PVC Solutions . . . . .	66
1.6	Designing of Experiments - <i>Taguchi</i> Method . . . . .	68
<b>2</b>	<b>Phase Inversion Studies of PVC Quaternary Solutions</b>	<b>71</b>
2.1	Objectives . . . . .	71
2.2	Materials and Methods for Phase Inversion Studies . . . . .	72
2.2.1	Materials . . . . .	72
2.2.2	Solutions Preparation Method for Phase Inversion Studies . . . . .	72
2.3	Results of the Phase Inversion Studies . . . . .	76
2.4	Conclusions of the Phase Inversion Studies . . . . .	84
<b>3</b>	<b>Rheological Studies of PVC Quaternary Solutions</b>	<b>85</b>
3.1	Objectives . . . . .	85
3.2	Materials and Methods used in the Rheological Studies of PVC Quaternary Solutions . . . . .	86
3.2.1	Materials for the Rheological Studies of PVC Quaternary Solutions . . . . .	86
3.2.2	Methods used in the Rheological Studies of PVC Quaternary Solutions . . . . .	86
3.3	Rheological Studies of PVC Solution Concentrations with Different Compositions . . . . .	87
3.3.1	Oscillatory Shear Rheology . . . . .	88
3.3.1.1	Results of the Amplitude Sweep Tests: Determination of the Linear Viscoelasticity Region (LVER) of the PVC Solutions . . . . .	88
3.3.1.2	Results of the Angular Frequency Sweep Tests: Deformation at Short and Long Time Scales, Relaxation Times and Gel Concentration of the PVC Solutions . . . . .	91
3.3.1.3	Results of the Temperature Sweep tests . . . . .	97
3.3.1.3.1	Differential Scanning Calorimetry Studies	104

---

3.3.2	Creep and Recovery tests . . . . .	106
3.4	Rheological Studies of a PVC Solution used for Membrane Spinning	127
3.4.1	Flow tests . . . . .	128
3.4.2	Flow model: Determination of the Shear Rate, Velocity and Stress Profiles in the Spinneret . . . . .	130
3.4.3	Oscillatory Shear Rheology . . . . .	133
3.4.3.1	Results of the Angular Frequency Tests: Deter- mination of the Relaxation Time . . . . .	133
3.4.3.2	Results of the Temperature Sweep tests . . . . .	135
3.4.4	Creep and Recovery tests . . . . .	136
3.5	Conclusions of Rheological Studies . . . . .	137
<b>4</b>	<b>Hollow Fibre Membrane Spinning and Gas Permeation Results</b>	<b>141</b>
4.1	Objectives . . . . .	141
4.1.1	Materials and Methods for Membrane Preparation and Per- meation Measurements . . . . .	142
4.1.1.1	Materials . . . . .	142
4.1.1.2	PVC Solution Preparation Method For Membrane Preparation . . . . .	142
4.1.1.3	Designing the Spinning Experiments using the <i>Taguchi</i> Method . . . . .	143
4.1.1.4	PVC Hollow Fibre Membrane Spinning Method . . . . .	148
4.1.1.5	Gas Permeation Measurements Method . . . . .	149
4.2	Gas Permeation Results . . . . .	149
4.2.1	Results Analysis Using the <i>Taguchi</i> Approach . . . . .	156
4.2.2	Discussion of the Gas Permeation Results using <i>ANOVA</i> Variance Analysis. . . . .	159
4.3	Conclusions of Hollow Fibre Membrane Preparation and Perme- ation Results Analysis . . . . .	162
<b>5</b>	<b>Structural Characterization of the Prepared PVC Hollow Fibre Membranes</b>	<b>165</b>
5.1	Objectives . . . . .	165
5.2	Structure Analysis Methods . . . . .	165
5.3	SEM Analysis of Prepared Membranes . . . . .	167
5.3.1	SEM Sample Preparation . . . . .	167
5.3.2	SEM Cross Section Analysis . . . . .	168
5.3.3	SEM Surface Analysis . . . . .	173
5.4	Conclusions of the Membranes Structure Characterization . . . . .	177
<b>6</b>	<b>Mass Transfer Modelling</b>	<b>179</b>
6.1	Objectives . . . . .	179
6.2	Principles of the Mass Transfer Model . . . . .	179

---

6.3	Results of the Mass Transfer Model - Prediction of the Active Layer Thickness . . . . .	185
6.4	Results of the Mass Transfer Model - Prediction of the Orientation Depth . . . . .	190
6.5	Conclusions of the Mass Transfer Modelling . . . . .	191
<b>7</b>	<b>Resistance Modelling</b>	<b>193</b>
7.1	Objectives . . . . .	193
7.2	Principles of the Resistance Model . . . . .	193
7.3	Results of the Resistance Model - Calculation of the Active Layer Thickness and Surface Porosity . . . . .	199
7.4	Conclusions of the Resistance Modelling . . . . .	203
	<b>Final Conclusions</b>	<b>205</b>
	<b>Future Work</b>	<b>211</b>
	<b>References</b>	<b>215</b>
	<b>Appendix A: Rheology Measurements Errors</b>	<b>234</b>
A.1	Rheological Studies of PVC Solution Concentrations with Different Compositions . . . . .	235
A.1.1	Oscillatory Rheology . . . . .	235
A.1.1.1	Amplitude Sweep Tests . . . . .	235
A.1.1.2	Frequency Sweep Tests . . . . .	236
A.1.1.3	Temperature Sweep Tests . . . . .	237
A.1.1.4	Creep and Recovery Tests . . . . .	238
A.1.2	Rheological Studies of a PVC Solution used for Membrane Spinning . . . . .	241
A.1.2.1	Flow Rheology . . . . .	241
A.1.2.2	Frequency Tests . . . . .	241
A.1.2.3	Creep and Recovery Tests . . . . .	242
	<b>Appendix B: Resistance Modelling Algorithm</b>	<b>242</b>

---



# List of Figures

1.1	Chemical structure of polyvinylchloride. . . . .	5
1.2	Schematics of the behaviour of a polymer chain when in contact with a "good" and a "bad" solvent . . . . .	8
1.3	Correlation between the use and the technological progress of some separation processes. . . . .	11
1.4	Schematic representation of a membrane separation process. . . . .	15
1.5	Evolution in the development of membrane processes industry until 2010. . . . .	16
1.6	Membrane classification accordingly with the pore size. . . . .	17
1.7	Schematic representation of a symmetric and asymmetric membrane structure. . . . .	18
1.8	<i>Robeson</i> "upper bound" for oxygen/nitrogen separation. . . . .	21
1.9	Schematics of viscous flow and <i>Knudsen</i> diffusion gas transport mechanisms through a porous membrane. . . . .	25
1.10	Membrane spinning apparatus. . . . .	27
1.11	Schematic of the <i>spinneret</i> outlet (1-Stainless steel, 2-Dope extrusion rig, 3-Bore fluid outlet). . . . .	28
1.12	Example of a polymer ternary diagram with the binodal and spinodal lines. . . . .	30
1.13	Phase diagram of a ternary mixture showing the vitrification and the gelation region. . . . .	32
1.14	Schematics of the two different compositions change pathways that lead to phase separation in the metastable region. . . . .	33
1.15	Schematics of the two different compositions change pathways that lead to the formation of asymmetric membranes. . . . .	35
1.16	Correspondence between the solution concentration change and the position of the fibre in the coagulation bath. . . . .	36
1.17	Example of structures obtained by nucleation and growth and spinodal decomposition. . . . .	36
1.18	Schematics representing the forces resulting from a polymer lean phase dispersed in a nodular polymer rich phase. . . . .	38
1.19	Schematics representing the glass transition temperature, the change in the specific volume and the chain segment status in the glassy and rubbery state. . . . .	39

---

1.20	Schematic representation of the conformation changes of polymer chains induced by elongation and shear rate. . . . .	47
1.21	Example of layers of a fluid sliding over one another under an applied force. . . . .	48
1.22	Flow curves of materials with different rheological features. . . . .	50
1.23	Example on how different structures may respond to shear. . . . .	51
1.24	Example of a flow curve and the range of applicability of the <i>Cross</i> model, <i>Power Law</i> model and <i>Sisko</i> model. . . . .	52
1.25	Relation between stress and strain for a purely elastic, purely viscous and a viscoelastic material. . . . .	56
1.26	Example of a typical graph for a viscoelastic material showing the critical strain that separates the LVER from the non-LVER. . . . .	58
1.27	Illustration of a spring and its behaviour when a force is applied. . . . .	59
1.28	Illustration of a dashpot and its behaviour when a force is applied. . . . .	60
1.29	Illustration of the <i>Maxwell</i> and the <i>Kelvin-Voigt</i> model as a combination of a spring a dashpot. . . . .	61
1.30	Illustration of the <i>Burgers</i> model. . . . .	62
1.31	Stress curve and typical response of a viscoelastic material to a creep and recovery test. . . . .	63
1.32	<i>Fancey's</i> representation of the <i>Weibull</i> model using springs and dashpots to describe the recovery viscoelastic response. . . . .	65
1.33	Loss tangent ( $\tan \delta$ ) as function of concentration at various angular frequencies and temperature for a system comprising PVC and DOP. . . . .	67
2.1	PVC quaternary solutions compositions represented in a pseudo-ternary diagram. . . . .	74
2.2	Dehydrochlorination reaction in PVC. . . . .	76
2.3	Time-temperature pathway followed to perform degradation tests to the PVC quaternary solutions. . . . .	77
2.4	Time-temperature pathway followed to avoid degradation of the PVC quaternary. . . . .	78
2.5	Weight loss (%) of set A solutions during the preparation period. . . . .	78
2.6	Visual appearance of the eleven prepared solutions with THF/DMAc equal to 12% (w/w) (set A). . . . .	79
2.7	Visual appearance of the eleven prepared solutions with THF/DMAc equal to 7.7% (w/w) (set B). . . . .	79
2.8	Visual appearance of the eleven prepared solutions with THF/DMAc equal to 16.7% (w/w) (set C). . . . .	80
2.9	Pseudo-ternary diagram variation over the solution preparation time. Results were similar for the three sets of solutions prepared. . . . .	81
2.10	Visual appearance of the eleven prepared solutions with THF/DMAc equal to 12% (w/w) two years after preparation. . . . .	82

---

2.11	Representation of the possible location of the binodal curve in relation with the position of the prepared solutions in a pseudo-ternary diagram. . . . .	83
3.1	PVC quaternary solutions compositions represented in the corresponding pseudo-ternary diagram. . . . .	88
3.2	Storage ( $G'$ ) and loss modulus ( $G''$ ) as function of strain (%) for composition 1 at 20°C and 60°C and at a frequency of 10 rad/s. . . . .	89
3.3	Storage ( $G'$ ) and loss modulus ( $G''$ ) as function of strain (%) for different compositions at 20°C and 60°C. . . . .	90
3.4	Typical behaviour of the storage ( $G'$ ) and loss modulus ( $G''$ ) with angular frequency for a generic polymer solution. . . . .	91
3.5	Storage ( $G'$ ) and loss modulus ( $G''$ ) as a function of angular frequency for composition 1 and 2 at 20°C. . . . .	92
3.6	Storage modulus ( $G'$ ) and loss modulus ( $G''$ ) as a function of angular frequency for different compositions at 20°C. . . . .	94
3.7	Solutions used to study the gel properties of the quaternary system represented in the pseudo-ternary diagram. . . . .	96
3.8	Loss tangent ( $\tan \delta$ ) as a function of polymer and solvent concentration with non-solvent concentration constant (16%) at various angular frequencies and constant temperature of 20°C and the respective 2D projection. . . . .	97
3.9	Storage ( $G'$ ) and loss modulus ( $G''$ ) as a function of temperature for composition 2 and 6 (at an angular frequency of 10 rad/s, with strain of 5%). . . . .	98
3.10	Storage ( $G'$ ) and loss modulus ( $G''$ ) as function of temperature at a frequency of 10 rad/s. . . . .	99
3.11	Storage ( $G'$ ) and loss modulus ( $G''$ ) as a function of temperature for compositions 1, 2, 5, 9, 10 and 11 (at an angular frequency of 10 rad/s, with strain of 5%). . . . .	100
3.12	$\tan \delta$ as a function of temperature for different compositions at 1, 10 and 100 rad/s. . . . .	101
3.13	Storage modulus ( $G'$ ) as a function of temperature for the compositions where a crossover between ( $G'$ ) and loss modulus ( $G''$ ) was observed, at different frequencies. . . . .	102
3.14	Fitting result obtained for the storage modulus ( $G'$ ) as a function of temperature for composition 1 at a frequency of 1 rad/s. . . . .	103
3.15	Calculated half point temperature corresponding to the behaviour change in the loss modulus vs. temperature graph for the studied compositions. . . . .	104
3.16	DSC experiment performed to composition number 2, between 20°C and -20°C at a heating rate of 10°C/min. . . . .	105

---

3.17	DSC experiment performed to pure PVC, between 20°C and 90°C at a heating rate of 10°C/min, highlighting the presence of the glass transition temperature. . . . .	106
3.18	Creep and recovery results obtained for composition 1 at 20°C and 50°C at different stresses. . . . .	107
3.19	Creep and recovery results obtained at 20°C and 50°C plotted in a pseudo-ternary phase diagram. . . . .	109
3.20	Rheological and phase inversion results at 20°C (left) and 50°C (right) plotted in a pseudo-ternary phase diagram. . . . .	110
3.21	<i>Burgers</i> model applied to creep curve for composition 1 at a stress of 40 Pa and a temperature of 20°C. . . . .	112
3.22	<i>Burgers</i> model parameters results for the solutions that showed a viscoelastic behaviour in the creep curve at 20°C. . . . .	113
3.23	Creep results: $G_1$ , $G_2$ and $\eta$ trends at 20°C plotted in a pseudo ternary diagram. . . . .	114
3.24	Creep results: $\lambda_r$ trend at 20°C plotted in a pseudo ternary diagram. . . . .	115
3.25	<i>Burgers</i> model parameters results for the solutions that showed a viscoelastic behaviour in the creep curve at 50°C. . . . .	116
3.26	<i>Weibull</i> model applied to creep data for composition 1 at a stress of 40 Pa and a temperature of 20°C. . . . .	117
3.27	Parameters obtained by fitting the <i>Weibull</i> distribution to the experimental creep data for the solutions showing viscoelastic behaviour, at 20°C. . . . .	118
3.28	Parameters obtained by fitting the <i>Weibull</i> distribution to the experimental creep data for the solutions showing viscoelastic behaviour, at 50°C. . . . .	120
3.29	<i>Weibull</i> model applied to recovery curve for composition 1 at a stress of 40 Pa and a temperature of 20°C. . . . .	122
3.30	Parameters obtained by fitting the <i>Weibull</i> distribution to the experimental recovery data for the solutions showing viscoelastic behaviour, at 20°C. . . . .	123
3.31	Parameters obtained by fitting the <i>Weibull</i> distribution to the experimental recovery data for the solutions showing viscoelastic behaviour, at 50°C. . . . .	126
3.32	Flow curves obtained for the spinning solution at 20°C and at 50°C. . . . .	129
3.33	Power law fit applied to flow curves for the spinning solution at 20°C and at 50°C. . . . .	130
3.34	Shear rate, shear stress and velocity profiles in the <i>spinneret</i> at 20°C and at 50°C. . . . .	132
3.35	Storage modulus ( $G'$ ) and loss modulus ( $G''$ ) of the spinning solution as a function of temperature for a frequency of 10 rad/s. . . . .	134
3.36	Storage modulus ( $G'$ ) as a function of temperature for the spinning temperature at 10 rad/s and 5% strain. . . . .	135

---

3.37	Creep and recovering test performed with the spinning solution at different temperatures and fixed stress of 20 Pa. . . . .	136
4.1	Experimental set-up for the quaternary polymer solution preparation. . . . .	143
4.2	Membrane spinning apparatus. . . . .	148
4.3	Nitrogen and oxygen fluxes obtained to the 9 sets of prepared uncoated membranes. . . . .	152
4.4	Selectivities obtained for the 9 sets of experiments for uncoated, once coated and twice coated membranes with respective standard deviations. . . . .	155
4.5	S/N ration effect for the different factors and levers. . . . .	158
5.1	External and internal membrane diameter estimated for each one of the categories of membranes prepared (obtained from SEM micrographs). . . . .	173
5.2	SEM surface view of a membrane from category number 4 showing defects (magnification of 150x). . . . .	174
5.3	SEM surface view for a membrane from category number 4 showing tearing (magnification of 150x). . . . .	175
5.4	SEM surface view of a membrane from category number 4 showing tearing (magnification of 8000x). . . . .	176
6.1	Schematics representing the forced convection chamber and the two different flow regimes presents in it. . . . .	181
6.2	Predicted membrane active layers using the mass transfer model considering the laminar flow region. . . . .	186
6.3	Comparison of the predicted membrane active layers using the mass transfer model applied to the impingement zone region and to the laminar flow region. . . . .	189
7.1	Schematics of the gas transport through an asymmetric uncoated membrane. . . . .	194
7.2	Representation of the gas resistances encountered in an uncoated asymmetric membranes. . . . .	196
7.3	Schematics of the gas transport through an asymmetric coated membrane. . . . .	197
7.4	Representation of the gas resistances encountered in a coated asymmetric membranes. . . . .	197
7.5	Results obtained for the membranes surface porosity using the resistance modelling. . . . .	200
7.6	Results obtained for the membranes active layer thickness using the resistance modelling. . . . .	200

---

7.7	Comparison of the results obtained for the membranes active layer thickness using the resistance modelling with the results obtained using the mass transfer model. . . . .	203
-----	---	-----





# List of Tables

1.1	Some mechanical and thermal properties of rigid PVC. . . . .	6
1.2	Different gas transport mechanisms depending on the membrane structure and pore size. . . . .	23
1.3	Permeability coefficients and intrinsic selectivities for polyvinyl chloride. . . . .	24
1.4	Molecular diameters obtained for oxygen and nitrogen by <i>Jones</i> using the kinetic theory. . . . .	26
1.5	Example of the mean free path distance for oxygen and nitrogen and the respective <i>Knudsen</i> number assuming a pore diameter of 100 Å. . . . .	26
1.6	Experimental techniques to determine interaction parameters. . . . .	46
1.7	Taguchi method orthogonal matrix selector. . . . .	69
2.1	Ratios of THF/DMAc used in each set of solutions prepared. . . . .	73
2.2	Composition of the quaternary polymer solutions prepared considering the THF/DMAc ratio equal to 12% (w/w) (set A). . . . .	74
2.3	Composition of the quaternary polymer solutions prepared considering the THF/DMAc ratio equal to 7.7% (w/w) (set B). . . . .	75
2.4	Composition of the quaternary polymer solutions prepared considering the THF/DMAc ratio equal to 16.7% (w/w) (set C). . . . .	75
3.1	Rheological behaviour of the solutions when subjected to different stresses at 20°C and 50°C and comparison with the results obtained in oscillatory temperature sweeps (at 10 rad/s and 5% strain). . . . .	108
3.2	Parameters values obtained by fitting the recovery results to the <i>Weibull</i> model for composition 2 at 20°C with the respective deviation for the different applied stresses. . . . .	124
3.3	Comparison of the preparation method and of the "ageing" time between composition number two studied before and the solution used to spin membranes. . . . .	128
3.4	Input parameters used in <i>Shilton's</i> methodology in order to calculate shear rate, velocity and stress profiles in the <i>spinneret</i> at 20°C and at 50°C. . . . .	131

---

4.1	Values chosen for the parameters to be studied (dope/spinning temperature, extrusion rate and external bath temperature). . . .	144
4.2	General Spinning conditions. . . . .	146
4.3	Orthogonal arrays (L9 Table). . . . .	147
4.4	L9 orthogonal matrix used to spinning experiment design. . . . .	147
4.5	Permeation results obtained for the 9 categories of uncoated membranes. . . . .	151
4.6	Permeation results obtained for the 9 categories of once coated membranes. . . . .	153
4.7	Permeation results obtained for the 9 categories of twice coated membranes. . . . .	154
4.8	S/N data obtained for each set of prepared membranes. . . . .	157
4.9	S/N mean for each factor and level. . . . .	158
4.10	ANOVA results obtained for the 3 parameters used to spin different PVC hollow fibre membranes. . . . .	161
5.1	Techniques used for surface characterization. . . . .	166
5.2	SEM cross section views of membranes from category 1, 2 and 3 (different magnifications). . . . .	169
5.3	SEM cross section views of membranes from category 4, 5 and 6 (different magnifications). . . . .	170
5.4	SEM cross section views of membranes from category 7, 8 and 9 (different magnifications). . . . .	171
6.1	General Spinning conditions. . . . .	181
6.2	Physical properties of nitrogen. . . . .	184
6.3	Vapour pressures for pure THF at different temperatures. . . . .	184
6.4	THF solvent evaporation for different temperatures and dope extrusion rates. . . . .	185
6.5	Active layer thickness predicted for different spinning temperatures and dope extrusion rates. . . . .	186
6.6	Comparison between the residence times in the forced convection chamber and the polymer relaxation time. . . . .	191
7.1	Permeability coefficients of oxygen and nitrogen through PDMS and PVC. . . . .	198
A.1	Relative error (%) of the storage ( $G'$ ) and loss modulus ( $G''$ ) as function of strain (%) for different compositions at 20°C and 60°C. . . . .	236
A.2	Relative error (%) of the storage ( $G'$ ) and loss modulus ( $G''$ ) as function of frequency for different compositions at 20°C. . . . .	236
A.3	Relative error (%) of the storage ( $G'$ ) and loss modulus ( $G''$ ) as function of temperature for different compositions at 10 rad/s. . . . .	237

---

A.4	Relative error (%) of $\tan \delta$ as function of temperature for different compositions at different frequencies. . . . .	238
A.5	Relative error (%) of strain (%) for different compositions at 20°C and 50°C. . . . .	239
A.6	Relative error (%) of the creep parameters fitted using the <i>Weibull</i> distribution, at 20°C. . . . .	239
A.7	Relative error (%) of the creep parameters fitted using the <i>Weibull</i> distribution, at 50°C. . . . .	240
A.8	Relative error (%) of the recovery parameters fitted using the <i>Weibull</i> distribution, at 20°C. . . . .	240
A.9	Relative error (%) of the recovery parameters fitted using the <i>Weibull</i> distribution, at 50°C. . . . .	241
A.10	Relative error (%) of viscosity as function of strain rate for different compositions at 20°C and 60°C. . . . .	241
A.11	Relative error (%) of the storage ( $G'$ ) and loss modulus ( $G''$ ) as function of frequency at 40°C, 50°C and 60°C. . . . .	242
A.12	Relative error (%) of strain (%) for different temperatures. . . . .	242



---



# Chapter 1

## Background

### 1.1 Ozone Production and Applications

Ozone is an inorganic compound with chemical formula  $O_3$ . It is known for its presence in Earth's atmosphere and associated with the global warming due to the effect of its depletion. This gas has a pale blue colour and it is detectable at concentrations above 0.1 ppm due to its strong odour.

In nature, ozone can be produced from diatomic oxygen using ultraviolet light or from natural electrical discharges. Due to its high reactivity, ozone can perform a lot of different reactions, being the conversion back to diatomic oxygen one of the most important due to the high explosive nature [1].

The safety implications connected with the use of ozone make this gas less attractive for industrial use. However, its applications across different sectors in industry never let its popularity to go down. In 1886, ozone was first recognized as a disinfectant for polluted water and the first full-scale application took place in the Netherlands in 1893 [2]. Industrially, the four main roles of ozone are disinfection, oxidation of inorganic and organic compounds (taste, colour and odour removal) and particle removal. Nowadays, ozone is used for several different applications such as purification of ground and surface waters, domestic and industrial waste water treatment as well as in swimming pools and cooling tower

systems. Other industries use this gas for bleaching (pulp and paper industry) and as a metal oxidizing (semiconductor industry), instrument sterilization and electronic component cleaning [2].

Because it is an unstable and short-life gas, ozone needs to be produced on-site by an ozone generator. There are four ozone production methods: ultraviolet light, cold plasma, electrolytic and corona discharge, the last one being the most commonly used one. The highest concentrations are achieved in the electrolytic method and can go up to 30% but at a high cost [1]. To improve the efficiency of ozone production some changes can be made in the process such as using pure oxygen in the feed instead of air. In this way higher ozone concentrations can be achieved and the production of by-products can be avoided. However, the cost of pure oxygen and the large amounts of oxygen that are not converted into ozone during the process makes this change a challenge. But, if the oxygen wastage could be recycled back into the ozone generator, the economics of the process could be improved.

A lot of processes can make use of the high reactivity of ozone, however this compromises the handling of this gas. This makes separation methods where chemicals are used not suitable. The use of membranes can be a good choice if the polymer used presents ozone resistant properties. At the same time, the polymer should have properties that allow the production of hollow fibre membranes. The use of polymers containing saturated molecules and that are at a glassy state at room temperature are desirable. Polyvinylchloride appears as a good candidate to produce ozone resistant membranes capable of performing gas separation.

## 1.2 Polyvinylchloride

### 1.2.1 Structure and Properties

Polyvinylchloride (PVC) is a glassy polymer (at room temperature) composed by repeated units of vinyl chloride monomer ( $C_2H_3Cl$ ) $_n$ , Figure 1.1.

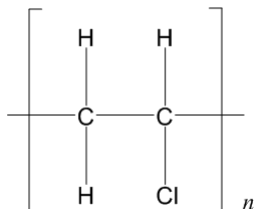


FIGURE 1.1: Chemical structure of polyvinylchloride.

PVC is one of the oldest synthetic materials in the world being discovered by accident twice in the 19th century, first by *Henri Victor Regnault* and later by *Eugen Baumann*. At both times, the polymer was found inside flasks containing vinyl chloride gas that was left exposed to the sunlight. By this time, this new material was a challenge in terms of applications because it was found to be difficult to work with. Later, in the early 90's, the polymerization of vinyl chloride using sunlight was patented by *Friedrich Heinrich August Klatte* and the material start to be popular as a replacement for costly natural rubber [3]. PVC started to be produced in bigger quantities around the world in the 1950's with the diversity of applications of the polymer increasing as well. Also, methods of improving PVC's durability were developed, allowing the material to be used in the building and construction industry due to its resistance to light, chemicals and corrosion. The improvements made to the material in terms of extreme temperatures resistance made this polymer important in water transportation to industries and also homes. As for some applications pure PVC showed to be too rigid, more modern products made of this polymer in combination with plasticizers are available in the market. These additional components, mainly species of the phthalate family, allow the production of a modified material easier to work with [4].

All these important features make PVC the third largest-selling plastic in the world, after polyethylene and polypropylene, and it is nowadays used in different industries - health care, IT, transport, textiles and construction.

60% of PVC applications have a lifetime superior to 40 years. PVC has many attractive properties for membrane production such as low cost and excellent

physical, chemical and mechanical properties [5]. Table 1.1 shows some mechanical and thermal properties of rigid PVC.

TABLE 1.1: Some mechanical and thermal properties of rigid PVC [6].

<b>Property</b>	<b>Value</b>
Density	1380 kg/m <sup>3</sup>
Young's Modulus	2900-3300 MPa
Tensile Strength	50-80 MPa
Elongation at Break	20-40%
Glass Transition Temperature	87°C
Melting Point	212°C

### 1.2.2 PVC as a Novel Material for Membrane Fabrication

PVC is ozone resistant, making this material interesting for some applications such as ozone/oxygen separation to enhance ozone production.

Accordingly to *Stern* [7], when choosing a polymer to produce membranes suitable for gas separation processes, some properties should be taken into account. The polymer should possess a stiff backbone in order to allow a better discrimination between the different gases, since the separation is related with the free volume present in the structure. A rigid structure will make the polymer molecules to bundle in a more efficient way leading to a more uniform structure and a lower free volume. Another important feature is a low inter-segmental packing of the polymer molecules that is related with what was discussed previously and will allow a more regular structure, benefiting the separation. Lastly, a low energy inter-chain interaction is desirable.

Accordingly with these, membranes prepared using PVC will have a packed structure with low free volume so the discrimination between the gases can happen. Although the selectivity will be good, a packed structure will lead to low permeabilities of the gases through the membrane. A membrane to have a good

performance should, apart from a good selectivity, have a reasonable permeability. A way to overcome this problem and increase permeability is by preparing asymmetric membranes with thin active layers supported by a porous structure.

Before the work carried out in our research group by *Jones* [8], the production and study of gas separation properties of PVC hollow fibre membranes were limited. Recently new modified PVC films for gas separation were produced replacing the chlorine atoms for fluorinated ones obtaining a higher permeability coefficient [9]. Also PVC membranes functionalized with mercapto pyridine groups were developed leading to an increase in the permeability by a factor of 4 [10]. Later, the same group studied the influence of the nucleophilic substitution of chlorine atoms by bulky groups (4-mercaptophenol sodium salt, 2-thionaphthalene, 4-(1-adamantyl) thiophenol, and thiophenolate sodium salt), concluding that these groups lead to an increase in the free volume and permeability because they prevent the chain packing [11]. *Sadeghi et al.* [12] prepared a series of polyvinylchloride/polyethyleneglycol (PVC/PEG) blend membranes with different PEG molecular weights (from 400 to 4000) that showed a significant increase in the gas selectivities. More recently, *Mohagheghian et al.* [13] investigated the gas properties of PVC/silica nanocomposite membranes. The results showed an improvement in the thermal properties and also in the permeability and selectivity of  $CO_2/CH_4$  and  $CO_2/N_2$ .

As can be seen, most of the research done in this area is related with the use of modified PVC to produce flat sheet membranes or films. However, hollow fibre membranes have some advantages when compared with flat sheet ones, such as high surface area and good self-support characteristics [14]. Also, the use of a modified material would result in an increase in the cost of the produced membranes, and the big advantage of using PVC - its low cost - would be lost.

### 1.2.3 PVC Solution Properties

In the previous section some properties of pure PVC were discussed. However, in polymeric membrane production, the first step is the preparation of a stable polymer solution. In this process, the polymer is mixed with a solvent (or mixture

of solvents). When in solution, if the molecules of a polymer have enough uniformity in the chains, they can pack and achieve crystalline structures with the polymer concentration playing an important role in the morphologies obtained [15].

For polymers containing some degree of crystallinity (such as PVC [16]), it is known that when in solution, these polymers can form thermoreversible physical gels when the temperature is decreased [17]. Opposite to chemical gelation, where the cross linking is achieved through covalent bonding, in physical gelation the gel structure is obtained due to hydrogen and *van der Waals* forces. The thermoreversible nature of the gels are due to the ability of the structure to form and destroy these bondings with temperature [18]. It was believed, initially, that the polymer gel structures were formed when the material was in contact with solvents characterized as bad solvents, promoting chain aggregation. However, years later, some studies showed that it is possible to achieve these type of structures using good solvents [19]. The definition of "good" and "bad" solvent is related to its interaction with the polymer. A solvent is considered "good" if there is a maximization of the polymer-solvent contact, resulting in chain expansion or swelling. A "bad" solvent will promote the minimization of the contact between the polymer and the solvent, provoking chain collapse, clustering or precipitation. The *Flory-Huggins* binary dimensionless parameter is a good way to evaluate the quality of a solvent in respect to another compound. If this parameter is less than 0.5 the solvent is characterized as "good" and if it is more than 0.5 the solvent is classified as "bad" [20]. Figure 1.2 exemplifies the behaviour of a polymer chain when in contact with a "good" and a "bad" solvent.

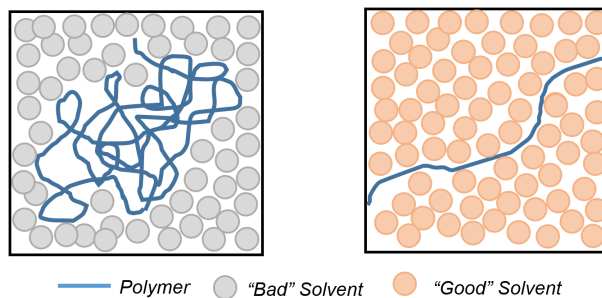


FIGURE 1.2: Schematics of the behaviour of a polymer chain when in contact with a "good" and a "bad" solvent

In 2008, *Rogovina* [21] and co-workers proposed a definition of polymeric physical gels. Accordingly to the authors, a polymeric gel is a solid material comprising at least two components where the polymer creates a three-dimensional network through non-covalent bonding. This 3D network is formed in the other component medium, that is liquid. The amount of the liquid phase should be enough to give the gel elastic properties.

PVC is well known to form gel structures while in contact with a solvent (or a mixture of solvents) and work done by *Li* [22–25] investigates the rheological properties of PVC in bis(2-ethylhexyl)phthalate (DOP) for different conditions. It is reported in the literature that the PVC network gels are formed due to junctions originated by the rearrangement of the polymer chains and that the polymer-solvent interaction plays an important role in the crystallinity of the gels [26–29]. The polymer-solvent interaction seems to have also effect in the thermal and phase separation properties of PVC gels. Good solvents result in higher gel melting points and no noticeable phase separation while poor solvents result in a lower gel melting point and liquid-liquid separation takes place [30]. These results suggest that the gel network properties can be tailored accordingly with the desired application by playing with the polymer-solvent interactions.

Early in 1983, a relationship between gelation and gel melting temperatures was established for systems containing chlorinated polyethylene. For crystallizable systems it was found that these temperatures are the same while in non crystallizable they are different. An explanation given for this phenomena is the presence of crystallites in the crystallizable systems [31, 32].

Some authors studied the system consisting of PVC and different solvents such as  $\gamma$ -butyrolactone, and attributed the gelation process as a consequence of hydrogen bonding with crystallization happening after this process [33, 34]. Other authors attribute the gel formation to the existence of crystallites that work as connecting points of the gel network [35, 36]. *Hong* and *Chen* [17] investigated the properties of PVC in different solvents (bromobenzene and dioxane) that originated gel structures. The study showed that, for this system, the gelation time decreases

with the concentration of polymer for both systems. The *Young's* modulus increased with the PVC molecular weight and also with the concentration.

As can be seen, different systems containing PVC were studied previously concerning its gel properties. However, in membrane preparation, the combinations are so many that it is difficult to find information in the literature about the gelation properties of these systems. In this work, a rheological assessment of the system containing PVC, dimethylacetamide, tetrahydrofuran and ethanol will be performed and some insight about this matter will be gained.

### 1.3 Separation Processes

Separation processes are defined as *"operations which transform a mixture of substances into two or more products which differ from each other in composition"* [37].

It is well known that it is easier to mix components than separate them. The reason behind this is that, when solids, liquids or gases are combined, the thermodynamic features of the system change as a result of the mixing. One of these features is the entropy that increases when two or more components are mixed - because the variation in entropy is always positive when mixing. For this reason, separation processes are always a challenge.

It can be very hard to name a chemical and process industry that does not have a separation process. Even in every day's life a lot of tasks can be found that involve separate one or more components from a mixture. In industry, these processes are used in the purification of raw materials, separation of reactions products and also in the treatment of the process effluents.

Separation techniques make use of the differences in chemical or physical properties between the components of a mixture. These properties can be size, shape, mass, density, or chemical affinity. Separation operations are crucial throughout the process industry with respect to energy consumption, contribution to investments and ability to achieve the desired product with the right specifications.

Separation technology is an area in constant grow - industry is constantly searching to improve the efficiency of these processes since they represent 40%-70% of the capital and operating costs [38].

The cost is not the only driving force to develop new technologies for separation processes. New legislation and an increasing awareness to topics such as climate change make companies walk in the direction of developing greener technologies in order to achieve the stipulated objectives. This means that the industries have to adequate their methods to these targets and, because of this, more efficient separation techniques need to be investigated.

Some examples of separation processes commonly used are distillation, crystallization, ion exchange and membranes.

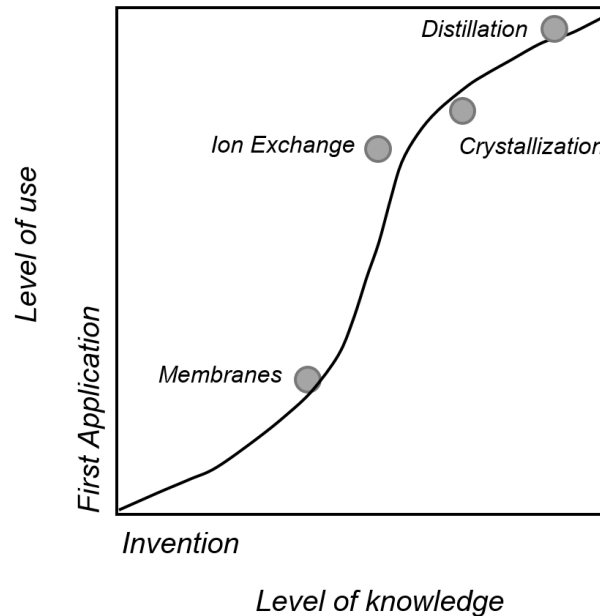


FIGURE 1.3: Correlation between the use and the technological progress of some separation processes. Adapted from [39].

In Figure 1.3 is represented the correlation between the use and level of knowledge of some separation processes. The maximum in the "level of knowledge" axis means that the process is well established and studied and no further improvements need to be made. If a process approaches the maximum of the "level

of use” axis it means that it is used in its full extent. As can be observed, distillation - the most frequently used separation process in industry - is the one that is closest to the maximum of both axis. It is a well known process that does not need any laboratory or pilot tests to be designed. In contrast, membrane processes are in the bottom part of the graphical representation and that means that these type of separation processes need extensive research before its design and implementation [39].

The use of membranes for gas separation has grown in the last decades, specially in the past 30 years. These membranes have a wide range of applications such as natural gas purification, hydrogen recovery,  $CO_2$  capture and  $O_2$  and  $N_2$  enrichment [40].

### **1.3.1 Advantages, Disadvantages and Challenges of Using Membranes in Separation Processes**

Processes involving membranes have a number of advantages and disadvantages when compared with alternative methods of separation. The growth in membrane technology is due to the need of making this separation process competitive when compared with others. The use of membranes for separation processes has grown due to its advantages comparing with other processes. The most important advantages of this type of technology are listed below.

- Can be easily coupled with other processes and operations with no moving parts or complex control schemes;
- Are normally easy to operate and require low maintenance;
- Allow separations from a molecular level to a scale at which particles can be seen, showing the large amplitude of different separations that can be performed (but through a different process);
- With pervaporation as an exception, membrane processes usually do not require a phase change leading to low energy requirements (unless high

pressures are needed in the feed stream in order for permeation to occur across the membrane as in the case of reverse osmosis);

- Can be made of many different materials like polymers or inorganic media allowing a control in the separation properties;
- The materials used in membrane technology are usually more environmental friendly than others involving chemical or additives;
- Membranes with extremely high selectivities can be prepared achieving in some cases higher values than the ones for relative volatilities in distillation processes;
- Membrane processes are easy to scale up as they can work as modules that can be used in series or in parallel.

However, there are also some disadvantages of membrane processes when compared with other separation processes.

- Membranes seldom produce pure components being one of the streams often contaminated with a minor amount of the other(s) component(s);
- In processes such as distillation it is possible to draw products at different stages and this is not easy to do using membranes;
- Some incompatibilities can happen when using high concentration of organic compounds. As most of the membranes are made of polymeric materials, these organic compounds can dissolve, swell or weaken the membrane structure, reducing the membrane life-time and efficiency;
- As the majority of the membranes are made of polymeric materials, the use of temperature above room temperature is prohibitive since a large amount of polymers will not maintain their physical properties compromising the integrity of the membrane;
- Depending on the feed streams fouling can be present and it can be a major problem mainly if it is difficult to remove. Fouling can affect the permeating of the component through the membrane, reducing the flow rate.

All the points refereed before make the use of membrane for separations as a promising technique if each membrane is designed accordingly with the intended separation in order to overcome some of the disadvantage highlighted before. This is the big challenge in membrane technology, to try to tailor these structures to make them attractive and cost beneficial when compared with other methods of separation.

### **1.3.2 Membrane Technology**

#### **1.3.2.1 Membrane Structures and Geometries**

A membrane is a selective physical barrier that allows the separation of a feed stream in two different streams [41]. The portion of the feed stream that flows through the membrane is the permeate and the portion retained is the retentate or concentrate. Some examples of driving forces for the separation are hydrostatic pressure, concentration gradient, temperature or electrical potential. Membranes have different applications such as production of potable water, effluent treatment, desalination of sea water or de-gasification of specific gases. The separation is achieved due to the membrane structure and material, allowing some components to flow through it and retaining others. This means that the membrane structure is very important and will depend on the application. Also the material must be chosen accordingly with the intended separation. A schematic representation of this process can be seen in Figure 1.4.

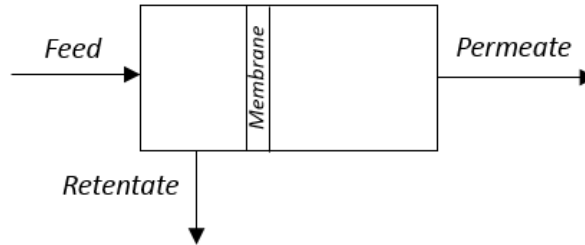


FIGURE 1.4: Schematic representation of a membrane separation process.

In a membrane separation process, the permeate stream will have a higher concentration of species that travel faster through the membrane, while the retentate will be richer in the compounds that travel slower.

The development of membrane technology started in 60's. Since then, different membrane processes became established such as micro filtration, ultra filtration, reverse osmosis and electrodialysis. Gas separation and pervaporation membranes started to be developed in the 80's and only in the mid 90's micro and ultra filtration processes became commercially available for applications such as municipal water treatment, Figure 1.5.

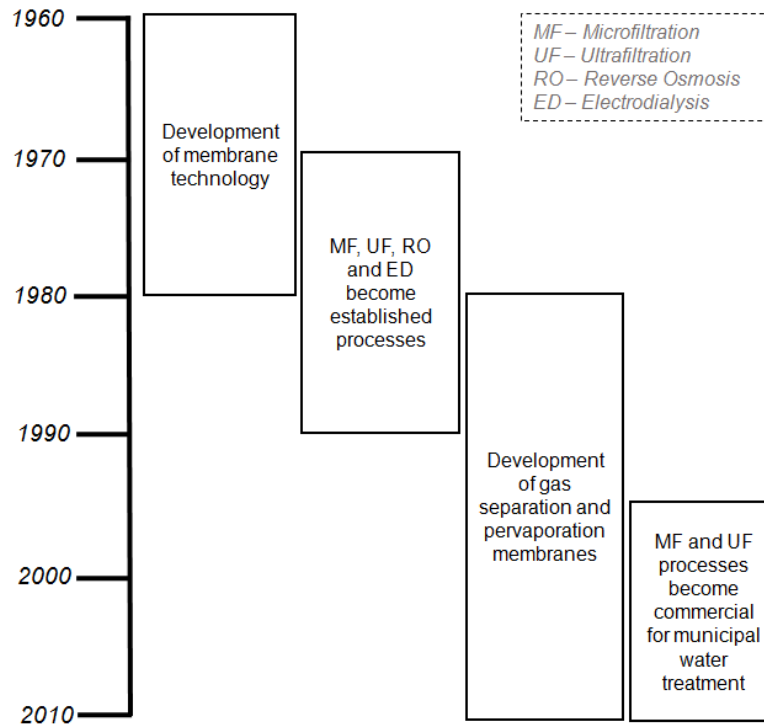


FIGURE 1.5: Evolution in the development of membrane processes industry until 2010. Adapted from [42]

### 1.3.2.1.1 Membrane Structures

Concerning their structure, membranes can be divided in porous, nonporous and carrier membranes. In carrier membranes, the separation is dictated by a specific carrier molecule that aids the species' transport. In this type of membranes the transport mechanism is not dependent on the membrane material [14].

In porous membranes, the separation process is controlled by the pore size in contrast with the nonporous membranes where it is the material permeation properties that control the separation [14]. A porous material is defined as a rigid, highly voided structure with randomly distributed interconnected pores [43]. In these type of structures the separation is achieved depending on the ability of the molecules to pass through the pores. This method relates with another method of separation - filtration - but at a smaller scale. Depending on the pore size of

the membrane, different classifications can be given, Figure 1.6.

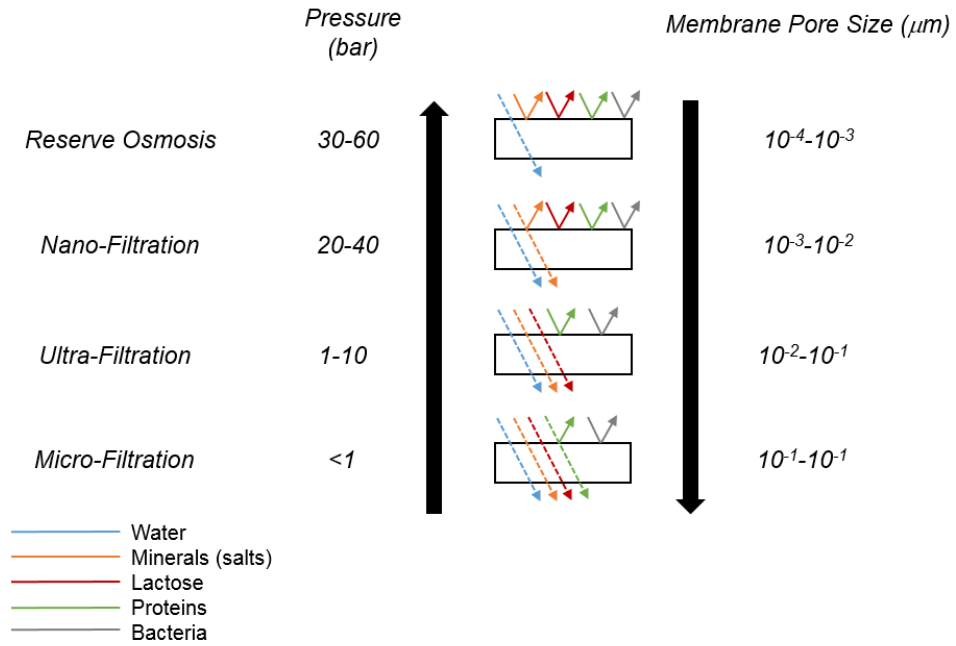


FIGURE 1.6: Membrane classification accordingly with the pore size. Adapted from [44].

Membranes can also be divided in symmetric and asymmetric. Symmetric membranes are characterized by an uniform structure and asymmetric ones by a non-uniform structure composed by a dense top layer supported by a porous sub-layer.

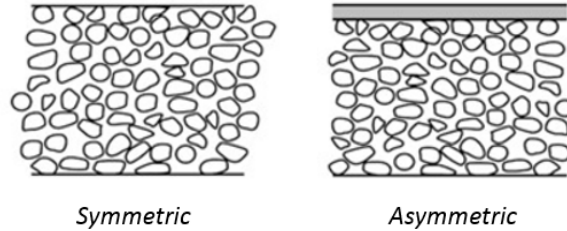


FIGURE 1.7: Schematic representation of a symmetric and asymmetric membrane structure.

Non-porous membrane can have very good selectivities but the use of thick membranes can lead to low permeation rates. On the other hand, reducing the thickness of the membrane can lead to a very fragile structure. The use of an asymmetric structure can be a good solution. In this approach, a thin dense active layer is supported by a thick porous structure with high mechanical support and low resistance to flow. The drawback is that this type of membranes are very susceptible to have defects in the thin active layer and that can cause a drop in the selectivity [45].

The first asymmetric membranes were prepared by *Loeb* and *Sourirajan* [46] in the early 1960's for reverse osmosis demineralization of saline water. These membranes were prepared using cellulose acetate as material. To prepare these reverse osmosis membranes, a short time should be allowed after casting the polymer solution for evaporation to happen so the dense layer can be formed succeeded by submersion in a solvent to allow the porous structure to form. This method was replicated in 1973 to originated the first membranes suitable for gas separation [47, 48].

### 1.3.2.1.2 Flat Sheet Membranes

Concerning the geometry, membranes can be divided, generally, in two different groups - flat sheets and hollow fibres. Both of these geometries have advantages and disadvantages and the choice of one against another is dependent on the application. Flat sheet membranes can be used in a number of different processes

including bioreactors, filtration and reverse osmosis systems [49–55].

Comparing with other type of geometries, flat sheet membranes offer mechanical strength but comparing with hollow fibers they have a lower surface area. A way to overcome this problem is to arrange flat sheets in a way in which the area per volume of membrane is increased. Some examples are the use of spiral wound modules that gain good reputation in gas separation techniques where 20% of gas separations are made with this type of modules [56].

The production of flat sheet membranes is done by casting a solution containing the membrane material on a support. Common used support materials are polymers with a high degree of porosity such as polyester.

### **1.3.2.1.3 Hollow Fibre Membranes**

The first hollow fibre membranes were reported in 1966 [57]. In the last decade, a lot of patents were release on the production of these type of membranes [58]. Hollow fiber membranes can be used for a variety of industrial applications such as bioseparations, drinking water purification, wastewater treatment, liquid phase separations and gaseous separations [58]. Due to the excellent mass transfer features achieved by the hollow fiber configuration there are many commercial applications in many different areas for these membranes.

The use of hollow fibers comparing with flat sheets can offer a lot o advantages. The production of modules can contain thousands of packed hollow fibers that can give a surface to volume ratio of  $2000 - 4000 ft^2/ft^3$  comparing with  $100 - 150 ft^2/ft^3$  for flat sheet membranes [1].

In the literature, a lot of different polymers are used to fabricate hollow fiber membranes with reasonable selectivities. In 2013 a review was published about the recent progresses made in the polymeric hollow fiber membranes production. Polyvinylidene fluoride (PVDF), polysulfone (PSf), polyethersulfone (PES) and polyethylenimine (PEI) are some of the polymers used to perform gas separation with hollow fiber membranes [58].

### **1.3.2.2 Membrane Materials**

There is a wide range of materials from which membranes can be produced. Materials such as ceramic [59–61], carbon [62], zeolites [63] and even metals [64] are some of the materials used for membrane production. However, polymeric materials are the most commonly used ones in membrane fabrication due to their properties such as low cost. Polymeric membranes have a wide range of industrial applications, such as microfiltration, ultrafiltration, reverse osmosis and gas separation [14, 15, 65, 66].

Nowadays, there are several polymeric membranes available in the market for different applications. Some of the polymers used are polysulfone, polyimides, cellulose acetate, ethyl cellulose and silicon rubber. There is a correlation between the polymer structure and the selectivity and permeability. Rubbery polymers tend to have high permeability and low selectivity and glassy polymers exhibit low permeability and high selectivity. In the glassy polymers, the gas passage is restricted due to its rigid structure and this results in a high selectivity. For the rubber polymers, the structure is more flexible so it is possible to achieve high gas fluxes but with low selectivities [41].

### **1.3.2.3 Membranes for Gas Separation**

For gas separations processes, polymeric membranes are widely used due to their mechanical strength, easy to produce modular structures and economic processing capacity. To select the adequate polymer to produce a membrane there are some aspects that have to be taken into account such as good permeability and selectivity, durability and thermal and chemical stability of the produced membranes. To evaluate the membrane performance there are two key properties that should be taken in account – selectivity and pressure-normalized flux. The pressure-normalized flux is obtained by simply dividing the flux by the pressure difference between the two sides of the membrane. The selectivity is defined as the ratio between the pressure-normalized fluxes of the different gases and this

ratio gives information about the degree of the separation. Ideally, a high performance membrane should have a high selectivity and a high pressure-normalized flux. These conditions will allow high productivity and purity at reduced operating costs.

In 1991, *Robeson* [67] published an empirical "upper bound" relationship for gas separation using polymeric membranes. In this work, permeability data in the literature for different pairs of gases were put together and plotted. In the produced graph it is possible to identify a "upper bound" where no data is present in the area above it. In 2008 this data was reviewed and updated, Figure 1.8 [68].

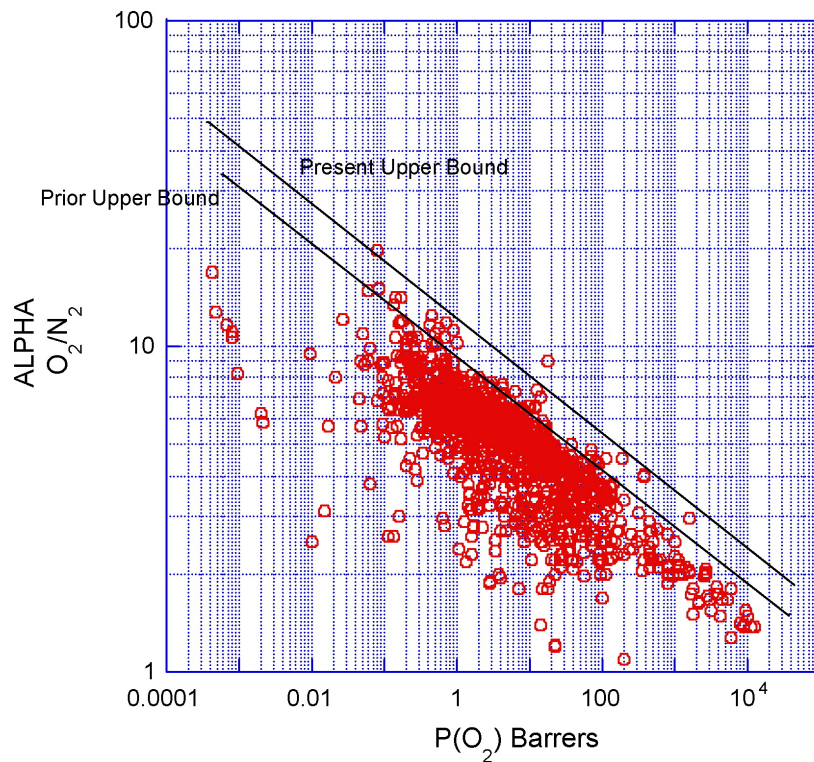


FIGURE 1.8: *Robeson* "upper bound" for oxygen/nitrogen separation [68].

In this graph, it is possible to see the selectivity plotted in the vertical axis and the permeability coefficient in the horizontal one. Each one of the dots represent a different polymer. In the area of high permeabilities and low selectivities are represented the rubbery polymers, that are above the glass transition temperature being their free volume fairly open and will not particularly discriminate the

gas molecules, presenting poor selectivities but high permeabilities. On the other extreme are represented the crystalline polymers (such as PVC) that are below the glass transitions temperature with a very tight free volume. They present low permeabilities but high selectivities. In order to produce membranes with higher fluxes using these promising polymers, it is necessary to obtain very thin and defect free active layers. In the middle of these two classes of polymers are located the amorphous glassy polymers (such as polysulfone) that reveal a good compromise between the permeability coefficient and the selectivities. These polymers tend to be the ones used in membrane fabrication because the technology to produce sufficient thin and defect free active layers has been already put in place in order to get these systems to compete with other gas separation techniques.

#### **1.3.2.4 Gas Transport Mechanisms Through a Membrane**

To perform the separation of a gas mixture it is possible to use a porous or a non-porous membrane, depending on the system being investigated. The difference between these two types of membranes is the mechanism involved in the separation. In porous membranes three different transport mechanisms can be considered - molecular diffusion, viscous diffusion, and *Knudsen* diffusion [69]. Non-porous membranes are defined as dense structures with pore size lower than 5 Å. In these dense materials, the differences in the solubility and diffusion coefficients of the species through the material will dictate the extent of the separation. This mechanism of transport is known as solution-diffusion. Surface area and membrane thickness also have a great impact in the separation. Big surface areas will allow a bigger flux through the membrane while big thickness will have the inverse effect, lowering the flux. In this type of membranes it is important to achieve a defect free dense structure in order to allow only solution-diffusion as transport mechanism, otherwise, if there are pores present, the membrane selectivity can be compromised. These structures are usually more difficult to achieve due to the degree of perfection that needs to be in place.

In non-porous membranes the mechanism is the difference in the solubility and diffusivity of the components in the membrane material [70]. For polymeric gas separation membranes, the separation is achieved according to the solubility of

the gas in the polymer and its diffusion through the polymeric structure. Table 1.2 elucidates the different mechanisms that can occur according to the membrane structure and pore size.

TABLE 1.2: Different gas transport mechanisms depending on the membrane structure and pore size. Adapted from [71].

Membrane	Non Porous	Mesoporous	Porous	
<b>Flow Mechanism</b>	Solution Diffusion	<i>Knudsen</i> Diffusion	Transition Region	Viscous Flow
<b>Pore Size</b>	< 5 Å	5-1000 Å	1000-30,000 Å	> 30,000 Å

As referred before, there are different gas transport mechanisms. These mechanisms will be explored now in more detail.

#### 1.3.2.4.1 Solution-Diffusion

Solution diffusion is the mechanism that occurs in non porous membranes (or membranes with pore size smaller than 5 Å). In this process, the separation is achieved due to two features: *dissolution* of the material in the membrane and *diffusion* of the material through the membrane. The separation is dictated by the difference in the amount of material dissolved and in the rate of diffusion between the different components. According to this model the separation is done in three different steps: A) The gas is dissolved in the high-pressure side of the membrane; B) The gas diffuses through the material; C) The gas suffers desorption in the low-pressure side of the membrane. The diffusion step is the limiting step since the other two are very fast comparing with this one.

At constant temperature and for a single gas, the flow  $Q$  through a material with permeability coefficient  $P$ , area  $A$ , length  $L$  and pressure difference of  $\Delta P$  (between the two sides of the membrane) is given by Equation 1.1.

$$Q = \frac{PA\Delta P}{L} \quad (1.1)$$

The permeability coefficients for the different gases through a material can be found in the literature. *Jones* [8] gathered all the information regarding the permeability coefficients and intrinsic selectivities of oxygen and nitrogen through PVC flat sheets, Table 1.3 (1 *Barrer* =  $10^{-10}\text{cm}^3(\text{SPT})\text{cmcm}^{-2}\text{s}^{-1}\text{cmHg}^{-1}$ ).

TABLE 1.3: Permeability coefficients and intrinsic selectivities for polyvinyl chloride [8].

PVC Intrinsic Selectivity ( $O_2/N_2$ )	Permeability Coefficient $\times 10^{10}$ (Barrer)	
	$O_2$	$N_2$
7.0	0.07	0.01
5.6	0.124	0.022
5.0	-	-
-	-	0.00945
-	-	0.00668
3.0	0.12	0.04
-	-	0.028
5.0	0.05	0.01

#### 1.3.2.4.2 *Knudsen* Diffusion and Viscous Flow

For porous membranes, *Knudsen* diffusion occurs in membranes with pore size between 5 and 1000 Å and viscous flow in membranes with pore size above 30,000 Å. To investigate which of the mechanism is present the *Knudsen* number ( $Kn$ ) is normally used and is defined as follows, Equation 1.2 [69].

$$Kn = \frac{\lambda}{d_p} \quad (1.2)$$

$d_p$  corresponds to the pore diameter and  $\lambda$  corresponds to the gas mean free path that can be calculated using Equation 1.3 [69].

$$\lambda = \frac{k_B T}{\sqrt{2} Pr \pi d_g^2} \quad (1.3)$$

$k_B$  corresponds to the *Boltzman* constant,  $Pr$  to the gas pressure,  $T$  to the gas temperature (in Kelvin) and  $d_g$  to the gas molecule diameter.

If the calculated *Knudsen* number ( $Kn$ ) is greater than 10, the gas molecules are colliding with the pore wall rather than between each other. If this number is lower than 0.1 it is considered that the interactions are mainly between gas molecules and the *Knudsen* diffusion becomes negligible. If the  $Kn$  is in between these two values (0.1 and 10) the two mechanisms need to be considered - viscous flow and *Knudsen* diffusion, Figure 1.9.

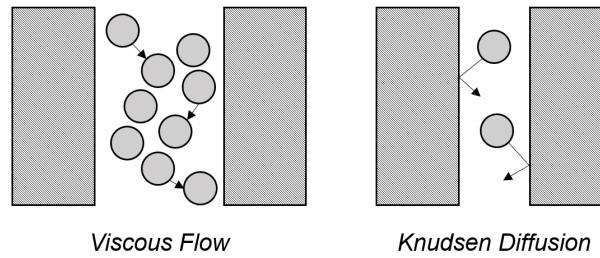


FIGURE 1.9: Schematics of viscous flow and *Knudsen* diffusion gas transport mechanisms through a porous membrane. Adapted from [14].

To calculate the gas mean free path in Equation 1.3, the molecular diameter of the gas molecules should be determined. *Jones* [1] used the kinetic theory, based on experimental gas viscosities, to determine the molecular diameter for the common gases tested in membrane separation (nitrogen, oxygen, carbon dioxide and methane). As in this work only oxygen and nitrogen will be used, only these are presented in Table 1.4.

TABLE 1.4: Molecular diameters obtained for oxygen and nitrogen by *Jones* using the kinetic theory [1].

Gas	Molecular Diameter (Å)
Oxygen	3.59
Nitrogen	3.74

After determining the molecular diameters it is possible to determine the gas mean free path for each one of the species using Equation 1.3. Experimentally, the membranes will be pressurized at a pressure of 5 bar being the interior of the membrane at atmospheric pressure. The pressure to be used in Equation 1.3 should be the average of these two [1]. The temperature used is room temperature and it will be established to be 20°C to perform the calculations. Knowing the mean free path, by assuming a pore diameter of 100 Å it is possible to calculate the *Knudsen* number using Equation 1.2. The results obtained are shown in Table 1.5.

TABLE 1.5: Mean free path for oxygen and nitrogen calculated using Equation 1.3 and the respective *Knudsen* number assuming a pore diameter of 100 Å.

Gas	Mean free path, $\lambda$ (Å)	<i>Knudsen</i> Number, $Kn$
Oxygen	235	65.45
Nitrogen	216	57.75

The selectivity in the *Knudsen* diffusion region for the pair oxygen/nitrogen is given by Equation 1.4.

$$\sigma_{O_2/N_2} = \sqrt{\frac{MW_{N_2}}{MW_{O_2}}} \quad (1.4)$$

Substituting the adequate values of the molecular weights in the equation a value of 0.94 is given for the *Knudsen* diffusion selectivity for the oxygen/nitrogen pair. This selectivity it is not desirable because it shows poor separation between the components.

### 1.3.2.5 Production of Hollow Fibre Membranes for Gas Separation

There are a three techniques to produce polymeric membranes - phase inversion process, thermally induced phase separation (TIPS) and diffusion induced phase separation (DIPS) [72]. To produce hollow fiber membranes the most used spinning methods are melt spinning, dry spinning, wet spinning and dry/wet spinning [1]. The central piece of equipment in a spinning technique is the *spinneret* with some studies already published about how this piece can influence the properties of the produced fibres [73, 74]. In this work hollow fibre membranes will be produced using the dry/wet method so a major importance will be given to this preparation technique.

A schematics of the spinning process is represented in Figure 1.10.

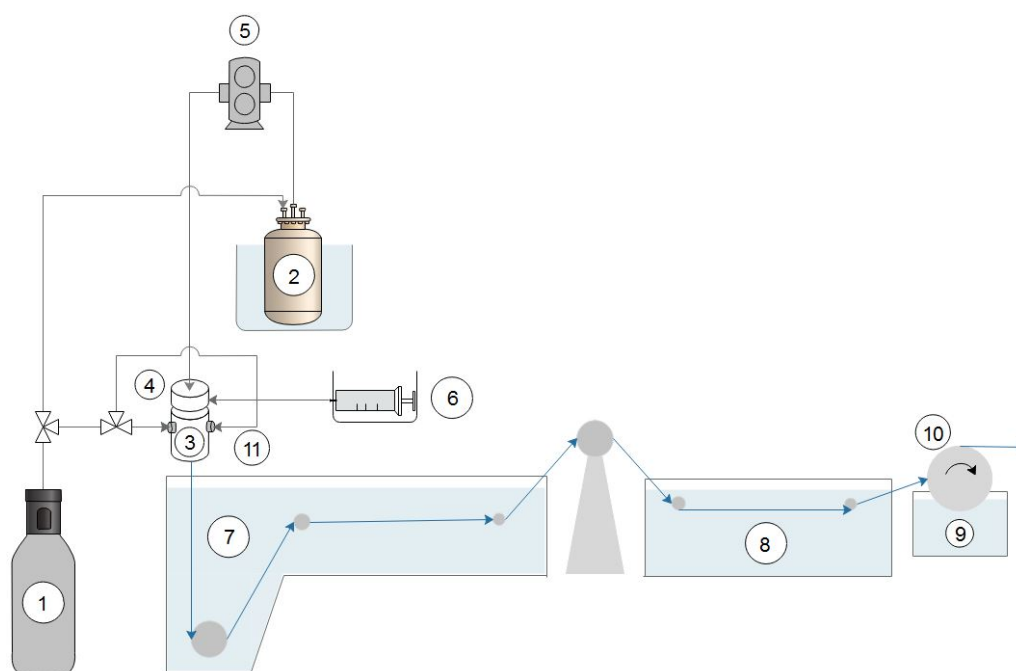


FIGURE 1.10: Membrane spinning apparatus (1-Nitrogen cylinder, 2-Polymer solution vessel, 3-Forced convection chamber, 4-Spinneret, 5-Gear pump, 6-Syringe pump, 7-External bath, 8-Wash bath, 9-Wind-up bath, 10-Wind-up drum, 11-Nitrogen entrance).

A schematic of the *spinneret* outlet is represented in Figure 1.11.

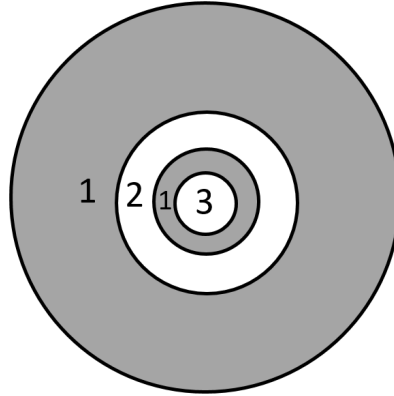


FIGURE 1.11: Schematic of the *spinneret* outlet (1-Stainless steel, 2-Dope extrusion rig, 3-Bore fluid outlet).

The first step when preparing membranes consists in the preparation of the polymer solution. All the components of the mixture must be soluble in each other in order to achieve homogeneity. During the production of hollow fibers there are two phase separation processes that occur simultaneously. While a dry phase separation happens in the outside surface of the membrane to obtain an ultra thin defect-free skin, in the inside surface a wet phase separation occurs due to the passage of a bore fluid to form the lumen of the fiber [75]. The solvents and the non-solvents have a major influence in the structure and performance of an asymmetric membrane. The preparation of the polymer solution involves the use of a high volatile solvent in combination with a low volatile one.

After preparation, the solution is pumped through the *spinneret*. The *spinneret* is constituted by an outer annulus through which will flow the polymer solution and by a central hole through which will flow the bore fluid. This fluid will allow the formation of the inner wall of the membrane giving it structural stability. After the *spinneret* a forced convection chamber is located. In this chamber the spun membrane will contact with nitrogen that will induce the coagulation of the external wall. After a residence time, the fiber is immersed in a non-solvent bath in which the phase inversion occurs. Finally, the fiber is collected in a drum. During this process there are a lot of parameters that should be optimized to obtain the hollow fibers with the desired characteristics. These parameters are the amount and type of polymer, solvents, extrusion rate of the polymer solution, the bore fluid rate, the “jet-stretch” ratio, the residence time in the air gap and

the dimensions of the *spinneret*. Also the composition of the polymer solution, the composition of the coagulation bath, and its temperature are important parameters [14].

To perform the gas permeation tests, single membranes are potted and tested. A major problem with asymmetric membranes is their susceptibility to have defects in the active layer that may cause a drastic fall in selectivity. Silicone coating is a technique that allows to repair the defects in the membrane wall and was first used by *Hines* and *Tripodi* [76]. This polymer exhibits high permeability and low selectivity and seals the defects effectively. Usually, the membranes are tested before and after the coating process to understand the influence of the coating in the properties of the membranes.

To obtain the physical properties of the hollow fiber membranes some techniques are used - surface morphology (Scanning Electron Microscope (SEM), Atomic force microscopy (AFM)) and state of the material evaluation (Differential Scanning Calorimetry (DSC)) [58].

One of the concerns in membrane technology is the use of harmful chemicals during the process of production. A recent research study shows that is possible to produce hollow fiber membrane using less hazardous solvents. Ionic liquids (ILs), methyl and ethyl lactate, dimethylsulfoxide are some examples of promising substitutes for dimethylformamide, methylpyrrolidone and dimethylacetamide [77].

## 1.4 Phase Inversion Mechanisms in Membrane Formation

### 1.4.1 Ternary Phase Diagrams

During membrane production, the phase inversion process is one of the most important steps since it dictates which membrane micro structure will be achieved. In the phase inversion process the starting point is the preparation of a thermodynamically stable solution that will be subjected to demixing. In this process

a polymer in solution is transformed in a solid via a liquid-liquid process - an initial liquid is separated in two liquid phases, one rich in polymer and another poor in polymer. The control of this process can lead to porous or nonporous membranes.

The use of phase diagrams is an important tool to better understand the phase separation phenomenon in membrane formation and if a specific polymer in a specific solvent (or solvent mixture) is suitable for membrane formation [15]. However, these diagrams only allow to predict the type of phase transitions that can occur based on thermodynamic aspects. The kinetics of the system is the key to determine which transitions are to follow and in which dimension.

Temperature dependent ternary diagrams are represented as a pyramid where each "slice" will be a triangle that represents the phase diagram for a specific temperature (isothermal).

An example of a polymer ternary diagram with the different regions highlighted can be seen in Figure 1.12.

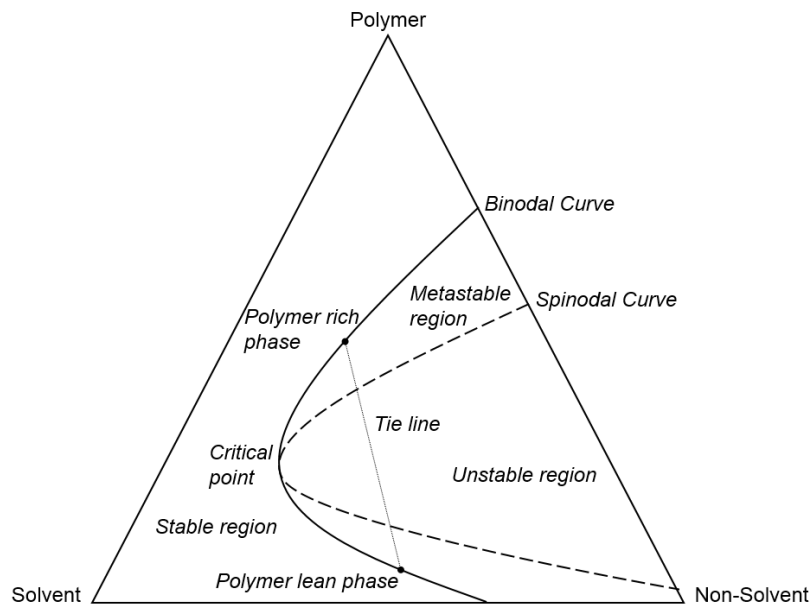


FIGURE 1.12: Example of a polymer ternary diagram with the binodal and spinodal lines. Adapted from [78]

In a ternary diagram, each pure component is represented in a corner and the

sides of triangle represents binary mixtures. All the points located inside the triangle are ternary mixtures. In a generic phase diagram, two different regions can be identified - a homogeneous and a heterogeneous region. These regions are delimited by a binodal curve and the area inside this region is the heterogeneous zone.

A system can also have a spinodal curve that divides the heterogeneous region in two - a unstable region, located inside the spinodal curve and a metastable region located between the spinodal and the binodal. The point where the binodal and the spinodal boundaries cross is named critical point.

In the unstable region, the phase separation will be very quick by spinodal decomposition and, in the metastable region, the solutions are stable while small variations in the compositions are present. However, liquid-liquid demixing will happen if these variations are large enough by a nucleation and growth process. If the final composition is located in the metastable region above the critical point, the liquid-liquid demixing occurs by nucleation of the polymer lean phase while this process occurs in the polymer rich phase if the final composition is located below the critical point in the metastable region. The growth of the formed nucleus is driven by the concentration gradient en route to the nucleus.

Inside the unstable region, where spinodal decomposition happens, even small variations in the compositions will lead to the solution to phase separate. Contrary to what happens in the metastable region, in this case a bi-continuous structure is formed where the polymer rich and the polymer lean phase are interlinked.

As mentioned before, when a solutions reaches the heterogeneous system, two phases are formed via a liquid-liquid demix process - a polymer rich phase and a polymer lean phase - and the compositions can be calculated using tie-lines and the lever rule. The solidification of the polymer-rich phase depends on the nature of the polymer and can occur via crystallization, gelation or vitrification. As crystallization is a slow process, during membrane formation this process is unlikely to occur [14]. Figure 1.13 exemplifies a phase diagram of a ternary mixture showing the gelation and the vitrification areas.

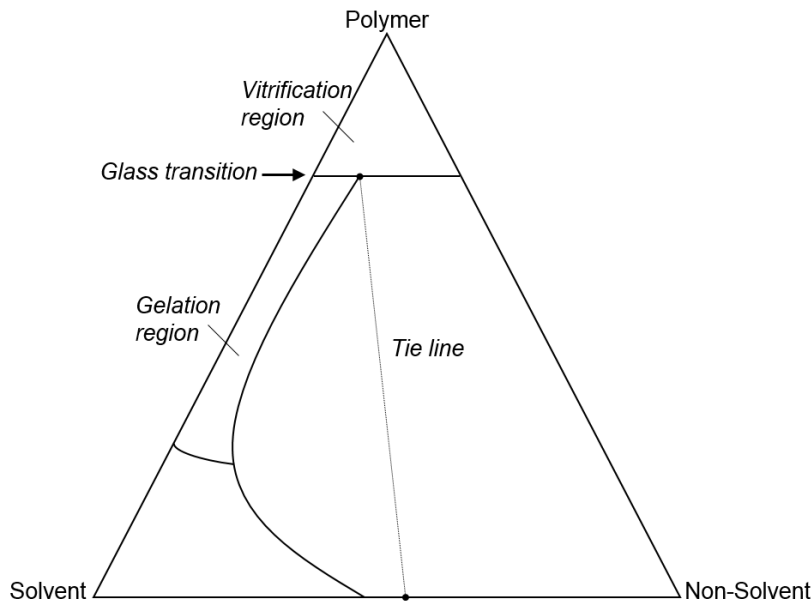


FIGURE 1.13: Phase diagram of a ternary mixture showing the vitrification and the gelation region. Adapted from [14].

Vitrification is a process that occurs when the glass transition temperature is exceeded and the mobility of the polymer chain decreases drastically being in a frozen state. In amorphous polymers this is the mechanism of solidification when crystallization or gelation does not occur. Gelation is a process when a three dimensional network is produced due to the physical or chemical cross linking. In this phenomena micro crystallites are formed and instead of growing they connect different polymer chains. A more viscous polymer is then converted in a system of infinite viscosity by a sol-gel transition. PVC is an example of a polymer that can exhibit gelation behaviour in membrane formation [14].

As PVC has around 10% of crystallinity, it is expected that the gelation process is initiated by the formation of microcrystallites that connect various polymer chains resulting in a three dimensional network [16, 79].

#### 1.4.2 Skin Formation Mechanisms and Techniques

Different coagulation pathways can occur in membrane production, leading to distinct final structures. As stated before, the starting point is a thermodynamic

stable solution. Considering a solution with starting composition near the critical point (point 1) and ending point in the metastable phase, two situations can occur in terms of path of composition change, Figure 1.14 [80].

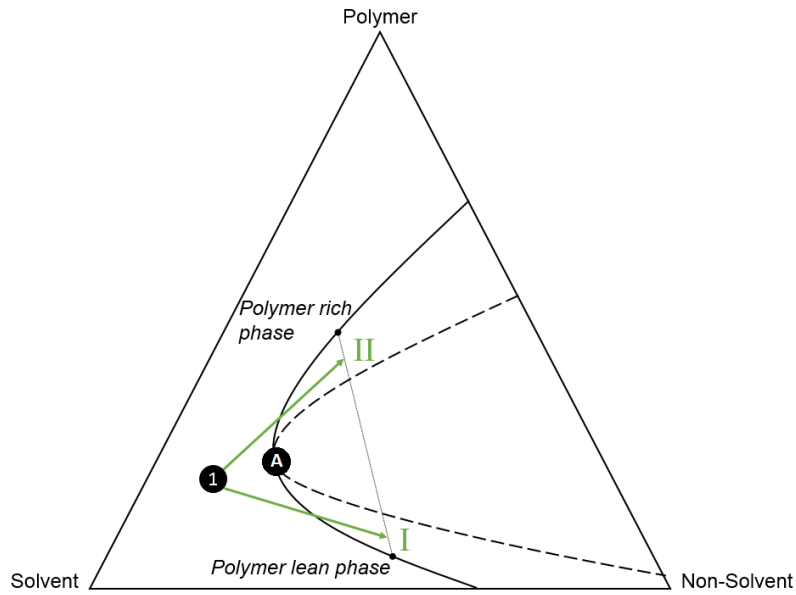


FIGURE 1.14: Schematics of the two different compositions change pathways that lead to phase separation in the metastable region.

- Coagulation path I: If the transfer of solvent and non-solvent is such that this is the pathway of composition change, nucleation and growth mechanisms are involved in the phase separation process. In terms of compositions, using the lever rule it is possible to see that the percentage of polymer lean phase will be much bigger than the one corresponding to the polymer rich phase. The polymer rich phase will nucleate and form particles within the polymer lean phase. The material that results from this process is a latex.
- Coagulation path II: Following this coagulation pathway, the phase separation will lead to two phases in equilibrium with a percentage of polymer rich phase higher than the polymer lean phase. There will be nucleation and growth sites on the polymer lean phase sitting within the predominant

polymer rich phase which is solid at this point. This originates a closed cell sponge structure.

However, both pathway I and II do not originate the structure desirable for membrane manufacture. In order to achieve good performances for gas separation it is necessary to obtain a structure containing a non-porous active layer with a porous support underneath.

For an asymmetric membrane to have ideal gas separation features, some requirements must be met [81]:

- The membrane surface (active layer) should be defect free in order to solution diffusion to be the only present transport mechanism in order to achieve the best selectivity;
- To achieve high fluxes, the active layer should be as thin as possible;
- The substructure should be porous in order to avoid any gas transport resistance, working only as a support for the membrane.

All these requisites make the production of asymmetric membranes a challenge. Two different fabrication processes were proposed in the literature in order to obtain membranes with non-porous skins. *Smolders* [14] and his co-workers at the University of Twente (Netherlands) proposed a mechanism called delayed demixing and *Pinnau* and *Koros* [81] and his co-workers at the University of Texas a nodule coalescence and growth mechanism (also known by forced convection spinning). These two mechanisms are represented in Figure 1.15 in terms of ternary diagram concentration pathway starting from point 1.

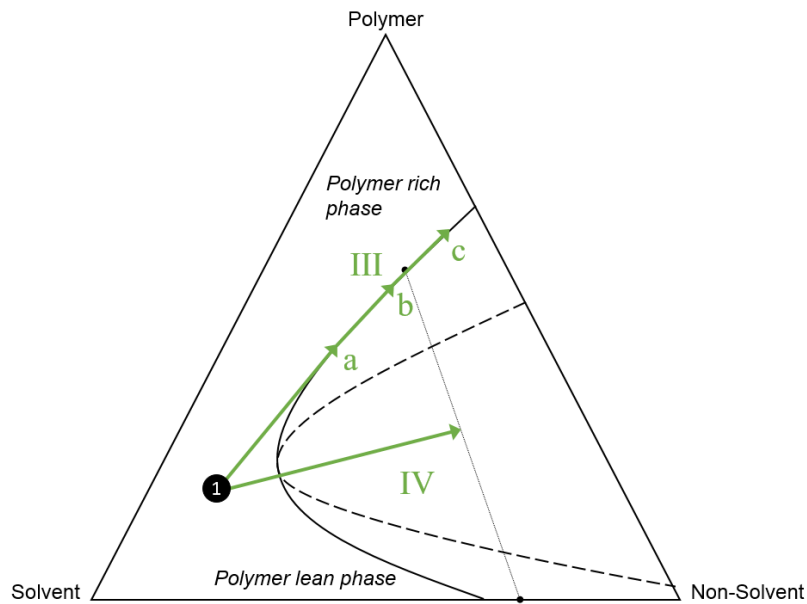


FIGURE 1.15: Schematics of the two different compositions change pathways that lead to the formation of asymmetric membranes.

- Coagulation path III: *Delayed Demixing* - Accordingly with this mechanism, starting from point 1, the mixture of solvent and non-solvent in the coagulation bath should be such that the pathway of precipitation as the fibre is passing through the bath is the one indicated with the arrows, along the polymer rich line. This path will generate an appreciable polymer rich phase and an infinitesimal amount of polymer lean phase. In practice, it will exist only one phase and pores will not be form since these are a consequence of the existence of a polymer lean phase. If the residence time in the bath is sufficiently high, by the end of the process point *c* will be reached. This point will represent such a high level of polymer that hopefully the vitrification point will be exceeded. If this point is reached, mechanical stability is achieved and the fibre is solid and fully formed, at least as far as the skin is concerned.

Figure 1.16 shows the correspondence between the different stages (a, b, and c) and the position in the coagulation bath for a hollow fibre membrane.

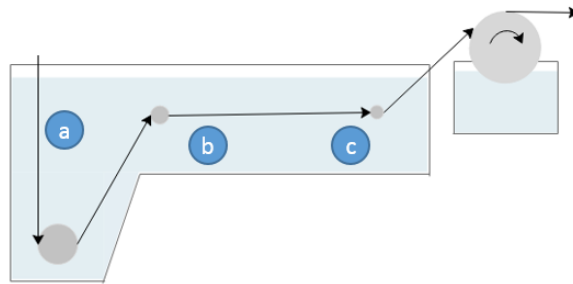


FIGURE 1.16: Correspondence between the solution concentration change position in Figure 1.15 and the position of the fibre in the coagulation bath.

- Coagulation path IV: *Nodule Coalescence and Growth/Forced Convection Spinning* - This method of membrane formation is called dry/wet process. In the first part of the process, the membrane passes through a forced convection dry gap and nitrogen gas is blasted into the membrane in order to evaporate the solvent from the polymer solution. During this forced convection dry gap, the pathway for precipitation can be represented by arrow IV. As this falls into the unstable region, the phase separation is very quick and spinodal decomposition is achieved. In this situation appreciable amounts of both polymer rich and polymer lean phase are present [82]. This will lead to a material where the two phases are continuous with a nodular structure composed by polymer rich phase with the polymer lean phase inter dispersed in it [83, 84].

Figure 1.17 shows examples of structures formed by nucleation and grow and spinodal mechanisms.

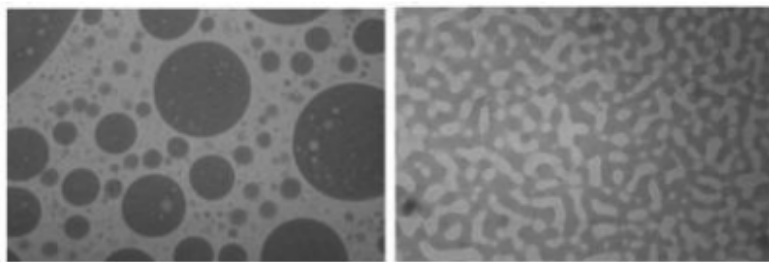


FIGURE 1.17: Example of structures obtained by nucleation and growth (left) and spinodal decomposition (right). [85]

Work published by *Kesting* [86] in 1973 suggested the existence of a coalescence of nodular structures as having a big contribution in membrane formation. Accordingly to *Cahn* [82], there is a periodicity in the characteristic lengths between these nodules. The mechanism for this process was later proposed by *Pinnau* and *Koros* [81] based on work done by *Brown* [87]. *Brown* studied film formation of emulsions containing water and latex. During the drying step he proposes that the film formation is due to capillary pressures. Ignoring the other forces present, if these capillary pressures ( $F_C$ ) are bigger than the resistance of the polymer to deform ( $F_G$ ), a dense film should be formed, Equation 1.5 [87].

$$F_C > F_G \quad (1.5)$$

Each one of the forces can be described as follows, Equation 1.6 and 1.7 [87].

$$F_C = 12.9 \left( \frac{\alpha}{r} \right) \times A \quad (1.6)$$

$$F_G = 0.37 \times 0.37 G_t \times A \quad (1.7)$$

In the equations above  $G_t$  corresponds to the shear modulus,  $\alpha$  to the surface tension,  $A$  to the sphere area and  $r$  to its radius.

For the film formation to be favourable to happen, a condition based on the shear modulus can be established, 1.8 [87].

$$G_t < 35 \times \left( \frac{\alpha}{r} \right) \quad (1.8)$$

As the shear modulus is used as condition for the film formation, and its value depends on the conditions, a wide range of polymers can be used for film formation if the right conditions are achieved. One of the parameters that influences the shear modulus is the temperature and this effect will be studied for quaternary PVC solutions later in this work. Making a comparison of this mechanism with a two-phase system resulting from a spinodal decomposition, the polymer rich phase will form nodules and the polymer lean phase will cause capillary pressure, Figure 1.18.

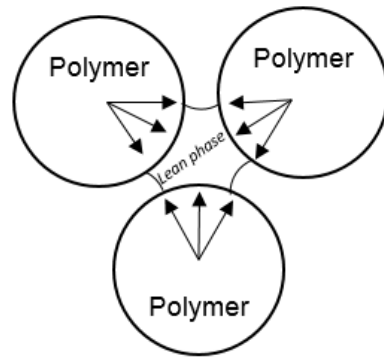


FIGURE 1.18: Schematics representing the forces resulting from a polymer lean phase dispersed in a nodular polymer rich phase. Adapted from [87].

Assuming that the vitrification point is not reached yet, the nodules are still "soft" and, if the capillary pressures are high enough the nodules will be drawn together, coalesce and form a non-porous active layer. If this mechanism happens in the first few angstroms, there will be a chance to produce a decent active layer that allows gas separation to occur.

The transition from a rubbery state to a glassy state (that happens at the glass transition temperature,  $T_g$ ) is usually achieved by changes in the temperature of the system. There are some conditions that can have influence on the  $T_g$  of a substance such as the heating rate and the molecular weight. For most of the polymers there is an increase in the glass transition temperature with the increasing in the molecular weight [88]. In 1950, *Fox* and *Flory* [89] developed an expression that relates the glass transition with the molecular weight, Equation 1.9.  $T_{g,\infty}$  corresponds to the glass transition temperature at infinite molecular

weight and  $K_{fv}$  is a constant related with the free volume present in the polymer sample.

$$T_g = T_{g,\infty} + \left( \frac{K_{fv}}{M_n} \right) \quad (1.9)$$

Studies made by some authors showed that a polymer solution achieves the glassy state if its polymer content is greater than 70% (v/v) [90, 91]. This shows that, by varying the concentration of polymer in the solution, the glassy state can be achieved. When the glassy state is reached the polymer molecules lose mobility with only vibrational and short range rotational motions being present. This will also lead to a lower specific volume of the polymer, reducing the space between the polymer molecules, Figure 1.19.

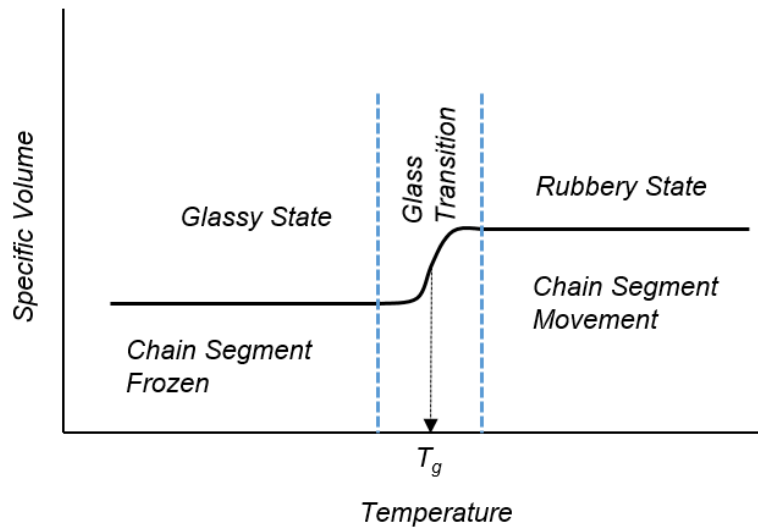


FIGURE 1.19: Schematics representing the glass transition temperature, the change in the specific volume and the chain segment status in the glassy and rubbery state. Adapted from [92].

In order for the glassy state to be achieved, the transition should be quick. This phenomena can be useful in membrane fabrication because any orientation that is achieved during a spinning/extrusion process can then be locked when the system

reaches the glassy state. The reduction in the specific volume can also benefit the separation since it will lead to a less porous structure. However, for a polymeric solution with 70% (v/v) of polymer concentration, and therefore in the glassy state, the shear modulus can vary from 100-1000MPa [81]. As can be seen by Equation 1.8, the nodule radius plays an important role to determine whether the conditions to film formation are met or not. Taking into account the particle size distribution in the polymer solution that allow the production of dense layers with adequate thickness for gas separation and the surface tension of organic solvents in polymer solutions, a range of shear modulus can be determined - from 7-70MPa - which is much smaller than the shear modulus obtained for the glassy state [1].

Compiling the information above, in order for a structure to be formed according to the coalescence and growth mechanism, the size of the nodules should be small enough in order to overcome the capillary forces and to deform the nodule. For this to happen, the spinodal decomposition should be such that the tie-line does not touch the vitrification area. Following these conditions it will be possible to obtain a dense layer formed by coalescence and growth of the polymer nodules that will seal the structure and the underneath layer will stay open since no capillary pressure is present any more, forming a porous structure.

### 1.4.3 Prediction of Polymer Ternary Diagrams

In order to produce membranes using the dry/wet methods, a polymer solution consisting of at least three components needs to be prepared. These components are the polymer, a solvent and a non-solvent. However, in some cases an additional solvent with high volatility can be added leading to "pseudo-ternary" diagrams where both solvents are plotted together. The addition of this solvent has the purpose of shift the composition position in the ternary diagram in the dry gap. In the dry gap, forced convection happens and the high volatile solvent is evaporated from the membrane surface, making the composition position in the diagram to change in the direction of the polymer/non-solvent axis (pathway

IV in Figure 1.15).

The structure of an asymmetric membrane is dependent on the thermodynamics and kinetics of the liquid-liquid phase separation [93]. In order to understand these mechanisms, it is important to have access to the ternary diagram (polymer/solvent/non-solvent) of the mixture that is being studied. This will allow to define the phase separation conditions in order to achieve the desired membrane structure, as discussed previously.

A ternary diagram gives information about the position of the binodal and the spinodal curves. When the phase separation occurs via binodal decomposition (by nucleation and growth) and the solution is divided in two accordingly with the tie-lines, these two solutions are in equilibrium and have the same chemical potential [80]. For a binary system, if the *Gibbs* free energy is plotted against the mole fraction of one of the species, a minimum is achieved, related with the binodal decomposition. Inflection points can be observed and correspond to the spinodal decomposition. For ternary systems the approach is not that simple and different mathematical models can be applied in order to build the phase diagrams and understand the thermodynamic and the kinetics of the system. The most common model used in the literature is the *Flory-Huggins* Model that will be discussed in the next section.

#### 1.4.3.1 *Flory-Huggins* Model

The *Flory-Huggins* model is commonly used to predict ternary phase diagrams and is based in a lattice model to describe the entropy of mixing of a polymer solution [14]. In the literature, many references can be found in which this model is used to predict polymer ternary phase diagrams [94–98].

Different quaternary systems were already studied comprising various combinations of components - a system composed by a non-solvent, two solvents and a polymer [99] and a system composed by three polymers and one solvent [100]. In 1998, *Kools* [101] studied a quaternary system formed by a polymer and three other components with low molecular weight using the *Flory-Huggins* approach. In the *Flory-Huggins* approach, the *Gibbs* free energy is related with the volume

fractions of each component and also considers the interactions between each pair in the system [20, 102, 103]. For a given system, the location and extent of the binodal and spinodal regions are depending on these parameters as follows [15]:

- *Polymer/non-solvent interaction*: Dictates the extent of the liquid-liquid demixing region. The bigger is this interaction parameter, the higher (in terms of polymer concentration) is the point at which the boundary crosses the polymer/non-solvent axis;
- *Polymer/solvent interaction*: Dictates the magnitude of the liquid-liquid demixing region. The bigger the affinity between this pair, the smaller is these magnitude.
- *Solvent/non-solvent interaction*: High affinity will increase the magnitude of the liquid-liquid demixing region.

Parameters such as molar volumes, molecular weight and molecular weigh distributions have a really low impact in the phase diagram structure when compared with the interaction between the different species present in the mixture.

For a quaternary system the variation in the enthalpy of mixing ( $\Delta G_m$ ) can be presented as follows, Equation 1.10 [101].

$$\begin{aligned} \frac{\Delta G_m}{RT} = & n_1 \ln \phi_1 + n_2 \ln \phi_2 + n_3 \ln \phi_3 + n_4 \ln \phi_4 + n_1 \ln \phi_2 g_{12} + n_1 \ln \phi_3 g_{13} + \\ & n_1 \ln \phi_4 g_{14} + n_2 \ln \phi_3 g_{23} + n_2 \ln \phi_4 g_{24} + n_3 \ln \phi_4 g_{34} \end{aligned} \quad (1.10)$$

$R$  represents the gas constant and  $T$  the temperature. The subscript numbers refers to each one of the four components in the mixture,  $n_i$  to the number of moles and  $\phi_i$  to the volume fraction of the component  $i$ . The parameter  $g_{ij}$  is

the concentration-dependent interaction parameter between the pairs of species present in the solution. Although this equation represents a quaternary system, these binary interaction parameters were referred in the literature as a success to describe these type of systems [104–107].

To calculate the chemical potential, the expression for the *Gibbs* free energy should be derived with respect to the molar fraction of each component, Equation 1.11 [101].

$$\mu_i = \left( \frac{\delta G_m}{\delta n_i} \right)_{T,P,n_j \neq i} \quad (1.11)$$

To simplify the appearance of the formula, the ratio between the different molar volumes  $V_i$  is expressed in the variables  $s$ ,  $r$  and  $t$ .

For simplification, the ratios between the different molar volumes ( $\bar{V}$ ) and volume fractions are defined by the variables  $s$ ,  $r$ ,  $t$ ,  $u_i$ ,  $\nu_i$  and  $w_i$ , defined as follows, Equation 1.12, 1.13, 1.14, 1.15 1.16 and 1.17 [101].

$$s = \frac{\bar{V}_1}{\bar{V}_2} \quad (1.12)$$

$$r = \frac{\bar{V}_1}{\bar{V}_3} \quad (1.13)$$

$$t = \frac{\bar{V}_1}{\bar{V}_4} \quad (1.14)$$

$$u_i = \frac{\phi_i}{\phi_i + \phi_1} \quad (1.15)$$

$$\nu_i = \frac{\phi_i}{\phi_i + \phi_2} \quad (1.16)$$

$$w_i = \frac{\phi_i}{\phi_i + \phi_3} \quad (1.17)$$

Using this equation, the chemical potentials for each one of the species can be derived, Equation 1.18, 1.19, 1.20 and 1.21 [101].

$$\begin{aligned} \frac{\Delta\mu_1}{RT} = & \ln \phi_1 - s\phi_2 - r\phi_3 - t\phi_4 + (1 + \phi_2g_{12} + \phi_3g_{13} + \phi_4g_{14})(1 - \phi_1) \\ & - sg_{23}\phi_2\phi_3 - sg_{24}\phi_2\phi_4 - rg_{34}\phi_3\phi_4 - \phi_2u_2(1 - u_2)\left(\frac{\delta g_{12}}{\delta\mu_2}\right) - \\ & \phi_3\mu_3(1 - \mu_3)\left(\frac{\delta g_{23}}{\delta u_3}\right) - \phi_4u_4(1 - u_4)\left(\frac{\delta g_{24}}{\delta\nu_4}\right) \end{aligned} \quad (1.18)$$

$$\begin{aligned} \frac{s\Delta u_2}{RT} = & \ln \phi_2 - \phi_1 - r\phi_3 - t\phi_4 + (s + \phi_1g_{12} + s\phi_3g_{23} + s\phi_4g_{24})(1 - \phi_2) \\ & - g_{13}\phi_1\phi_3 - g_{14}\phi_1\phi_4 - rg_{34}\phi_3\phi_4 + \phi_1u_2(1 - u_2)\left(\frac{\delta g_{12}}{\delta u_2}\right) - \\ & s\phi_3\nu_3(1 - \nu_3)\left(\frac{\delta g_{23}}{\delta\nu_3}\right) - s\phi_4\nu_4(1 - \nu_4)\left(\frac{\delta g_{24}}{\delta\nu_4}\right) \end{aligned} \quad (1.19)$$

$$\begin{aligned} \frac{r\Delta\mu_3}{RT} = & \ln \phi_3 - \phi_1 - s\phi_2 - t\phi_4 + (r + \phi_1g_{13} + s\phi_2g_{23} + r\phi_4g_{34})(1 - \phi_3) \\ & - g_{12}\phi_1\phi_2 - g_{14}\phi_1\phi_4 - rg_{24}\phi_2\phi_4 + \phi_1u_3(1 - u_3)\left(\frac{\delta g_{13}}{\delta u_3}\right) + \\ & s\phi_2\nu_3(1 - \nu_3)\left(\frac{\delta g_{23}}{\delta\nu_3}\right) - r\phi_4w_4(1 - w_4)\left(\frac{\delta g_{34}}{\delta w_4}\right) \end{aligned} \quad (1.20)$$

$$\begin{aligned}
\frac{t\Delta\mu_4}{RT} = & \ln \phi_4 - \phi_1 - s\phi_2 - r\phi_3 + (t + \phi_1g_{14} + s\phi_2g_{24} + r\phi_3g_{34})(1 - \phi_4) \\
& - g_{12}\phi_1\phi_2 - g_{13}\phi_1\phi_3 - sg_{23}\phi_2\phi_3 + \phi_1u_4(1 - u_4)\left(\frac{\delta g_{14}}{\delta u_4}\right) + \\
& s\phi_2\nu_4(1 - \nu_4)\left(\frac{\delta g_{24}}{\delta \nu_4}\right) - r\phi_3w_4(1 - w_4)\left(\frac{\delta g_{34}}{\delta w_4}\right)
\end{aligned} \tag{1.21}$$

$\Delta\mu_i$  corresponds to the difference between the chemical potential of a component  $i$  in the mixture and in the pure state. For two phases, a and b, in a liquid-liquid equilibrium, for a component  $i$ , Equation 1.22 is verified.

$$\Delta\mu_{i,a} = \Delta\mu_{i,b} \tag{1.22}$$

Using all the equations above it is possible to obtain the binodal boundary and the tie-lines for a quaternary system. To obtain the spinodal curve, the second derivative of the *Gibbs* free energy in relation to the volume fraction of the component is used, in a similar way of what was done to calculate the binodal curve.

The drawback of using the *Flory-Huggins* model is difficulty in obtaining the interaction parameters that must be polymer concentration dependent in order to achieve a model that correlates the experimental data with accuracy. Depending on the system being studied, it may be possible to find the binary interaction parameters in the literature. In the case of these parameters not being already determined, they can be estimated using group contribution theory or experimentally.

Table 1.6 shows some experimental techniques that can be used to determine this parameters.

TABLE 1.6: Experimental techniques to determine interaction parameters.

<b>Interaction Parameter</b>	<b>Technique</b>	<b>Reference</b>
Polymer/Solvent	Swelling Measurements, Intrinsic Viscosities	[108–110]
Solvent/non-solvent	Activity data	[107]
Polymer/non-solvent	Light Scattering, Osmometry	[111, 112]

## 1.5 Rheology of Polymer Solutions

### 1.5.1 Importance of Rheology in Membrane Spinning

During the spinning process, due to the passage of the solution through the *spinneret*, the polymer experiences high shear rates. Due to the experimental conditions experienced during the spinning, the shear rates at the outer wall within the *spinneret* can achieve thousands of reciprocal seconds [113]. Also, after the *spinneret*, the new produced fibre experiences an elongation process due to the gravitational force. However, this effect can be negligible if the jet-stretch is equal to one (velocity of extrusion is equal to the velocity of the wind-up drum) [114]. These two phenomena will have a role in the final conformation of the polymer chains, as can be seen in Figure 1.20.

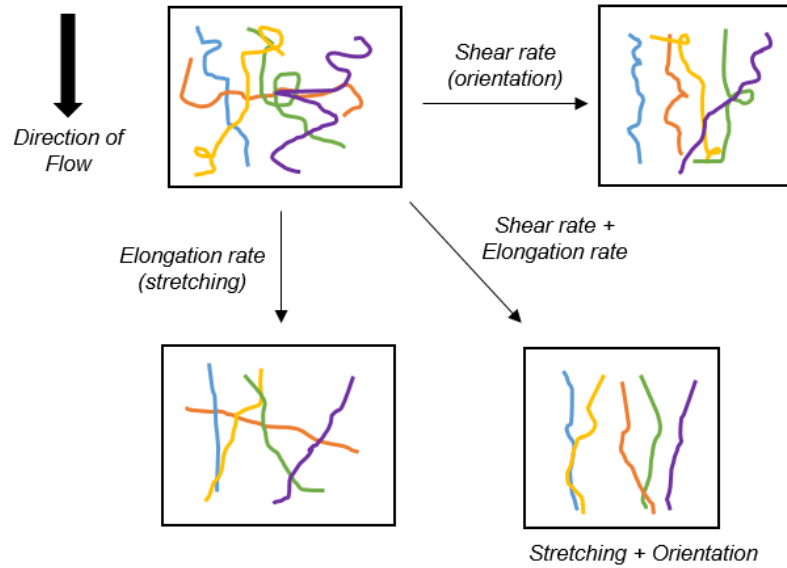


FIGURE 1.20: Schematic representation of the conformation changes of polymer chains induced by elongation and shear rate. Adapted from [58].

The effect of these two parameters, shear and elongation, was already shown to be important to the performance of polysulfone hollow fibre membranes [71, 113]. It is suggested that the performance of these membranes are related with the orientation of the polymer molecules in the membrane active layer and this is supported by plane-polarized infra-red spectroscopy measurements [115, 116]. For the polysulfone membranes prepared, it was observed that an increasing in the membrane dope extrusion rate (and consequently, in the shear rate) resulted in selectivities above the polymer intrinsic selectivity [116, 117].

Before membranologists start giving attention to this subject, *Wolf* [118, 119] had already published studies about the effect of shear in the phase separation properties of polymer blends and solutions. In his studies, the author finds that the introduction of shear in a polymer solution can change the phase diagram and alter the phase separation thermodynamic properties of the system.

When working with polymer solutions with shear thinning behaviour (viscosity decreases with the shear rate) it is expected that the molecular orientation is enhanced by increasing the shear rate. Also, it is expected that this orientation (or alignment) happens in the flow direction [120]. *Ferry* [121] explains this

phenomena using the viscoelastic theory, where the alignment is achieved by stretching the polymer chains between entanglement junctions.

When performing membrane spinning, the higher shear rates are located in the *spinneret* wall and increase with the dope extrusion rate. This suggests that the polymer molecules in the membrane surface became aligned and this orientation is "locked" in the forced convection chamber where the polymer precipitates and the membrane skin is formed. This happens if the polymer relaxation time is greater than the residence time in the chamber.

### 1.5.2 Concepts of Polymer Solution Rheology

Rheology is described as the science that studies the deformation and flow of a material under applied forces and is usually measured using a rheometer [122]. This measurements can be applicable to all different kind of materials - concentrated and diluted solutions, semi-solids, melts, solids, etc [123].

For some materials, depending on the application, the study of rheological features is important in all stages - from formulation to final product performance. Most of the materials can present complex rheological behaviours depending on the conditions applied - stress, strain, time scale and temperature. Shear stress ( $\sigma$ ), shear rate ( $\dot{\gamma}$ ) and viscosity ( $\eta$ ) are the main concepts for a first understanding of rheology aspects. Shear stress corresponds to the force applied per unit of area, shear rate to the change in velocity per distance and, finally, viscosity is the resistance of a material to flow [124]. Figure 1.21 illustrates these basic concepts.

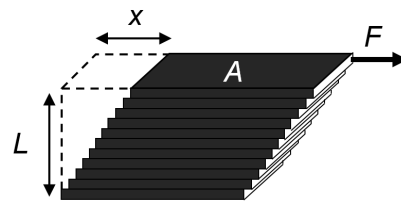


FIGURE 1.21: Example of layers of a fluid sliding over one another under an applied force.

Shear flow can be compared with layers of fluid sliding over each other under an applied force. The applied force is defined as the force  $F$  that is applied on the area  $A$  - shear stress ( $\sigma$ ). This force will originate a gradient of velocity - shear rate ( $\dot{\gamma}$ ) - over the fluid where the top layer moves faster while the bottom layer as zero velocity. The displacement obtained due to the shear stress - shear strain ( $\gamma$ ) - is equal to  $X/L$ .

If a shear stress is applied to a fluid, energy is transferred to the top layer being after transported through the layers by collisions and interactions. This process will reduce the fluid velocity and kinetic energy. Viscosity is the quantitative measurement of the internal fluid friction related with the loss of kinetic energy in the system and is defined as the quotient between shear stress and shear rate, Equation 1.23 [124].

$$\eta = \frac{\sigma}{\dot{\gamma}} \quad (1.23)$$

Fluids can be classified in two big groups concerning its rheology features - *Newtonian* and non-*Newtonian* fluids. The first group corresponds to a fluid which viscosity is independent of the shear rate and the latter to one which viscosity is dependent of the shear rate, for a given temperature. Polymeric solutions are known as non-*Newtonian* fluids so a big emphasis will be give to this class of materials in this work [125].

In the non-*Newtonian* group, four different rheological behaviours can be observed Figure 1.22.

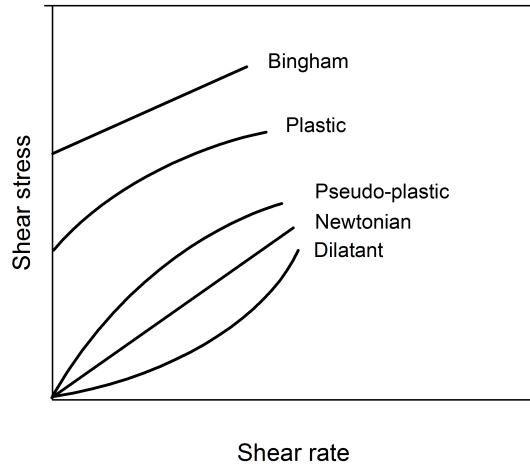


FIGURE 1.22: Flow curves of materials with different rheological features. Adapted from [122].

If the viscosity of a fluid increases with the shear rate the material is called dilatant (shear thickening), contrasting with a fluid in which the viscosity decreases with the shear rate - a pseudo-plastic material (shear thinning). In shear thinning materials, when a material is subjected to sufficient high shear rates particles can rearrange. Polymers can stretch out and align, droplets can organize and deform and elongated particles may align with the flow. All these rearrangements will originate a decrease in the interactions between the molecules and will increase the free space between the particles resulting in a decrease in the viscosity. The three examples described before can be seen in Figure 1.23.

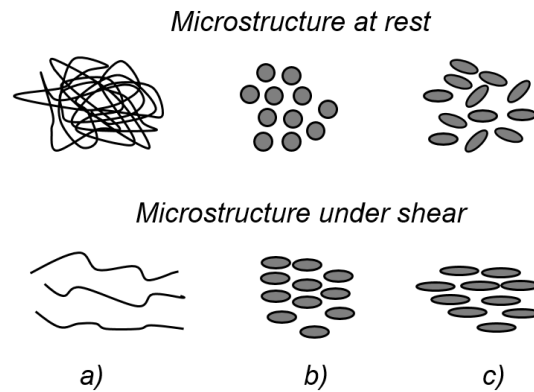


FIGURE 1.23: Example on how different structures may respond to shear. a) polymer chains may disentangle and stretch; b) emulsion droplets can organize and deform; c) elongating particles may align with the flow.

Shear thickening materials are less common in industrial applications. The increase in the viscosity with the increase in shear rate is present in colloids where particles are suspended in a liquid. Initial, at lower shear rates, due to repellent forces between the molecules, they float in the liquid without aggregating. If the shear rates are low this materials can exhibit shear thinning behaviour. However, at a critical shear rate, the energy put into the sample by shear will be enough to counteract the initial repellent forces and the molecules start to stick and form hydro clusters. All this process will conduct to a material with high viscosity [126, 127].

The fluids following Bingham model will show a linear relationship between shear stress and shear rate (like in a *Newtonian* fluid) with the difference that this only happens after an initial shear stress threshold has been reached. Lastly, in a plastic material, also a initial yield stress required for flow to happen but the relationship between shear stress and shear rate is not linear [128].

If the time element is added another type of fluids can be considered. In these materials the viscosity changes over time under constant shear rate - a phenomena called thixotropy [129]. Thixotropy can occur in combination with the flow behaviours described before. This new variable (time) can have different effects on a material under constant shear - some fluids can achieve the final viscosity in seconds while other may take days.

Flow rheology tests are used to determine the general flow behaviour of a sample.

In these experiments, viscosity is measured against shear rate. When the results are plotted (viscosity *vs.* shear rate) a flow curve is obtained. Usually the axes appear in logarithmic scale to facilitate the analysis. In a flow test it is possible to identify the behaviour of a material at slow motions (low shear rates) and at fast motions (high shear rates). If a material under shear is used in a specific application where a particular viscosity is needed, these experiments become very important.

To better understand the results, different models can be fitted to the experimental data accordingly with the behaviour observed. For shear thinning materials (as the solutions studied in this work), the most common models are the *Cross* model, *Power Law* model and *Sisko* model [130]. In Figure 1.24, an example of a flow curve can be observed as well as the ranges of applicability of the three different models mentioned above.

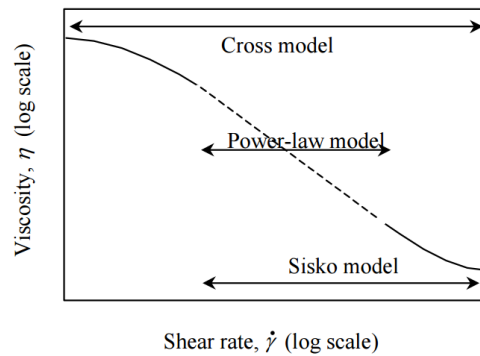


FIGURE 1.24: Example of a flow curve and the range of applicability of the *Cross* model, *Power Law* model and *Sisko* model [130].

These three models are described by the following equations [122]:

$$\text{Cross Model} \quad \frac{\eta - \eta_0}{\eta_0 - \eta_\infty} = \frac{1}{1 + (K_c \dot{\gamma})^m} \quad (1.24)$$

$$\text{Power Law Model} \quad \eta = k_p \dot{\gamma}^n \quad (1.25)$$

$$\text{Sisko Model } \eta = K_c \dot{\gamma}^n + \eta_\infty \dot{\gamma} \quad (1.26)$$

$\eta_0$  corresponds to the shear viscosity;  $\eta_\infty$  to the infinite shear viscosity;  $K_c$  is the *Cross* constant that accounts for the onset of shear thinning behaviour;  $m$  is the shear thinning index (ranges from 0 (*Newtonian*) to 1 (infinitely shear thinning));  $n$  is the power law index and is equal to  $1-m$  and relates with the extent of *Newtonian* behaviour (the more  $n$  is close to 1, the more *Newtonian* is the response);  $k_p$  represents the consistency index, numerically equal to the viscosity at a shear rate of  $1 \text{ s}^{-1}$ .

In 1996, *Shilton* developed a methodology to simulate the flow profile in a spinneret during the extrusion of hollow fibre membranes [115]. This model was built considering a power law fluid passing through a concentric annulus. Using this model it is possible to predict the velocity, shear rate and shear stress profiles. It is well known that the flow conditions affect the properties of hollow fibre membranes due to their direct relation with molecular orientation [115].

Using the appropriate boundary conditions, the shear stress ( $\sigma$ ) profile in a concentric annulus is given by Equation 1.27.

$$\sigma = \frac{1}{2} \left( \frac{dPd}{dZ} - \rho g \right) + \left( r - \frac{r_0^2}{r} \right) \quad (1.27)$$

$r$  corresponds to the annulus radius,  $Pd$  to the pressure drop,  $Z$  to the distance,  $\rho$  to the density,  $g$  to the gravity force.

The shear rate ( $\dot{\gamma}$ ) profile is given by Equation 1.28.

$$\dot{\gamma} = dU_z = \left( \frac{1}{2kp} \left( \frac{dPd}{dZ} - \rho g \right) \left( r - \frac{r_0^2}{r} \right) \right)^{\frac{1}{n}} dr \quad (1.28)$$

$kp$  corresponds to the power law fluid constant and  $n$  to the power law index. Finally, the velocity profile ( $u_z$ ) is given by Equation 1.29.

$$u_z = \frac{U_z}{K_2} \quad (1.29)$$

with,

$$K_2 = R_2 \left( \frac{R_2}{2kp} \left( \rho g - \frac{dPd}{dZ} \right) \right)^{\frac{1}{n}} \quad (1.30)$$

$R_2$  corresponds to the outer radius of the spinneret.

*Shilton* wrote a computer program to calculate these profiles that is available on request. The inputs needed are the *spinneret* dimensions (inner radius, outer radius and *spinneret* length), power law index, power law constant, dope extrusion rate and density.

### 1.5.2.1 Viscoelasticity

Each time a structured fluid is subjected to an applied force and its equilibrium state is perturbed the material responds in order to recover the initial state, as energy is stored in the structure during this process. This response is what is often called an elastic response [122].

Due to energy dissipation, viscous forces are also present. When this two forces are present, a material is referred as viscoelastic. Some examples of viscoelastic materials are polymer melts and polymer solutions [121]. Normal stresses are the forces generated when the material tries to counter the imposed stresses [131].

Viscoelasticity can be linear or non-linear depending if the stress and strain have a linear or non-linear relationship between each other. Also, for a material to

have such "ideal" behaviour, this relationship must be true at any given time.

In the majority of viscoelastic materials, the time is an important factor as it has a significant impact in their flow features. In 1964, *Reiner* [132] introduced another important concept in rheology - the dimensionless Deborah number, defined as the ration between relaxation time and observation time. There is a relationship between the time scale and the rheological features of a material. According to the author, *"the greater the Deborah number, the more solid the material; the smaller the the Deborah number, the more fluid it is"*. The explanation behind this quote is related with the fact that if the experiment time scale is inferior to the relaxation time, elastic features will be predominant. However, if the experiment time scale is bigger, the elastic domains will have sufficient time to relax making viscous features to predominate. This suggests that all materials will flow if sufficient time is given (glass is a good example of a material with a large Deborah number) [132].

#### **1.5.2.1.1 Oscillatory Rheology**

Oscillatory rheology becomes very important when testing materials that have the ability to experience macro or micro structural rearrangements as function of time that will have influence on their rheological properties. This type of experiments will allow to understand how the material changes over time. In an oscillatory experiment, a sinusoidal shear or stress is introduced in the sample and the stress or strain response is recorded. Usually this test is made over a range of oscillation frequencies ( $\omega$ ) and this is what determines the time scale of the deformation (as the frequency corresponds to the inverse of time). Short times are represented by high frequencies and long times by small frequencies.

In the case that a specific strain is applied and the stress is measured:

- For an ideal elastic solid, the stress response is in phase with the sinusoidal strain applied. In this case, the stress will be proportional to the imposed strain with a proportional constant that corresponds to the shear modulus of the sample.

- For a purely viscous material, the stress response is out of phase (with a phase angle of  $\pi/2$ ). In this case, the stress is proportional to the applied strain rate with viscosity being the proportional constant.
- If a material has both elastic and viscous features, a mix of the previous two responses will be obtained, and the material is said to be viscoelastic.

Figure 1.25 shows the relation between stress and strain for a purely elastic, purely viscous and a viscoelastic material and the values of the phase angle ( $\delta$ ) for each case.

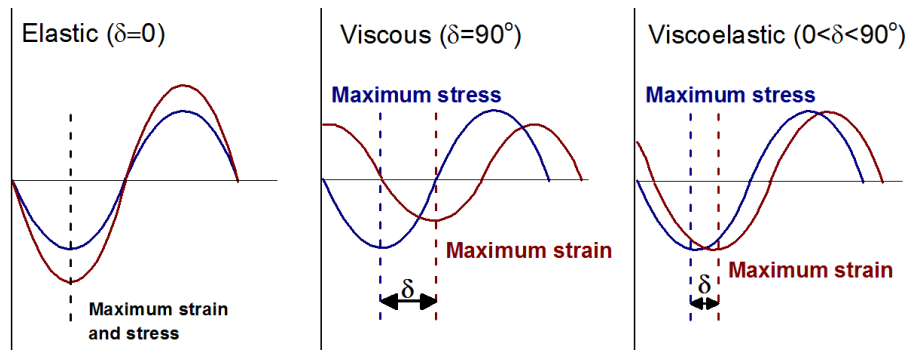


FIGURE 1.25: Relation between stress and strain for a purely elastic, purely viscous and a viscoelastic material ( $\delta$ =phase angle).

It is the phase difference between the strain and the stress waves that allows the measurement of viscous and elastic characteristics of the material. For a purely elastic material  $\delta=0$ , for a purely viscous  $\delta=90^\circ$  and for a viscoelastic material  $0<\delta<90^\circ$ . A phase angle of  $45^\circ$  represents the boundary between liquid like and solid like features.

The complex modulus  $G^*$  is given by Equation 1.31 and measures the resistance of a material to deformation [133].

$$G^* = \frac{\sigma_{max}}{\gamma_{max}} \quad (1.31)$$

In an oscillatory experiment, a material that exhibits viscoelastic features can be characterised by two parameters - the storage modulus ( $G'$ ) and the loss modulus ( $G''$ ).  $G'$ , the storage modulus, accounts for the elastic solid like behaviour and the loss modulus for the viscous response.  $G^*$  can be expressed by these two parameters according to Equation 1.32. For polymer systems, the phase angle can be given by the loss tangent ( $\tan \delta$ ) that is given by  $G''/G'$ .

$$G^* = \sqrt{G'^2 + G''^2} \quad (1.32)$$

The storage modulus characterizes the solid behaviour of a material while the loss modulus characterizes the fluid-like behaviour. If a sinusoidal strain, given by Equation 1.33, is imposed to a viscoelastic material, the stress response will be defined by Equation 1.34 (where  $\omega$  represents the frequency) [133].

$$\gamma(t) = \dot{\gamma} \times \sin(\omega t) \quad (1.33)$$

$$\sigma(t) = \gamma_0 [G'(\omega) \sin(\omega t) + G''(\omega) \cos(\omega t)] \quad (1.34)$$

In order to characterize the solid or fluid features of the material,  $G'$  and  $G''$  are measured at different frequencies that will reproduce short and long time scales behaviour. These frequency dependent experiments are made at constant applied strain. To decide with strain rate should be used an amplitude strain test is performed, with  $G'$  and  $G''$  recorded against the strain rate. As showed in Figure 1.26, until a critical strain is reached,  $G'$  and  $G''$  are independent of the strain and, beyond this point, the material will behave in a non-linear fashion.

The idea is to perform the oscillatory tests in the Linear ViscoElastic Region (LVER) ) where the micro-structure of the material remains intact. Even if the

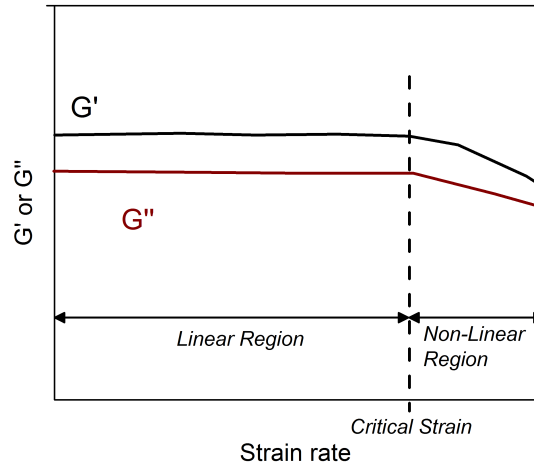


FIGURE 1.26: Example of a typical graph for a viscoelastic material showing the critical strain that separates the LVER from the non-LVER.

material shows a big strain rate range where the behaviour is linear, usually small strain rates deformations are generally used to guarantee that the material properties are not affected by the experiment.

The relaxation time can also be obtained from oscillatory experiments (frequency sweeps) and corresponds to the inverse of the frequency at which  $G'$  and  $G''$  crosses in the transition to flow region. Another way to look at this parameter is by using the definition of the Deborah number ( $De$ ), Equation 1.35.

$$De = \frac{\text{Relaxation Time}}{\text{Test Time Scale}} \quad (1.35)$$

At the crossover  $G' = G''$ , the Deborah number is equal to 1 and the relaxation time is equal to the test time. This means the relaxation time is equal to  $1/\omega$  at the crossover.

### 1.5.2.1.2 Mechanical Models to Describe Viscoelastic Materials

As discussed before, a viscoelastic material combines viscous (liquid) and elastic (solid) behaviours. Due to this dual behaviour the mechanical models have to take this into account. The elastic behaviour is commonly described as a spring that, when subjected to a force (or deformation), will leave its equilibrium state. To counteract this, the spring will create an elastic force that tries to return the structure to its initial state of minimum energy. Obeying to *Hooke's* law, the spring represents a linear elastic solid where the stress that is applied is proportional to the deformation of the material [134]. If the yield stress is not exceeded the material will recover to its initial conformation. On the other hand, if the yield stress is exceeded a permanent deformation will be in place. The elastic modulus ( $G$ ) corresponds to the quotient between the stress and the deformation. Figure 1.27 shows a spring and its behaviour when a force is applied.

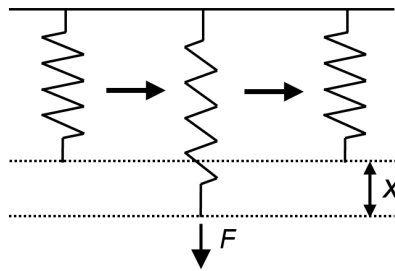


FIGURE 1.27: Illustration of a spring and its behaviour when a force ( $F$ ) is applied.  $X$  represents the displacement.

The strain is given by Equation 1.36.

$$\gamma = \frac{\sigma}{G} \quad (1.36)$$

$G$  will give an idea about how stiff or how resistant is the material to a deformation. The higher the elastic modulus, the stiffer is the material. In the case of a purely viscous material, its representation corresponds to a dashpot obeying to *Newton's* law [134]. A dashpot is defined as a mechanical device containing a

plunger that moves through a viscous fluid. When a viscous material represented by a dashpot is subjected to a stress the device starts to deform at a constant rate (strain rate) until the force is removed. Figure 1.28 shows a dashpot and its behaviour when a force is applied.

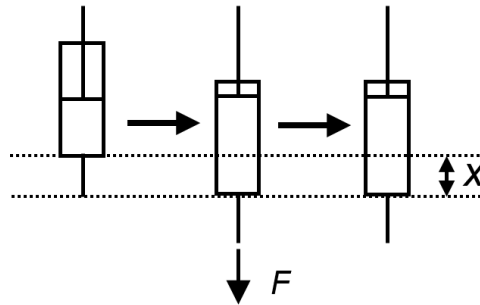


FIGURE 1.28: Illustration of a dashpot and its behaviour when a force ( $F$ ) is applied.  $X$  represents de displacement.

For a viscous material the strain is given by Equation 1.37.

$$\gamma = \frac{\sigma t}{\eta} \quad (1.37)$$

When a material presents the two features described before (elastic and viscous behaviours), they both must be combined in order to describe the viscoelastic behaviour. The most simple model consist in connect a spring and a dashpot in series and its called *Maxwell* model. If the same combination is made but in parallel, the *Kelvin-Voigt* model is obtained [122]. Figure 1.29 illustrate these two models.

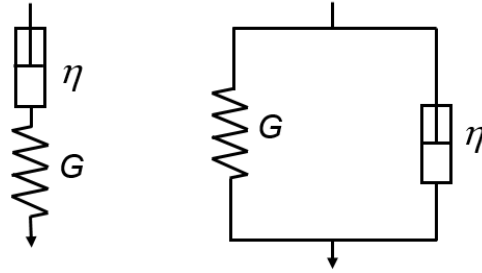


FIGURE 1.29: Illustration of the *Maxwell* model (left) and the *Kelvin-Voigt* model (right) as a combination of a spring a dashpot.

If a stress is applied to a material described by the *Maxwell* model, at short times the response will be essentially elastic (governed by the elastic modulus  $G$ ) while at long times viscous features will be predominant (governed by viscosity  $\eta$ ). In the *Maxwell* model the total strain is given by the sum of the strain of each individual elements, Equation 1.38.

$$\gamma = \sigma \left( \frac{1}{G} + \frac{t}{\eta} \right) \quad (1.38)$$

In a *Kelvin-Voigt* model the stress will take time to develop due to the dashpot that retards the response of the spring. In this case the material behaves as a viscous liquid initially and at longer times as an elastic solid. The transitions between these two behaviours is dependent on the retardation time ( $\lambda$ ) and is give by the quotient between the viscosity ( $\eta$ ) and the elastic modulus ( $G$ ). The retardation time is defined as the time needed for the strain to reach approximately 63% of its final value [122]. In the *Kelvin-Voigt* model the total strain is given by Equation 1.39.

$$\gamma = \frac{\sigma}{G} \left( 1 - e^{-\frac{t}{\lambda}} \right) \quad (1.39)$$

Generally, to describe real systems a combination of the two models described

above is frequently used. This combination is named *Burgers* model and is composed by the *Maxwell* and *Kelvin-Voigt* models connected in series, Figure 1.30.

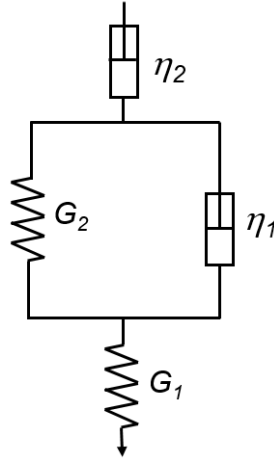


FIGURE 1.30: Illustration of the *Burgers* model.

In the *Burgers* model the strain is described by Equation 1.40.

$$\gamma = \sigma \left( \frac{1}{G_1} + \frac{1}{G_2} \left( 1 - e^{-\frac{t}{\lambda}} \right) + \frac{t}{\eta_2} \right) \quad (1.40)$$

### 1.5.2.1.3 Creep and Recovery Tests

Creep and recovery tests are another way to study viscoelastic properties of a material. In a creep and recovery test where a constant stress is used and the strain is recorded, the obtained response is usually measured in terms of creep compliance ( $J(t)$ ).  $J(t)$  corresponds to the quotient between obtained strain at each point and the constant applied stress (inverse of the elastic modulus - Equation 1.36). In Figure 1.31, a typical response of a viscoelastic material following the *Burgers* model is shown.

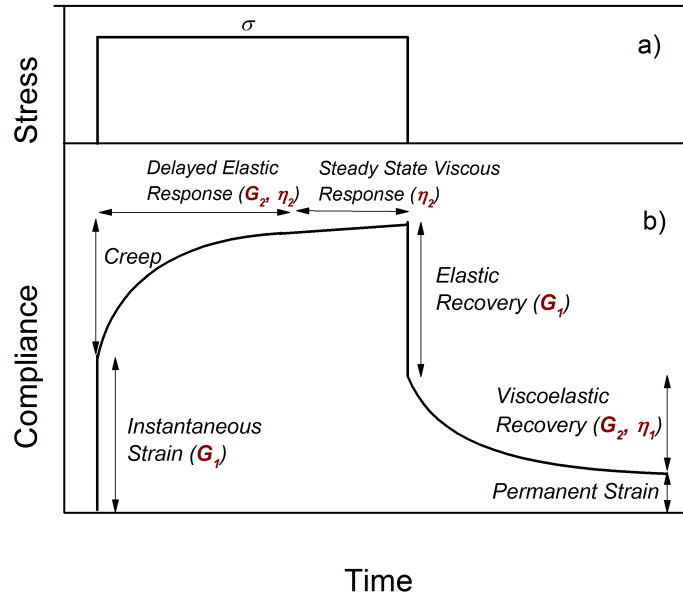


FIGURE 1.31: a) Stress curve; b) Typical response of a viscoelastic material to a creep and recovery test. Adapted from [122].

As described before, in these experiments the sample is subjected to a constant applied stress and the compliance response is recorded. In a typical test the material will show a instantaneous elastic response after which the strain will increase over time (delayed elastic response) and finally a steady state viscous response. This part of the experiment is known as creep. In the second part of the experiment, the load is removed and the compliance of the material is recorded. Upon load removal, some of the strain will recover being the elastic strain recovered immediately. After this point more strain will be recovered over time and is often called delayed elastic recovery. In some materials, a permanent strain (deformation) can be identified.

In some cases multiple *Kelvin-Voigt* elements can be added in series to better fit the experimental results. This will result in the addition of more terms to the creep equation as described by Equation 1.41.

$$J(t) = \frac{1}{G_1} + \frac{1}{G_2} \left(1 - e^{-\frac{t}{\lambda_2}}\right) + \frac{1}{G_3} \left(1 - e^{-\frac{t}{\lambda_3}}\right) + \dots + \frac{t}{\eta_2} \quad (1.41)$$

All the equations presented before were developed to fit experimental results for the creep curve. However, in a creep and recovery test, also a curve showing how the strain recovery, after the removal of the stress, is obtained. The equation that describes the compliance for the recovery curve over time, according to the *Burgers* model, is expressed in Equation 1.42.

$$J_r(t) = \frac{t_{cr}}{\eta_0} + \frac{1}{G_1} \left(1 - e^{-\frac{t_{cr}}{\lambda_1}}\right) e^{-\frac{t}{\lambda_1}} + \frac{1}{G_2} \left(1 - e^{-\frac{t_{cr}}{\lambda_2}}\right) e^{-\frac{t}{\lambda_2}} \quad (1.42)$$

The models discussed above are mechanical models that treat the viscoelastic materials as if they were composed by springs and dashpots. However, there is a statistic model used in reliability engineering that is frequently used to describe creep and recovery curves - *Weibull* model. This model, proposed by *Fancey* [135] and based on the *Weibull* distribution that has no theoretical basis, allows to predict time dependent and time independent strain using experimental results.

Considering that a material is composed by different latch elements, this model was built using a function that allows to calculate the amount of elements that will fail at a given time. The argument of failure behind the model can be adapted to the creep and recovery experiments. The viscoelastic response is characterize by latch elements that are dependent on the time and that can fail. Also, instead of the mechanisms happening at once (continuously), this model proposes that these are made in steps or jumps. This argument is supported by the similarity in form between *Weibull* and the *Kohlrausch-Williams-Watts* (KWW) equation being the latter connected with the *Eyring's* potential energy barrier relationship where motion of matter is associated with molecular jumps. Evidence of this is the work carried out by *Fancey* [136] where stress relaxation curves are fitted

using *Weibull* and *Eyring* models with good correlations.

The author defends that characterizing a material with a small number of elements (springs and dashpots) will lead to low accuracy. These theory makes sense in the way that it is more realistic to think about a material - a polymer solution containing entanglements - composed by domains with different characteristics. This would lead to a distribution in retardation times instead of having only one (as it happens the case of *Burgers* model with 4 parameters). In Figure 1.32 is possible to observe *Fancey's* representation of the *Weibull* model using springs and dashpots to describe the recovery viscoelastic response.

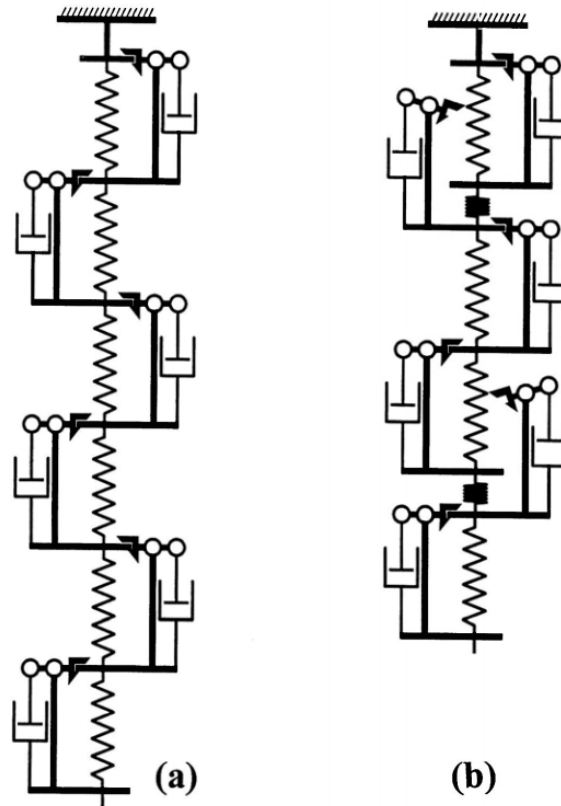


FIGURE 1.32: a) All the present elements are extended; b) Only some elements are able to recover the strain. [135]

The *Weibull* model is widely used in reliability engineering to predict the failure of discrete elements. Accordingly with the model, the latches can only fail after they were triggered. Looking into Figure 1.32 it is possible to see that in a) all

the latches were triggered by the stress imposed; in b) two latches fail. Equation 1.43 and 1.44 represent equations used to quantify the strain response for creep and recovery using the *Weibull* model [135].

$$\varepsilon_{creep} = \varepsilon_i + \varepsilon_c \left[ 1 - \exp\left(-\left(\frac{t}{s_c}\right)^{\beta_c}\right) \right] \quad (1.43)$$

$\varepsilon_i$  represents the instantaneous response,  $\varepsilon_c$  is the creep strain that takes into account the cumulative number of activations with time,  $\beta$  is the shape parameter,  $s_c$  is the creep characteristic life.

$$\varepsilon_{recovery} = \varepsilon_r \left[ \exp\left(-\left(\frac{t}{s_r}\right)^{\beta_r}\right) \right] + \varepsilon_f \quad (1.44)$$

$\varepsilon_r$  represents the viscoelastic strain recovery and  $\varepsilon_f$  the residual strain. In the recovery curve, the parameter  $\beta$  is useful to understand if the distribution of failure is increasing ( $\beta > 1$ ), decreasing ( $\beta < 1$ ) or is constant ( $\beta = 1$ , exponential decay) with time.

### 1.5.3 Rheology of PVC Solutions

As discussed before, PVC is well known for forming gel structures while dissolved in a solvent (or a mixture of solvents). A series of six papers were published between 1997 and 1998 with a detailed rheological study of gels constituted by PVC and bis(2-ethylhexyl)phthalate (DOP). In these studies the influence of some parameters in the dynamic viscoelastic properties of PVC gels were investigated, such as concentration and temperature [22–25, 137, 138].

The gel point is defined as the point in time at which a material changes from liquid to solid through a process called gelation [139]. In a rheology test, the gel point is defined as the critical point (temperature, concentration, time, etc.) at which there is a crossover between the loss modulus and the storage modulus

[25, 137]. The classical way to conduct these experiments is through changes in temperature. Initially, it was thought that the temperature gel point would correspond to the temperature point where  $G'$  and  $G''$  cross for a given frequency. However, later studies showed that this should be true for any frequency to allow a correct gel point determination [140]. Following this, temperature sweep tests should be designed at different frequencies and, to facilitate the analysis, when plotting  $\tan \delta$  ( $\tan \delta = G''/G'$ ) vs. temperature, a crossover should be identified if a gel point is present. The same can be made in terms of concentration. Figure 1.33 shows an example of the gel point determined in terms of polymer concentration and temperature for a systems composed by PVC and di-octyl phthalate (DOP).

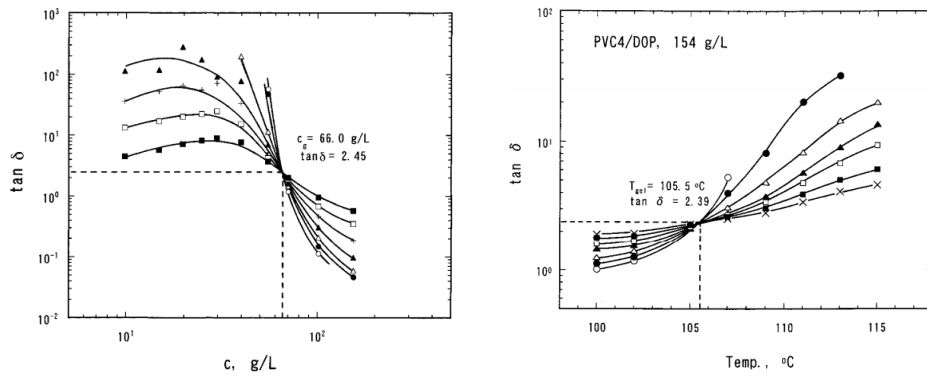


FIGURE 1.33: Frequency tests for a system comprising PVC and DOP. Left - Loss tangent ( $\tan \delta$ ) as function of concentration at various angular frequencies. Right - Loss tangent ( $\tan \delta$ ) as function of temperature at various angular frequencies. Source: [25]

As showed, rheological experiments can be very useful to characterize polymer systems and to determine the sol-gel concentration and temperature.

The gel point is relevant in the industry context since many materials such as food, pharmaceuticals, adhesives or foams are usually close to their gel point (liquids right before the gel point or solids just after it) [139].

## 1.6 Designing of Experiments - *Taguchi* Method

In a multi parameter experiment, the objective is to change each one of the parameters and observe its influence in the property being studied. However, if each one of parameters is studied independently a big number of experiments would need to be performed. However, there are (statistical) models that can be used in order to design experiments in an efficient way. These statistical models allow to analyse the data in an efficient way to get objective conclusions. A correct Design of Experiments (DOE) is very important and includes the detailed planning of the experiments to carry out in the laboratory. A good design will optimize the amount of data that can be collected for a given amount of experimental effort.

*Taguchi* made a big contribution by developing new methodologies in order to optimize the design of experiments, often known as *Taguchi Methods*. Since 1960 the *Taguchi Methods* are used in Japan to improve quality. These methods are classified as robust because they are "engineering methodologies for improving productivity during research and development so that high quality products can be produced quickly and at low cost" [141]. Accordingly to the author's philosophy, the quality of a product should be taken into account before its production and not after. He also believes that this quality is achieved by diminishing the deviation from the final objective [142].

In membrane production, this method was already applied in different processes such as vacuum membrane distillation [143], electrodialysis [144], filtration [145], fuel cells [146–148], reverse osmosis [149, 150] and gas separation [1].

The *Taguchi* method is often used in experimental design and aggregates two components - use of orthogonal arrays to build a matrix of experiments to perform and a method to analyse the results obtained - making this method consistent and with a reproducibility seldom found in other statistical methods [114]. In *Taguchi's* approach the parameters to study are named factors and the different values for the parameters are named levels. After deciding the number of factors and levels to be studied, the adequate orthogonal matrix can be selected, Table 1.7.

TABLE 1.7: Taguchi method orthogonal matrix selector.

		<b>Factors</b>			
		<b>2</b>	<b>3</b>	<b>4</b>	<b>5</b>
<b>Levels</b>	<b>2</b>	L4	L4	L8	L8
	<b>3</b>	L9	L9	L9	L18
	<b>4</b>	L16	L16	L16	L16
	<b>5</b>	L25	L25	L25	L25

Each one of the matrices indicated in Table 1.7 will have a different set-up that tells the user the combination between the factors and levels that should be used in the experiments. The number associated with the matrix indicates the number of experiments to be performed - a L9 orthogonal matrix will correspond to 9 experiments.

After the experiments are performed, an analysis of the results can be made using *ANOVA* (analysis of variance) that is a method that allows to analyse the variance of the results with respect to the experimental parameters used and to evaluate which have more influence in the results obtained. This analysis will be touched in more detail in the results section. After Taguchi's analysis an optimal level for each factor is obtained. In the end of the analysis it will be possible to identify the optimal conditions, to understand which parameters contribute the most and in which extent and finally, what should be the results expected at the optimal conditions. To confirm the method results a final experiment should be done using the optimal conditions predicted in order to validate the method [142].



## Chapter 2

# Phase Inversion Studies of PVC Quaternary Solutions

### 2.1 Objectives

One of the processes to obtain asymmetric hollow fibre membranes is to create the conditions so the phase separation follows a spinodal decomposition followed by nodule coalescence and grow process [81]. This can be achieved by preparing membranes using the dry/wet phase inversion process, also known as forced convection spinning. In the case of hollow fibre membranes preparation following this method, a spinning solution is extruded through a spinneret and is then passed inside a forced convection chamber where the fibre filament is contacted with a gas (dry step) before is immersed in a coagulation bath (wet step). In the dry step, the membrane defect free active layer is formed due to the rapid evaporation of the most volatile solvent while, at the same time, the bore fluid contacted the inner surface in order to form the fibre lumen. In the wet step, while contacting with the non-solvent, the phase separation continues in order to fully form the membrane structure [75]. As discussed previously, the knowledge of the ternary diagram of a membrane forming system is very important in order to understand which pathway the change in composition should follow to

achieve the desired membrane morphology. However, these diagrams are not easy to produce because they require concentration depended interaction parameters between the species that are not experimentally ease to obtain.

In this section, three sets of eleven quaternary PVC solutions composed by PVC, THF, DMAc and EtOH were prepared and studied in relation to their phase inversion properties. The objective is to try to identify the position of each one of the solutions studied in the ternary diagram in terms of miscibility to have an idea of the localization of the binodal boundary, that separates the one phase region from the two phase one, for this system. Having information about the position of this curve is important since, in order to achieve a quick phase separation in the dry step, it is necessary to start with a solution which composition is close to the demixing zone.

## **2.2 Materials and Methods for Phase Inversion Studies**

### **2.2.1 Materials**

Poly(vinylchloride) (PVC) used is commercially available and was purchased from Sigma Aldrich with an average  $M_w$  of approximately 43,000 ( $M_n \approx 22,000$ ).

N,N-Dimethylacetamide (DMAc) (purity  $\geq 99.9\%$  w/w, CHROMA SOLV Plus for HPLC), tetrahydrofuran (THF) (purity  $\geq 99.9\%$  w/w, CHROMA SOLV Plus for HPLC) and ethanol (EtOH) (purity  $\geq 99.5\%$  w/w, Absolut for HPLC) were purchased from Sigma-Aldrich.

### **2.2.2 Solutions Preparation Method for Phase Inversion Studies**

In order to investigate the phase inversion process in quaternary solutions composed by PVC, THF, DMAc and EtOH, three sets of eleven solutions with different compositions were prepared. It is conventional to map polymer solutions in a

ternary diagram. However, when there are four components present, two of them need to be plotted together. When the system is composed by one polymer, one non-solvent and two solvents, is it common to lump the two solvents together. Because of this, it was decided to prepare solutions with different ratios between the two solvents in order to understand the effect of this parameter in the miscibility properties of the system.

The different ratios of THF/DMAc considered can be seen in Table 2.1.

TABLE 2.1: Ratios of THF/DMAc used in each set of solutions prepared.

Set	THF/DMAc (%w/w)
A	12%
B	7.7%
C	16.7%

For each one of the sets, eleven quaternary solutions were prepared. The PVC solutions compositions studied in this work were chosen based on work already done by *Jones* [1] that prepared PVC hollow fibre membranes using the same quaternary system. In his work, the concentration used was the composition number 2 studied in this work. The idea was to choose solutions in the vicinity of composition number 2 and study its phase inversion properties in order to identify compositions that might be located in the two phase region of the ternary phase diagram. Also, different rates between the two solvents were considered in order to evaluate the impact of this parameter in the ternary diagram.

The representation of these compositions in a pseudo-ternary phase diagram, where the solvents (THF and DMAc) are plotted together in the same axis, can be seen in Figure 2.1. As it is only the proportion between THF/DMAc that is varying (with the total amount of solvent kept constant), the position of the compositions in the pseudo-ternary diagram will be identical for each one of the sets, since it is the total amount of solvent that is plotted in the graph.

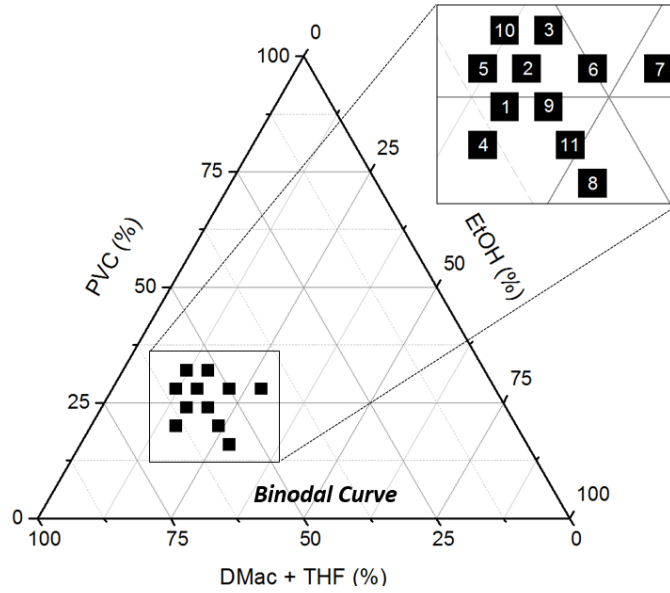


FIGURE 2.1: PVC quaternary solutions compositions represented in a pseudo-ternary diagram.

The quantitative representation of the solutions compositions for the different sets can be seen in Table 2.2, 2.3 and 2.4.

TABLE 2.2: Composition of the quaternary polymer solutions prepared considering the THF/DMAc ratio equal to 12% (w/w) (set A).

	Solution composition (%)										
	1	2	3	4	5	6	7	8	9	10	11
<b>PVC</b>	24	28	32	20	28	28	28	16	24	32	20
<b>THF</b>	6	6	6	7	6	5	5	6	6	6	6
<b>DMAc</b>	54	50	46	57	54	45	39	50	50	50	50
<b>EtOH</b>	16	16	16	16	12	22	28	28	20	12	24

TABLE 2.3: Composition of the quaternary polymer solutions prepared considering the THF/DMAc ratio equal to 7.7% (w/w) (set B).

	Solution composition (%)										
	1	2	3	4	5	6	7	8	9	10	11
<b>PVC</b>	24	28	32	20	28	28	28	16	24	32	20
<b>THF</b>	4	4	4	5	4	4	3	4	4	4	4
<b>DMAc</b>	56	52	48	59	56	46	41	52	52	52	52
<b>EtOH</b>	16	16	16	16	12	22	28	28	20	12	24

TABLE 2.4: Composition of the quaternary polymer solutions prepared considering the THF/DMAc ratio equal to 16.7% (w/w) (set C).

	Solution composition (%)										
	1	2	3	4	5	6	7	8	9	10	11
<b>PVC</b>	24	28	32	20	28	28	28	16	24	32	20
<b>THF</b>	9	8	7	9	9	7	6	8	8	8	8
<b>DMAc</b>	51	48	45	55	51	43	38	48	48	48	48
<b>EtOH</b>	16	16	16	16	12	22	28	28	20	12	24

The solutions were prepared in a fume cupboard using 20 mL glass vials with PTFE (polytetrafluoroethylene) lined caps to avoid solvent evaporation. The first component added to the vial was the polymer, then DMAc, THF and finally ethanol to minimise evaporation. The PVC was weighed in using a balance and all the solvent additions were made in a fume cupboard using a micro pipette. After the preparation all the vials were weighed in to register any solvent losses over time.

A preliminary test was made in order to evaluate the time-temperature features at which the solutions would start to degrade. These tests were made with the three sets of solutions. The solutions were left at room temperature for 11 days and, to achieve completely dissolved solutions, the vials were placed in the oven with temperature increasing gradually until degradation was noticed and the temperature and time recorded.

After this study, fresh solutions were prepared accordingly with the same preparation method described before and placed in the oven where the temperature was increased gradually until a maximum of 69°C. Visual appreciations of the solutions were made during the preparation in order to evaluate the dissolution

of the components.

### 2.3 Results of the Phase Inversion Studies

In order to help and speed up the solutions preparation, high temperature need to be used during the process to achieve homogeneity. However, it is known that PVC can degrade with temperature through a dehydrochlorination reaction, Figure 2.2 [151].

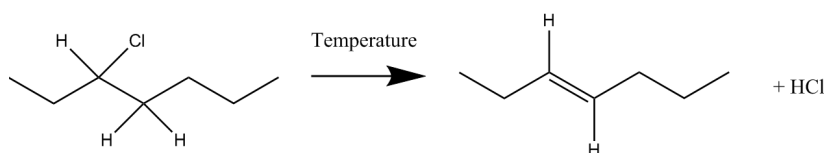


FIGURE 2.2: Dehydrochlorination reaction of PVC [151].

To understand the temperature at which the quaternary would show signs of degradation, the temperature was increased over time accordingly with the information displayed at Figure 2.3.

After the preparation, the solutions were kept at room temperature for eleven days. The reason not to use temperature right after the preparation was to avoid degradation of the polymer that was still as a powder at this stage.

All the solutions were completely dissolved at around  $58^{\circ}\text{C}$  except the solutions 6 and 7 for all THF/DMAc ratios (6 solutions in total). To achieve homogeneity, the temperature was gradually increased until a maximum of  $75^{\circ}\text{C}$ . After 15 days at  $75^{\circ}\text{C}$ , all the compositions except number 7 were homogeneous and some of the solutions became yellowish. Although some of the solutions were already completely dissolved at  $58^{\circ}\text{C}$ , to keep the same temperature history, all of them were left in the oven in order to follow the same heating process.

Having these results in mind, fresh solutions were prepared and placed in a oven

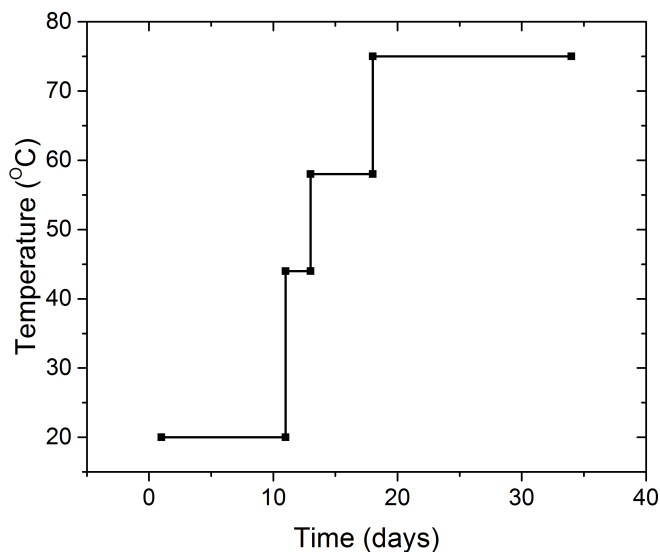


FIGURE 2.3: Time-temperature pathway followed to perform degradation tests to the PVC quaternary solutions.

for over a week, with the temperature increased over time until a maximum of 69°C with total time in the oven equal to 24 days, Figure 2.4. Following this procedure, no degradation was visually detected.

As volatile solvents (THF and EtOH) and high temperature were used in the preparation of these solutions a weight control was made during the process to detect any solvent loss. Despite using PTFE lined caps to seal the vials, it was not possible to completely avoid solvent evaporation. Being THF more volatile than EtOH at atmospheric pressure (boiling point around 66°C) and the maximum temperature achieved in the preparation 69°C, it was assumed that any decrease in the weight would correspond to THF loss.

The results obtained for mass variation of the solutions corresponding to set A can be seen in Figure 2.5. Similar results were obtained for set B and C.

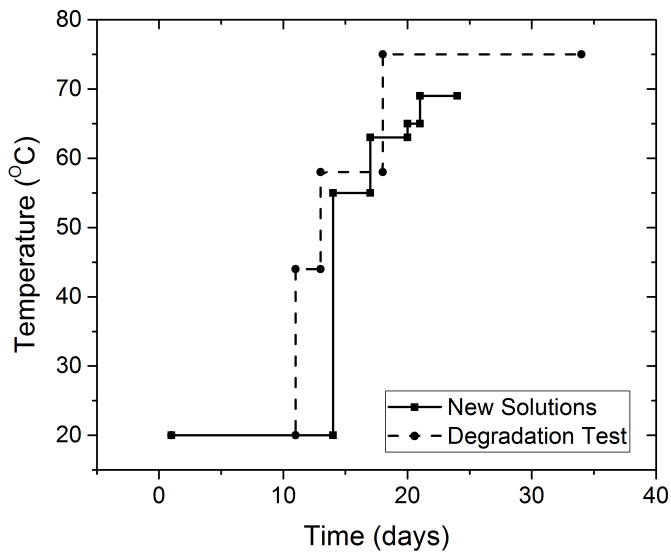


FIGURE 2.4: Time-temperature pathway followed to avoid degradation of the PVC quaternary.

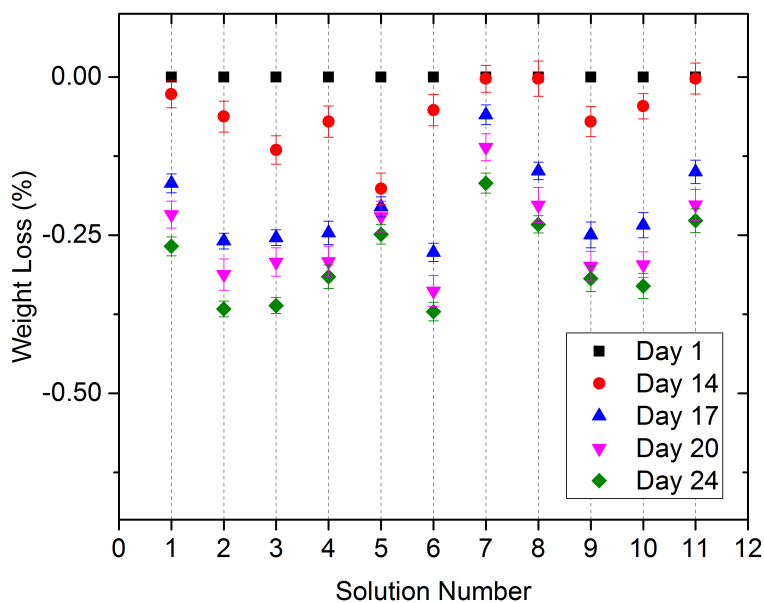


FIGURE 2.5: Weight loss (%) of set A solutions during the preparation period.

After 24 days the maximum mass loss achieved in set A of solutions corresponds to composition 2, 3 and 6 and it is about 0.35% (w/w) of the total mass. The different behaviours obtained are related with the vials' sealing. The vials were closed using PTFE lined caps to avoid solvent evaporation and, although the effort to complete seal the vials, it is possible that different levels of sealing were achieved for different solutions. Looking to the concentrations of THF expressed in Table 2.2 - that vary from 5% to 7% (w/w) - it can be concluded that the maximum loss of THF will be around 10% of its initial value. The same was found for the sets B and C.

After three weeks since the preparation, a visual evaluation was made to the three sets of eleven solutions, Figure 2.6, 2.7 and 2.8 . This evaluation will allow to understand which compositions achieve complete homogeneity in the given time and temperature profile.

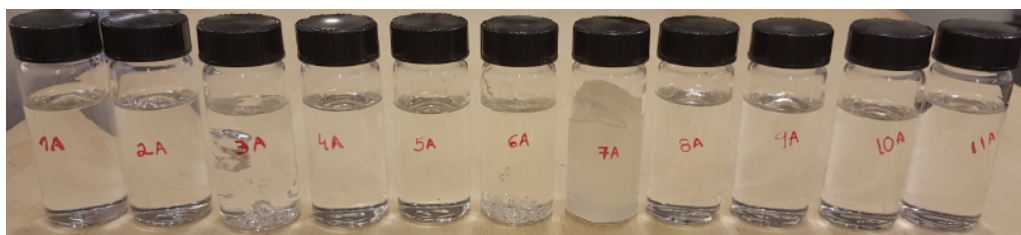


FIGURE 2.6: Visual appearance of the eleven prepared solutions with THF/D-MAc equal to 12% (w/w) (set A).

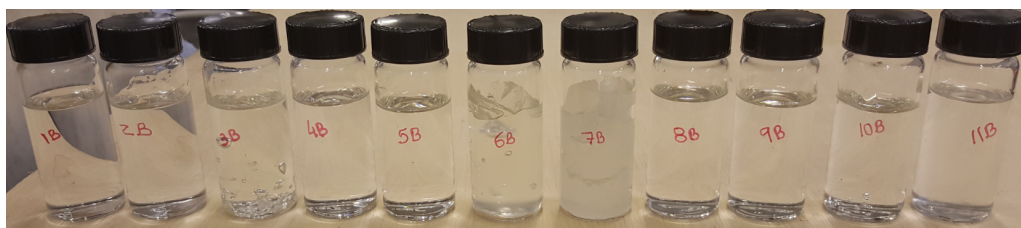


FIGURE 2.7: Visual appearance of the eleven prepared solutions with THF/D-MAc equal to 7.7% (w/w) (set B).

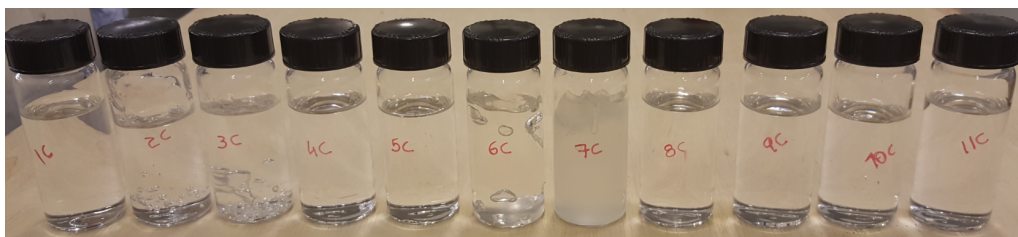


FIGURE 2.8: Visual appearance of the eleven prepared solutions with THF/D-MAc equal to 16.7% (w/w) (set C).

Analysing Figure 2.6, 2.7 and 2.8 it is possible to observe that, apart from composition number 7, all the compositions are visibly clear at naked eye, suggesting that complete homogeneity was achieved. The non-homogeneity appearance of composition number 7 suggests that, concerning a ternary phase diagram, it is probably located inside the two phase area, for the given conditions.

In Figure 2.9 the results of a visual evaluation of the prepared solutions can be seen in terms of pseudo-ternary diagram evolution. The same behaviour with temperature was obtained for the three sets of solutions.

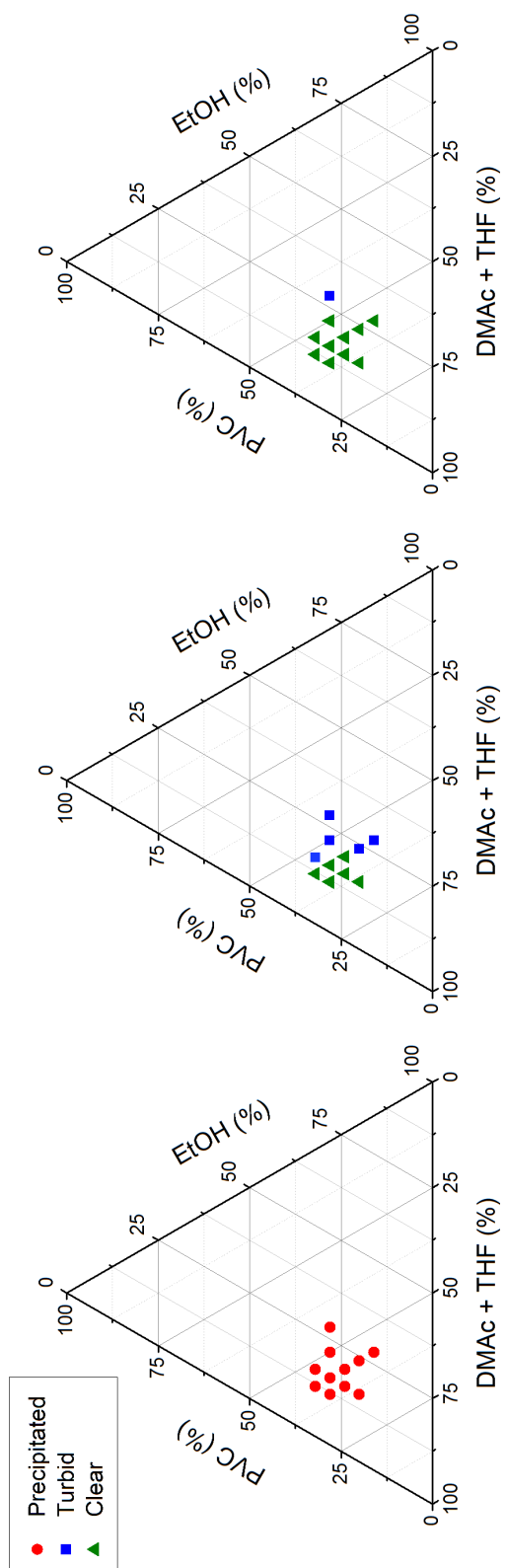


FIGURE 2.9: Pseudo-ternary diagram variation over the solution preparation time. Results were similar for the three sets of solutions prepared.

The diagrams reveal the visual appearance of the solutions at room temperature (day 1), 63°C (day 17) and 69°C (day 24). As expected, the visual appearance of the solutions changes over time, starting from being precipitated at day one to being clear (except for solution number 7) at day 24.

After the heating process, the solutions were left at room temperature to cool down. It was noticed that, after the cooling, all the solutions remained the same in terms of visual aspect (clear), with composition 6 remaining turbid (for all the THF/DMAc ratios). It is also possible to observe bubbles in some vials that are created due to the movement of the solvent due to the use of temperature. Temperature Induced Phase Inversion (TIPS) is a process through which the phase separation of a system is induced by decreasing the temperature [14]. In the TIPS the phase separation occurs due to the decreasing of the solvent quality with temperature, that means that the solubility of the polymer in the solvent will decrease [15]. In this study, this mechanism was not identified since no phase inversion was visualised when the temperature was decreased. It is true that this can indicate that these systems are thermodynamic stable at room temperature and because of this there is no phase separation. In some of the cases, the solutions obtained were gels structures (a detailed study on this matter will be done in the next chapter) where the kinetics for phase separation is slowed down. However, two years after the preparation is possible to observe that all the solutions (apart from composition 6 for all the THF/DMAc ratios) remain visually clear. Figure 2.10 shows the visual appearance of the eleven compositions of the set with THF/DMAc ratio equal to 12% (w/w) as an example.



FIGURE 2.10: Visual appearance of the eleven prepared solutions with THF/DMAc equal to 12% (w/w) two years after preparation.

The fact that a gel is turbid or clear can be related with the size of the crystallites formed. Polymers with high crystallinity content are likely to produce bigger crystallites and, because of that, the solutions have a turbid appearance [15]. However, in this case, the concentration of polymer is the same for composition 7 as for composition number 5 for example, that presents a clear gel aspect. The difference between these two solutions is the solvent and non-solvent content. As it moves to the right in the phase diagram, the concentration of non-solvent increases and it is more likely for the polymer to precipitate due to the poor affinity of the non-solvent with the polymer. Also, as the crystallinity content of PVC is low (around 10%) it is suggested that the turbid appearance of these compositions (number 7 for all the THF/DMAc ratios) is not due to the presence of crystallites. Using these results, it is possible to have an idea about the possible location of the binodal boundary in relation to the prepared compositions and to draw it in the ternary phase diagram to elucidate the separation between the one phase and the two phase region, Figure 2.11.

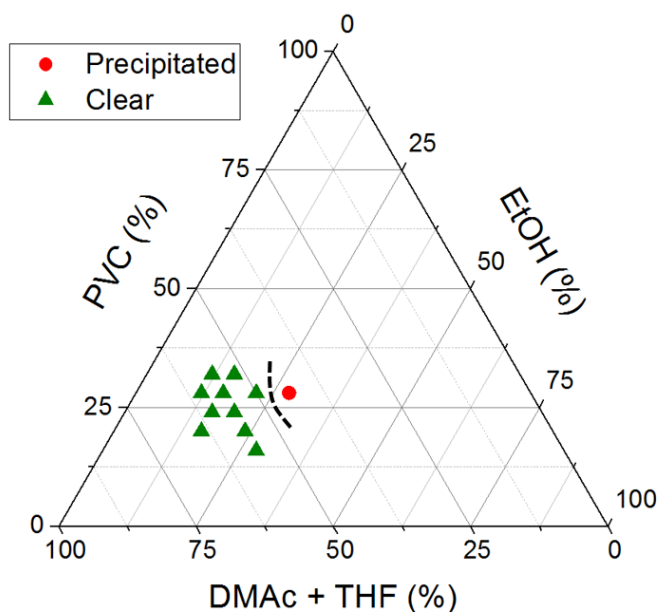


FIGURE 2.11: Representation of the possible location of the binodal curve in relation with the position of the prepared solutions in a pseudo-ternary diagram (dashed line).

## 2.4 Conclusions of the Phase Inversion Studies

In order to study the phase inversion studies of PVC solutions, 3 sets of 11 solutions with different THF/DMAc ratios were prepared with different compositions. As it is known that PVC can degrade when in contact with high temperature, preliminary degradation tests were made. Achieving a maximum of  $75^{\circ}\text{C}$  in the oven with a total time in the oven equal to 20 days, the solutions presented a yellowish colour. Fresh solutions were prepared and placed in the oven for a week with a maximum temperature achieved of  $69^{\circ}\text{C}$ . In this conditions, no yellowish colour was observed, suggesting that degradation was avoided.

The evolution of the homogeneity appearance with the temperature was studied and from all the concentrations prepared, only three cases showed that homogeneity was not achieved (composition 7 for all the THF/DMAc ratios) for the given time and temperature, suggesting that these concentrations were inside the two phased region, making this sample not suitable for hollow fibre preparation.

With this results it was possible to have an idea about the location of the binodal boundary of the system in respect to the region analysed. Solution with composition number 2 appears as a good candidate for membrane spinning since it is located in the homogeneous region (and not too close to the suggested binodal boundary as composition 6). This solution composition was already used in previous successful work done with this quaternary systems, which reinforces this choice.

## Chapter 3

# Rheological Studies of PVC Quaternary Solutions

### 3.1 Objectives

To produce hollow fibre membranes, the first step is the preparation of a homogeneous polymer solution. In this work, in order to produce PVC hollow fibres, a polymer solution composed by PVC, dimethylacetamide (DMAc), tetrahydrofuran (THF) and ethanol (EtOH) is prepared and then extruded through a *spinneret*. The extrusion process subjects the solution to a high wall shear rate that can be of thousands of reciprocal seconds [115]. The magnitude of this wall shear rate is strongly dependent on the rheology properties of the polymeric solution and influences the morphology of the produced hollow fibres [116]. In this section, a set of 11 polymer quaternary solutions with different concentrations of polymer, solvent and non-solvent were studied in terms of their rheological profile. Oscillatory and creep and recovery tests were conducted at different conditions. Oscillatory shear tests allow a better understanding of how the material behaves at small and at long time scale deformations and also to investigate the polymer chains relaxation time. Creep and recovery tests allow to study the effect that

the applied stress has in the material and how it recovers after the stress is removed. As temperature is an important factor for rheology properties, the tests are performed in the range of expected spinning temperatures [137].

The main objective is to understand how the distinct rheological properties can affect the permeation results obtained for the hollow fibres prepared and if a correlation between them can be established.

## **3.2 Materials and Methods used in the Rheological Studies of PVC Quaternary Solutions**

### **3.2.1 Materials for the Rheological Studies of PVC Quaternary Solutions**

The solutions used for the rheological studies were the ones prepared to investigate the phase inversion process (Chapter 2).

### **3.2.2 Methods used in the Rheological Studies of PVC Quaternary Solutions**

All the rheological experiments were performed in a TA Instruments rheometer, model DHR-2 and a plate-plate configuration (parallel plates) was chosen. The plate diameter was 40 mm and the gap used 0.4 mm. A solvent trap containing THF (most volatile solvent) was used in order to minimize the solvent evaporation effect. All rheological experiments were carried out twice in order to ensure reproducibility. The errors obtained in each experiment can be seen in the Appendices section.

The top plate had a diameter of 40 mm and the bottom plate was a *peltier* static unit used to control de temperature of the sample. The 4 cm plate was chosen

over a larger diameter one, in order to avoid high shear gradients across the sample. Accordingly with the manufacturer, the gap used should not be less than a hundred of the plate diameter, so a 400  $\mu\text{m}$  gap was used. In this work, three different types of tests were performed - oscillatory, flow and creep and recovery.

*Flow Tests:* Flow tests were performed with shear rates ranging between 10 to 5000  $\text{s}^{-1}$ . Start-up (shear rate increasing) and start-down (shear rate decreasing) curves were obtained at both 20°C and 50°C.

*Oscillatory Shear Tests:* A preliminary test (amplitude sweep test) was performed to find out a suitable test strain amplitude well within the linear dynamic viscoelasticity region. This test was made at a frequency of 10 rad/s and was performed at 20°C and at 60°C. Angular frequency sweep tests were performed at 20°C with frequency ranging from 0.1 to 100 rad/s. Following the amplitude tests, a strain of 5% was chosen to guarantee linear viscoelastic behaviour at both temperatures.

Temperature sweep experiments were performed between 20°C and 60°C at 3 different angular frequencies (1, 10 and 100 rad/s).

*Creep and Recovery Tests:* Creep and recovery tests were performed at 20°C and 50°C using a set of different applied stresses - 5, 10, 20, and 40 Pa. A typical experiment is composed by two minutes of creep followed by two minutes of recovery.

### **3.3 Rheological Studies of PVC Solution Concentrations with Different Compositions**

The position of the compositions studied in the corresponding pseudo-ternary diagram can be seen in Figure 3.1.

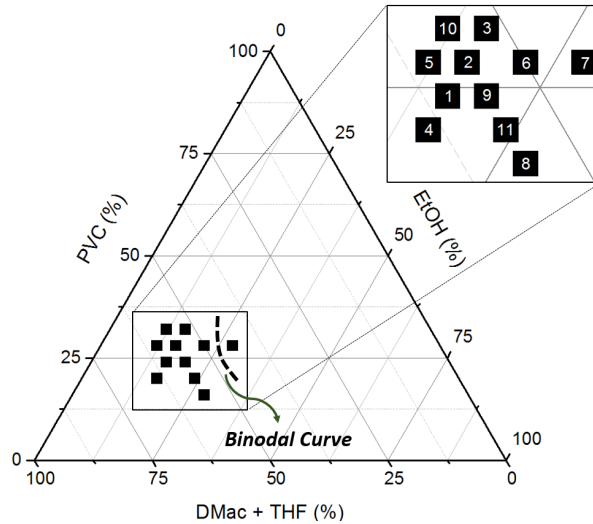


FIGURE 3.1: PVC quaternary solutions compositions represented in the corresponding pseudo-ternary diagram.

### 3.3.1 Oscillatory Shear Rheology

#### 3.3.1.1 Results of the Amplitude Sweep Tests: Determination of the Linear Viscoelasticity Region (LVER) of the PVC Solutions

The first step before starting the oscillatory experiments is to define the linear viscoelastic region (LVER) of the prepared solutions. In this region, the stress and the strain have a linear relationship [152]. This analysis is made by performing a shear amplitude sweep test. In this experiment, the storage modulus  $G'$  and the loss modulus  $G''$  are recorded against strain at a constant frequency equal to 10 rad/s. This test also allows to understand the mechanical stability of a material/solution by looking into the extension of  $G'$  and  $G''$  in the LVER. The wider the LVER, the more stable and homogeneous is the sample [153]. Since the tested spinning temperature will range from 20°C to 60°C, both temperatures were tested to ensure we were working in the LVER in the whole interval of temperatures. Figure 3.2 shows the results obtained for composition 1 at 20°C and 60°C. The errors obtained can be seen in the Appendix section (Table A.1).

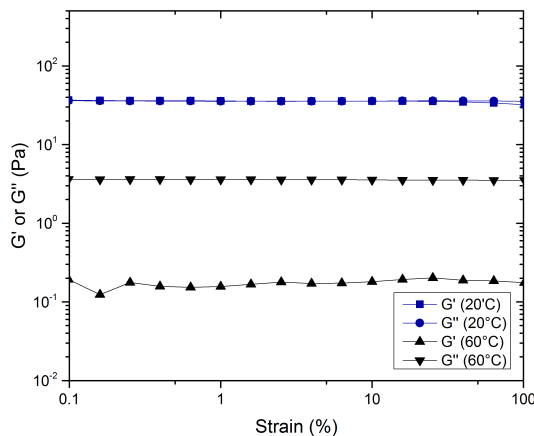


FIGURE 3.2: Storage ( $G'$ ) and loss modulus ( $G''$ ) as function of strain (%) for composition 1 at 20°C and 60°C and at a frequency of 10 rad/s.

The results obtained for composition 1 at both temperatures show clearly the linear viscoelastic regime in which the storage and the loss modulus are constant regardless of the strain amplitude. At 60°C, it is possible to notice a variation in the first points for  $G'$  that is attributed to experimental error. It is also possible to observe that at the higher temperature that both  $G'$  and  $G''$  are smaller. As the modulus measure the resistance to deformation this means it is easier to deform the solutions at higher temperature. Also, while at 20°C both curves are practically identical, at 60°C  $G''$  becomes higher showing the predominant liquid-like features of the material at this temperature. Despite being possible to identify some effects of changing the temperature in these experiments, detailed temperature sweeps will be performed later to further study this parameter.

The length of the LVER covers the whole range of tested strains suggesting that the sample is stable and homogeneous. The results for the remaining studied compositions follow the same trend as can be seen in Figure 3.3. The errors obtained can be seen in the Appendix section (Table A.1).

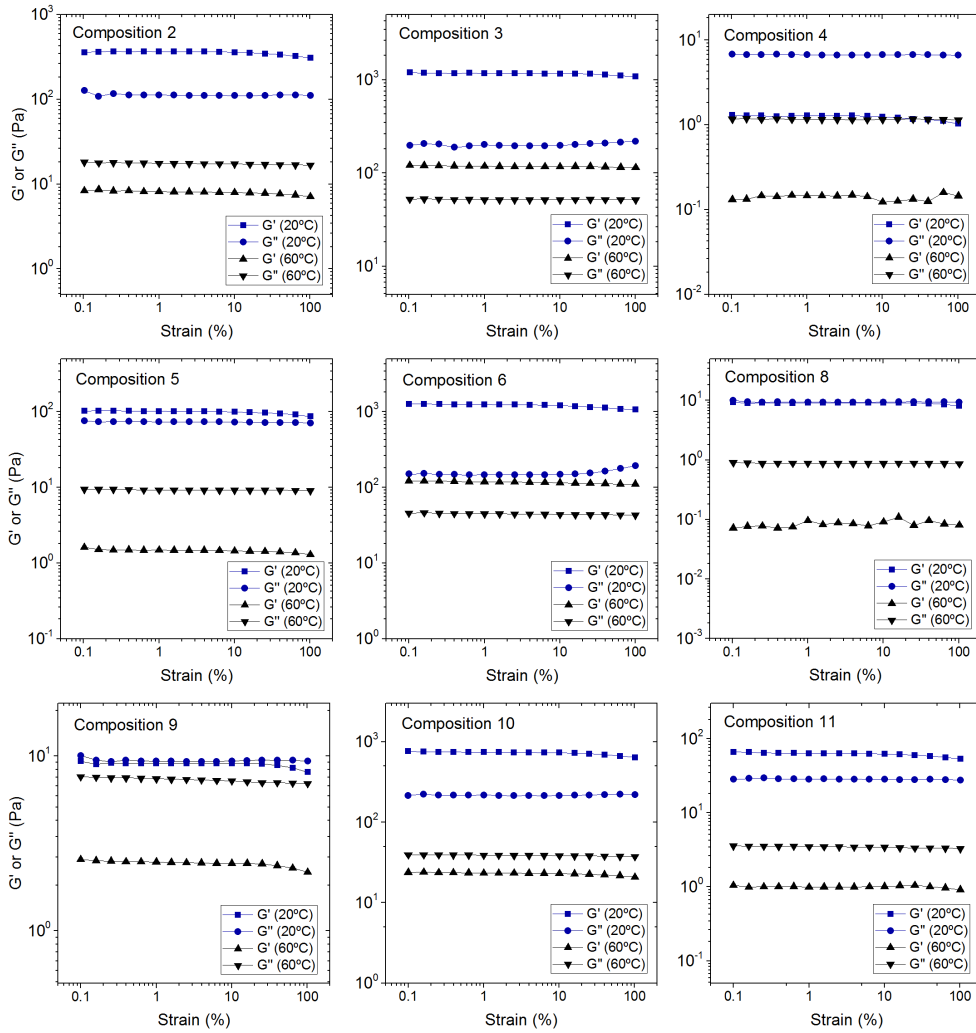


FIGURE 3.3: Storage ( $G'$ ) and loss modulus ( $G''$ ) as function of strain (%) for different compositions at 20°C and 60°C.

Based on these results, a small strain amplitude of 5% was chosen for the following oscillatory tests. This small strain amplitude was selected in order to avoid changing the material microstructure.

### 3.3.1.2 Results of the Angular Frequency Sweep Tests: Deformation at Short and Long Time Scales, Relaxation Times and Gel Concentration of the PVC Solutions

#### a) Deformation at short and long time scales

After identifying the material's linear viscoelastic region, further information can be acquired by doing a frequency sweep at a strain well within the LVER (in this case 5%). In the frequency sweep tests, the behaviour of  $G'$  and  $G''$  is investigated through a range of oscillation frequencies - in this case between 0.1 and 100 rad/s - at constant temperature. This test is used to understand how the material deforms at different time scales, as frequency is the reciprocal of time. Low frequencies will simulate long time-scales performance - slow motion - and high frequencies will simulate short time-scales performance - fast motion.

Figure 3.4 presents the typical behaviour of  $G'$  and  $G''$  as a function of angular frequency ( $\omega$ ) for a generic polymer solution.

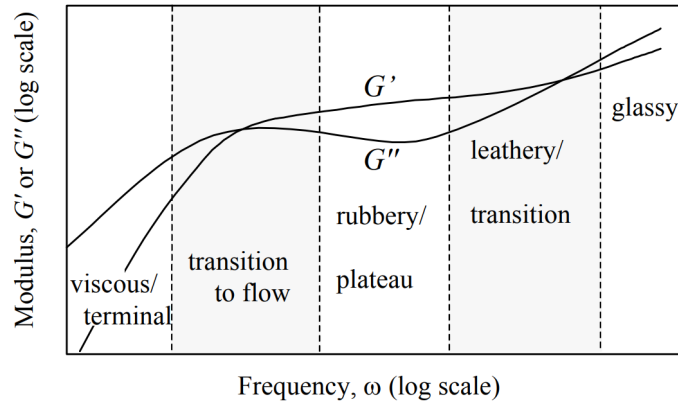


FIGURE 3.4: Typical behaviour of the storage ( $G'$ ) and loss modulus ( $G''$ ) with angular frequency for a generic polymer solution. Source: [122].

In this figure, the different regions that can be obtained in an oscillatory frequency sweep are shown. At low frequencies there is a predominance of the viscous response, and at the higher ones, the response is glassy. In between there are three additional regions that can be identified as the frequency increases. The

transition to flow region, where a crossover between the moduli appears and  $G'$  becomes higher than  $G''$ , the rubbery region where there is a predominance of the storage modulus and a plateau can be identified and, finally, the leathery region where another crossover is identified and  $G''$  becomes again higher than  $G'$ . The rubbery plateau region is more visible in concentrated solutions and in solutions with higher polymer molecular weight with entanglements [154].

In Figure 3.5, it is possible to see the results obtained for composition number 1 and 2. The errors obtained can be seen in the Appendix section (Table A.6).

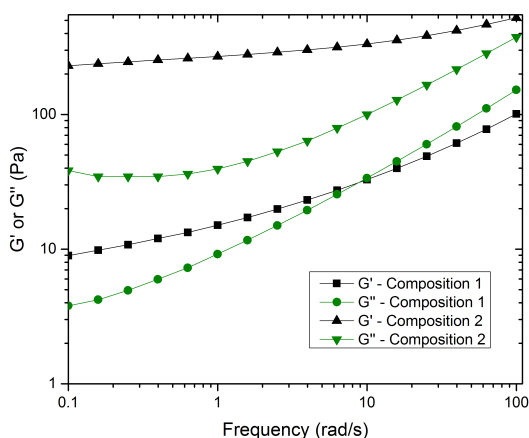


FIGURE 3.5: Storage ( $G'$ ) and loss modulus ( $G''$ ) as a function of angular frequency for composition 1 and 2 at 20°C.

The first observation that can be made is that both modulus are bigger for composition 2 than for composition 1. The explanation for this result is easy to understand when looking to the pseudo-ternary diagram (Figure 3.1) where it is possible to see that composition number 2 has higher polymer and non-solvent contents. This will result in a higher complex viscosity and also in a higher storage and loss moduli.

In the low frequency region,  $G'$  exceeds the value of  $G''$  for both compositions indicating that these solutions have a dominant elastic nature under this conditions. This behaviour can be observed for composition 2 in the whole range of frequencies studied. In a structured material with dominant solid features  $G'$  is

expected to be larger and independent of the frequency. If the elastic modulus shows a high frequency dependence, this suggests that the material, at some point of frequency, might change its characteristics and become more liquid-like [155]. For composition 1 it is possible to notice this as  $G'$  varies over the frequency range. For composition 2 there is also a variation in  $G'$  but less accentuated. This evaluation can be useful to understand the relationship between the different solutions in terms of solid/fluid behaviour, depending on the time scale.

The results of the angular frequency sweep tests obtained for all the compositions are presented in Figure 3.6. The errors obtained can be seen in the Appendix section (Table A.2).

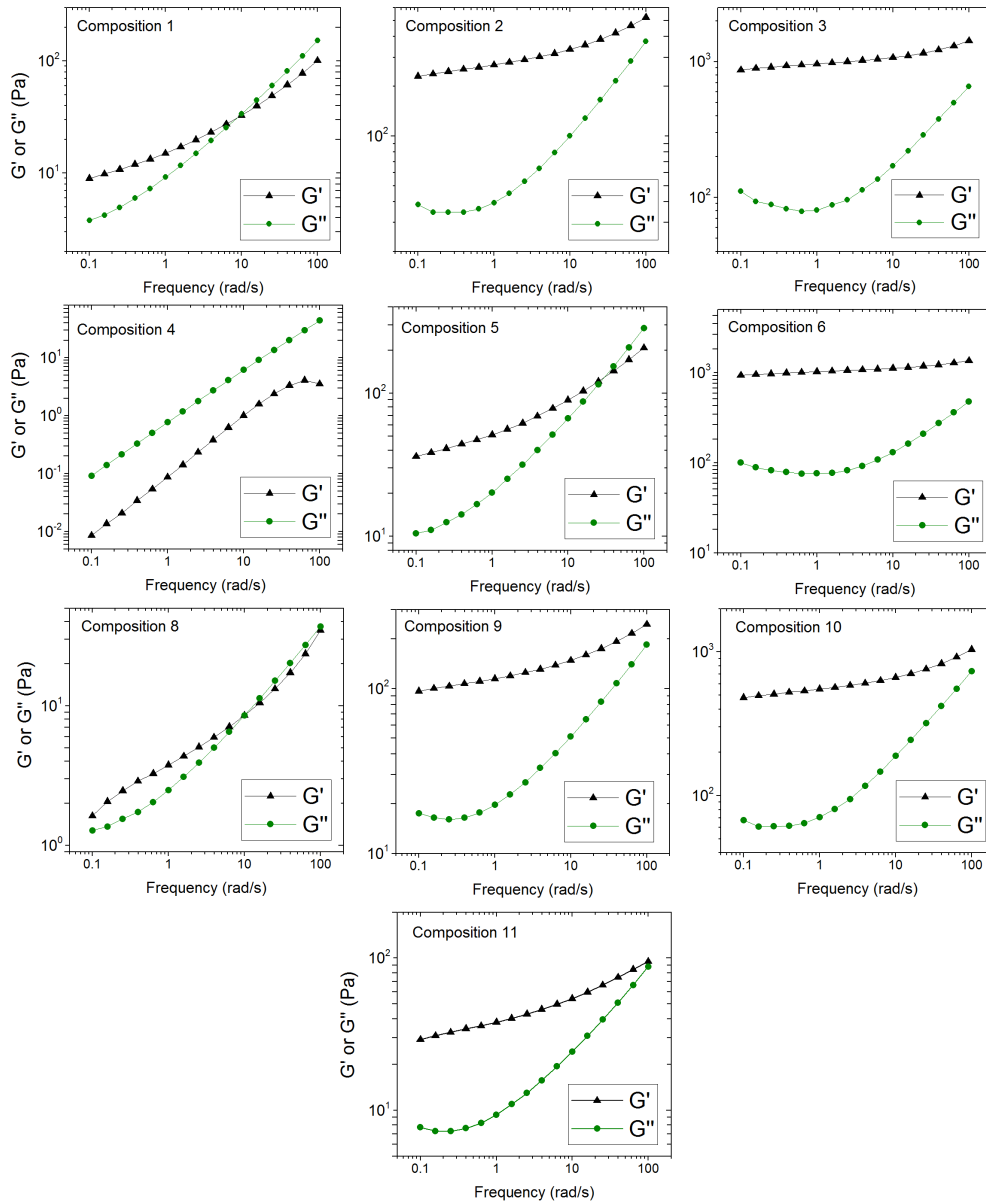


FIGURE 3.6: Storage modulus ( $G'$ ) and loss modulus ( $G''$ ) as a function of angular frequency for different compositions at 20°C.

As can be seen, different behaviours are observed for the different compositions. Compositions 3, 6, 9, 10 and 11 present a solid-like behaviour while composition 4 presents a liquid-like behaviour in the whole range of frequencies studied. Compositions 5 and 8 showed a changed in behaviour - from solid to liquid-like - at a

certain frequency.

### **b) Relaxation times**

In hollow fibre membrane spinning, after the polymer solution exits the *spinneret*, it is desirable that the active layer precipitates before the polymer molecules relax. The time that takes for a polymer molecule to relax after being subjected to a force (shear in this case) is called relaxation time [113]. The relaxation time can also be obtained from oscillatory experiments. However, in the region of frequencies studied it was not possible to observe the transition to flow region where  $G'$  becomes higher than  $G''$ . In fact, the results obtained show that we are always after the crossover, since  $G'$  is already higher than  $G''$  and the transitions observed in composition 1, 5 and 8 are from the rubbery to the leathery region. This means that, in the range studied, it was not possible to identify the exact relaxation time for the compositions studied. However, it is possible to suggest that this time is located at frequencies always below 0.1 rad/s, meaning that the relaxation time will be always greater than 10 seconds.

### **c) Gel concentration of the system**

As stated before, PVC is well-known as a physically gelling polymer when in solution [25]. The gel point (concentration point or temperature point) can be determined using multi frequency rheology experiments. A plot of  $\tan \delta (=G''/G')$  as a function of the three components (polymer, solvents (DMAc and THF) and the non-solvent (EtOH)) as function of  $\tan \delta$  can be built with the results obtained for each frequency in order to find the composition at which all the curves crossover. That composition will correspond to the gel point concentration ( $C_g$ ).

For the angular frequency sweeps, the series of homologue solutions at constant non-solvent concentration of 16% were used to determine the gel concentration of the system at 20°C, Figure 3.7.

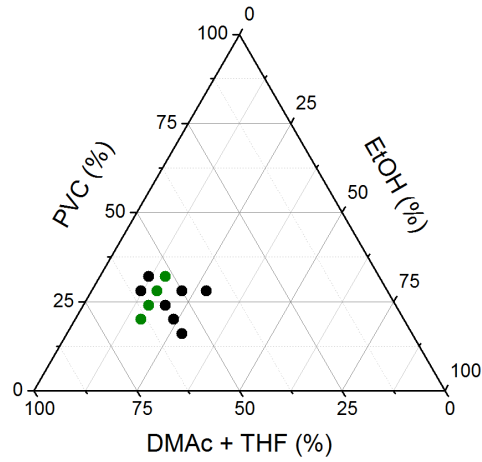


FIGURE 3.7: Solutions used to study the gel properties of the quaternary system represented in the pseudo-ternary diagram (green dots correspond to EtOH composition of 16%).

The method used to calculate the gel point is described by Equation 3.1 and is known as frequency-independence of  $\tan \delta$  [25]. *Winter* [140] and his co-workers found that  $G'(w)$  and  $G''(w)$ , at the gel point, obey to Equation 3.2.

$$\frac{G''(\omega)}{G'(\omega)} = \tan \delta = \tan \left( \frac{n\pi}{2} \right) \quad (3.1)$$

or

$$G''(\omega) \sim G'(\omega) \sim \omega^n \quad \text{with} \quad 0 < n < 1 \quad (3.2)$$

In Figure 3.8 it is possible to observe the results obtained in a 3D perspective (left) as well as the 2D projection (right).

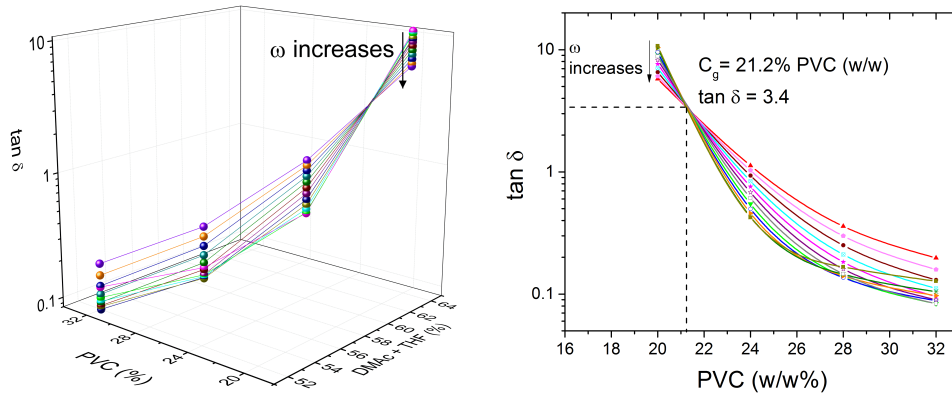


FIGURE 3.8: Left - Loss tangent ( $\tan \delta$ ) as a function of polymer concentration and solvent with non-solvent concentration constant (16%) at various angular frequencies and constant temperature of 20°C. Right - 2D projection of graph in the left.  $C_g$  represents the gel concentration.

The parameter  $n$  is suggested to be related with the nature of the system being studied [140]. For this system  $\tan \delta = 3.4$  and  $C_g = 21.2\% \text{ PVC (w/w)}$ . This means that, for this system (ethanol composition constant = 16%) a gel is obtained for PVC compositions above 21.2%.

The value obtained for the scaling exponent  $n$  was 0.8179. Different studies already showed that this parameter is not universal but varies with the gelling system [25]. In the work done by *Li* and *Aoki* [25], where polymer solutions composed by PVC and DOP with different concentrations and molecular weights were studied, the value of  $n$  obtained for the different molecular weights fell in the interval of 0.753-0.749, supporting the fact that this parameter is specific of the system that is being studied.

This type of study can be useful to identify gel structures in a system. This preliminary study can be an important tool to develop materials where a gel structure is desirable.

### 3.3.1.3 Results of the Temperature Sweep tests

Since it is intended to carry out membrane spinning at different temperatures, the effect of temperature on the viscoelastic behaviour of the potential spinning

solutions was studied in order to understand its impact on the spinning process. The moduli  $G'$  and  $G''$  were measured between 20°C and 60°C. The results obtained for composition 2 and 6 are shown in Figure 3.9 as an example. The errors obtained can be seen in the Appendix section (Table A.3).

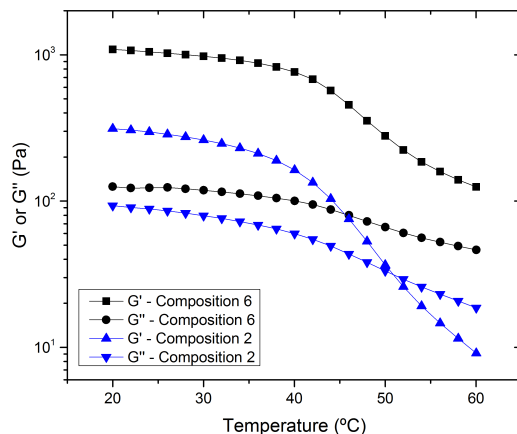


FIGURE 3.9: Storage ( $G'$ ) and loss modulus ( $G''$ ) as a function of temperature for composition 2 and 6 (at an angular frequency of 10 rad/s, with strain of 5%).

Figure 3.9 shows that, for all the curves, there is a decreasing in  $G'$  and  $G''$  over the temperature. It is also possible to notice two different behaviours - one where a crossover between  $G'$  and  $G''$  is identified and another where no crossover is present in the temperature range studied. The results obtained for the remaining solutions are presented in Figure 3.10. The errors obtained can be seen in the Appendix section (Table A.3).

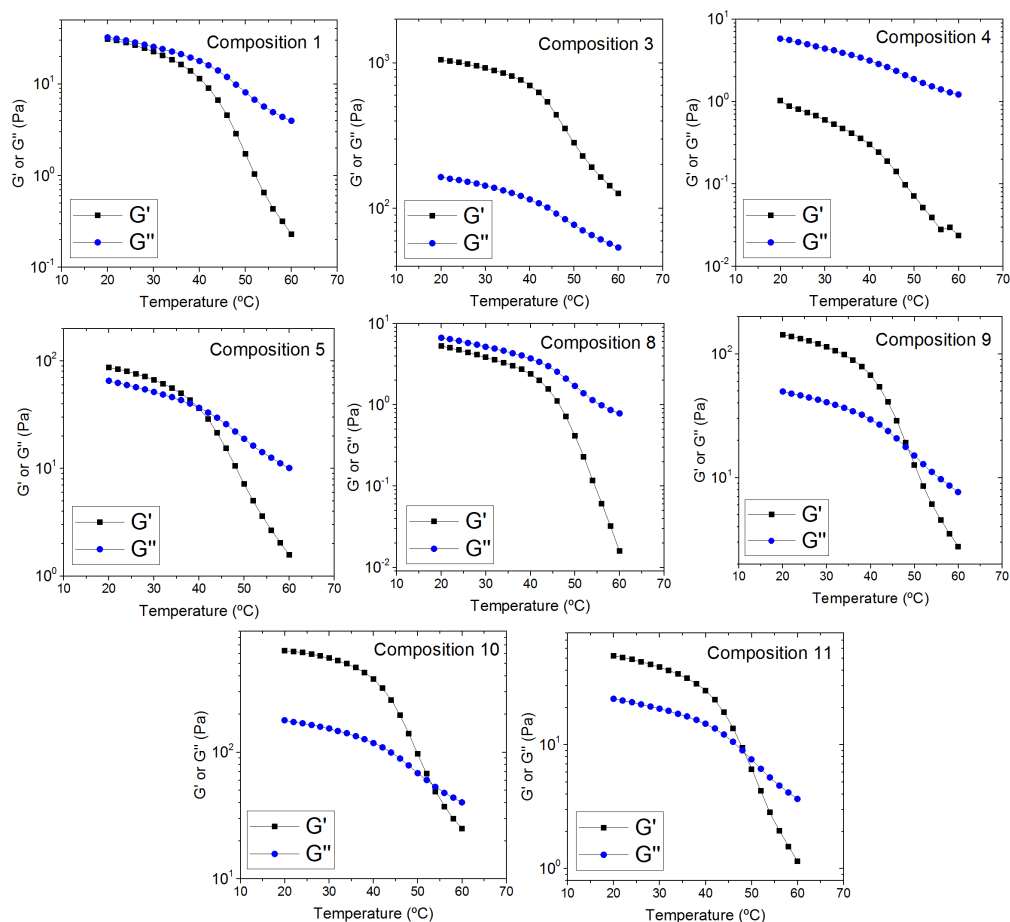


FIGURE 3.10: Storage ( $G'$ ) and loss modulus ( $G''$ ) as function of temperature at a frequency of 10 rad/s.

As discussed above, in order to determine the accurate crossover point as the gel point, a multi frequency experiment must be designed. Keeping in mind that, although the gel point can't be determined at only one frequency and that the "real" gel point should be in the vicinity of this point [140], only the solutions that showed a crossover at an angular frequency of 10 rad/s were further studied since the others showed no crossover in the temperature range studied. Figure 3.11 shows the results obtained for the compositions showing a crossover between  $G'$  and  $G''$  in the range of temperatures studied.

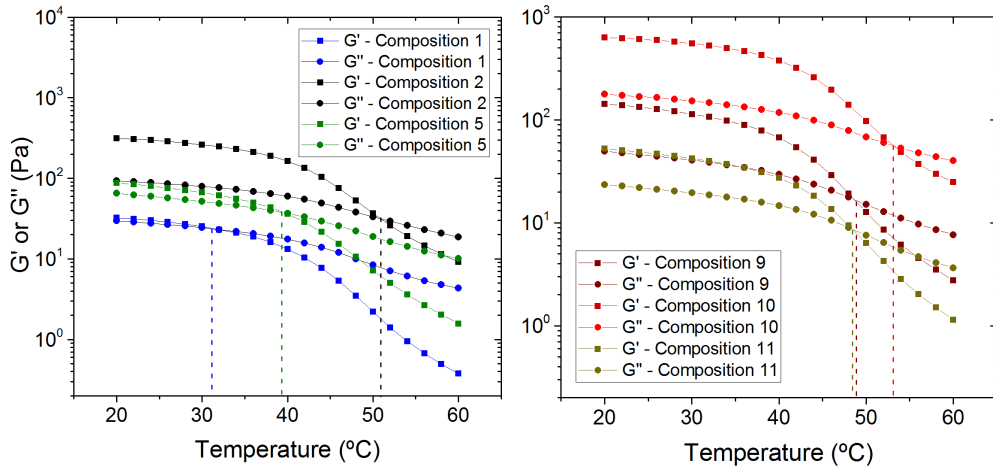


FIGURE 3.11: Storage ( $G'$ ) and loss modulus ( $G''$ ) as a function of temperature for compositions 1, 2 and 5 (left) and for compositions 9, 10 and 11 (right) (at an angular frequency of 10 rad/s, with strain of 5%).

As stated before in the frequency studies, in order to have a so called gel point (in this case, temperature gel point) of a material, the crossover between  $G'$  and  $G''$  should occur at the same temperature independent of the frequency. A simpler way to represent these results is by plotting  $\tan \delta$  versus temperature for each frequency and see if the three lines cross at any point. The results obtained are represented in Figure 3.12. The errors obtained can be seen in the Appendix section (Table A.4).

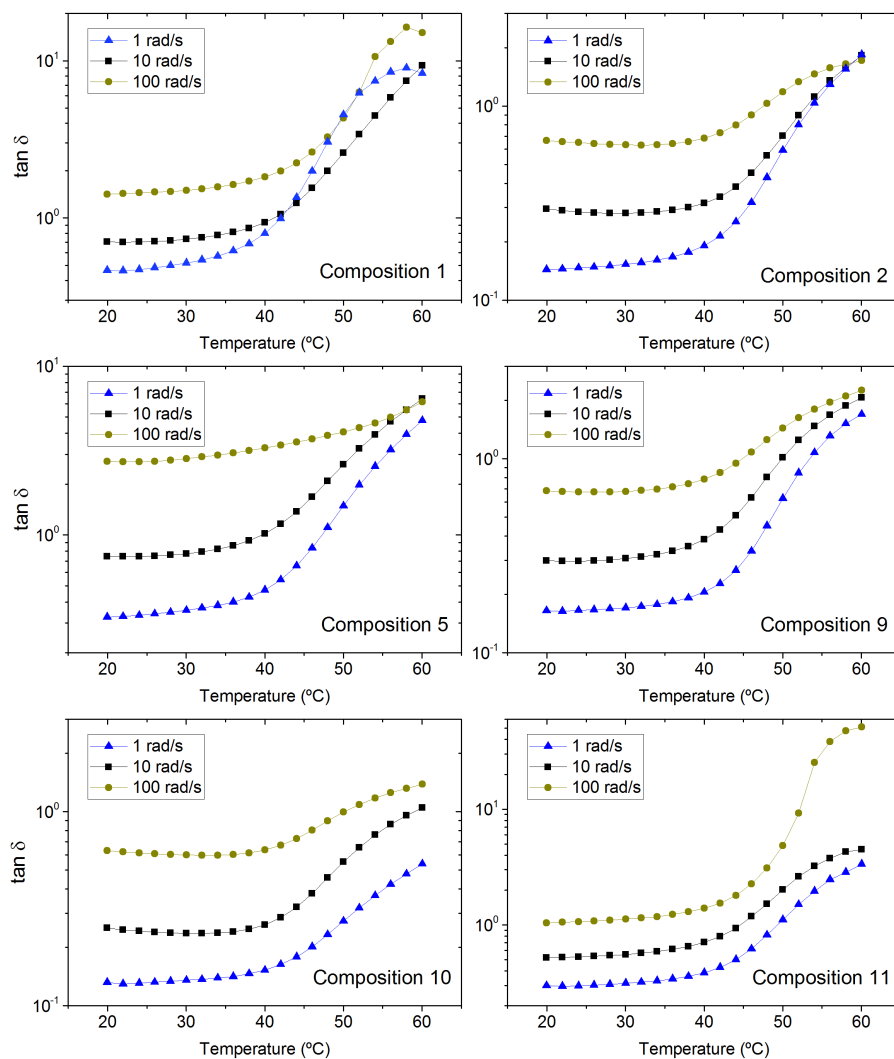


FIGURE 3.12:  $\tan \delta$  as a function of temperature for different compositions at 1, 10 and 100 rad/s.

According to the results in Figure 3.12 it can be seen that it was only possible to observe the "gel point" for one of the solutions studied - composition 2. For solution 1 it is possible to observe more than one crossover between different curves. Composition 5 presents a crossover between only two curves (10 rad/s and 100 rad/s) and for the remaining solutions an intersection was not identified. The fact that the crossovers were not obtained for compositions 9, 10 and 11 can be related to the nature of the sample that is being studied and it suggests that the

”gel point” might be located at higher temperatures than the ones studied.

One possible reason for the difficulty in obtaining the gelling temperature is related with solvent evaporation and consequently changes in the rheological behaviour of the samples. These results show the influence of working with a solution that has high volatile components in its composition and how difficult can be to characterize them when temperature is involved.

Another factor that can have contributed to these results is the fact that, for the different angular frequencies (for a given composition), different samples were used. This was done because, as each temperature sweep took around 20 minutes to perform and temperature was used, there was a high probability of solvent evaporation leading to changes in the solution composition.

In order to investigate the effect of temperature in the storage modulus ( $G'$ ), a plot of the evolution of  $G'$  with temperature for the compositions represented in Figure 3.12, at different frequencies, was built and can be seen in Figure 3.13.

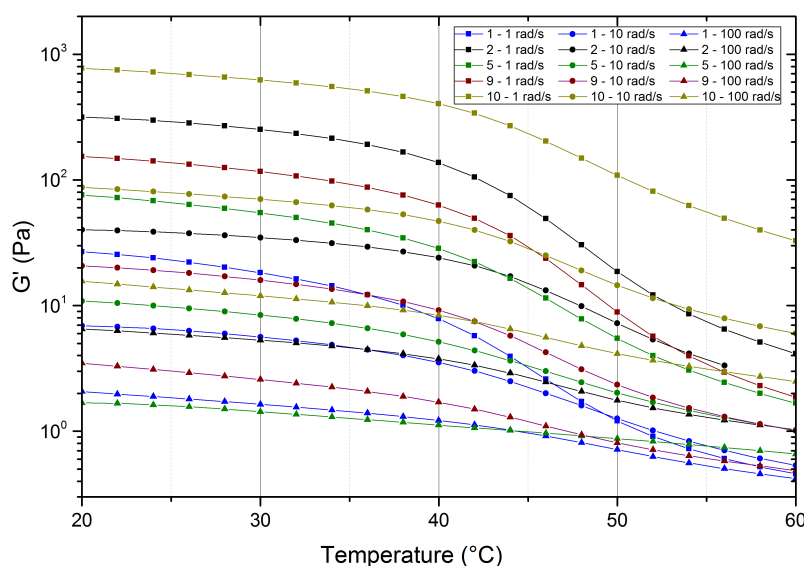


FIGURE 3.13: Storage modulus ( $G'$ ) as a function of temperature for the compositions where a crossover between ( $G'$ ) and loss modulus ( $G''$ ) was observed, at different frequencies.

Looking again to Figure 3.13 a pattern can be identified in the curves represented.

$G'$  is decreasing with temperature and this decrease is more pronounced at the lowest frequency used - 1 rad/s. At lower frequencies the experiment time is greater, when compared with 100 rad/s, and this will mean that the sample will be at each temperature for a longer time period, making the temperature effect more accentuated.

To identify the temperature at which these curves change behaviour, the half point of the curves was calculated by fitting the results to a sigmoid type of curve, since this is the shape of the curves obtained. The half point ( $T_{half}$ ) can be calculated using Equation 3.3.

$$\log_{10}(G') = \frac{\log(G' \rightarrow \infty)}{1 + \exp(-a \times (T - T_{half}))} \quad (3.3)$$

An example of the fitting obtained for composition 1 at 1 rad/s is showed in Figure 3.14.

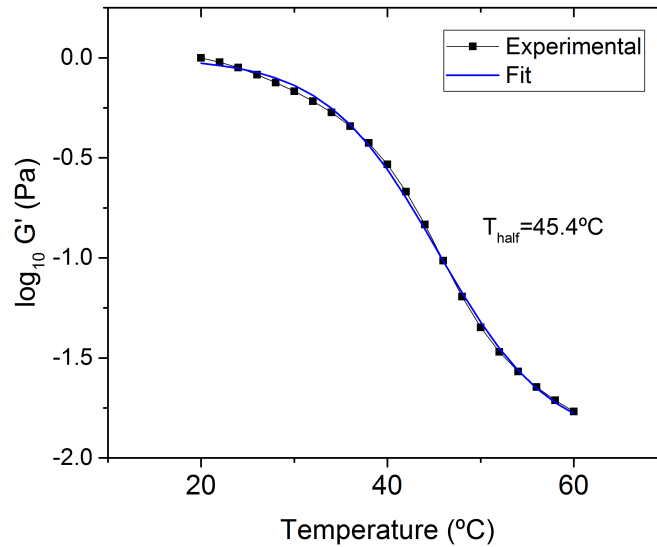


FIGURE 3.14: Fitting result obtained for the storage modulus ( $G'$ ) as a function of temperature for composition 1 at a frequency of 1 rad/s.

The obtained results for  $T_{half}$  are shown in Figure 3.15.

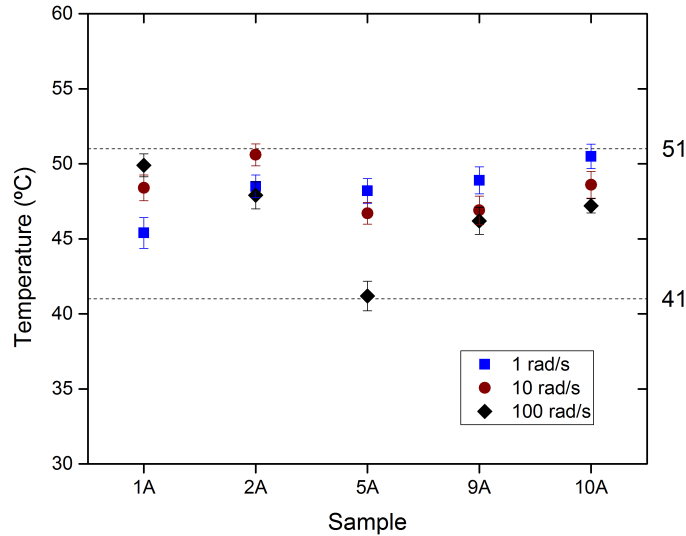


FIGURE 3.15: Calculated half point temperature corresponding to the behaviour change in the loss modulus vs. temperature graph for the studied compositions.

Figure 3.15 shows the interval where  $T_{half}$  values are located in terms of temperature. It is possible to see that all the values are located in the interval of temperatures between 41°C and 51°C.

### 3.3.1.3.1 Differential Scanning Calorimetry Studies

As PVC usually has some degree of crystallinity [16], it was initially thought that this drop in the storage modulus was caused by the melting of crystalline domains in the structure since they are known by creating gel structures. The melting of the crystallites would "destroy" the gel network and the solutions would become more liquid. Differential Scanning Calorimetry (DSC) experiments were performed to one of the samples to search for melting transitions. The results

obtained can be seen in Figure 3.16.

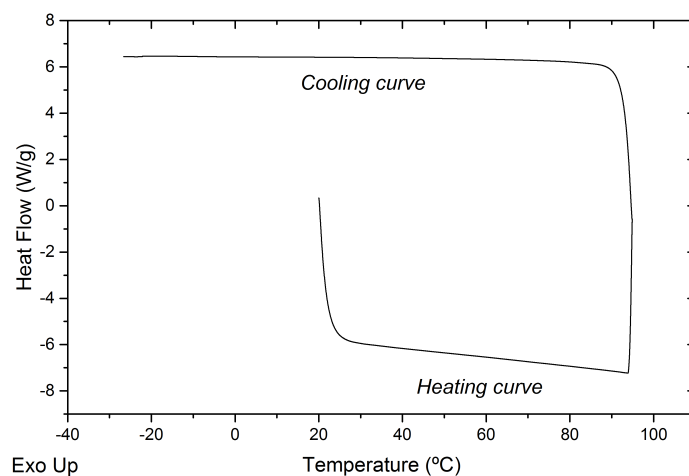


FIGURE 3.16: DSC experiment performed to composition number 2, between 20°C and -20°C at a heating rate of 10°C/min.

In the DSC experiments no thermal transitions were observed in this temperature range, Figure 3.16. This result suggests that thermal transitions are not involved in the rheological results obtained and that the gels are not formed due to the present of crystallites but probably due to entanglements. A DSC experiment was also performed to pure PVC, Figure 3.17.

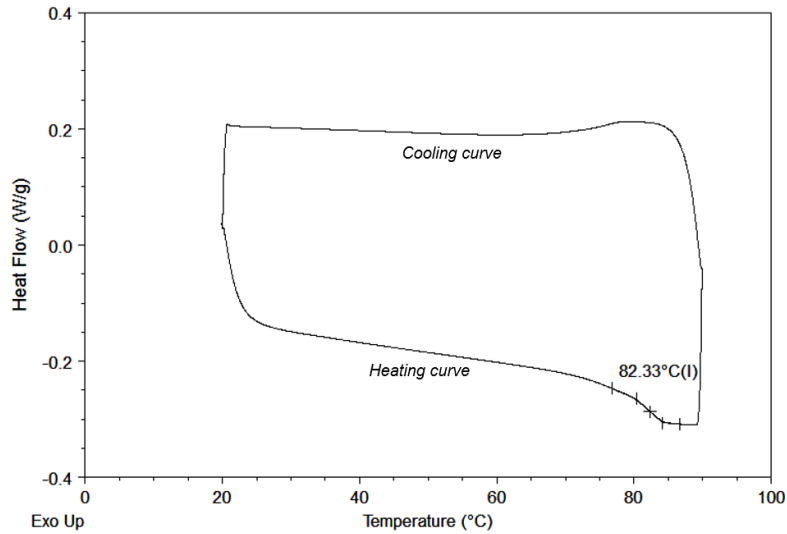


FIGURE 3.17: DSC experiment performed to pure PVC, between 20°C and 90°C at a heating rate of 10°C/min, highlighting the presence of the glass transition temperature.

As can be seen, the only thermal transition detected in the temperature interval tested was the glass transition temperature at around 83°C that is similar with the value obtained in the literature (87°C) [6].

To try to understand more deeply the temperature sweep results and to further study the viscoelastic properties of samples, creep and recovery tests were performed.

### 3.3.2 Creep and Recovery tests

Creep tests allow to understand how a material behaves while being subjected to a certain stress for a period of time. On the other hand, recovery tests allow to observe how a material responds to the removal of the stress. These tests were performed at 20°C and 50°C at different stresses (5, 10, 20, and 40Pa) for all the compositions. The creep duration was 120 seconds as well as the recovery. The reason why this test was performed at 50°C is related with the previous results obtained in the oscillatory measurements, where this temperature seems to play

a role.

In Figure 3.18 the results obtained for composition 1 are shown for 20°C (left) and 50°C (right). The errors obtained can be seen in the Appendix section (Table A.5).

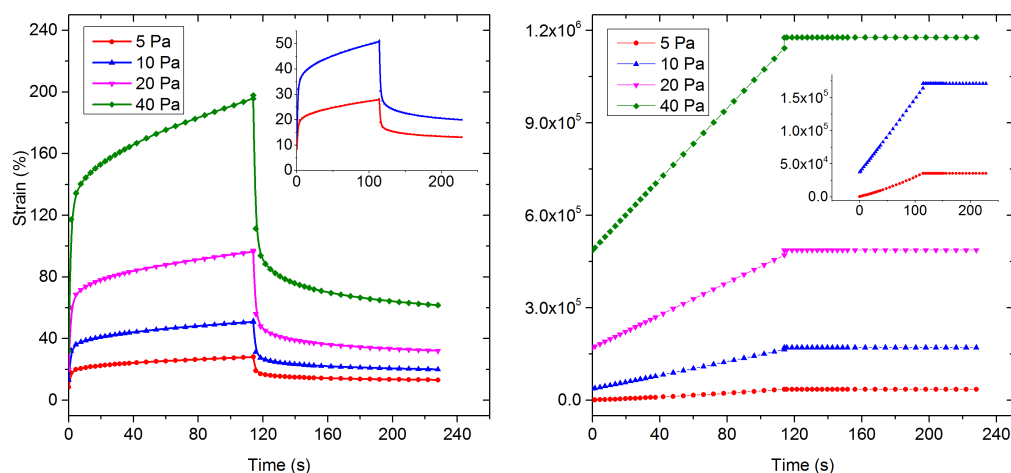


FIGURE 3.18: Creep and recovery results obtained for composition 1 at 20°C (left) and 50°C (right) at different stresses.

Concerning the stress applied it can be observed that this parameter does not affect the trend of the results (true for all samples). The only visible alteration is in the strain observed that is higher for bigger applied stresses. These results can be correlated with the strain amplitude tests performed earlier that show a constant behaviour of  $G'$ , meaning that the properties of the system are not affected by the strain rate imposed. However, in relation with temperature the same cannot be said. There is a change in the rheological response in the creep and recovery test that is dependent on temperature. At 20°C the sample shows viscoelastic behaviour and at 50°C only viscous response is observed, since no strain recovery is observed. This graph suggests that these temperatures are playing an important role in the viscoelastic/viscous properties of the solutions. In Table 3.1 are presented the creep and recovery results obtained for all the solutions studied in terms of viscoelastic/viscous properties. These results are also compared with the results obtained previously in the oscillatory studies.

TABLE 3.1: Rheological behaviour of the solutions when subjected to different stresses at 20°C and 50°C (results were the same for all the stresses studied) and comparison with the results obtained in oscillatory temperature sweeps (at 10 rad/s and 5% strain).

Composition	Creep and Recovery		Oscillatory Temperature Sweeps
	20°C	50°C	Crossover temperature (°C)
<b>1</b>	Viscoelastic	Viscous	< 50°C
<b>2</b>	Viscoelastic	Viscoelastic	≈ 50°C
<b>3</b>	Viscoelastic	Viscoelastic	-
<b>4</b>	Viscous	Viscous	-
<b>5</b>	Viscoelastic	Viscous	< 50°C
<b>6</b>	Viscoelastic	Viscoelastic	-
<b>8</b>	Viscous	Viscous	-
<b>9</b>	Viscoelastic	Viscous	< 50°C
<b>10</b>	Viscoelastic	Viscoelastic	> 50°C
<b>11</b>	Viscoelastic	Viscous	< 50°C

The dependence of the viscoelastic properties with the temperature was already observed in the oscillatory measurements. Some of the solutions behaved as viscous fluids even at 20°C (composition 4 and 8). Others changed behaviour from viscoelastic materials to viscous fluids (composition 1, 5, 9 and 11) and some solutions did not change their behaviour, behaving as viscoelastic materials at both temperatures.

As can be seen, the solutions that presented a cross over where  $G''$  became higher than  $G'$  at a temperature lower than 50°C in the oscillatory experiments, also present a change in the viscoelastic properties from 20°C to 50°C in the creep and recovery results. For compositions 2 and 10 the results from both tests are not concordant. The fact that a different sample was used in each one of the experiments might be reason why the results are not concordant for these compositions.

These results can be very helpful to foresee how a material will behave at different temperatures concerning the final application. A relation between this results and the position of the solutions studied in the pseudo-ternary diagram can be

made, Figure 3.19.

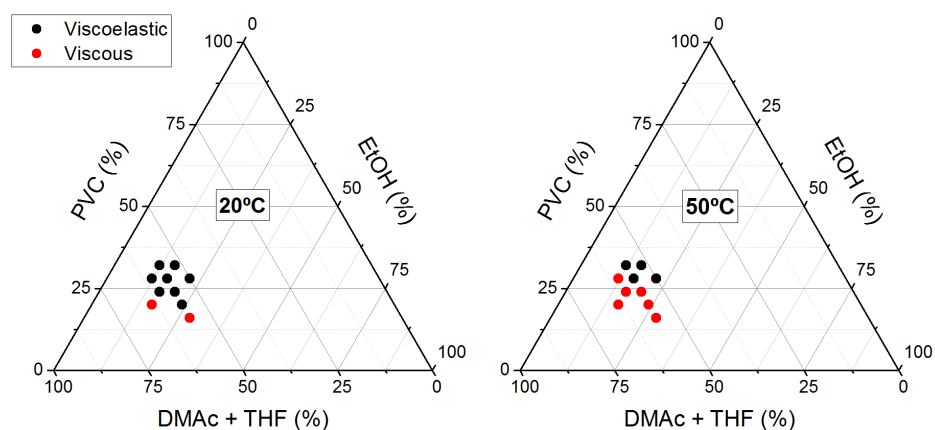


FIGURE 3.19: Creep and recovery results obtained at 20°C (left) and 50°C (right) plotted in a pseudo-ternary phase diagram.

In Figure 3.19 it is easy to understand not only the influence of the temperature but also the influence of the percentage of polymer in the rheological properties of the system. At 50°C, there is a region where the solutions "lose" their elasticity feature becoming purely viscous materials.

Creep and recovery tests are relatively easy to perform and can be useful to understand the features of a material under different conditions. Concerning the spinning process, these tests help to predict how the solution will behave in and after the *spinneret* since it is subjected to a stress that is then released when the solution leaves the *spinneret*.

A combination of all the information obtained in the rheological measurements and in the phase inversion studies is plotted in the system's ternary diagram, Figure 3.20 is obtained.

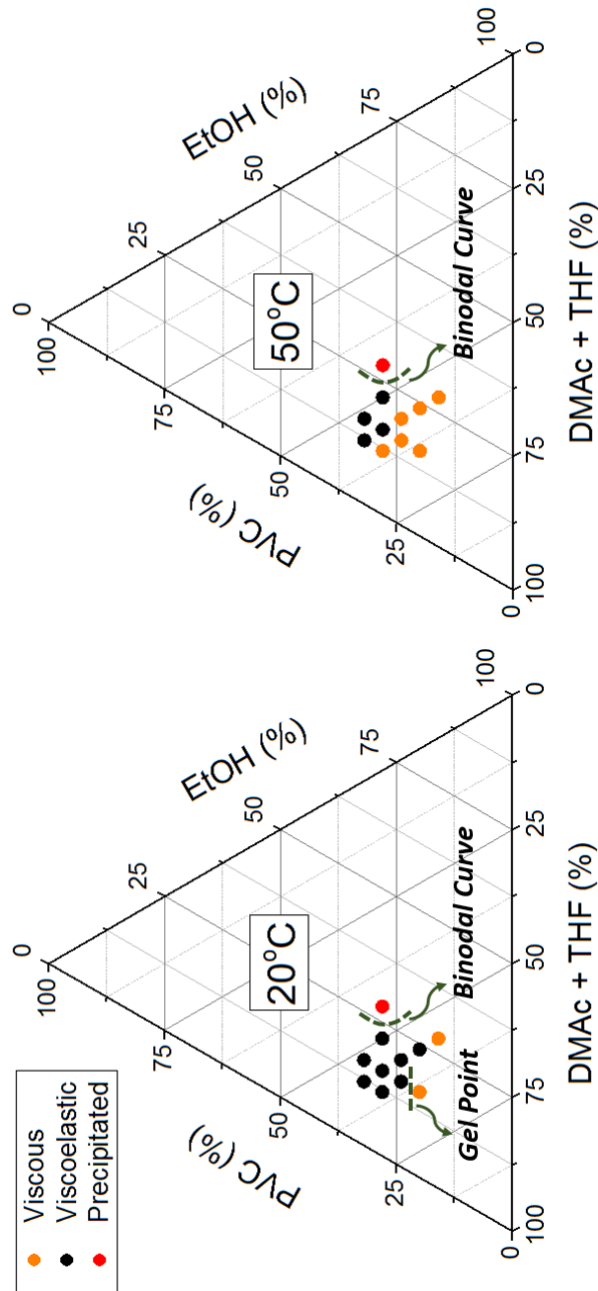


FIGURE 3.20: Rheological and phase inversion results at 20°C (left) and 50°C (right) plotted in a pseudo-ternary phase diagram.

A quick evaluation of the material behaviour can be made in terms of viscoelastic properties by looking into Figure 3.18. However, a more detailed analysis can be made in order to try to get quantitative data. Different rheological models are available in the literature and can be very useful to interpret experimental data.

In this work, the *Burgers* model was used to fit the creep results and the *Weibull* distribution to fit the recovery data.

#### a) Adjusting creep results using *Burgers* model

The *Burgers* model is a combination of *Maxwell* and *Kelvin-Voigt* elements and it is well known as a good approach to describe creep features in linear polymers [156]. Despite the *Weibull* model, discussed in the theory section, be a better representation of a real system, the *Burgers* model was used to fit the creep results because it gives quantitative data about the system. The *Burgers* model with 4 parameters ( $G_1$ ,  $G_2$ ,  $\lambda_{ret}$  and  $\eta$ ) used to adjust the creep curves obtained in this work is described by Equation 3.4.

$$J(t) = \frac{\gamma(t)}{\sigma} = \frac{1}{G_1} + \frac{1 - e\left(\frac{-t}{\lambda_{ret}}\right)}{G_2} + \frac{1}{\eta_2} \quad (3.4)$$

As this model is a combination of springs and dashpots,  $G_1$  and  $G_2$  correspond to the spring constants,  $\lambda_{ret}$  to the dashpot retardation time and  $\eta$  to the viscosity.

In Figure 3.21 it possible to observe the results obtained for composition 1 at 40 Pa and 20°C.

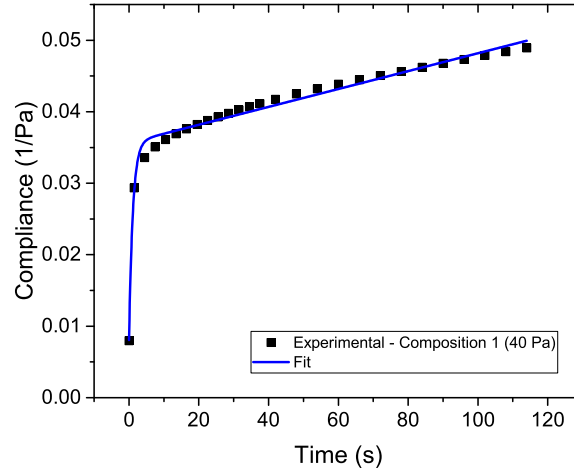


FIGURE 3.21: *Burgers* model applied to creep curve for composition 1 at a stress of 40 Pa and a temperature of 20°C.

As can be seen in Figure 3.21 the *Burgers* model with 4 parameters is in good agreement with the experimental results, apart from the first points. Fitting this equation to the results it is possible to obtain the numerical values for  $G_1$ ,  $G_2$ ,  $\lambda_{ret}$  and  $\eta$ . Equation 3.4 was fitted for all the compositions at different stresses and two studied temperatures - 20°C and 50°C. The results obtain for each one of the parameters at 20°C can be seen in Figure 3.22. The average of the parameters obtained for the different stresses (5, 10, 20 and 40 Pa) was taken since these parameters relate to intrinsic properties that are not expected to vary with the imposed stress. Along with these results, the standard deviations were also plotted in Figure 3.22.

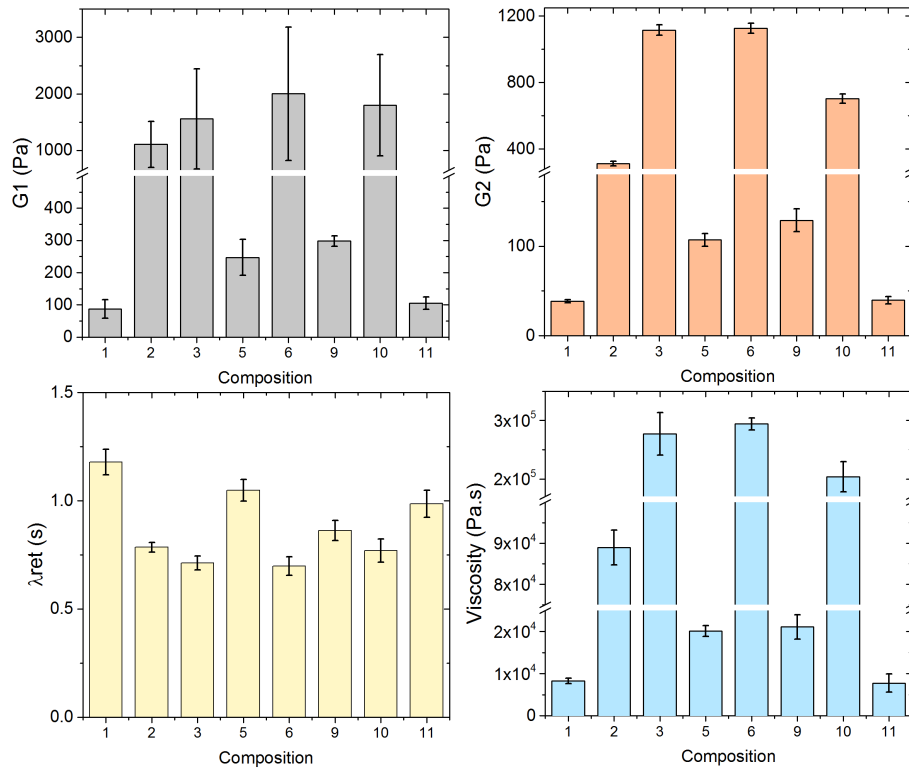


FIGURE 3.22: *Burgers* model parameters results with corresponding standard deviation for the solutions that showed a viscoelastic behaviour in the creep curve at 20°C.

Observing the results obtained and the corresponding standard deviations it can be concluded that the parameter  $G_1$  is the one that presents bigger deviations.  $G_1$  is obtained by using the first points of the curve and as can be seen in Figure 3.21 the fit it is not the best in this section of the curve. This might be the reason for the big standard deviation values. This variable represents the first spring constant in the model that relates with the instantaneous strain. The other 3 parameters ( $G_2$ ,  $\lambda_{ret}$  and  $\eta$ ) that represent the second spring constant, retardation time and viscosity, respectively, seem to have good agreement for the different stresses studied since the standard deviation is small. It is expected a small variation in the parameters since the material is the same (and these parameters are characteristic of the material) and the only variable is the applied stress.

Observing the results obtained for  $G_1$ ,  $G_2$  and  $\eta$  it is easier to see that all of

them follow the same pattern when the compositions are compared with each other. Compositions number 2, 3, 6 and 10 have comparatively higher values and compositions 1, 5, 9 and 11 the lowest. These results are not surprising and are easy to assimilate when plotted in a pseudo ternary diagram, Figure 3.23.

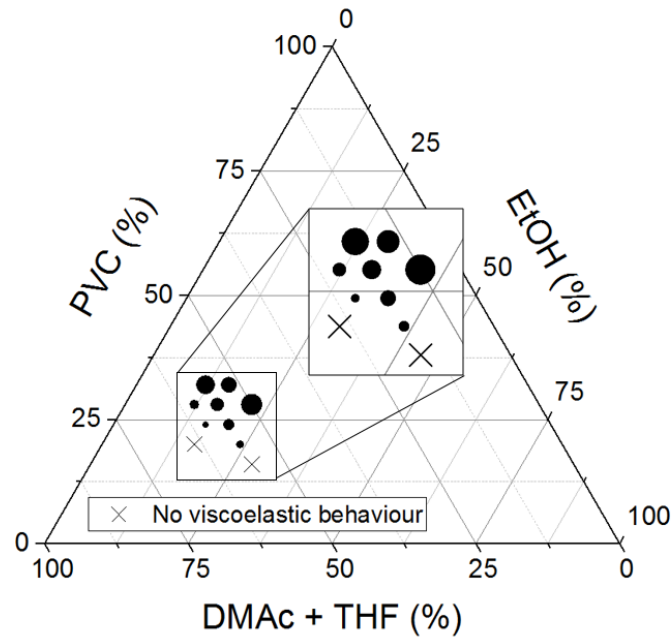


FIGURE 3.23: Creep results:  $G_1$ ,  $G_2$  and  $\eta$  trends at 20°C plotted in a pseudo ternary diagram. Parameters value increasing as colour increment and circle size increases.

According to Figure 3.23  $G_1$  and  $G_2$ , the highest values for the three parameters are located in the region of higher polymer concentration and high non-solvent content. The parameters  $G_1$  and  $G_2$  are related to elasticity. The bigger the values for these parameters the bigger the elasticity of the material [157].

The same analysis can be made for  $\lambda_{ret}$ , however the same trend is not obtained, Figure 3.24.

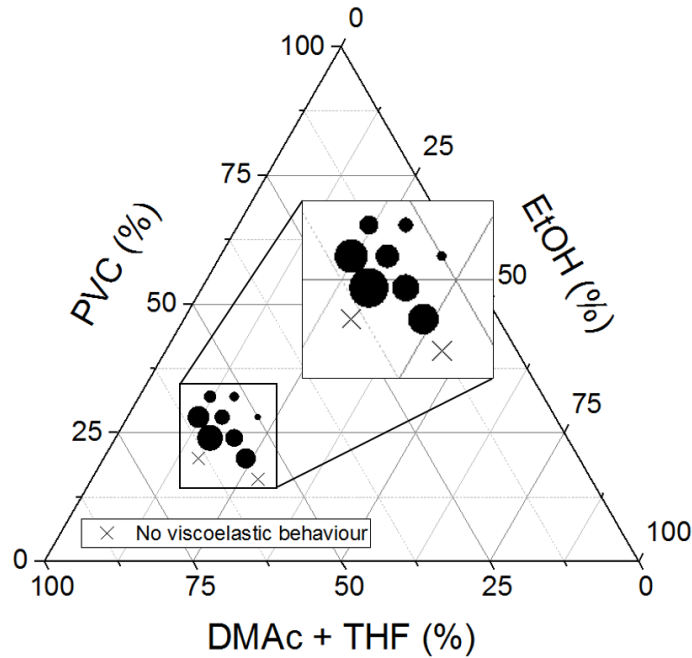


FIGURE 3.24: Creep results:  $\lambda_r$  trend at 20°C plotted in a pseudo ternary diagram. Parameters value increasing as colour increment and circle size increases.

Concerning the retardation time ( $\lambda_{ret}$ ), that represents the delay in the elastic response, it can be observed that the highest value is obtained for composition 1 and lowest is composition number 6. Looking into the phase diagram it is possible to observe that sample 1 is the closest to the polymer-solvent corner by opposition to composition number 6. The compositions that are closest to the polymer-solvent corner are more likely to have a "predominant" viscous behaviour because the polymer and non-solvent content is lower (as it happens for composition 4 that has purely viscous features). As  $\lambda_{ret}$  corresponds to the delayed elastic response, also defined as "delayed elasticity" [124] and accordingly with these results it can be suggested that if a solution as a "predominant" viscous behaviour (and consequently lower viscosity), it will have a larger retardation time. This makes sense because this retardation time is caused by the viscous part of the sample.

$\eta$  represents the viscosity of the sample. As it can be seen in Figure 3.24, the compositions further from the polymer-solvent are the ones with higher viscosity, as expected.

Figure 3.25 shows the same set of results obtained at 50°C. Note that at this

temperature only some compositions show viscoelastic behaviour, explaining why only some are studied at this temperature in this case.

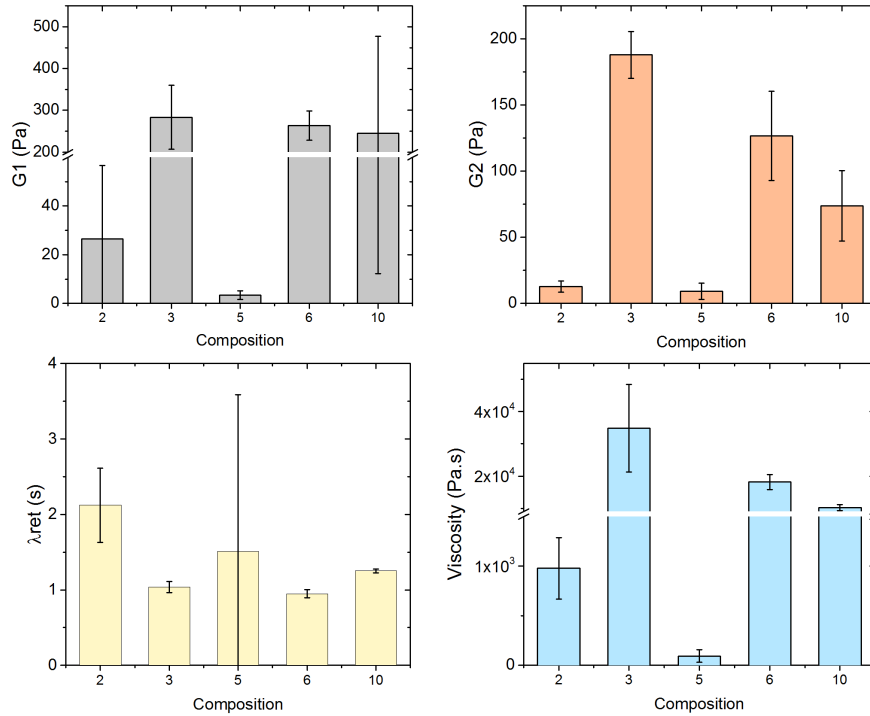


FIGURE 3.25: *Burgers* model parameters results with respective standard deviation for the solutions that showed a viscoelastic behaviour in the creep curve at 50°C.

The data obtained at 50°C reflects one more time how difficult it is to study this system at high temperature. Comparing with the results obtained at 20°C it is possible to notice bigger standard deviations observed at higher temperature. This results suggest that solvent evaporations might be involved in the big deviations, producing uncertainties in the results.

Due to these deviations it becomes more difficult to analyse the data in terms of accuracy. However, some qualitative comments can be made. Ignoring the error bars, the same observations as in Figure 3.22 can be observed about the trends of  $G_2$ ,  $\lambda_{ret}$  and  $\eta$  between samples. In terms of pseudo ternary diagram it becomes more difficult to build a representation because the relationship between the compositions may not correspond to the reality due to the big uncertainties

obtained.

### b) Adjusting recovery results using *Burgers* model

To fit the recovery results it was not possible to use the *Burgers* model because the curves obtained do not present exponential decay.

### c) Adjusting creep results using *Weibull* distribution

Using the *Weibull* model, the creep is described by Equation 3.5 [135].

$$\varepsilon_{creep} = \varepsilon_i + \varepsilon_c \left[ 1 - \exp\left( - \left( \frac{t}{s_c} \right)^{\beta_c} \right) \right] \quad (3.5)$$

In Figure 3.26 an example of the fit made to the creep data using *Weibull* distribution for composition 1 at 40 Pa is shown. The errors obtained can be seen in the Appendix section (Table A.6).

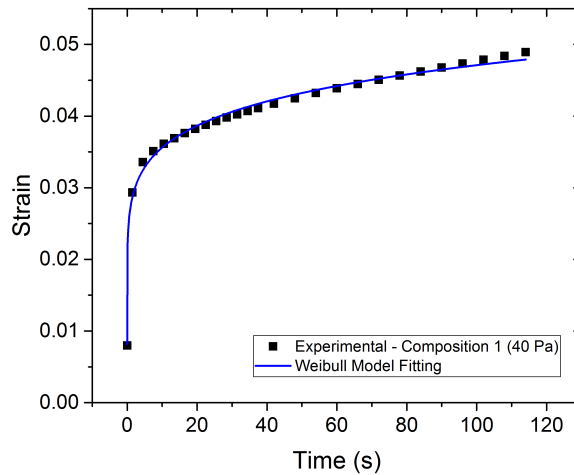


FIGURE 3.26: *Weibull* model applied to creep data for composition 1 at a stress of 40 Pa and a temperature of 20°C.

In Figure 3.26, it can be seen that the *Weibull* distribution is in good agreement with the experimental creep results. In Figure 3.27 it is possible to observe the parameters values obtained for each composition and stress - instantaneous response ( $\varepsilon_i$ ), final creep strain ( $\varepsilon_c$ ), shape parameter from the creep test ( $\beta_c$ ) and creep characteristic life parameter from a creep test ( $s_c$ ). The errors obtained can be seen in the Appendix section (Table A.6).

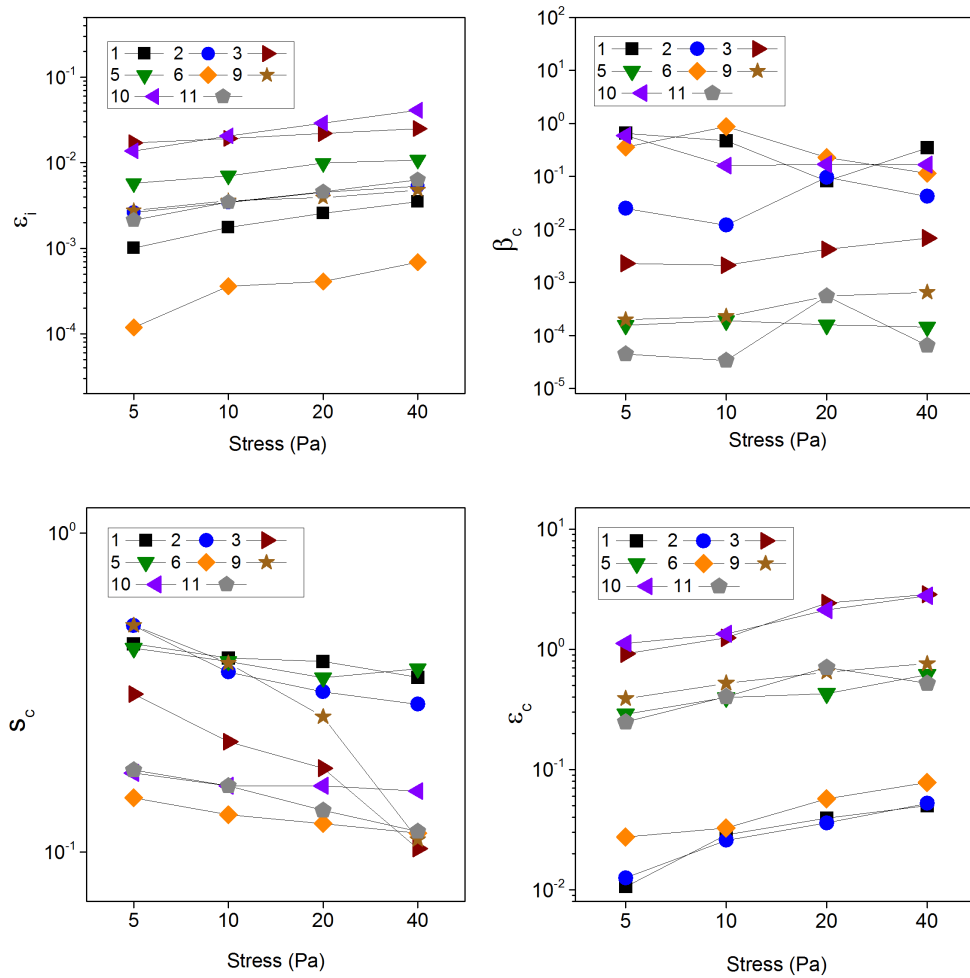


FIGURE 3.27: Parameters obtained by fitting the *Weibull* distribution to the experimental creep data for the solutions showing viscoelastic behaviour, at 20°C.

Parameter  $\varepsilon_i$  corresponds to the initial instantaneous response in terms of strain.

As can be seen in Figure 3.27, this parameter increases with the increasing of the applied stress, since strain is proportional to the applied stress. It is also possible to see different values for this parameter depending on the solution composition. The compositions with higher instantaneous response correspond to the ones with higher polymer content (composition 10 and 3).

Parameter  $s_c$  decreases with the increasing of the applied stress and this fact can be due to the higher strain rates that result from the faster activation of the available latch elements. For the parameter  $\beta_c$  it was not possible to obtain a trend that allows the correlation between the different stresses or compositions. However, creep strain is normally observed to decrease with time, as is reflected in the  $\beta_c$  values always lower than 1.

$\varepsilon_c$  represents the final creep strain. The results show an increasing of this parameter with the applied stress and, in terms of compositions, the trends are very similar to the ones obtained for  $\varepsilon_i$ , as expected.

As showed before, when the *Burgers* model was used for the creep tests at 50°C, only some compositions present viscoelastic behaviour at this temperature. The compositions that present viscoelastic features at 50°C are 2, 3, 5, 6 and 10. The *Weibull* model was also applied to the creep curves obtained at 50°C. The results can be seen in Figure 3.28. The errors obtained can be seen in the Appendix section (Table A.7).

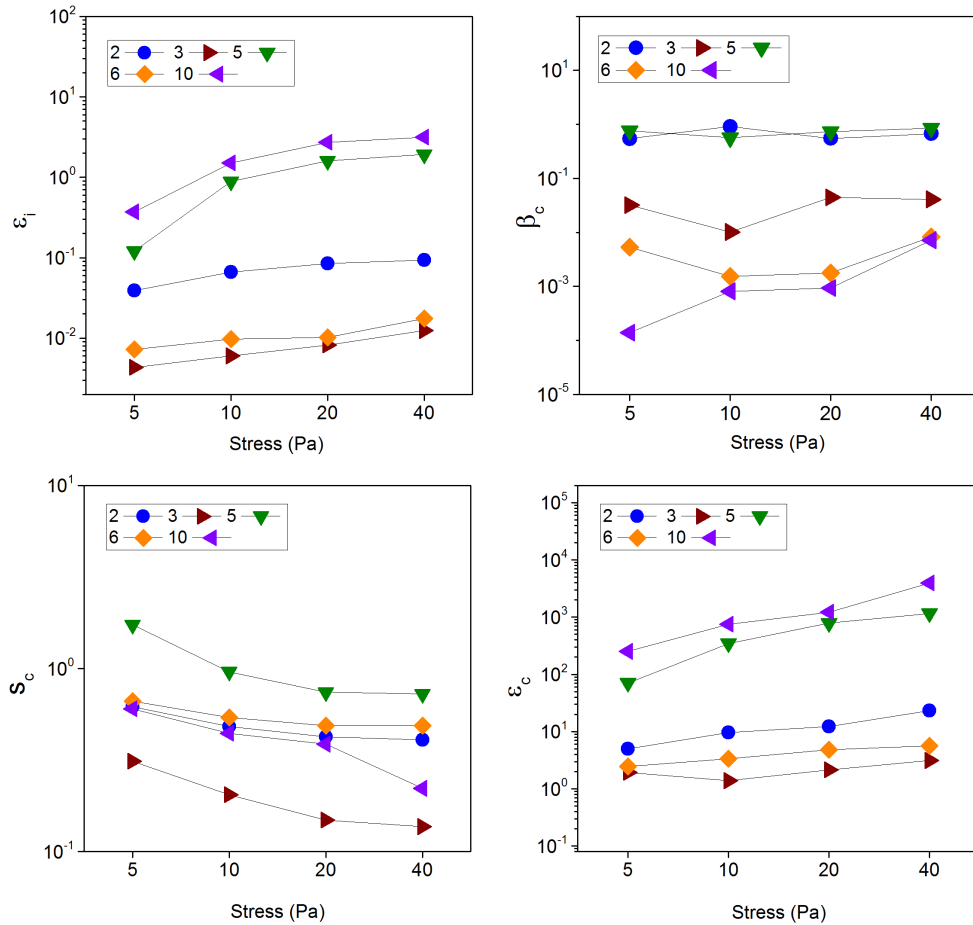


FIGURE 3.28: Parameters obtained by fitting the *Weibull* distribution to the experimental creep data for the solutions showing viscoelastic behaviour, at  $50^\circ\text{C}$ .

At  $50^\circ\text{C}$  it is possible to observe an increasing in the instantaneous strain ( $\varepsilon_i$ ) and final creep strain ( $\varepsilon_c$ ) values when compared with the values obtained at  $20^\circ\text{C}$ . At  $50^\circ\text{C}$  the viscoelastic strain is higher because at higher temperature the viscosity is lower so the deformation of the material will be bigger.

Once again, for the parameter  $\beta_c$  it was not possible to obtain a trend that allows the correlation between the different stresses or compositions but as the values are lower than 1, the strain rate is observed to decrease with time.

Parameter  $s_c$  decreases with the increasing of the applied stress and this fact can be due to the higher strain rates that result from the faster activation of the

available latch elements.

**d) Adjusting recovering results using *Weibull* distribution**

For the recovery, the *Weibull* model is described by Equation 3.6 [135].

$$\varepsilon_{recovery} = \varepsilon_r \left[ \exp\left(-\left(\frac{t}{s_r}\right)^{\beta_r}\right) \right] + \varepsilon_f \quad (3.6)$$

As the *Weibull* model for the recovery curve does not include the instantaneous elastic recovery this part of the graph needs to be excluded from the fitting. In this particular case, in the recovery curve it was not possible to observe graphically the instantaneous elastic recovery because not enough points were recorded in this region to notice it. In this situation, as this portion of strain is the same obtained in the creep curve for the instantaneous elastic response [158], this strain was subtracted to the first point obtained in the recovery curve before the fittings were made.

In Figure 3.29 an example of the fit made to the recovery curve using *Weibull* distribution for composition 1 at 40 Pa is shown. The errors obtained can be seen in the Appendix section (Table A.8).

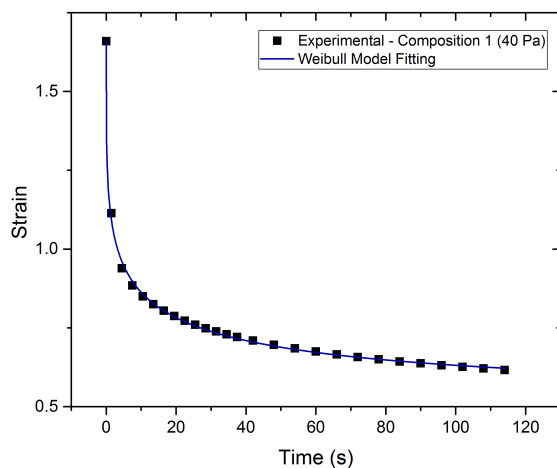


FIGURE 3.29: *Weibull* model applied to recovery curve for composition 1 at a stress of 40 Pa and a temperature of 20°C.

As can be seen in Figure 3.29 the *Weibull* distribution is in good agreement with the experimental results. In Figure 3.30 it is possible to observe the parameters values obtained for each composition and stress - viscoelastic strain recovery ( $\varepsilon_r$ ), creep characteristic life ( $s_r$ ), shape parameter ( $\beta_r$ ) and residual strain ( $\varepsilon_f$ ). The errors obtained can be seen in the Appendix section (Table A.8).

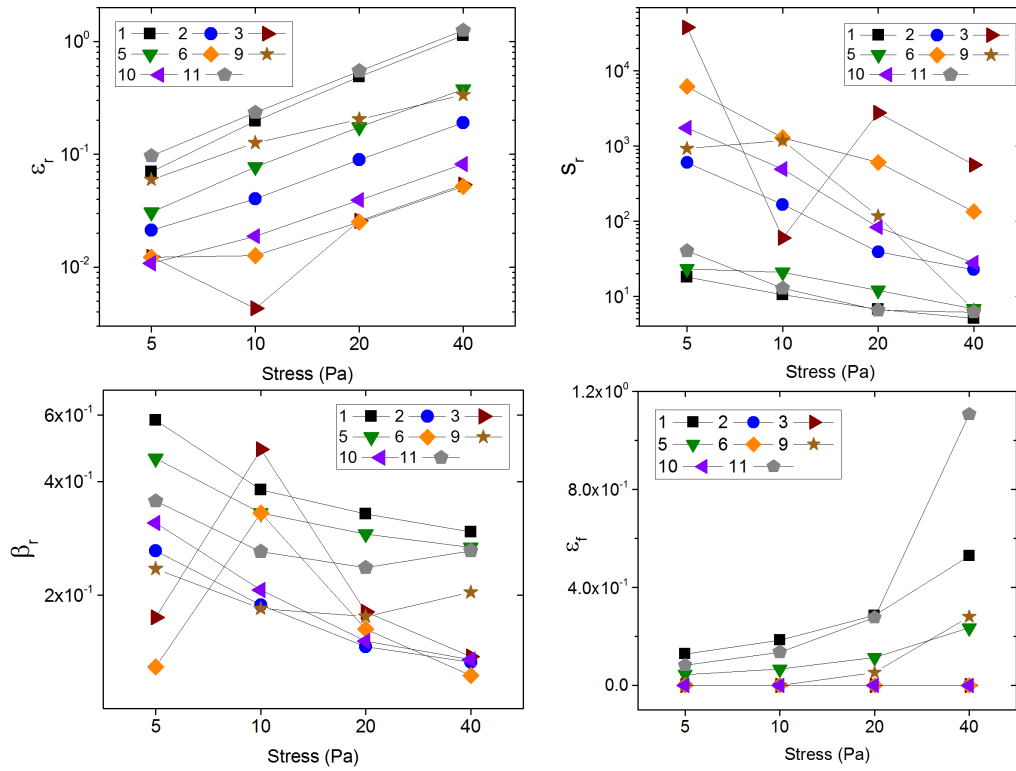


FIGURE 3.30: Parameters obtained by fitting the *Weibull* distribution to the experimental recovery data for the solutions showing viscoelastic behaviour, at 20°C.

An example of the parameters values obtained with the respective deviation for composition 2 at 20°C can be observed in Table 3.2.

TABLE 3.2: Parameters values obtained by fitting the recovery results to the *Weibull* model for composition 2 at 20°C with the respective deviation for the different applied stresses.

Parameter	5 Pa	10 Pa	20 Pa	40 Pa
$\varepsilon_r$	$0.021 \pm 0.004$	$0.041 \pm 0.005$	$0.089 \pm 0.008$	$0.191 \pm 0.009$
$s_r$	$601 \pm 725$	$166 \pm 183$	$39 \pm 45$	$23 \pm 15$
$\beta_r$	$0.26 \pm 0.02$	$0.19 \pm 0.01$	$0.15 \pm 0.01$	$0.133 \pm 0.007$
$\varepsilon_f$	$0 \pm 0.004$	$0 \pm 0.005$	$0 \pm 0.009$	$0 \pm 0.01$

As before, looking to Equation 3.6 it is possible to see that the parameter  $s_r$  appears as a denominator of a fraction that has  $\beta_r$  as exponent. Being  $\beta_r < 1$  for all the compositions and applied stresses, the value of  $s_r$  is not much relevant to obtain a good fit. This is easy to see in the values obtained for this parameter, where the deviations are in some cases bigger than the value itself. This makes  $\eta_r$  a parameter difficult to analyse in a quantitative manner. However, for the other parameters the deviations are acceptable and it is possible to make a comparative analysis between the different compositions and stresses.

$\beta_r < 1$  for all the compositions and stresses, meaning that there is a decreasing in the failure rate with time [135]. In this situation, a failure happens when, after a material is extended and all the latch elements are also fully extended, the stress is removed and some latches fail and there is a partial recovery of the strain. Failure is, in this case, associated with elastic features. This means that with increasing time, the rate of elastic recovering is decreasing. This makes sense because it means that most of the elastic strain is recovered in the initial instants after the load is removed and that is actually the behaviour that is observed in the recovery curves obtained. Looking now to  $\varepsilon_r$  it is possible to see that, apart from composition 3 where there is a decreasing from the first point to the second, there is an increasing of this parameter for all the compositions with the applied stress. This makes sense since the more stress is imposed to the sample, the bigger will be the strain that needs to be recovered (looking to the creep curve it is easy to see that the bigger the applied stress the bigger is the maximum strain achieved). Comparing this with the latch model it can be suggested that with the increasing applied stress more latches will be activated and, as the strain keeps increasing and a  $\varepsilon_r$  plateau was not achieved, an increase

in the stress will continuing increasing the obtained strain.

$\varepsilon_f$  corresponds to the residual strain (viscous flow) that is not recoverable. As can be observed, only some compositions show residual strain, meaning that all the other compositions not represented here are able to recover all the strain at some point in time - suggesting that they don't have purely viscous domains. It is also possible to see that, for composition 9, a recovery is possible for stresses equal to 5 and 10 Pa but not for 20 and 40 Pa showing that there is a threshold point from where the solution cannot recover to the initial strain. In terms of the latch model this means that some of the latches that were activated during creep time will possess trigger times near infinity in the recovery curve that will correspond to viscous flow [136]. This shows again the different rheological features of the batch of solutions studied.

The *Weibull* model was also applied to the recovery curves obtained at 50°C. The results can be seen in Figure 3.31. The errors obtained can be seen in the Appendix section (Table A.9).

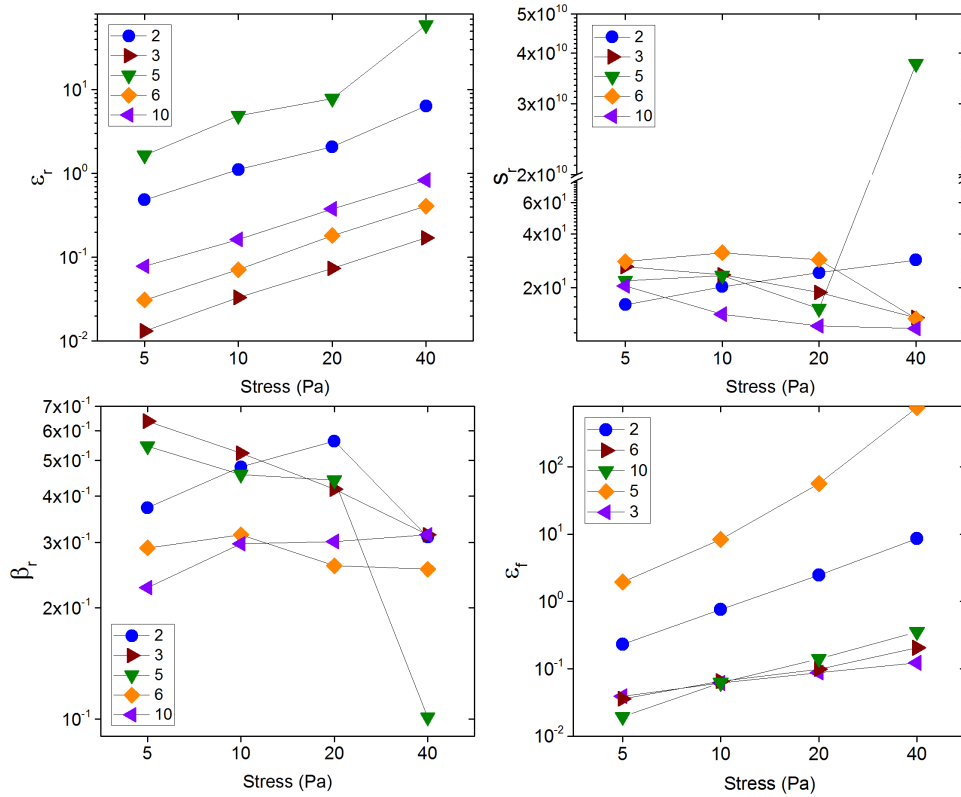


FIGURE 3.31: Parameters obtained by fitting the *Weibull* distribution to the experimental recovery data for the solutions showing viscoelastic behaviour, at  $50^\circ\text{C}$ .

Starting with  $s_r$ , big deviations were again obtained for this parameter. The reasons for this were already discussed previously and are related with the instability of the system at high temperature due to possible solvent evaporation.  $\beta_r$  values are  $<1$ , showing that there is a decreasing in the rate of elastic recovering as it happened at  $20^\circ\text{C}$ .  $\varepsilon_r$  increase with the applied stress as before, however, at  $50^\circ\text{C}$  the viscoelastic strain recovered is bigger. This happens because at higher temperature the viscosity is lower so the deformation of the material will be bigger and consequently the recovered deformation. Regarding  $\varepsilon_f$ , opposing to what happen at  $20^\circ\text{C}$ , all the samples present residual strain. A possible explanation for this results is the fact that, at higher temperature the solutions become more liquid-like (and with lower viscosity) losing some of the solid features such as

elasticity (this was already observed in Figure 3.13 where  $G'$  decreases with temperature increasing). Due to this, the viscous nature of the sample is bigger than before and this part of the deformation is not recoverable.

### **3.4 Rheological Studies of a PVC Solution used for Membrane Spinning**

The rheological results presented in the previous section were related with the study of 11 solutions with different compositions. In this section, a rheological evaluation of the solution that was prepared to conduct the spinning experiments (same composition as sample number 2 in previous section - 28% PVC, 50% DMAc, 6% THF and 16% EtOH (w/w)) is performed.

This composition was chosen to conduct the spinning runs because of the results obtained in the phase inversion studies that show that this solution is located in the one phase region and is sufficiently far from the binodal boundary in order to be stable and, at the same time, close enough for phase separation to occur when the thermodynamic conditions change. Also, good selectivity results were already obtained for fibres produced with this composition [8]. In this section, the objective of studying this sample is to understand the rheology role in the separation features of the prepared membranes.

What distinguishes this solution from the one studied in the previous section is the preparation method. For the spinning solution preparation, mechanical stirring was used and the time used in the preparation was about 24 hours. In the previous section, the solutions were prepared without stirring and 24 days were needed to achieve homogeneity. Also the time elapsed to perform the experiments after the solutions were prepared was different. All these differences are compiled in Table 3.3.

TABLE 3.3: Comparison of the preparation method and of the "ageing" time between composition number two studied before and the solution used to spin membranes.

	<b>Composition 2</b>	<b>Spinning Solution</b>
<b>Type of stirring</b>	No stirring	Mechanical stirring
<b>Time to achieve homogeneity</b>	25 days	20 hours
<b>Maximum temperature during preparation</b>	69°C	50°C
<b>Time since preparation until experiments were performed</b>	2 months	2 days

This study will allow to discuss the influence of the preparation method and solution "ageing" time in the final rheological results.

### 3.4.1 Flow tests

To produce hollow fibres membranes, a polymer solution is subjected to high shear rates when passing through the *spinneret*. In line with this, it makes sense to study how the solutions behaves under the influence of shear rate. Flow tests allow to understand the behaviour described before. In this experiment the material is subjected to a range of shear rates and the corresponding viscosity is recorded.

For this analysis, shear rates from  $10\text{s}^{-1}$  to  $5000\text{s}^{-1}$  were used (up and down curves) at 20°C and 50 °C. The results obtained can be seen in Figure 3.32. The errors obtained can be seen in the Appendix section (Table A.10).

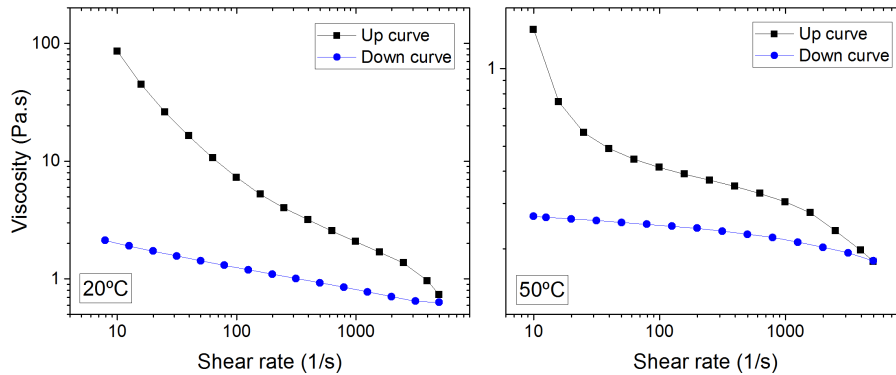


FIGURE 3.32: Flow curves obtained for the spinning solution at 20°C and at 50°C.

As can be seen in Figure 3.32, the spinning sample behaves as a shear thinning material as the viscosity decreases with increasing shear rate (up curve) [122]. These curves show typical flow behaviour for polymer solutions [113]. As can be noticed, up and down curves are not identical. Initially, it was thought that the high shear rates used might be causing some structural damage to the material that seems not to be able to "recover". However, flow tests were performed ending at different shear rates and the result was identical to the previous one. Another possible reason for this difference between up and down curves can be the time dependent behaviour of the material. Accordingly to *Barnes* [130], this phenomenon occurs because the micro structures of a material will take time to respond to stress or flow. In polymer solutions, these micro structures are suggested to be related with the entanglements so, if a polymer solution has a concentration sufficiently high for chain entanglements to occur, thixotropy should be expected.

Looking into the end part of the up curve (for both temperatures) it is possible to observe a sudden decrease in the viscosity value. This phenomenon is often called as slippage and occurs because the contact between the sample and the plate is lost making the plate slip across the sample instead of rotating it. However, as the viscosity starts to increase when the shear rate decreases, it is suggested that the apparatus recovers from the slippage condition detected before.

### 3.4.2 Flow model: Determination of the Shear Rate, Velocity and Stress Profiles in the Spinneret

In 1996, *Shilton* [115] developed a methodology to determine shear rate, velocity and stress profiles of a power law fluid flowing through concentric annulus. This methodology was aimed to be applied to membrane spinning giving information about what is happening in the *spinneret*. Flow experiments are useful to use this methodology since power law fluid parameters are needed to predict the profiles.

A power law fluid is described by Equation 3.7.  $K$  corresponds to the power law constant and  $n$  to the power law index and both are needed to apply *Shilton's* model.

$$\eta = K\dot{\gamma}^n \quad (3.7)$$

Fitting Equation 3.7 to the flow results in the power law region it is possible to obtain the parameters needed to draw the profiles using *Shilton's* methodology. Figure 3.33 shows how a power law fitting applied to the flow results obtained.

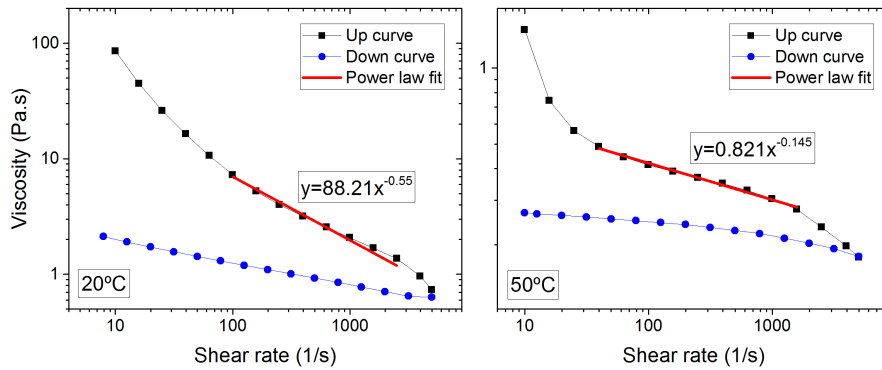


FIGURE 3.33: Power law fit applied to flow curves for the spinning solution at 20°C and at 50°C.

All the inputs needed to draw the profiles accordingly with *Shilton's* methodology are presented in Table 3.4. The dope extrusion rates modelled were 1, 3 and 5  $\text{cm}^3/\text{min}$  because these are the ones that will be later investigated in the spinning runs.

TABLE 3.4: Input parameters used in *Shilton's* methodology in order to calculate shear rate, velocity and stress profiles in the *spinneret* at 20°C and at 50°C.

Parameter	20°C	50°C
Inner Radius (mm)	0.229	
Outer Radius (mm)	0.635	
Spinneret Length (mm)	0.284	
Power Law Index	0.44	0.855
Power Law Constant (Based on SI units)	88.21	0.821
Dope Density ( $\text{g}/\text{cm}^3$ )	1.025	
Dope Extrusion rate ( $\text{cm}^3/\text{min}$ )	1, 3 and 5	

The polymer solutions flows through the *spinneret* that is an annulus with an inner and outer wall. With all the parameters, it is now possible to draw the profiles at 20°C and at 50°C, Figure 3.34.

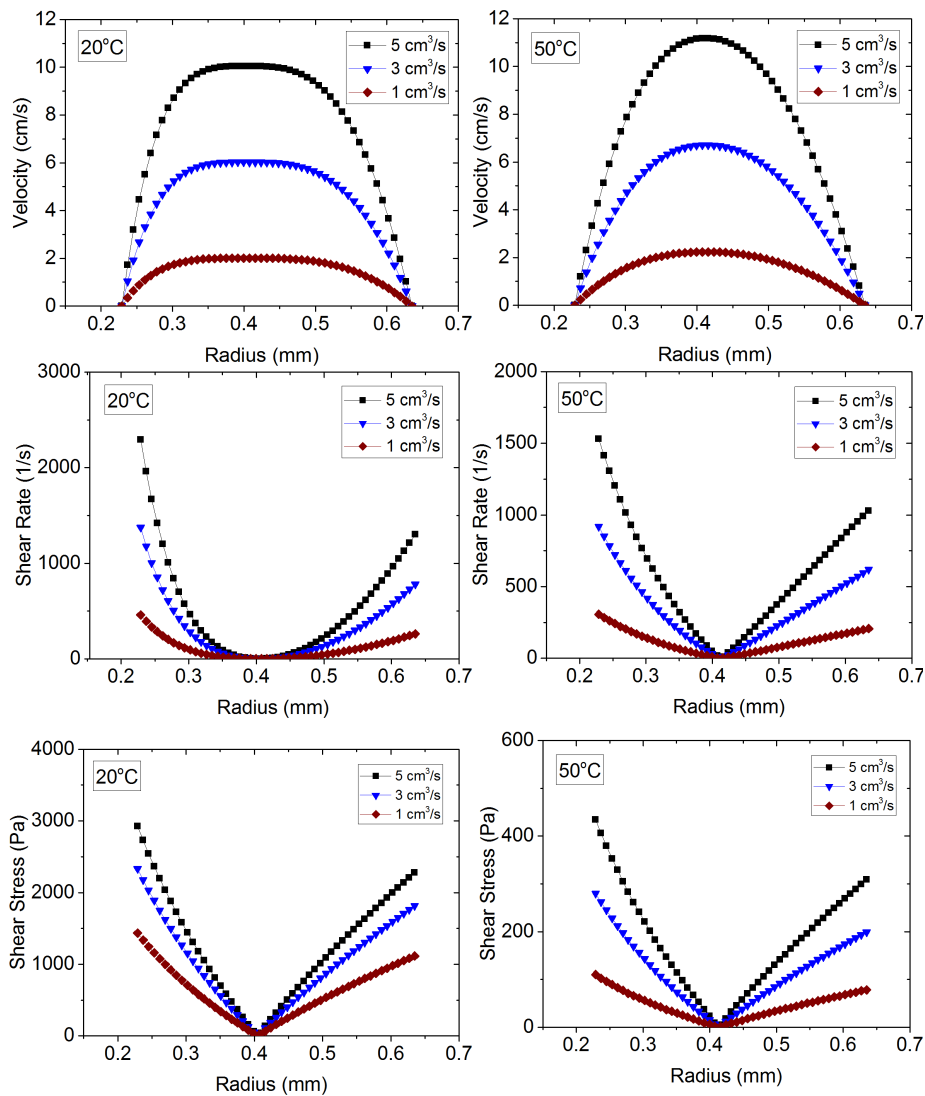


FIGURE 3.34: Shear rate, shear stress and velocity profiles in the *spinneret* at 20°C and at 50°C.

As expected, at high extrusion rates the profile curves have higher values. In terms of velocity, it can be noticed that the profiles are slightly shifted to the left (inner wall). The reason for this results is the fact that the material being studied is flowing through an annulus with an inner and an outer wall. This situation will result in two different boundaries with different *Reynold* numbers that in combination will give a slightly shifted curve [1]. This shift is also noticeable in the shear rate and shear stress profiles. At 20°C, the maximum velocity varies from 2 to 10 cm/s and at 20°C from 2 to 11 cm/s. The maximum velocities

achieved are not very different for the two temperatures, however at 20°C the curves are flat in the centre indicating that we are in the presence of a plug flow. At 50°C, due to the lower viscosity of the sample, plug flow is not identified.

Looking into the shear stress profiles it is possible to observe that the bigger stresses are observed in the walls of the annulus since they offer resistance to the flow. It is also possible to observe a bigger variation with temperature when compared with the velocity or shear rate profiles. At 20°C the values vary from 1500 to around 3000Pa and at 50°C from 100 to 450Pa.

Lastly, concerning the shear rate profiles, it's easy to see that they follow the same trend as the shear stress ones with values ranging from 500 to 2400 s<sup>-1</sup> at 20°C and from 250 to 1500 s<sup>-1</sup> at 50°C. The shear rates closer to the outer wall are most important since the active layer will be formed in this region (due to the *spinneret* configuration) and molecular orientation will take place. For the conditions studied the shear rates observed vary from 250 to 2400 s<sup>-1</sup>. Looking into Figure 3.33 it is possible to see that the power law model adjusted curves cover this interval. If shear rates higher than 2400 s<sup>-1</sup> (at 20°C) or 2000 s<sup>-1</sup> (at 50°C) are achieved in the *spinneret* outer wall, slippage can occur and the shear imposed to the sample will be lower than expected. This can be important concerning the molecular orientation induced by shear rate producing membranes that are less oriented than predicted, affecting the performance of the formed fibre. This shows the importance of the temperature in the spinning process.

### 3.4.3 Oscillatory Shear Rheology

#### 3.4.3.1 Results of the Angular Frequency Tests: Determination of the Relaxation Time

Oscillatory experiments were performed to the solution used to perform the membrane spinning. As the LVER was tested before for this composition by performing amplitude sweep tests, and the LVER was clearly identified, this test was not performed here.

As discussed before, frequency sweep test allow to understand the behaviour of a

material at different time scales. Also, they allow to determine the polymer chains relaxation time that is a very important parameter when conducting membrane spinning experiments.

As the membrane spinning was performed at high temperatures, frequency tests were performed to the spinning solution in order to study its properties at different temperatures. Figure 3.35 shows the results obtained at 40°C, 50°C and 60°C. The errors obtained can be seen in the Appendix section (Table A.11).

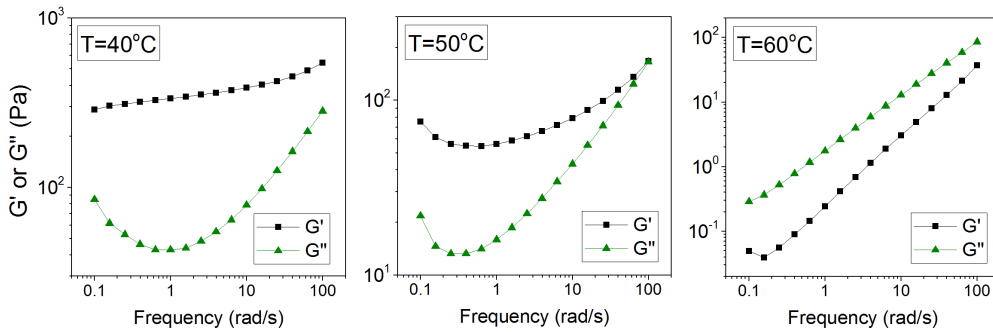


FIGURE 3.35: Storage modulus ( $G'$ ) and loss modulus ( $G''$ ) of the spinning solution as a function of temperature for a frequency of 10 rad/s.

Observing these results, it is possible to see that, with the increasing of the temperature, the curves are moving towards the glassy region (Figure 3.4). The crossover observed at 50°C corresponds to the transition from the leathery to the glassy region. As the results obtained before, it is not possible to visualise the cross over frequency that represents the inverse of the relaxation time. However, once again, it is possible to say that the relaxation time for each one of the temperatures is always bigger than 10 seconds (cross over frequencies always lower than 0.01 rad/s).

The dope extrusion rates that were used to perform the membrane spinning correspond to residence times in the forced convection chamber of less than 2 seconds. As the relaxation times obtained in the angular frequency tests are always bigger than 10 seconds, it can be suggested that the orientation achieved in the *spinneret* is "locked" when the fibre passes in the forced convection chamber and solidifies.

### 3.4.3.2 Results of the Temperature Sweep tests

In order to compare the results obtained before for composition number 2, temperature sweep tests were also performed to the spinning solution in order to understand if the behaviour of  $G'$  as a function of temperature is the same and which value  $T_{half}$  has. In Figure 3.36 the behaviour of the storage modulus ( $G'$ ) can be observed as function of temperature.

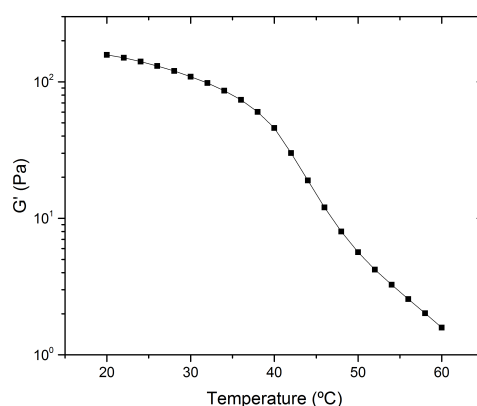


FIGURE 3.36: Storage modulus ( $G'$ ) as a function of temperature for the spinning temperature at 10 rad/s and 5% strain.

As before, Equation 3.3 allowed to determine  $T_{half}$ , which represents the temperature at which the curve changes its behaviour. For this sample, the temperature obtained was 43°C. For the composition studied in the previous section (composition 2) the temperature obtained was 51°C (Figure 3.15). What distinguished this two solutions is the preparation method and the elapsed time to perform the experiments. The solution that was left to age (composition 2) presents a higher "transition" temperature compared with the one studied one day after preparation (spinning solution). A suggestion for this result is related with the fact that the solution that was studied two months after preparation had more time to "create" entanglements making the transition to appear later because more energy is needed to "destroy" these entanglements.

### 3.4.4 Creep and Recovery tests

As it was concluded before, the creep and recovering results appear to be independent of the stress applied (Figure 3.18). Having this in mind, the spinning solution was studied keeping the stress constant and varying the temperature to check its influence. The results obtained can be found in Figure 3.37. The errors obtained can be seen in the Appendix section (Table A.12).

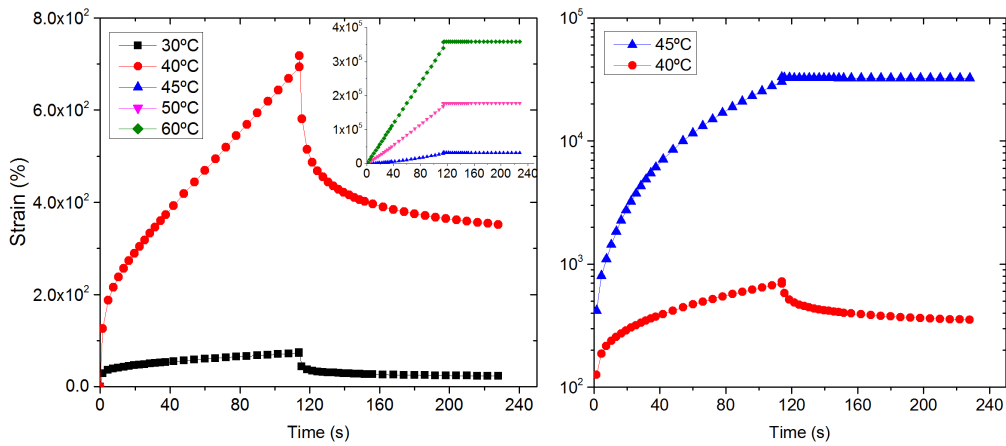


FIGURE 3.37: Creep and recovering test performed with the spinning solution at different temperatures and fixed stress of 20 Pa.

Looking to Figure 3.37 it can be easily observed a change in the behaviour of the sample between 40°C and 45°C. From 30°C to 40°C the sample behaves as a viscoelastic material, recovering part of the deformation suffered. In between 40°C and 45°C it seems to exist a temperature above which the material starts behaving as a viscous liquid. The curious aspect of these results is that they are related with the results obtained previously in the oscillatory measurements for this solution where  $T_{half}$  was calculated and corresponds to 43°C. These results seem to be aligned. In the results obtained in the temperature sweep test a decreasing in the storage modulus of the material can be observed with with half point equal to 43°C, suggesting a reduction in the complex viscosity value. On the other hand, the creep and recovering shows a transition between a viscoelastic regime to a purely viscous one located somewhere between 40°C and 45°C.

Accordingly with the literature [159] and experimental evidence, a liquid-liquid transition (viscoelastic to viscous behaviour) can be the possible explanation for this phenomenon.

*Jones et al.* [8] performed spinning runs at 20°C and at 50°C obtaining better membrane performances for the ones spinning at high temperature. Looking into the rheological results obtained in this work there is the possibility that these are related with the performances obtained by the author.

The high selectivities obtained by the author at 50°C might be related with this transition. Accordingly with these results, at 50°C the solution has no elasticity, being purely viscous. This will mean that, after the *spinneret*, the solution is not able to recover the deformation suffered, keeping the characteristics acquired during the extrusion. One of these characteristics might be the alignment of the polymer chains in the active layer - that is actually the part of the solution that suffers more shear stress. This alignment can help the active layer to be more uniform in the sense that the concentration of polymer will be more evenly distributed instead of having regions with more polymer than the others, producing defects on the surface when the solvent evaporates.

### 3.5 Conclusions of Rheological Studies

A rheological analysis of PVC quaternary solutions was carried out in order to study the influence of solution composition and temperature in the rheological properties of the solutions. The results showed that the solution composition and temperature have high influence in the rheological results obtained, as expected.

In the frequency tests, different behaviours were obtained for the different concentrations. In the frequency range studied it was not possible to obtain the exact value for the relaxation times. However, it is possible to suggest that these times are always bigger than 10 seconds. These experiments also allowed the

determination of the gel point in terms of concentration.

There is a range of temperatures in which there is an accentuated decrease in the storage modulus for all the compositions. DSC experiments were performed and no thermal transitions were present suggesting that the cause of for the drop in the storage modulus is a liquid-liquid transition (change from viscoelastic to viscous behaviour). The mid-point temperatures corresponding to the change in the behaviour of the storage modulus were calculated for all the compositions and ranged from 41°C to 51°C.

Creep and recovery experiments results showed that the intensity of the applied stresses does not affect the viscoelastic properties of the solutions while the temperature showed to have a strong influence in the these properties. Some samples that behaved as viscoelastic materials at 20°C behaved as purely viscous materials at 50°C.

Mechanical and statistical models were fitted to the experimental creep and recovery results in order to obtain quantitative data. The creep model used (*Burgers* model with four parameters) correlated well the experimental data and some conclusions were taken by looking into the parameters obtained. Creep and recovery results were fitted to a statistical model - *Weibull* model - since it was not possible to obtain a good correlation with the *Burgers* model used to fit creep data, compromising the use of this model for this system. This model allowed to predict the final non-recoverable strain achieved at infinite time after the load is removed ( $\epsilon_f$ ). This parameter cannot be determined by the *Burgers* model and it can be important for some applications. It was observed that for some solutions it is possible to recover all the deformation imposed at some point in time.

After the rheological experiments, spinning runs were conducted using a fresh solution with the same composition as solution number 2. The choice of this composition is related with the phase inversion studies performed before and with the fact that this composition was used in previous successful work in our research group. The sample used in the spinning was also analysed rheologically because the preparation method was different from the one used to prepared the eleven solutions studied earlier.

Flow results at 20°C and 50°C allowed to simulate velocity, shear rate and shear stress profiles in the *spinneret* by fitting the experimental data to a power law

model. These results showed one more time the importance of high temperature in the extrusion process.

Temperature sweep tests showed again a decreasing in the storage modulus with half-point equal to 43°C. The value obtained for the same composition but with a different preparation method was 51°C, suggesting that the preparation method and the time until the tests was performed might have an impact in these results. Creep and recovery tests were made using the spinning solution by using different temperatures ranging from 30°C to 60°C. A change from viscoelastic to purely viscous was detected between 40°C and 45°C.

Results published before by *Jones et. al* [8], for the same system, showed higher selectivities for the fibres prepared at 50°C when compared with fibres prepared at 20°C. Relating these results with the ones obtaining in this work, a possible explanation is the fact that, at 50°C the solution has no elasticity, so the possible orientation achieved in the *spinneret* is "locked" when the coagulation of the membrane surface occurs.

Is important to note, once again, the complexity of the system being studied. One of the components is a solvent with a boiling point of around 66°C (THF) that make evaporation an issue when high temperature is used. Although this effect was minimised by the use of a solvent trap, its not guaranteed that this phenomenon have no effect in the results.

In the next chapter, the rheological results obtained will be used to set the spinning parameters and to compared with the performance of the prepared hollow fibre membranes to try to understand how they can relate.



## Chapter 4

# Hollow Fibre Membrane Spinning and Gas Permeation Results

### 4.1 Objectives

Considering the rheological results of the different compositions of the quaternary PVC solutions, dry/wet spinning experiments are designed. The objective is to study the influence of different operational parameters in the performance of the prepared hollow fibre membranes and, for that, the adequate study parameters must be chosen.

The influence of three different parameters on the performance of the prepared hollow fibre membranes was studied - spinning temperature, dope extrusion rate and external bath temperature. Adequate values for these parameters were discussed and the *Taguchi* approach was used to design the experiments. After, the spinning experiments were carried out in the laboratory and the permeation results were analysed in order to try to establish a correlation to determine the optimal conditions. *ANOVA* variance analysis was explored to understand which of the parameters has a bigger impact in the selectivity results obtained.

### **4.1.1 Materials and Methods for Membrane Preparation and Permeation Measurements**

#### **4.1.1.1 Materials**

All the components used to prepare the polymer solutions are the same mentioned in Chapter 3. Methanol (MeOH) (purity  $\geq 99.9\%$  w/w, CHROMA SOLV for HPLC) and hexane (purity  $\geq 99.9\%$  w/w, CHROMA SOLV for HPLC) and potassium acetate (puriss., meets analytical specification of Ph. Eur, E261, 99-101%) were also purchased from Sigma-Aldrich. Polydimethylsiloxane (PDMS) (Sylgard<sup>®</sup> 184) was acquired from Dow Corning and polyurethane resine (PU3410) from Alchemie.

Oxygen (purity  $\geq 99.999\%$ ) and nitrogen (purity  $\geq 99.9992\%$ ) were purchased from BOC.

#### **4.1.1.2 PVC Solution Preparation Method For Membrane Preparation**

A volume of 250mL of a solution composed by PVC (28% w/w), DMAc (50% w/w), THF (6% w/w) and EtOH (16% w/w) was prepared in a fume cupboard. The experimental set-up can be seen in Figure 4.1.

In the day prior to the spinning run, the DMAc was added to a vial placed in a water bath. The mechanical stirrer was turned on, the temperature set to 50°C and the polymer was slowly added to the vial to avoid agglomeration. The mixture was left stirring overnight with a condenser operating with tap water attached to the solution container in order to avoid any loss of solvent. On the day after (spinning day), THF was added to the mixture and finally the EtOH. The solution was left stirring for another hour and was after transferred to the

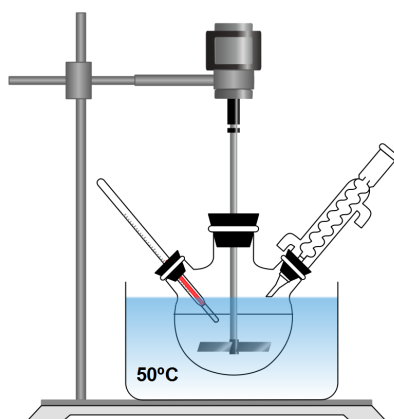


FIGURE 4.1: Experimental set-up for the quaternary polymer solution preparation.

dope reservoir that was kept warm at the desirable spinning temperature using a water bath.

#### 4.1.1.3 Designing the Spinning Experiments using the *Taguchi* Method

In the previous chapter, eleven solutions with different compositions were studied in order to understand the impact of composition regarding its rheological properties. Along with these, other parameters were studied such as temperature and shear rate. Despite the big impact that the different concentrations have in the rheology features, it was decided that this parameter would remain constant. The reason for this choice is related with the phase inversion studies performed before and with the work done by *Jones* [1] that spun PVC hollow fibre membranes with decent selectivities using this composition. Because of this, it was decided to keep this parameter constant in order to study the influence of other parameters.

In total, three parameters will be studied - dope spinning temperature, dope extrusion rate and coagulation bath temperature. As discussed before, the spinning temperature is considered as an important factor due to the rheological behaviour dependence on this parameter. The dope extrusion rate was also chosen due to literature indications that this factor has influence on the performance of the

prepared membranes [71, 114, 117]. Lastly, previous tests conducted by the research group suggested that the coagulation bath temperature has influence in the microscopic structure of the membranes [160].

As the rheological examination showed interesting behaviours at 50°C, 40°C and 60°C were chosen as well to understand what happens before and after this point. 10°C difference between the studied temperatures seemed reasonable in order to identify possible differences in the prepared membrane features.

Concerning the extrusion rate, this parameter will affect the shear rate suffered by the solution in the *spinneret* and also the residence time in the forced convection chamber (since the chamber height used was always the same). In this work, the extrusion rates studied were 1, 3 and 5 cm<sup>3</sup>/min since they are within the normal values used in the literature and the idea is to study the influence of different velocities of spinning.

Lastly, also the external bath temperature was investigated. In previous work done in the laboratory, there was evidence of tearing happening at the surface of the membranes at low temperatures (room temperature), disappearing at higher temperatures [160]. Due to the impossibility to have the water bath at temperatures above 40°C this was the highest temperature studied. To check the effect of this parameter also 20°C and 30°C were chosen.

In Table 4.1 it is possible to find the values chosen for each parameter studied.

TABLE 4.1: Values chosen for the parameters to be studied (dope/spinning temperature, extrusion rate and external bath temperature).

<b>Dope/Spinning Temperature (°C)</b>	<b>Extrusion Rate (cm<sup>3</sup>/min)</b>	<b>External Bath Temperature (°C)</b>
40, 50, 60	1, 3, 5	20, 30, 40

All the other spinning conditions were maintained constant in all of the spinning runs, as follows:

- *Spinneret Dimensions*: The *spinneret* used in the spinning runs was the one already available in the research group with external diameter of 635  $\mu\text{m}$ , internal diameter of 229  $\mu\text{m}$  and aspect ratio (length to gap) of 1.4.
- *Internal coagulant composition and temperature*: The internal coagulant fluid (or bore fluid) used was a 20% solution of potassium acetate in water. The use of different bore fluid compositions will result in different membrane characteristics [75, 161–163]. Since this composition was already used by Jones *et. al* [8] to produce membranes with decent selectivities, it was decided to keep this parameter constant. The reason to use potassium acetate in water instead of using pure water is to reduce water activity and consequently the energy of the fluid so it will have a lower probability of interacting with the active layer, avoiding damage. The temperature used for the bore fluid was room temperature.
- *Internal Coagulant Injection Rate*: This factor affects the velocity that the bore fluid (that acts as a non-solvent) will approach the active layer. This rate needs to be big enough to form the hollow in the membranes but not too big that will damage the active layer before it is fully formed. Usually this rate is related with the dope extrusion rate and it is practice in this group to maintain it at a third of the dope extrusion rate.
- *Forced Convection Flow Rate*: This factor was already investigated in Jones' [1] work. Due to this, it was decided to maintain this variable constant. In Jones' work it was suggested that a flow rate of 8 L/min would be the best condition to produce membranes with decent selectivities. However, due to the difficulty to spin membranes at 60°C with this gas flow rate, a flow rate of 4 l/min was chosen due to stability in the process and because it is not intended to study the impact of this factor in the present experiments.
- *Forced convection height*: For all the spin runs, the chamber used was always the same (as it was the only one available in the laboratory) - a 9 cm cylinder with the impingement zone located at 2.5 cm from the top. This means that the residence time will vary with the extrusion rate and this effect will be studied as well together with the dope extrusion rate effect.

- *Jet-Stretch Ratio*: The jet-stretch used in these experiments was 1 in order to minimize the stretch in the membranes so the other effects can be analysed without other interferences.

The general spinning conditions can be found in Table 4.2.

TABLE 4.2: General Spinning conditions.

Polymer solution temperature	40°C, 50°C or 60°C
Spinneret dimensions	OD 635 $\mu\text{m}$ , ID 229 $\mu\text{m}$ aspect ratio (length to gap) 1.4
Internal coagulant composition	20% (w/w) potassium acetate in water (water activity 0.9)
Internal coagulant temperature	Room temperature
Dope extrusion rate	1, 3 or 5 $\text{cm}^3/\text{s}$
Dope extrusion rate:internal coagulant injection rate	3:1
Forced convection gas	Nitrogen
Forced convection flow rate	4 L/min
Forced convection chamber height	9 cm
Forced convection temperature	Room temperature
External and wash bath composition	Water
External bath temperature	20°C, 30°C or 40°C
Wash bath temperature	Room temperature
Wind-up bath	Room temperature
Jet stretch ratio (wind-up speed : extrusion speed)	1:1

As stated before, the *Taguchi* method was used to design the spinning experiments. The first step in the *Taguchi* approach is to build a matrix of orthogonal arrays in order to define the experiments to be performed. The number of factors to be considered in this work is three (spinning temperature, dope extrusion rate and coagulation bath temperature) and each of the factors as three levels. In this situation the array is described by the symbol L9, that contains three three-level columns, Table 4.3.

TABLE 4.3: Orthogonal arrays (L9 Table).

Experiment Number	Factor 1	Factor 2	Factor 3
1	Level 1	Level 1	Level 1
2	Level 1	Level 2	Level 2
3	Level 1	Level 3	Level 3
4	Level 2	Level 1	Level 2
5	Level 2	Level 2	Level 3
6	Level 2	Level 3	Level 1
7	Level 3	Level 1	Level 3
8	Level 3	Level 2	Level 1
9	Level 3	Level 3	Level 2

For this study, nine experiments should be performed, accordingly with the L9 table. Table 4.4 shows the nine runs indicating which value for each parameters should be used in each run. These arrays considers that there is no interaction between any two factors.

TABLE 4.4: L9 orthogonal matrix used to spinning experiment design.

Experiment Number	Dope/Spinning Temperature (°C)	Extrusion Rate (cm <sup>3</sup> /min)	External Bath Temperature (°C)
1	40	1	20
2	40	3	30
3	40	5	40
4	50	1	30
5	50	3	40
6	50	5	20
7	60	1	40
8	60	3	20
9	60	5	30

**4.1.1.4 PVC Hollow Fibre Membrane Spinning Method**

In order to produce asymmetric hollow fibre membranes, a dry/wet spinning process with forced convection in the dry gap was followed. A representation of the spinning equipment can be seen in Figure 4.2.

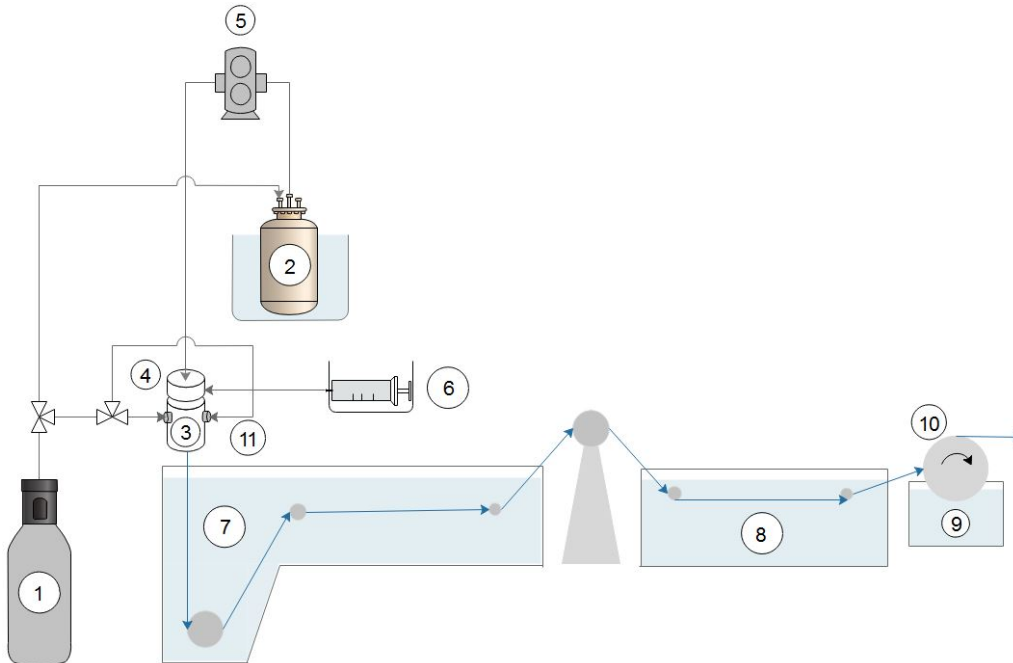


FIGURE 4.2: Membrane spinning apparatus (1-Nitrogen cylinder, 2-Polymer solution vessel, 3-Forced convection chamber, 4-Spinneret, 5-Gear pump, 6-Syringe pump, 7-External bath, 8-Wash bath, 9-Wind-up bath, 10-Wind-up drum, 11-Nitrogen entrance).

The fibers were extruded vertically through the *spinneret* at a chosen dope extrusion rate (DER). Using a syringe pump, the bore fluid - a 20% w/w aqueous solution of potassium acetate - was fed into the *spinneret* at a constant flow rate (1/3 of DER). The forced convection chamber was located underneath the *spinneret* and consists of a cylinder with 5 cm diameter and 9 cm height and is flushed with nitrogen. After extruded, the fibers passed through this chamber and the nitrogen was introduced into chamber through three tubes 120° apart from each other located at 2.5 cm from the top of the chamber. The coagulation baths were

composed by water being the first one (external bath) at the desired temperature and the second one (wash bath) at room temperature. The jet stretch ratio (wind up speed/extrusion speed) was kept constant at 1. Finally, the fibers were collected in a wind-up drum that is submerged in water at room temperature. The produced fibers went through a solvent exchange process. First they were immersed in water for 2 days and after in methanol during 3 days. Finally, the hollow fiber membranes were left to dry at room temperature.

#### **4.1.1.5 Gas Permeation Measurements Method**

To perform the gas permeation tests it is necessary to prepare single membrane modules (1 membrane/module). The membranes were selected by looking into its surface and hole with a magnifying glass to exclude membranes with visible defects. Then they were potted into single fibre modules using a polyurethane resin (PU3410) and were tested before and after coating.

A 3% w/w silicone (PDMS) solution in hexane was prepared in order to coat the produced membranes. This solution was left to age for 20 minutes after preparation and then the fibres were submerged in the solution for 10 minutes. Finally, the membranes were left to dry at room temperature for two days. The single modules were tested for oxygen and nitrogen at a pressure difference of 5 bar. 10 membranes of each set of conditions were tested.

## **4.2 Gas Permeation Results**

After the spinning, potting and coating, the membranes are characterized in terms of oxygen and nitrogen permeabilities. The permeation fluxes are measured using a manual bubble flow meter where the time taken to achieve a specific volume is recorded. Then the Pressure Normalised Fluxes (PNF) (also known as permeance) are calculated using Equation 4.1.

$$PNF = \frac{V}{A \times t \times \Delta P} \quad (4.1)$$

$V$  refers to the volume of gas measured in the manual bubble flow meter and  $t$  to the correspondent time.  $A$  is the membrane surface area and  $\Delta P$  the pressure difference used to do the measurement.

Usually the PNF are measured in GPU ( $1 \text{ GPU} = 1 \times 10^{-6} \text{ cm}^3 \text{ cm}^{-2} \text{ s}^{-1} \text{ cmHg}^{-1}$ ).

The gas pair selectivity ( $\Omega$ ) is calculated by simply dividing the obtained permeation fluxes of oxygen and nitrogen, Equation 4.2.

$$\Omega_{\text{O}_2/\text{N}_2} = \frac{PNF_{\text{O}_2}}{PNF_{\text{N}_2}} \quad (4.2)$$

In this work, the selectivity of each individual membrane was calculated and then the average of the selectivities (10 membranes of each category were tested) was used along with the respective standard deviation. The standard deviation ( $\sigma$ ) is calculated using Equation 4.3.

$$\sigma = \sqrt{\frac{\sum_{i=1}^n (x - \bar{x})^2}{n - 1}} \quad (4.3)$$

In Table 4.5 the permeation results obtained for the uncoated membranes can be found.

TABLE 4.5: Permeation results obtained for the 9 categories of uncoated membranes.

Experiment Number	Selectivity ( $O_2/N_2$ )	$N_2$ Flux (GPU)	$O_2$ Flux (GPU)
1	$0.89 \pm 0.03$	$19.05 \pm 4.27$	$16.92 \pm 3.95$
2	$0.92 \pm 0.04$	$36.29 \pm 13.28$	$33.62 \pm 12.66$
3	$0.92 \pm 0.03$	$95.11 \pm 6.55$	$87.81 \pm 5.53$
4	$0.92 \pm 0.03$	$28.34 \pm 2.57$	$26.06 \pm 2.64$
5	$0.93 \pm 0.03$	$55.7 \pm 6.7$	$52.10 \pm 7.50$
6	$0.93 \pm 0.03$	$124.90 \pm 15.74$	$116.71 \pm 14.92$
7	$0.94 \pm 0.03$	$34.77 \pm 5.17$	$32.57 \pm 4.69$
8	$0.93 \pm 0.06$	$57.51 \pm 13.17$	$53.21 \pm 12.28$
9	$0.92 \pm 0.03$	$74.50 \pm 6.19$	$72.81 \pm 3.64$

As can be seen in Table 4.5, the membrane categories present  $O_2/N_2$  gas selectivities between 0.89 and 0.94 with standard deviations showing good agreement and consistency within the set of fibres tested. These results for uncoated membranes are a result of the different permeabilities of oxygen and nitrogen, being oxygen slightly less permeable than nitrogen. Assuming *Knudsen* diffusion, a theoretical number for the gas selectivity can be calculated using the molecular weight of both gases being testes, Equation 4.4.

$$\Omega_{Oxygen/Nitrogen} = \frac{\sqrt{Mw(N_2)}}{\sqrt{Mw(O_2)}} \quad (4.4)$$

Using the equation above, it is possible to calculate a *Knudsen* diffusion selectivity of 0.94 that are in agreement with the obtained experimental results.

Regarding the fluxes, big differences can be found between the different categories. A pattern can also be observed if the fluxes are grouped in batches of three (1 to 3, 4 to 6, 7 to 9), Figure 4.3.

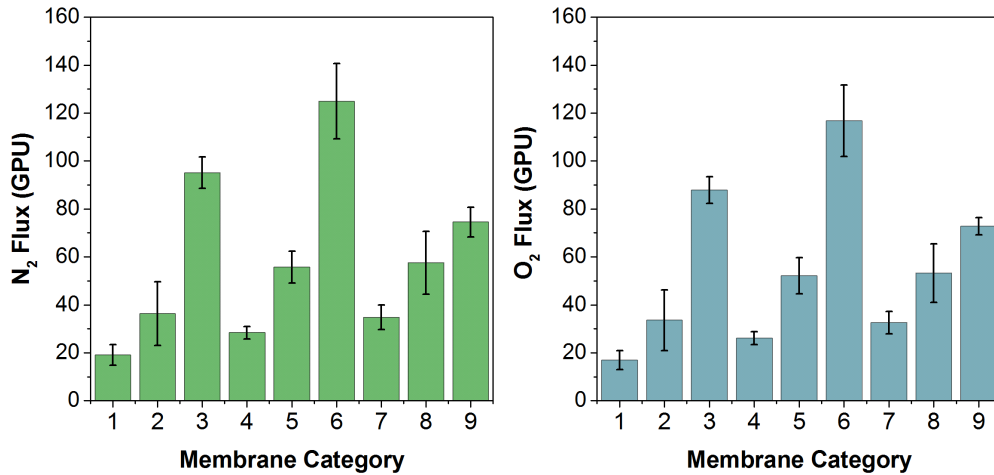


FIGURE 4.3: Nitrogen (left) and oxygen (right) fluxes obtained to the 9 sets of prepared uncoated membranes.

In each one of these three batches the spinning temperature is different and the dope extrusion rate increases with the number of the batch (e.g. for category 1, 2 and 3 the spinning temperature is 40°C and the dope extrusion rate for is 1 cm<sup>3</sup>/min, 3 cm<sup>3</sup>/min and 5 cm<sup>3</sup>/min, respectively). Also the external bath temperature varies, but this effect is not noticeable in the plot of the permeation results. For each batch, with the increasing of dope extrusion rate, the fluxes increase. This result can be linked with the residence time and therefore with the thickness of the active layer of the formed membranes. Higher residence times (that correspond to lower dope extrusion rates) will lead to higher solvent evaporation that will result in thicker skins and therefore low fluxes.

After the measurement of the permeations in the uncoated membranes, these are coated with silicone in order to repair possible defects in the active layer. The results obtained for once coated and twice coated can be found in Table 4.6 and 4.7, respectively.

TABLE 4.6: Permeation results obtained for the 9 categories of once coated membranes.

<b>Experiment Number</b>	<b>Selectivity (<math>O_2/N_2</math>)</b>	<b><math>N_2</math> Flux (GPU)</b>	<b><math>O_2</math> Flux (GPU)</b>
1	$1.13 \pm 0.20$	$2.98 \pm 1.24$	$3.18 \pm 0.94$
2	$1.00 \pm 0.14$	$7.65 \pm 4.37$	$7.30 \pm 3.60$
3	$0.99 \pm 0.23$	$31.39 \pm 14.13$	$28.74 \pm 12.33$
4	$2.14 \pm 1.74$	$2.35 \pm 1.58$	$3.25 \pm 1.21$
5	$0.97 \pm 0.04$	$6.99 \pm 1.51$	$6.78 \pm 1.36$
6	$0.93 \pm 0.02$	$33.57 \pm 7.31$	$31.11 \pm 6.74$
7	$1.06 \pm 0.10$	$5.15 \pm 1.86$	$5.37 \pm 1.59$
8	$0.97 \pm 0.08$	$13.52 \pm 2.68$	$13.05 \pm 2.17$
9	$0.92 \pm 0.06$	$19.10 \pm 2.82$	$17.54 \pm 2.37$

Observing the results obtained for once coated membranes it can be seen that the fluxes for both gases reduced drastically. It is also possible to observe that no big improvements were achieved in terms of gas selectivity. Apart from category 4, where a average selectivity of around 2 was obtained, all the other categories show poor selectivities around 1. If the error bars are considered, it is possible to see that the majority of the categories will fall into the *Knudsen* selectivity. Although category number 4 has the biggest improvement, it is also important to notice the big standard deviation observed for this category of membranes - 1.74 - shows that there is no consistency in the selectivities obtained for this set of membranes. For the other categories, it is also visible the bigger standard deviations obtained when compared with the uncoated membranes for both fluxes and selectivities. A possible reason for this is the fact that, as the fluxes being measured are lower, it is possible that the external factors such as temperature or pressure could have impacted the measurements.

Looking to the results in terms of fluxes the same pattern between the categories discussed before can be identified showing again the effect of the dope extrusion rate (and the residence time).

TABLE 4.7: Permeation results obtained for the 9 categories of twice coated membranes.

<b>Experiment Number</b>	<b>Selectivity (<math>O_2/N_2</math>)</b>	<b><math>N_2</math> Flux (GPU)</b>	<b><math>O_2</math> Flux (GPU)</b>
1	$1.68 \pm 0.52$	$0.88 \pm 0.38$	$1.37 \pm 0.46$
2	$1.64 \pm 0.39$	$1.78 \pm 1.22$	$2.61 \pm 1.33$
3	$1.12 \pm 0.36$	$12.59 \pm 4.85$	$12.64 \pm 3.96$
4	$2.82 \pm 1.23$	$0.83 \pm 0.46$	$1.86 \pm 0.47$
5	$1.49 \pm 0.17$	$1.65 \pm 0.38$	$2.41 \pm 0.42$
6	$1.71 \pm 0.63$	$5.10 \pm 4.01$	$6.82 \pm 4.71$
7	$1.38 \pm 0.61$	$2.58 \pm 1.48$	$2.82 \pm 1.30$
8	$1.39 \pm 0.31$	$2.99 \pm 1.17$	$3.85 \pm 0.78$
9	$1.59 \pm 0.35$	$3.10 \pm 1.54$	$4.51 \pm 1.53$

Looking into the results obtained for twice coated membranes, a slightly improvement in the selectivity can be seen with the second coating, but not enough to overcome a selectivity of 2. Only category number 4 shows selectivities bigger than 2 but with the consistency of the batch again compromised.

Again, a reduction in the fluxes are observed after the second coating suggesting that the coating material is blocking the possible defects existing in the membrane surface. However, the poor selectivities might be an indicator of high surface porosity. Even if the coating material has sealed the pores, if the membrane presents a high surface porosity, the gases will prefer to pass through these sealed pores since less resistance to flow is offered in this situation.

Later in this work, membrane surface analysis will be carried out in order to try to have a better insight about the membranes structure and establish a link between it and the permeation results.

Figure 4.4 shows the graph of selectivities obtained for the 9 categories of membranes (uncoated, once coated and twice coated) for a better visualisation of the experiments results and respective standard deviations.

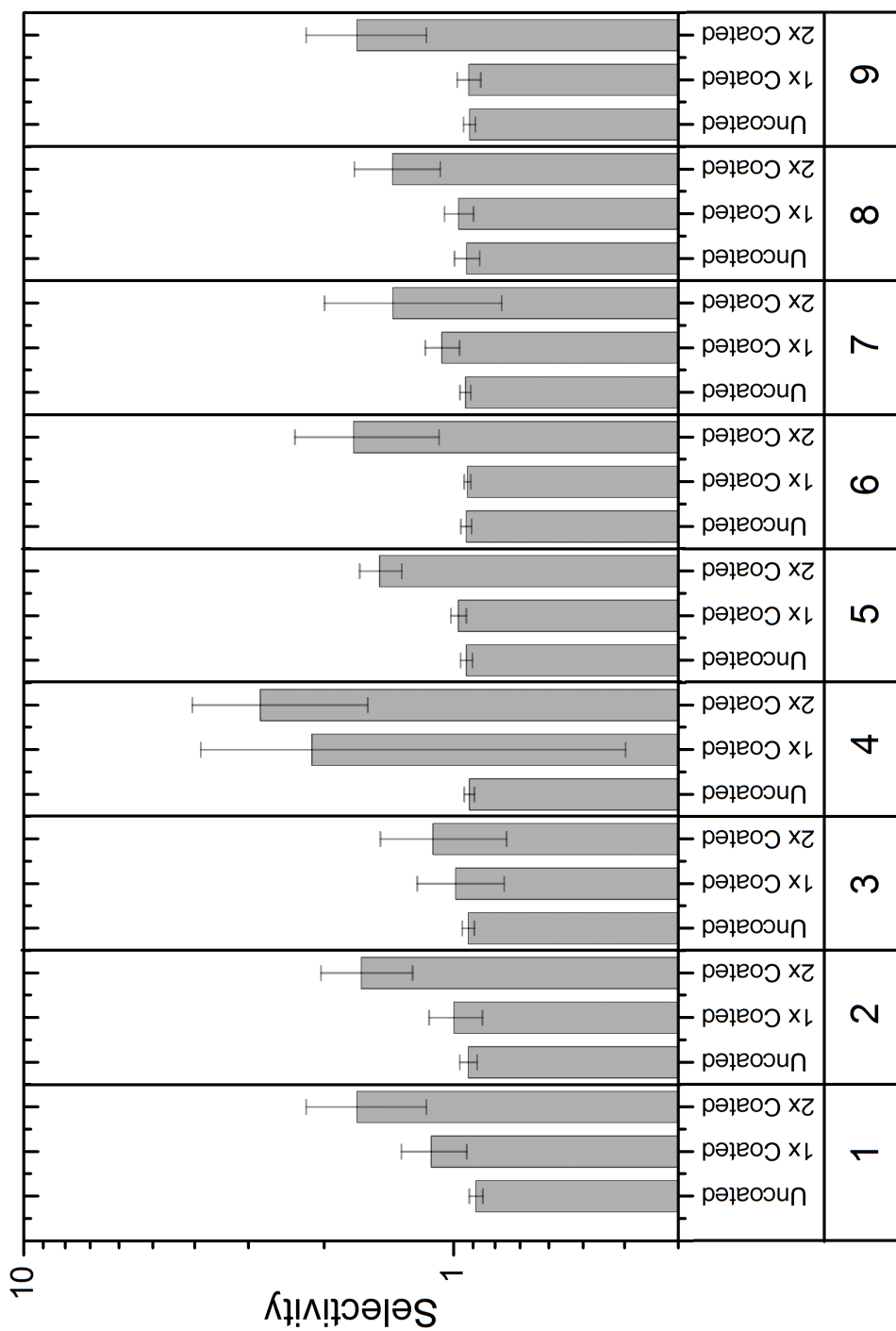


FIGURE 4.4: Selectivities obtained for the 9 sets of experiments for uncoated, once coated and twice coated membranes with respective standard deviations.

### 4.2.1 Results Analysis Using the *Taguchi* Approach

In this work the selectivities (derived from the fluxes) are the parameter that will be evaluated in order to characterize the membranes performance. Accordingly with *Taguchi*, the variations in the response obtained should be studied using the signal-to-noise ratio (S/N). *Signal* refers to the response obtained (selectivity in this case) and *noise* to the noise factors that might affect the final results. The objective is to minimise these uncontrollable noise factors that contribute for variations in the response obtained. S/N ratio can be considered as a measurement of the sensitivity that a parameters has to external influencing factors. In its basic form, S/N is defined as the ration between the average and the standard deviation of a set of results, Equation 4.5.

$$S/N = \frac{x}{\sigma} \quad (4.5)$$

The S/N ration allows to:

- Determine the optimal conditions for a parameter based on the standard deviation obtained
- Compare two or more sets of experimental results

To calculate the S/N ratio, Equation 4.6 is used.

$$S/N = -\log_{10}(MSD) \quad (4.6)$$

*MSD* is the mean square deviation and different expressions can be used depending on the objective of the analysis. In this work, the objective is to minimize the squared difference between a target selectivity value and the experimental results, Equation 4.7.

$$MSD = (Y_1 - Y_0)^2 + (Y_2 - Y_0)^2 + \dots + (Y_N - Y_0)^2 \quad (4.7)$$

$Y_0$  corresponds to the target value for the parameter that is being measured (selectivity in this case). A value of 5.1 was selected in this study as selectivity target. This value corresponds to the mean for the oxygen/nitrogen selectivities for PVC flat membranes available in the literature (see Chapter 1, Table 1.3).

The data obtained for S/N can be seen in Table 4.8.

TABLE 4.8: S/N data obtained for each set of prepared membranes.

<b>Experiment Number</b>	<b>S/N</b>
1	-11.6
2	-11.8
3	-12.6
4	-9.3
5	-12.1
6	-12.0
7	-12.4
8	-12.3
9	-11.9

In this study, the objective is to minimize the the S/N ratio (that will mean a minimization of the difference between the obtained selectivity value and the target). The mean for each factor and level in terms of S/N ratio is shown in Table 4.9. This mean is obtaining by selecting in Table 4.8 the S/N values corresponding to each level and calculating the average.

TABLE 4.9: S/N mean for each factor and level.

Level	Spinning Temperature	Dope Extrusion Rate	External Bath Temperature
1	-11.99	-11.13	-11.99
2	-11.15	-12.05	-10.99
3	-12.19	-12.15	-12.35

Figure 4.5 shows the S/N mean graph for selectivity where the absolute minimum S/N mean obtained can be graphically identified.

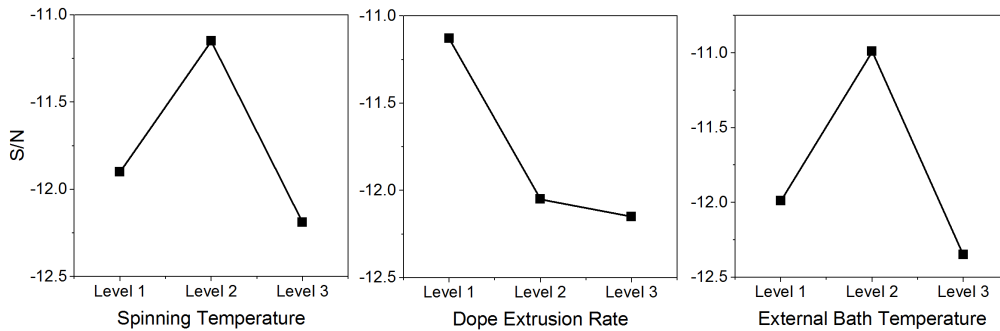


FIGURE 4.5: S/N ratio effect for the different factors and levers. *Note: S/N smaller the better.*

Accordingly with the S/N ratio results, the best conditions for the parameters studied are:

- Spinning Temperature at Level 2 - 50°C;
- Dope Extrusion Rate at Level 1 - 1 cm<sup>3</sup>/min;
- External Bath Temperature at Level 2 - 30°C.

After this evaluation, the next step in the *Taguchi* analysis is to perform a confirmation experiment with the parameters found as the best. However, the conditions above correspond to the experiment number 4 that is, in fact, the membrane category with a smaller S/N ratio and therefore with a less deviation from the

target value for the selectivity. Due to this, a confirmation experiment is not needed.

#### 4.2.2 Discussion of the Gas Permeation Results using *ANOVA* Variance Analysis.

Another investigation that can be made is related with the analysis of the variance of the results obtained. With this analysis it is possible to understand which of the factors studied has the bigger impact in the results obtained. This analysis is made using *ANOVA*, a tool that is used to make decisions based on statistics [150, 164].

For the *ANOVA* analysis, the S/N ratios obtained earlier are used in order to calculate the percentage of contribution of each of the factors studied (dope/spinning temperature, dope extrusion rate and external bath temperature). To obtain the percentage of contribution, different parameters need to be calculated first.

The degrees of freedom (*DOF*) for a factor F are calculated using the number of levels investigated as follows, Equation 4.8.

$$DOF_F = \text{number of levels} - 1 \quad (4.8)$$

The *DOF* for the error parcel are the total *DOF* minus the *DOF* assigned for each factor, Equation 4.9:

$$DOF_{Error} = \text{Total DOF} - \sum_{i=1}^n DOF_F \quad (4.9)$$

The effect of factor A at level 1 is calculated using Equation 4.10.

$$A_1 = \frac{1}{3} \sum_{i=1}^3 S/N_i - \frac{1}{9} \sum_{i=1}^9 S/N_i \quad (4.10)$$

The effects for the remaining factors and levels are calculated in a similar way. The sum of squared deviations for factor A is calculated using Equation 4.11.

$$SSA = \text{number of levels} \times \left( \sum_{i=1}^3 A_i^2 \right) \quad (4.11)$$

For the remaining factors (B and C), the same approach is used. The sum of squared deviations for the error is calculated using Equation 4.12.

$$SSE = \sum_{i=1}^9 (S/N_i)^2 - \frac{1}{9} \left( \sum_{i=1}^9 S/N_i \right)^2 - (SSA + SSB + SSC) \quad (4.12)$$

The variance is obtained dividing the sum of squared deviations by the respective *DOF* for each factor F, Equation 4.13.

$$\text{Variance}_F = \frac{SSF}{DOF_F} \quad (4.13)$$

The *F-ratio* represents the ratio between the variance due to a factor and the variance due to error, Equation 4.14:

$$F - \text{ratio} = \frac{\text{Variance}_F}{\text{Variance}_{Error}} \quad (4.14)$$

Finally, the percentage of contribution for the variance due to each factor is calculated using the total variance, Equation 4.15:

$$\% \text{ Contribution} = \frac{\text{Variance}_F}{\text{Total Variance}} \quad (4.15)$$

The results obtained for the variance analysis can be seen in Table 4.10.

TABLE 4.10: ANOVA results obtained for the 3 parameters used to spin different PVC hollow fibre membranes.

Source of Variation	DOF	SSF	Variance	F-Ratio	% of Contribution
Spinning Temperature (A)	2	2.24	1.120	2.10	23%
Dope Extrusion Rate (B)	2	1.53	0.765	1.44	16%
External Bath Temperature (C)	2	4.93	2.464	4.63	50%
Error	2	1.07	0.535		11%
Total	8	9.76	4.880		

The results obtained show that the external bath temperature is the parameter that has the most significant effect in the selectivity of the prepared membranes with a percentage of contribution of 50%. The spinning temperature has a contribution of 23% and the dope extrusion rate contributes with 16% for the final variation. The *F-ratio* gives an indication about the significance of the effects and, as it is higher than 1 for the three parameters, this means these effects are significant. The percentage that is attributed to error is 11%, that is considered low [150]. Although it is an acceptable value, there are some reasons that can be discussed about its existence. This error corresponds to the factors that might have influence in the process and that are not being controlled. One of this factors is the solution used to spin the membranes. As the spinning process involves the used of different spinning and external bath temperatures and the volume of polymer solution to be processed by spinning run is limited, each one of the membrane categories were spun using different solutions. In such delicate process as membrane spinning this might be enough to produce discrepancies in the results. Also, five different gas chambers were used to measure the permeation

fluxes. All these factors could not be better controlled and are reflected in the error variance.

### 4.3 Conclusions of Hollow Fibre Membrane Preparation and Permeation Results Analysis

Membranes were spun using the dry/wet method accordingly with the conditions defined by the *Taguchi* approach. After potting and coating the fluxes of nitrogen and oxygen through the membranes were quantified and the selectivities calculated. Uncoated membranes showed poor selectivities, as expected, and the gas transport was governed by *Knudsen* diffusion with selectivities around 0.94 that corresponds to the *Knudsen* selectivity for the species being studied (oxygen and nitrogen). This shows that the objective of achieving a defect free active layer in the first place was not possible.

A pattern was identified, with the fluxes increasing with the increasing of the dope extrusion rate. This pattern was identified in the uncoated, once and twice coated membranes and might be related with the residence time of the membranes in the chamber (residence time is varies inversely in relation to the dope extrusion rate).

In general, after coating cycles, the membranes did not exhibit an improvement in the selectivity, being category 4 the only one with a selectivity above 2. However, big standard deviations were obtained for coated membranes in terms of selectivity and flux. This big differences show that the batches are not consistent, existing a big variability in the membranes produced for a fixed set of conditions.

The S/N ratios, calculated in relation to a target selectivity, showed that the smaller S/N ratios were obtained for a spinning temperature of 50°C, a dope extrusion rate of 1 cm<sup>3</sup>/min and an external bath of 30°C. This conditions correspond to the membrane category number 4, that is actually the category with the best results. Because of this, a confirmation experiment was not needed.

An analysis of variance of the results was also made using the S/N ratio results

with the intend of understand which of the parameters has a higher influence in the selectivity results. The external bath temperature was revealed as the parameter having the bigger impact with a percentage of contribution of 50% comparing with 23% for the spinning temperature and 16% for the dope extrusion rate. The percentage of variance attributed to the errors was 11%.



## Chapter 5

# Structural Characterization of the Prepared PVC Hollow Fibre Membranes

### 5.1 Objectives

In this section, the prepared PVC hollow fibre membranes were characterized in terms of structural properties using Scanning Electron Microscopy (SEM) technique. The cross section and the surface of the prepared membranes were observed with the final aim of relate these structures with the spinning conditions used and the selectivity results obtained.

### 5.2 Structure Analysis Methods

Different gas transport mechanisms can be present in membranes depending on its structure. As it was discussed before, the pore size in a membrane surface plays an important role in the separation because it is this parameter that will

dictate which mechanism will be present/dominant. If the pore size is below 5 Å the membrane is characterized as non-porous and solution diffusion will be the present gas transport mechanism. This is the mechanism that allows to achieve separation since a gas molecule has around 5 Å and if the pore size is bigger there will be no discrimination between the gases and no separation is achieved. Above a pore size of 5 Å other mechanisms can be present - *Knudsen* diffusion and viscous flow.

It is then really important to understand what is the pore size present in the surface of the membrane so the flow mechanism can be identified. The use of surface image to look into the properties of membranes is a commonly used technique. It is true that the pore size is important but it is also relevant to understand the number of pores that exist in a membrane surface. However, in surface area imaging, only a small portion of the membrane is analysed so it becomes difficult to evaluate this parameter.

There are several techniques that can be used in order to determine porosity, pore size and pore size distribution, Table 5.1.

TABLE 5.1: Techniques used for surface characterization (various sources).

Technique	Parameter analysed	Reference
Bubble Pressure	Maximum Pore size	[165, 166]
Molecular Weight Cut Off (MWCO)	Pore size	[167]
Scanning Electron Microscopy (SEM)	Surface porosity, pore size distribution, qualitative analysis	[168–171]
Atomic Force Microscopy (AFM)	Surface porosity	[172, 173]
Gas adsorption/desorption	Pore size distribution	[174, 175]
Mercury intrusion method	Pore size distribution	[176]

The most commonly used technique in the membrane field is the SEM. In this technique, a focused beam of electrons is produced and hits the material surface. The sample is introduced in a chamber that operates under vacuum conditions and the electron beam scans the surface allowing to collect information about the examined area through the electron-sample interaction that produces a signal

that is then detected by appropriate components in the equipment. For materials that do not present conducting features a thin coat of an electrically-conducting metal, such as gold or silver, should be applied to the surface to be analysed, through a process called sputter coating.

In this work, the SEM technique was used in order to investigate the prepared hollow fibre membranes structure hoping that a relationship between the spinning conditions and the observed structure could be stated. An attempt of using gas absorption/desorption to get information about pore size distribution was also made, however, there was not enough surface area available in the sample in order to get decent results.

### **5.3 SEM Analysis of Prepared Membranes**

Surface and cross section membrane imaging was performed using the equipment HITACHI SU-6600 (10 kV), a high resolution analytical variable pressure, field emission scanning electron microscope.

#### **5.3.1 SEM Sample Preparation**

*Cross-Section Analysis:* The hollow fibre membranes were fractured using liquid nitrogen to achieve a brittle fracture. The membranes were immersed in liquid nitrogen for about 10 seconds and after, keeping them immersed, were fractured using a pair of tweezers. These samples were then positioned in the sampler with black carbon tape with the fractured cross section faced up.

After coating the membranes for cross section analysis with gold, it was observed that they collapsed, probably due to the use of vacuum in the coating process. Because of this, new samples were prepared and no coating was applied. This means that the resolution obtained was not as good as it could be if a coating material was applied on the membrane surface. Because of this, a variable pressure (VP) mode had to be used, where air is introduced in the system to help to

conduct the beam to reach the material surface. An Environmental Secondary Electron Detector (ESED) was used in order to provide surface observation in VP mode. Magnifications used varied from 120x to 700x.

*Surface Analysis:* To analyse the surface of the prepared membranes, samples of each batch of membranes were displaced in the sampler, side by side, and were then coated with gold. In this analysis a Secondary Electron (SE) detector was used providing high-resolution imaging suitable for detailed topographical characterisation of samples allowing magnifications from 600x to 8000x.

### **5.3.2 SEM Cross Section Analysis**

Figures 5.2, 5.3 and 5.4 show the images obtained for the different membrane categories.

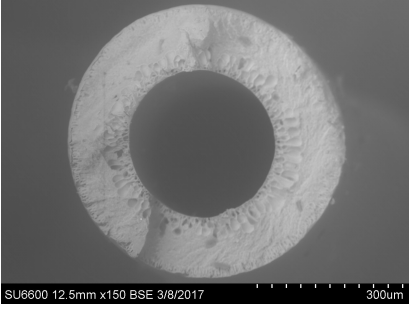
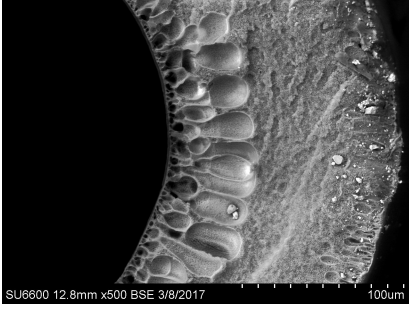
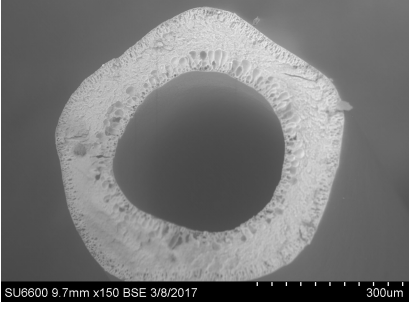
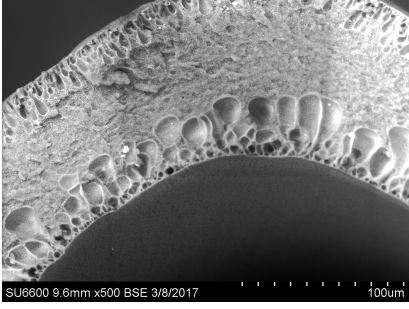
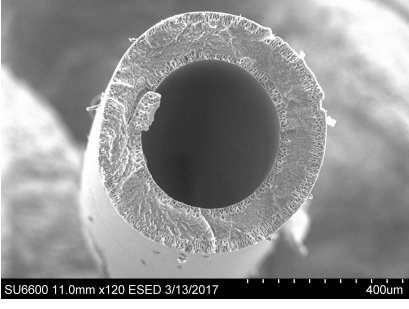
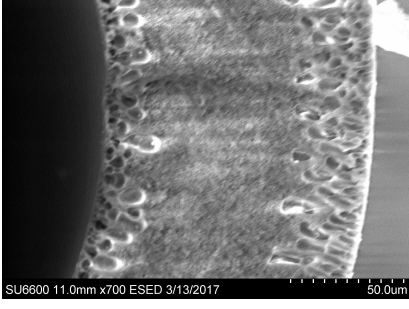
Category	View 1	View 2
1		
2		
3		

TABLE 5.2: SEM cross section views of membranes from category 1, 2 and 3 (different magnifications).

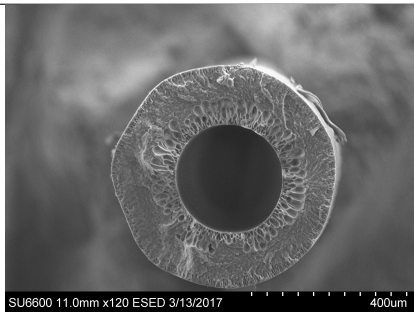
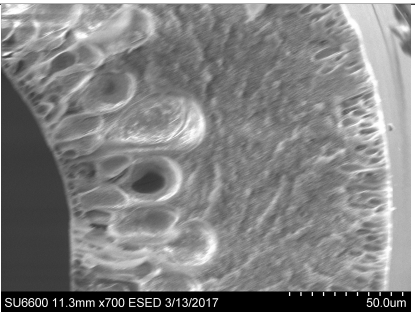
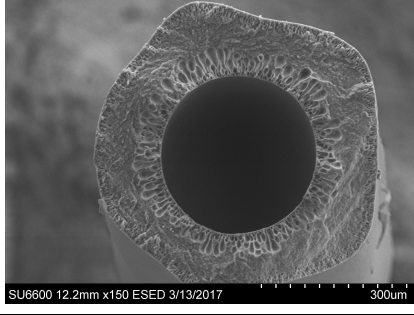
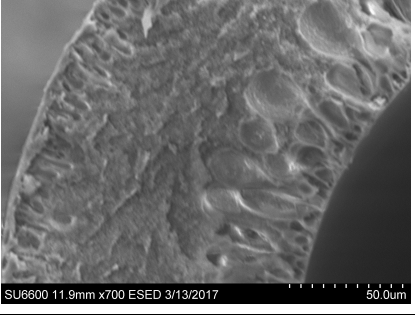
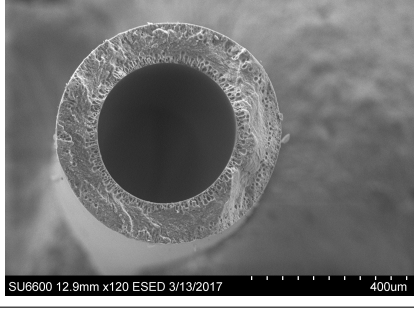
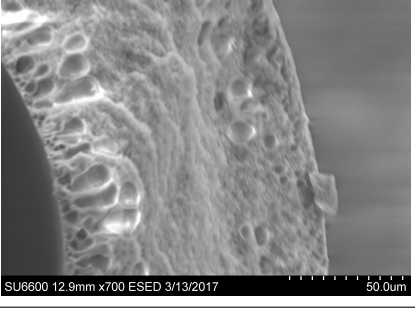
Category	View 1	View 2
4		
5		
6		

TABLE 5.3: SEM cross section views of membranes from category 4, 5 and 6 (different magnifications).

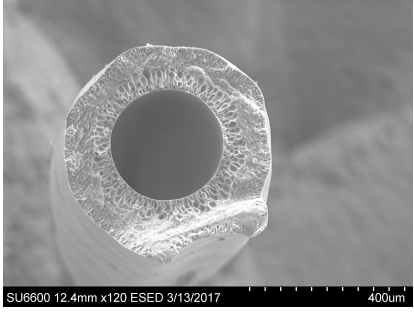
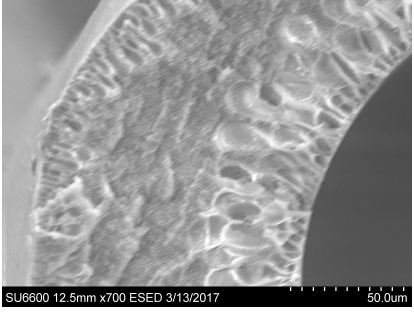
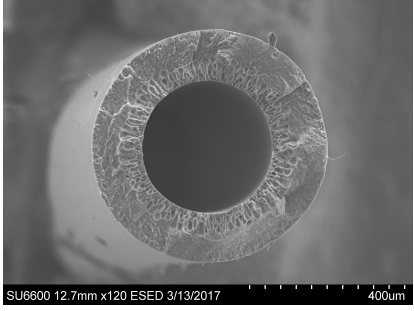
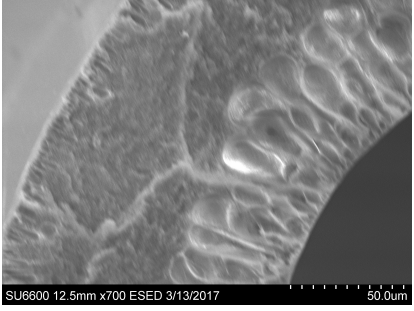
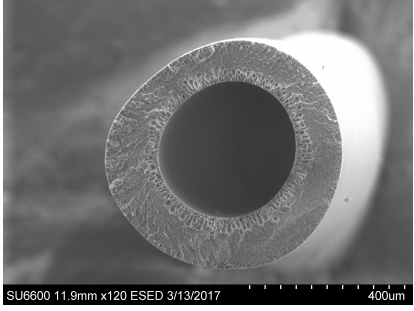
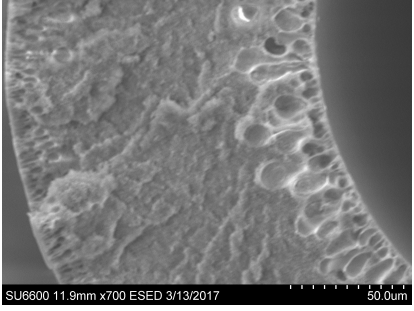
Category	View 1	View 2
7		
8		
9		

TABLE 5.4: SEM cross section views of membranes from category 7, 8 and 9 (different magnifications).

In the cross section analysis of the membranes it was difficult to use a magnification that allowed to investigate the active layer thickness of the membranes. This is due to the fact that the membranes were not coated with gold and a different detector was used that does not give clear images when bigger magnifications than the ones presented were used. However, it is possible to observe the hole of the fibre and the aspect of the membrane cross section.

For all the membranes, there is a region near the inner wall of the membrane

where there are big pores present that are related with the passage of the bore fluid. The contact of this fluid with the polymer solution produces open pores because of the quick phase inversion due to the high affinity of the DMAc with the non-solvent in the coagulation bath (water) [169]. The use of a bore fluid with lower water activity decreases the velocity of the solvent from the inner wall, avoiding damaging the active layer located in the outer wall of the membrane. In the middle region of the membrane it can be observed a layer with smaller porous that is formed due to a slower phase inversion. This process is slower due to a reduction in the velocity of the non-solvent front as it progresses into the membrane. This type of structure was also found in the PVC membranes prepared by *Jones* [1].

In terms of shape, apart from category number 2, all the samples taken present a almost perfect circular shape that is important for the mechanical characteristics of the membranes. It was hoped that a relation could be established between the cross section outer wall shape of the membrane and the spinning conditions but that was not verified. It was expected that the solutions spun at higher temperatures (and hence, lower viscosities) would present a less circular form due to the effect of the convective gas bombarding the structure outer layer. However, the solution showed to be able to counteract those forces.

Using SEM micrographs, is it also possible to estimate the external and the internal diameter of the hollow fibre membranes and compare them with the specifications of the *spinneret* and the experimental conditions. The results obtained can be seen in Figure 5.1.

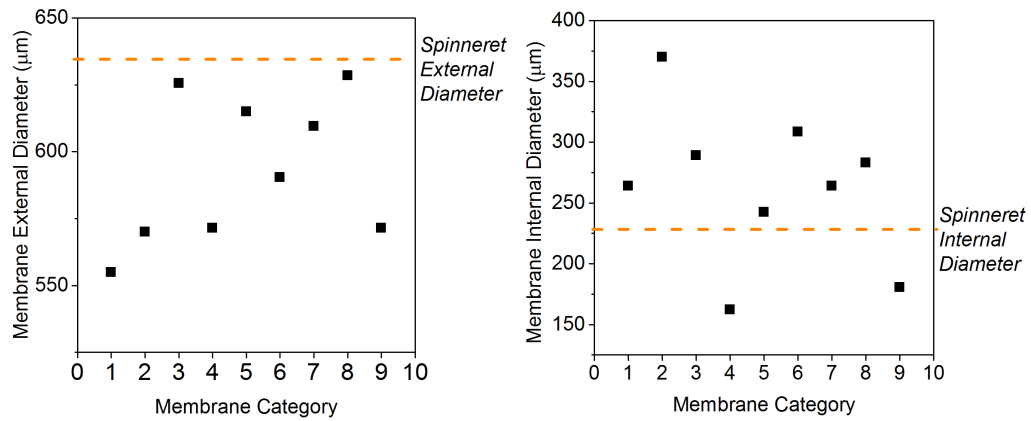


FIGURE 5.1: External and internal membrane diameter estimated for each one of the categories of membranes prepared (obtained from SEM micrographs).

Looking to the results obtained for the membranes' external diameter, it is possible to see that all categories present diameters lower than the *spinneret* diameter. Concerning the internal diameter, apart from categories number 4 and 9, all the membranes presented an internal diameter bigger than the *spinneret* one. This is due to contraction of the polymer and was already found in textile production [177]. This effect can also be observed in the surface images presented in the next section.

Once again, it was not possible to relate the trends observed with the spinning conditions.

### 5.3.3 SEM Surface Analysis

Scanning the surface of the membranes, it was possible to identify, for all of the categories, the presence of defects that are suggested to be polymer agglomerates in the membrane outer surface. As these defects were found in all categories, no relation could be established between them and the spinning conditions. An example of these defects present in a membrane from category number 4 is shown in Figure 5.2.



FIGURE 5.2: SEM surface view of a membrane from category number 4 showing defects (magnification of 150x).

This agglomerates suggests that the quaternary polymer solution was probably not completely homogeneous leading to this type of structure once the phase inversion occurs. Although the solution, visually, looked like homogeneous, it is possible that in the microscopic scale there were some regions where this was not true, leading to the formation of these type of agglomerates once solidified.

It was also possible to observe axial tearing effects also in all the categories investigated. Figure 5.3 shows the surface analysis of a membrane from category number 4.

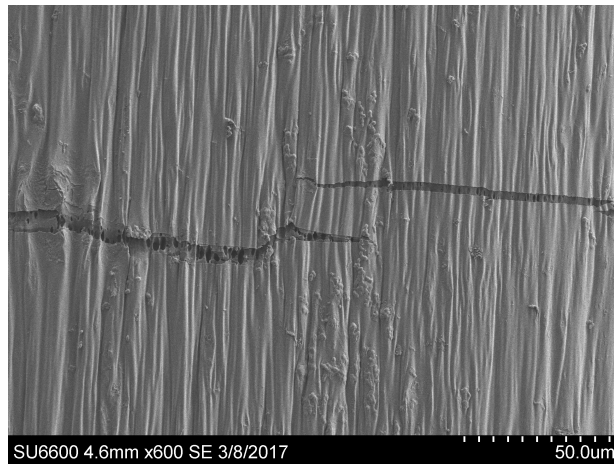


FIGURE 5.3: SEM surface view for a membrane from category number 4 showing tearing (magnification of 150x).

These structural defects were also identified by *Jones* [1] on his PVC hollow fibre membrane investigation prepared using the same method (dry/wet phase inversion). Investigations done earlier in this research group, where PVC membranes structure were prepared using an coagulation cold bath and then compared with ones produced using a warm coagulation bath, suggested that the use of temperature in the coagulation bath could minimize this effect [160]. However, in this work, some categories were produced with warm coagulation baths and this effect was still visible. There are some reasons that can be behind this. One of them is the decreasing in the membrane volume that happens when it coagulates and the inability of the structure to accompany these changes without damaging the surface. Mechanical damage can also be another explanation for this, since the membranes travel through the coagulation and external bath until their collection in the wind-up drum by the help of rollers. Figure 5.4 shows a magnification of one of the fractures.

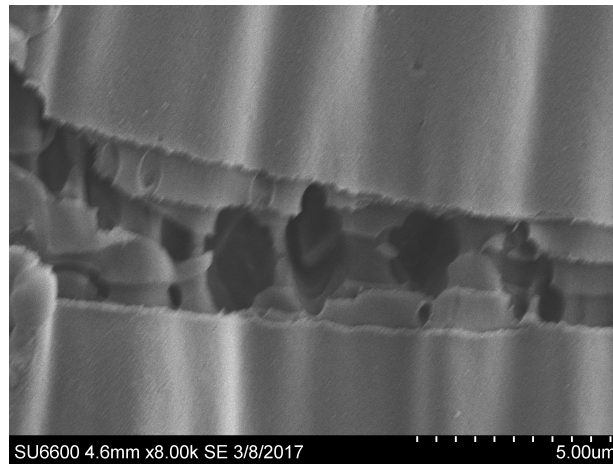


FIGURE 5.4: SEM surface view of a membrane from category number 4 showing tearing (magnification of 8000x).

In this picture, it is possible to observe an exposed sub layer containing macro pores. The fact that these rips are only superficial, since the sub layer does not look damaged, it is suggested that these defects appear before the sub layer is totally formed. Since the sub structure is fully formed by the end of its passage through the baths, it is suggested that these defects appear before that - in the forced convection chamber or in the first instants in the coagulation bath. Since these defects are present across the membrane and it is thought that they are formed somewhere between the forced convection chamber and the first instant of the coagulation bath, it is suggested that two different forces acting on the membrane can be behind the problem. In the forced convection chamber and in the first instants in the bath, the membrane is subjected to stretching due to the weight of the extruded thread. If the membrane structure is not able to counter these forces, this will result in a fracture in the membrane structure. It is true that this effect can be negligible if the jet-stretch ratio used during the membrane spinning, that relates the velocity of extrusion with the velocity of fibre collection, is kept constant at 1. However, if, for some instants, the velocity at which the membrane is being collected is faster than the velocity at which it is being extruded, this will cause the membrane to stretch and to fracture since the structure is very fragile at this point. From the SEM micrographs, the fraction of surface area occupied by the mechanical defects (furrows) was estimated to be of the order of  $10^{-4}$ .

More detailed images of these structures were not possible to obtain due to the

difficulty in obtaining clear pictures when larger magnifications were used. This means that it was not possible to observe the surface in detail in order to get important information such as the pore size.

Finally, it is important to note that the samples analysed are just a small part of the big amount of membranes prepared and that they are not, because of that, representative. Also, it was verified in the permeation tests, the pressure normalized fluxes obtained for the different categories had a big standard deviation showing the big variability that exists between the membranes from the same category, supporting this statement.

## 5.4 Conclusions of the Membranes Structure Characterization

Scanning Electron Microscopy was used in order to get some insight about the structural properties of the PVC prepared membranes by the dry/wet phase inversion technique. Cross section images show membranes with circular shape, suggesting that no major flow instabilities occurred during spinning. These images also show contraction of the membranes, a phenomena also found in the production of textiles, reflected in the internal and external diameters measured using the SEM micrographs when compared with the *spinneret* dimensions [177].

Surface imaging showed the presence of defects such as polymer aggregates and fractures across the membranes for all the categories of membranes tested. The existence of non-homogeneity domains, not visible at naked eye, in the starting polymer solution is thought to be the reason for the presence of polymer aggregates in the membranes surface. The tears are suggested to be a result of the stretching due to the weight of the extruded thread and/or due to mechanical damage during the contact of the membranes with the rollers that help the membrane to travel through the spinning equipment. From the SEM micrographs,

the fraction of surface area occupied by the mechanical defects (furrows) was estimated to be of the order of  $10^{-4}$ .

The drastic decrease in the fluxes through the membrane with the coating cycles and the presence of *Knudsen* diffusion in the non coated membranes suggest that these fractures are not the main reason for the poor membrane performance. Unfortunately, it was not possible to identify patterns between the batches and relate them with the different experimental conditions.

## Chapter 6

# Mass Transfer Modelling

### 6.1 Objectives

In this chapter, a theoretical model developed by *Shilton* [178] was used in order to predict the active layer thickness of hollow fibre membranes prepared by the dry/wet forced convection spinning method using different experimental conditions.

### 6.2 Principles of the Mass Transfer Model

In hollow fibre membrane fabrication there are some parameters that are very important to control in order to obtain structures suitable for gas separation. One of these parameters are the conditions in the forced convection chamber. In 2004, *Gordeyev* and *Shilton* [179] studied the influence of different conditions in the forced convection chamber such as residence time and gas flow rate in the properties of polysulfone hollow fibre membranes. The authors concluded that these parameters are important in order to obtain a membrane with attractive selectivities. Different models, related with hollow fibre membrane production,

can be found in the literature [180–183].

In 2013, *Shilton* proposed a mass transfer model to predict hollow fibre membrane properties such as active layer thickness and orientation depth [178]. These two parameters are very important in the final performance of the prepared membranes. A thin defect free active layer should be obtained in order to achieve good separation results. The molecular orientation obtained during the extrusion of the solution should be locked during the active layer formation to achieve enhanced selectivities.

This model is proposed for membranes produced by the dry/wet forced convection process where the dry region plays an important role in the active layer formation. Based on the most volatile solvent evaporation rate in the forced convection chamber, it allows to predict the active layer thickness of a hollow fibre membrane. The method was design using simple equations that allow it to be applicable to any membrane forming system.

As was discussed before, in the dry/wet forced convection process, a polymer solution is extruded through a *spinneret*, then passed through a forced convection chamber and finally enters a coagulation bath before being collected in a wind drum. In the forced convection chamber is where the most volatile solvent is removed in order to start the growth of the membrane active layer. This evaporation occurs due to the contact of the solution with nitrogen that is entering the chamber. Two distinct flow regions can be identified - a laminar flow region and an impingement zone. The latter corresponds to the point where the gas is entering the chamber and the flow regime is more aggressive. The laminar flow is present in the upper parts of the chamber (above the impingement zone). Figure 6.1 outlines these two regions.

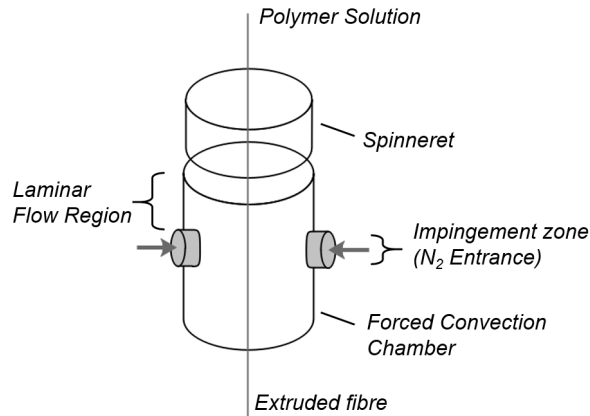


FIGURE 6.1: Schematics representing the forced convection chamber and the two different flow regimes presents in it. Adapted from [178].

Different chamber configurations (height, width and gas entrance height) can be used, depending on the characteristic to be achieved. Table 6.1 shows the characteristics of the forced convection chamber and the general spinning conditions used in this work and that will be used in the model.

TABLE 6.1: General Spinning conditions.

Polymer solution composition	6% THF, 50% DMAc, 16% EtOH, 28% PVC
Polymer solution temperature	40°C, 50°C or 60°C
Spinneret dimensions	OD 635 $\mu\text{m}$ , ID 229 $\mu\text{m}$
Spinneret cross section area	$3.17 \times 10^{-7} \text{ m}^2$
Dope extrusion rate	1, 3 or 5 $\text{cm}^3/\text{s}$
Forced convection gas	Nitrogen
Forced convection flow rate	4 L/min
Forced convection chamber height	9 cm
Forced convection chamber height at gas entrance	2.5 cm
Forced convection chamber cross section area	$0.00196 \text{ m}^2$
Jet stretch ratio (wind-up speed : extrusion speed)	1:1

In order to develop the mass transfer model, some preliminary assumptions were made by the author [178]:

- The more volatile solvent is the one that has the biggest influence in the active layer formation in the dry gap;
- The active layer is considered to be fully formed in the upper part of the chamber where laminar forced convection flow is present;
- The flow entering the chamber is assumed to split equally between the upper and the bottom part of the chamber;
- *Raoult's* law is used to describe the solvent concentration in the convective gas at the equilibrium;
- The percentage of the fibre that corresponds to the active layer is equal to the percentage of the most volatile solvent evaporated.

Accordingly with the mass transfer model, the membrane active layer thickness is calculated using Equation 6.1 [178].

$$L = \frac{D_0 - \sqrt{(D_0^2(1 - X) + XD_i^2)}}{2} \quad (6.1)$$

$X$  corresponds to the fraction of solvent (THF in this case) that is evaporated in the forced convection chamber.  $D_0$  is the external diameter of the fibber and  $D_i$  the internal one. In the case where the jet-stretch is equal to 1, these diameters approach the *spinneret* dimensions (inner and outer diameter). As in this work the jet-stretch was kept at 1, the *spinneret* dimensions will be used in this equation. The fraction of solvent evaporated is determined using Equation 6.2 [178].

$$X = \frac{R}{DER \times THF(\%)} \quad (6.2)$$

$DER$  corresponds to the dope extrusion rate and  $THF$  (%) to the concentration of THF in the initial polymer solution.  $R$  is the rate of THF evaporation from the membrane surface in the chamber and is determined using Equation 6.3 [178].

$$R = FA\Delta y \quad (6.3)$$

$F$  refers to the rate at which the solvent is lost from the fibre per unit of surface area ( $A$ ), per mole fraction and per unit of solvent and per mole fraction driving force ( $\Delta y$ ). ( $\Delta y$ ) is calculated using Equation 6.5 [178].

$$\Delta y = \frac{y_{i1}}{2} \quad (6.4)$$

$y_{i1}$  corresponds to the mole fraction of THF in the convective gas at the equilibrium and it is estimated using the *Raoult's* law, Equation 6.5 [178].

$$y_{i1} = \frac{xP^*(T)}{P} \quad (6.5)$$

The parameter  $F$  is calculated using Equation 6.6 [178].

$$F = \rho_m \times k \quad (6.6)$$

$\rho_m$  refers to the molar density of the convective gas and  $k$  to the mass transfer coefficient that is determined using Equation 6.7 [178].

$$k = \frac{D}{x} \times 0.664\sqrt{Re_x} \times Sc^{0.33} \quad (6.7)$$

The *Reynolds* number is calculated using Equation 6.8.

$$Re_x = \frac{\rho xv}{\mu} \quad (6.8)$$

$\rho$  is the density of the convective gas and  $x$  is the length of the fibre. Finally,  $v$  is the velocity of the convective gas entering the chamber and can be calculated using Equation 6.9 [178].

$$v(N_2) = \frac{\frac{Q_{N_2}}{2}}{XSA_{chamber}} + \frac{DER}{XSA_{Spin}} \left( \frac{1 + JS}{2} \right) \quad (6.9)$$

In Table 6.2 the physical properties of the convective gas (nitrogen) can be found.

TABLE 6.2: Physical properties of nitrogen [178].

Parameter	Value
Nitrogen viscosity, $\mu$	$1.8 \times 10^{-5}$ Pa.s
Nitrogen density, $\rho$	$1.2$ kg/m <sup>3</sup>
Diffusivity of THF in Nitrogen, D	$1.07 \times 10^{-5}$ m <sup>2</sup> /s
Nitrogen molar density, $\rho_m$	$0.041$ kmol/m <sup>3</sup>

In this work, the active layer thickness will be calculated for different process conditions such as spinning temperature and dope extrusion rate. The various vapour pressures of THF at different temperatures investigated can be found in Table 6.3.

TABLE 6.3: Vapour pressures for pure THF at different temperatures [184].

Temperature (°C)	Vapour Pressure (mmHg)
25	161.08
30	201.02
40	301.52
50	439.53
60	623.30

### 6.3 Results of the Mass Transfer Model - Prediction of the Active Layer Thickness

The results obtained for the rate of THF loss (R), for different conditions, can be seen in Table 6.4.

TABLE 6.4: THF solvent evaporation for different temperatures and dope extrusion rates.

Temperature	Rate of THF Loss (kmol/s) $\times 10^{11}$		
	Dope Extrusion Rate (cm <sup>3</sup> /s)		
	1	3	5
25	0.61	0.97	1.22
30	0.77	1.21	1.53
40	1.15	1.81	2.29
50	1.68	2.64	3.33
60	2.37	3.74	4.86

The active layer thickness predicted for the spinning conditions investigated can be seen in Table 6.5. The residence times above the impingement zone (IZ) are also presented.

TABLE 6.5: Active layer thickness predicted for different spinning temperatures and dope extrusion rates.

Temperature	Active Layer Thickness ( $\text{\AA}$ )		
	Dope Extrusion Rate ( $\text{cm}^3/\text{min}$ )		
	1	3	5
25	6218	3327	2532
30	7762	4152	3160
40	11649	6230	4741
50	16996	9086	6914
60	24129	12893	9809
Residence time above IZ (s)	0.475	0.158	0.095
Total residence time (s)	1.596	0.532	0.319

The results are plotted in Figure 6.2 for a clear visualisation of the influence of the two parameters being studied.

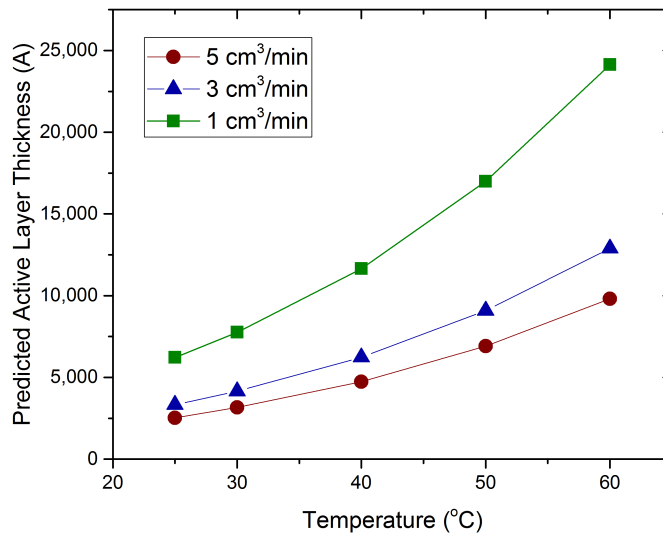


FIGURE 6.2: Predicted membrane active layers using the mass transfer model considering the laminar flow region.

In this figure, the influence of the spinning temperature and the dope extrusion rate (DER) can be analysed. It is important to notice that, in this work, the

dope extrusion rate and the residence time are coupled together so it is not possible to discern the effect of each one of these factors in the predicted active layer thickness separately. The temperatures used to perform the spinning of the membranes were 40°C, 50°C and 60°C. However, more temperatures were incorporated into the model results for a better understanding of the evolution of the predicted active layer thickness with this parameter.

The active layer thickness obtained with the model ranged from 2.500-25.000 Å. As can be seen, there is an increase in this parameter with the temperature for all the extrusion velocities. These results were expected since the model is based on the fraction of THF evaporated in the chamber and the solvent vapour pressure increases with the temperature, increasing the driving force for mass transfer to occur (Table 6.3). These results were also observed experimentally by *Shilton* [178] when studying the influence of the spinning temperature in the active layer growth.

The same effect can be seen with the decreasing of the dope extrusion rate. Two effects occur with the variation of the DER - the shear stress suffered by the solution in the *spinneret* wall and the residence time in the chamber (since the same chamber was used for all the DER). In the predictions made by *Shilton* [178], at fixed residence time, decreasing thickness were observed with increasing dope extrusion rate. These results were in accordance with what the author found experimentally by using the pressure-normalized fluxes to obtain the active layer thickness of the membranes, and are related with the molecular orientation of the molecules created during the spinning [114]. In the same study, the effect of the residence time was tested, keeping the dope extrusion rate constant. The model predicted an increasing in the active layer thickness with the increasing in the residence time. However, the experimental results showed an existence of a critical DER from which the active layer thickness starts to decrease. The authors suggest that the behaviour of the bore fluid, and its relation with the phase inversion, is not being taken into account and can be behind these results. In the present work, both effects described before seem to be present. With the increasing DER, the residence time decreases and both effects contribute for a decreasing in the active layer thickness.

The active layer thickness predicted by the mass transfer model is based on the

argument that the active layer is fully formed in the upper part of the forced convection chamber. However, it was suggested in other studies that the use of high temperature in the spinning processes enhances the importance of the impingement zone in the growth of the active layer [179]. In the impingement zone, since the mass transfer is more aggressive (due to the higher gas velocity in this region), the solvent evaporation rate will be much bigger and the model will predict a much bigger active layer thickness. As high spinning temperatures were used in this work, prediction of the active layer thickness were also made using the mass transfer model applied to the impingement zone region.

The impingement zone relates with the region in the chamber where the gas enters. The area of the membrane exposed to this section can be calculated using the diameters of the pipe from where the gas is entering the chamber. The mass transfer coefficient is calculated based on a turbulent regime, so the adequate expression for the *Sherwood* dimensionless number should be used, Equation 6.10.

$$k = \frac{D}{x} \times 0.43 + 0.532Re_x^{0.5} \times Sc^{0.31} \quad (6.10)$$

From this point, the calculations are made in the same way as for the laminar region. The results obtained for the predicted active layer thickness considering that it is fully formed in the the impingement zone can be seen in Figure 6.3. The results obtained earlier for the laminar region are plotted as well for comparison.

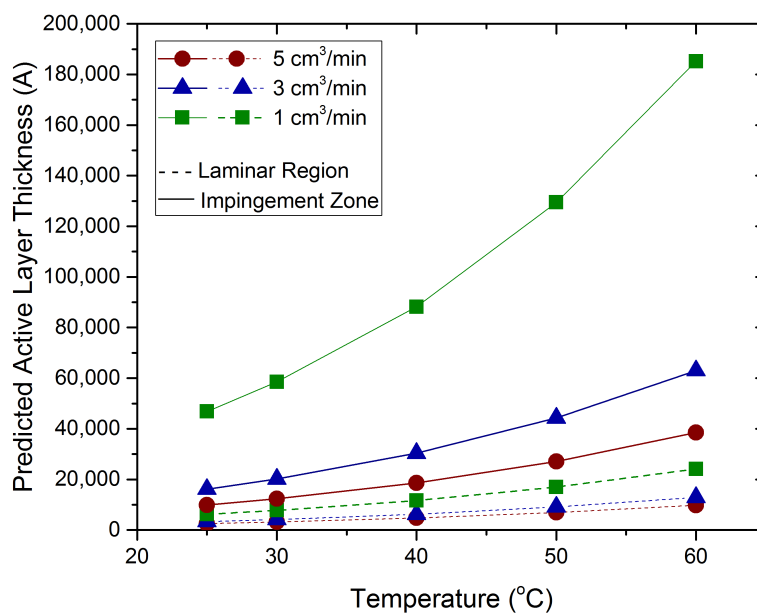


FIGURE 6.3: Comparison of the predicted membrane active layers using the mass transfer model applied to the impingement zone region and to the laminar flow region.

If the impingement zone is considered, the predicted active layers range from 10.000-190.000 Å. These results show a big increase in the active layer thickness if the impingement zone is considered in the model instead of the laminar region. As discussed before, since the conditions of this region are more aggressive in terms of flow regime, bigger solvent evaporation rates are in place, translating in bigger active layer thickness. This results also suggest that the DER has a bigger effect in the results for this region when compared with the laminar one. This might be related with the residence time and with the mass transfer coefficients. The mass transfer coefficients calculated for the impingement zone escalate faster with the DER than the ones calculated for the laminar region. For the smallest residence time this will translate in a faster grown in the predicted active layers thickness.

Unfortunately, the general selectivities of the prepared membranes were low so it

was not possible to determine experimentally the active layer thickness of these membranes using the pressure normalized fluxes results and the permeability coefficients. This makes it impossible to compare the obtained results with experimental evidence. However, the comparison of these results with the ones obtained experimentally by *Shilton* [178], even considering a different system, gives some confidence in using this model to have an idea of the expected magnitude of active layer thickness of the prepared membranes as well as the effect of the different parameters.

## 6.4 Results of the Mass Transfer Model - Prediction of the Orientation Depth

The mass transfer model also allows to predict the orientation depth in the membrane active layer using Equation 6.11.

$$R_{relax} = F_{relax}A_{relax}\Delta y \quad (6.11)$$

$R_{relax}$  refers to the rate of THF evaporation during the relaxation of the polymer chains considering the length of fibre extruded within the relaxation time. The parameter  $F_{relax}$  is similar to the  $F$  calculated earlier but in this case considering only the relaxation period.  $A_{relax}$  corresponds to the area of the membrane extruded in the relaxation time and, finally,  $\Delta y$  represents the mole fraction difference driving force.

To do these calculations, it is necessary to know the relaxation time of the polymer. There are different methods available to determine this parameter. One of these consist in conducting rheological angular frequency experiments. As it was discussed before, in the rheological studies performed it was not possible to quantify the relaxation time of the samples studied. However, it was possible to suggest that the relaxation time is always greater than 10 seconds, for all the

spinning temperatures. Table 6.6 contains the residence times for each one of the dope extrusion rates used as well as the suggested relaxation times.

TABLE 6.6: Comparison between the residence times in the forced convection chamber and the polymer relaxation time.

	Dope Extrusion Rate (cm <sup>3</sup> /min)		
	1	2	3
<b>Residence Time (s)</b>	1.596	0.158	0.095
<b>Relaxation Time (s)</b>	>10	>10	>10

As can be seen, the residence time is always smaller than the relaxation time. This suggests that the orientation achieved in the *spinneret* is "locked" when the active layer is formed in the dry gap. This means that all the active layer thickness will be orientated and the orientation depth corresponds to the active layer thickness.

## 6.5 Conclusions of the Mass Transfer Modelling

The mass transfer model developed by *Shilton* allowed to predict the active layer thickness of hollow fibre membranes prepared by the dry/wet phase inversion technique for different experimental conditions. This model is based on the solvent evaporation rate (of the most volatile component) that happens in the dry gap (forced convection chamber).

Using this model, the effect of the spinning temperature and the dope extrusion rate was evaluated and the increasing of the active layer with the increasing of the spinning temperature and decreasing of the dope extrusion rate was predicted. The active layer thickness predicted considering the laminar flow region as responsible for the fully growth of the active layer ranged from 2.500-25.000 Å. If the impingement zone is considered as the region responsible for the active layer formation, thicker layers are predicted (10.000-190.000 Å). Experimental evidence obtained by the author of the model suggests that, when membranes are spinning at high temperatures, the impingement zone should be considered

as responsible for the growth of the membranes skin. This suggest that very thick active layers should be obtained for the conditions studied in this work.

As the relaxation time is greater than the residence time, it is suggested that all extent of the active layer of the membranes is oriented.

In the next chapter a different model, based on experimental data, will also be used to predict the active layer thickness and hopefully a comparison can be made with the predictions made using the mass transfer model.

## Chapter 7

# Resistance Modelling

### 7.1 Objectives

Previously, permeation data for oxygen and nitrogen was obtained experimentally for the membranes prepared using different spinning conditions. Using this data the resistance model, developed by *Shilton* [71] was used in order to determine the membrane active layer thickness and surface porosity.

### 7.2 Principles of the Resistance Model

The first papers to relate the gas flow through membranes with electrical resistances were published in the 80's by *Henis* and *Tripodi* [185, 186]. In their work they introduced the concept of membrane coating to repair membranes with defects in order to achieve suitable selectivities for gas separation. Later, in the 90's, since the model was not fitting experimental data accurately, it was improved by other authors by incorporating the *Wheatstone* bridge model [187]. *Shilton* [71], in 1996, developed a modified version of the *Wheatstone* bridge model where an expression for *Knudsen* diffusion was incorporated in order to determine the pore

size and other structural parameters using gas permeation measurements.

A schematics of a structure of an uncoated asymmetric membrane, Figure 7.1.

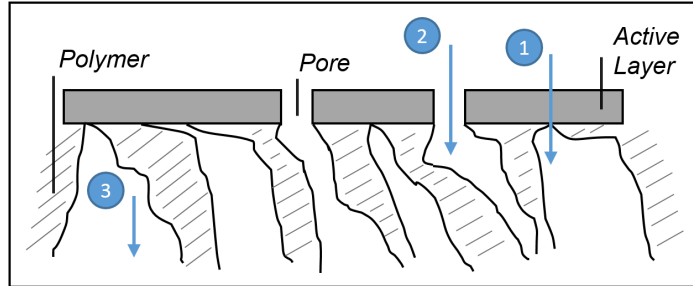


FIGURE 7.1: Schematics of the gas transport through an asymmetric uncoated membrane.

The arrows indicate the different flows that can be present:

1. Solution-diffusion through the polymer;
2. *Knudsen* diffusion through the active layer pores;
3. Viscous flow through the substructure containing big pores.

The gas transport through a membrane can be achieved by three different mechanisms that are related with the structural features of the material - *Knudsen* diffusion, viscous flow and solution-diffusion. These three flows are described by Equation 7.1, 7.2 and 7.3, respectively [71].

$$\text{Knudsen Diffusion : } Q = \frac{8}{3} \sqrt{\frac{1}{2\pi R_0 T M}} \frac{r}{L} A p \times A \times \Delta p \quad (7.1)$$

$$\text{Viscous Flow : } Q = \frac{r^2}{8R_0 T} \frac{1}{L\eta} \left( \frac{p_f + p_p}{2} \right) A p \times A \times \Delta p \quad (7.2)$$

$$\text{Solution-Diffusion : } Q = \frac{P_{gas/polymer}}{L} A p \times A \times \Delta p \quad (7.3)$$

Solution-diffusion mechanisms occurs in non-porous membranes. Viscous and *Knudsen* flows occur depending on the the *Knudsen* number ( $Kn$ ), Equation 7.4.

$$Kn = \frac{d}{\lambda} \quad (7.4)$$

$d_p$  corresponds to the pore diameter and  $\lambda$  corresponds to the gas mean free path that can be calculated using Equation 7.5.

$$\lambda = \frac{R_0 T}{2^{0.5} p N \pi d_m^2} \quad (7.5)$$

If  $Kn$  is greater than 10, *Knudsen* diffusion occurs. If it is less than 0.01, viscous flow is present. In between these two  $Kn$ , a transition region is present. Relating the general expression for the flow (Equation 7.6) with the different flow equations above, it is possible to obtain the permeation expressions for each one of the different flows.

$$Q = P \times A \times \Delta p \quad (7.6)$$

As it was not possible to use SEM to determine the pore size, it is assumed that the surface membrane pore radius is smaller than 100 Å [71]. Calculating the *Knudsen* number, it is concluded that *Knudsen* diffusion is the mechanism present in this section of the membrane, that is concordant with the uncoated pressure normalized fluxes that show *Knudsen* selectivity. In the sub layer the pores are big, so the *Knudsen* number is lower than 0.01 and viscous flow is present.

If these flows are represented as resistances, Figure 7.2 is obtained where each one of the resistances represents the mechanisms listed before.

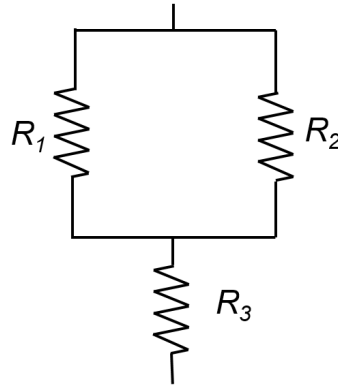


FIGURE 7.2: Representation of the gas resistances encountered in an uncoated asymmetric membranes.

A simplification can be made to these diagram by removing resistance number 3 since this resistance represents the flow of the gas through the sub layer of the membrane that is composed by big pores that offer low resistance when compared with the other two resistances. The total resistance is given by the sum of  $R_1$  and  $R_2$ , Equation 7.7.

$$\frac{1}{R_{unc}} = \frac{1}{R_1} + \frac{1}{R_2} \quad (7.7)$$

In these resistances are substituted by the respective pressure normalizer fluxes,  $P_{unc}$ , Equation 7.8 is generated (note that the resistance to permeation is the inverse of the product between the permeation and area).

$$P_{unc} = \frac{P_{gas/polymer}}{L_1} + \frac{8}{3} \sqrt{\frac{1}{2\pi R_0 T M}} \frac{r}{L_1} A p \quad (7.8)$$

In order to repair the membrane from eventual defects in the surface, a coating material is used. After the coating process, an additional resistance needs to be considered. Figure 7.3 illustrates a membrane structure after coating.

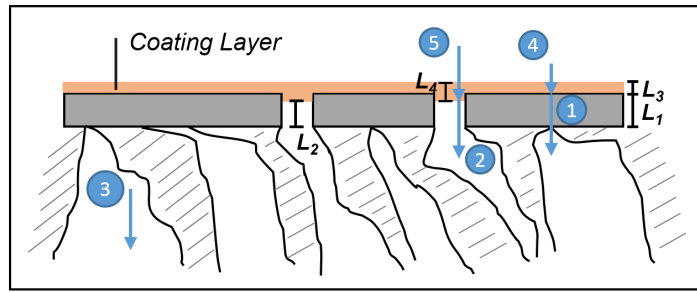


FIGURE 7.3: Schematics of the gas transport through an asymmetric coated membrane.  $L_1$  - Active layer thickness;  $L_2$  - Height of the pore not filled by the coating material;  $L_3$  - Coating height above active layer;  $L_4$  - Coating penetration in the pore.

As can be seen, with the introduction of the coating material a new resistance needs to be considered. Arrow number 4 corresponds to the solution-diffusion mechanism of the gas through coating material above the active layer and number 5 to the same mechanism but in the porous region, Figure 7.4.

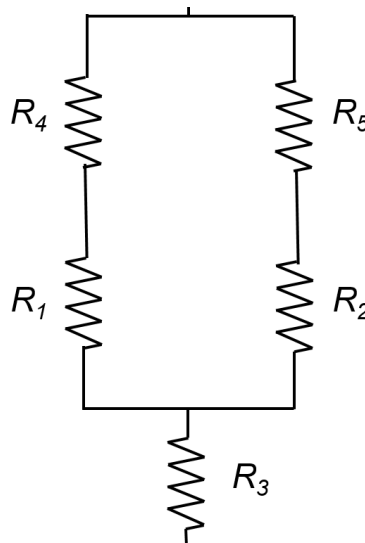


FIGURE 7.4: Representation of the gas resistances encountered in a coated asymmetric membranes.

In this case, the total resistance is given by Equation 7.9.

$$\frac{1}{R_{coat}} = \frac{1}{R_1 + R_4} + \frac{1}{R_2 + R_5} \quad (7.9)$$

However, the resistance  $R_4$  is much smaller than  $R_1$  because the coating material has much high permeability to the gases when compared with the polymer and is, because of that, negligible. Also, as the penetration of the coating material is not good, it is considered that  $L_2$  is approximately equal to  $L_1$  and  $L_4$  is approximately equal to  $L_3$ . The expression in terms of fluxes can then be obtained, Equation 7.10.

$$P_{coat} = \frac{P_{gas/polymer}}{L_1} + \frac{1}{\frac{8}{3} \sqrt{\frac{1}{2\pi R_0 T M} \frac{r}{L_1} A_p} + \frac{P_{gas/coating}}{L_3}} \quad (7.10)$$

With the equations available it is possible to calculate the active layer thickness ( $L_1$ ), surface porosity ( $A_p$ ) and coating height ( $L_3$ ).

To calculate the unknown parameters, the permeabilities of the gases through the polymer and the coating material need to be known. The coating material used in this work is polydimethylsiloxane (PDMS) (also known as Sylgard<sup>®</sup> 184) and the polymer is PVC. Table 7.1 shows the permeability coefficients for oxygen and nitrogen through these two materials.

TABLE 7.1: Permeability coefficients of oxygen and nitrogen through PDMS and PVC.

Gas	Material	Permeability Coefficient (barrer)
Oxygen	PDMS	620 [188, 189]
	PVC	0.091 [8]
Nitrogen	PDMS	280 [189]
	PVC	0.01802 [8]

### 7.3 Results of the Resistance Model - Calculation of the Active Layer Thickness and Surface Porosity

Due to the experimentally obtained selectivity results for the uncoated membranes show that the flow mechanism present is *Knudsen* diffusion, Equation 7.8 can be simplified by removing the parcel correspondent to the flux through the polymer. Two other equations can be obtained by using Equation 7.10 for each one of the gases tested (nitrogen and oxygen).

The system of non-linear equations was solved using the software *Mathcad* (see Appendix). In the first attempt it was not possible to obtain a valid solution since the system was not converging. This results was not surprising since the coated selectivities obtained in this work are low (less than two in the majority of the membranes tested for the different conditions). This result suggests that the mechanisms that were assumed to be involved in the gas flow through the membrane do not correspond to the reality, more concretely the solution-diffusion of the gases through the polymer. To try to solve this problem a new approach was considered. In this new approach, for the coated membranes with selectivities bellow 2, it was considered that the only flow mechanism is through *Knudsen* diffusion, eliminating the solution-diffusion term in Equation 7.10. With this assumption, Equation 7.11 is generated.

$$P_{coat} = \frac{1}{\frac{8}{3} \sqrt{\frac{1}{2\pi R_0 T M}} \frac{r}{L_1} Ap + \frac{P_{gas/coating}}{L_3}} \quad (7.11)$$

Taking this approach, by solving the system of equations, it was possible to determine the active layer thickness and surface porosity for the tested membranes with selectivities below 2, based on the permeation data obtained. The *Mathcad* algorithm used can be found in the Appendix. The obtained results can be found in Figure 7.5 and 7.6.

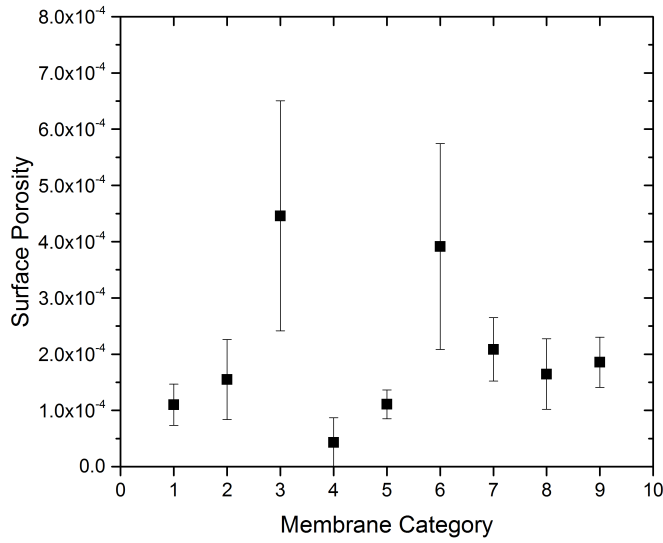


FIGURE 7.5: Results obtained for the membranes surface porosity using the resistance modelling.

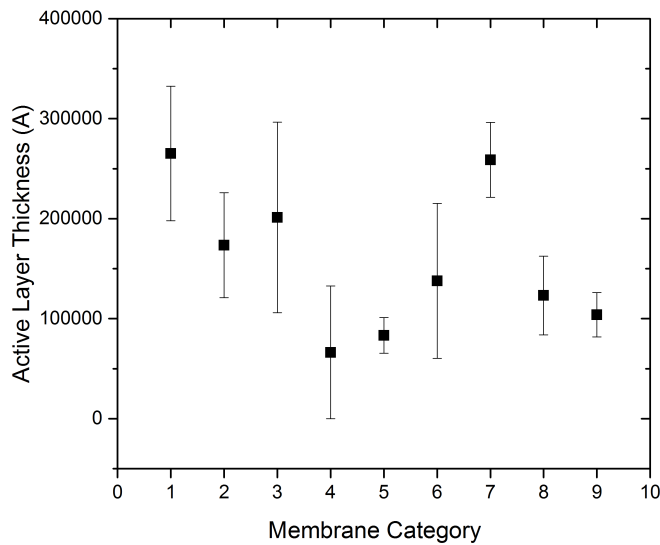


FIGURE 7.6: Results obtained for the membranes active layer thickness using the resistance modelling.

The first comment that can be made to these results are the big standard deviations presented. However, these results were expected since they were obtained

using the permeation data acquired experimentally that already presented big standard deviations, reflecting the big variability that exists in each one of the batches.

As these experiments were designed using the *Taguchi* approach, the evaluation of the influence of the three studied parameters is not linear. However, some general comments can be made about the results obtained.

Concerning the surface porosity (area of pores per area of the membrane), the results show that it is in the region of  $10^{-5}$  with category number 4 being the one presenting lower surface porosity ( $10^{-4}$ ). However, no pattern between the values obtained and the spinning conditions can be outlined. The fact that the other categories are predicted to have higher surface porosities can be a possible explanation for the low selectivities presented (near the coating material selectivity). This can be linked with the fact that, due to the high surface area that is covered with pores, even if these are sealed with the coating material, the gases would have a preference to pass through the pores sealed with silicone, compromising the separation. The PVC hollow fibre membranes prepared by Jones [1] that showed a decent selectivity presented porosities around  $10^{-7}$ , which shows that the separation properties of the membranes prepared in this work might have been compromised by the presence of a big number of pores in the surface.

From the SEM micrographs of the membranes' surface, the fraction of surface area occupied by the mechanical defects (furrows) was determined to be of the order of  $10^{-4}$ . This is at least one order of magnitude greater than the surface porosity calculated by the resistance modelling. This results is encouraging as it indicates that the mechanical striations cannot be cracks all the way through the active layer (if they were, the resistance modelling surface porosities would be much larger). Thus the striations can simply be dismissed as aesthetic displeasing features.

A possible reason for the big porous area is the incomplete coalescence of the polymer nodules during the nodule coalescence and growth phase, compromising the achievement of a defect free active layer.

In terms of the active layer thickness, the results obtained suggest the existence of thick active layers in the prepared membranes. In this work the results show thickness ranging from 65.000-270.000 Å. It is also important to notice once again,

the big standard deviations obtained in these calculations that results from the variability in the fluxes measured.

It was expected that the membranes extruded with lower rates would present thicker active layers since the residence time in the chamber is bigger, allowing a more extended growth of the skin due to the contact with the convective gas. However, no relation can be established between these results and the different spinning conditions, since no patterns are identified. With the increase of the active layer thickness it is expected to observe a decrease in the pressure normalized fluxes. If these results are compared with the experimental ones, it is possible to verify that category number 3 has one of the lowest experimental fluxes and accordingly with the resistance modelling one of the highest active layer thickness. Even if the transport mechanism considered for the membranes is *Knudsen* diffusion, it is possible to see in Equation 7.1 that the active layer thickness is a parameter to have in account to calculate the flux and, as a denominator, will generate lower fluxes with its increase.

If these results are compared with the active layers predicted by the mass transfer model studied earlier, it can be seen that they are in the same order of magnitude of those predicted by considering the impingement zone, Figure 7.7. This suggests that, in this system, this part of the chamber is playing an important role in the formation of the active layer of the membranes. It was already outlined before the importance of the impingement zone when spinning at high temperatures is performed, conducting to thick active layers [178].

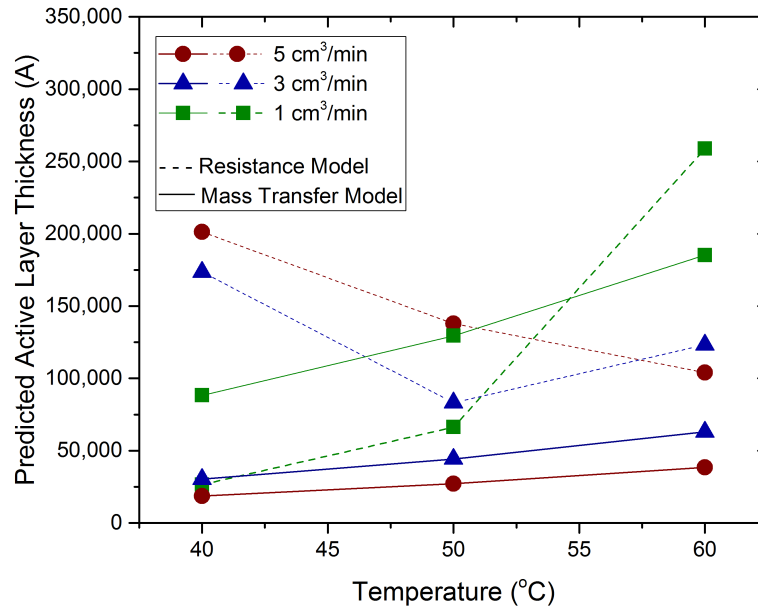


FIGURE 7.7: Comparison of the results obtained for the membranes active layer thickness using the resistance modelling with the results obtained using the mass transfer model.

## 7.4 Conclusions of the Resistance Modelling

In this work, two different models were explored in order to predict the active layer thickness of PVC hollow fibre membranes prepared by the dry/wet phase inversion process. The first one, the mass transfer model, predicts the active layer thickness based on the solvent evaporation rate happening in the dry gap (forced convection chamber) while the second, the resistance model, predicts the same parameter using the experimental pressure normalized fluxes and an approach that considers the flow through membranes as resistances. The latter also allows to determine the membranes surface porosity.

In the mass transfer model, the temperature and the dope extrusion rate were evaluated and the model predicted the increasing of the active layer with the increasing of the temperature and decreasing of the dope extrusion rate. If the impingement zone is considered as the region responsible for the active layer

formation, thicker layers are predicted.

The resistance model, based on experimental data, estimates the existence of thick active layers in the prepared membranes. If the quantitative results are compared with the mass transfer model it can be seen that they are of the same magnitude, suggesting that the impingement zone had a big influence in the growth of the active layers of the prepared membranes. The resistance model allowed to estimate the surface porosity of the membranes, showing that this parameter was higher when compared with results already obtained for PVC membranes in previous published work [1].

The SEM micrographs suggested that the fraction of surface area occupied by the mechanical defects is of the order of  $10^{-4}$  that is at least one order of magnitude greater than the surface porosity calculated by the resistance modelling. For this reason, the striations can simply be dismissed as aesthetic displeasing features.

The high surface porosity obtained is suggested to be due to the incomplete coalescence of the nodules during the formation of the active layer. High porosity and the existence of thick active layers, are suggested to be the reasons for the low fluxes and low selectivities obtained for the membranes prepared.

# Final Conclusions

The preparation of a polymer solution is the first step in the production of hollow fibre membranes using the dry/wet phase inversion spinning process. Following the work previously carried out by *Jones* [1], the polymer solutions used to produce the hollow fibres were composed of PVC, DMAc, THF and EtOH.

In order to study the phase inversion properties of the PVC solutions, solutions with different compositions were prepared. Preliminary degradation tests were performed to evaluate the maximum temperature to be used in order to achieve homogeneity and avoid the degradation of the PVC in solution. A visual appearance of the solution was made to evaluate its homogeneity. This results of the solubility tests helped to understand the possible location of the binodal curve for this polymer system and, based on that, choose the appropriate polymer solution composition in order to conduct the membrane spinning (composition number 2 - 28% PVC, 50% DMAc, 6% THF and 16% EtOH (w/w)).

As the spinning process subjects the polymer solutions to high shear rates and different degrees of deformation. A rheological analysis of the PVC quaternary solutions with different compositions was made in order to study the influence of parameters such as composition and temperature. The results showed that composition and temperature have a strong influence in the viscoelasticity of the solutions. Rheological tests also allowed to obtain information about the polymer relaxation time, a very important parameter in membrane spinning. It was not possible to obtain the exact value for the relaxation times for the compositions studied but the results suggested that these are always greater than 10 seconds. Since the residence times in the forced convection chamber are lower than two seconds for the dope extrusion rates used in the spinning runs, it is suggested

that the alignment of the polymer chains achieved in the *spinneret* is "locked" when the coagulation of the membrane surface occurs.

The rheological results allowed also the determination of the gel point in terms of concentration, giving more information about the phase diagram of the system. The temperature sweeps detected a range of temperatures (between 45°C and 51°C) in which there is an accentuated decrease in the storage modulus for all compositions investigated. Creep and recovery experiments results showed that the temperature has a strong influence in the viscoelastic properties of the solutions in the temperature range studied (20°C to 50°C). Some solutions that presented viscoelastic properties at 20°C behaved as purely viscous materials at 50°C. This suggests that the drop in the storage modulus observed in the temperature sweep tests is due to the transition between the viscoelastic regime to the viscous regime (liquid-liquid transition). No thermal transitions (such as melting) were detected in the DSC experiments between 20°C and 50°C, strengthening the hypothesis of a liquid-liquid transition.

Previous published results for the same polymer system showed higher selectivities for membranes prepared at 50°C when compared with fibres prepared at 20°C. The fact that there is a change in the viscoelastic properties from 20°C to 50°C might be the reason for the difference in the selectivities observed by *Jones* [8] when spinning fibres at both temperatures. These results suggest that, for this system, it is desirable to have solutions with purely viscous features, i.e. without any viscoelasticity.

Two different models were used to fit the creep and recovery data - *Burgers* (only creep data) and *Weibull* model (creep and recovery data). Both models fitted well the experimental data and allowed to obtain quantitative parameters about the system, such as retardation times. The results obtained in the rheological tests were useful to understand the features of the ternary phase diagram for this system.

Using the phase inversion and the rheological investigation results, the spinning runs were designed in order to produce hollow fibres using different experimental conditions. A fresh solution with the same composition as solution number 2, was prepared. This solution was also subjected to rheological tests, since its preparation method and "ageing" time was different from the one tested before

with the same composition. Temperature sweep tests showed a decreasing in the storage modulus at around 43°C. Creep and recovery tests showed a change from a viscoelastic to a purely viscous material was detected between 40°C and 45°C. These results reinforce the presence of a liquid-liquid transition in this temperature range, with the preparation method and "ageing" time having a moderate effect on the temperature at which this transition occurs.

Results from rheological flow tests carried out at 20°C and 50°C allowed to simulate velocity, shear rate and shear stress profiles in the *spinneret* by fitting the experimental data to a power law model. These results showed once more the effect of temperature in the extrusion process.

The detailed rheological study of the quaternary PVC solutions showed how difficult it can be to characterise a system where one of the components is a solvent with a low boiling point ( $T_b(\text{THF}) \approx 66^\circ\text{C}$ ) thus making evaporation an issue when high temperature is used. Although this effect was minimised by the use of a solvent trap, it is not guaranteed that this phenomenon has no effect on the observed results.

The experimental design of the spinning runs followed the *Taguchi* method. Three experimental parameters were evaluated (spinning temperature, dope extrusion rate and external bath temperature) and nine categories/batches of membranes were prepared with different experimental conditions in order to study the effect of these parameters in the performance of the membranes.

After preparation and potting, the nitrogen and oxygen fluxes through the membranes were measured and the selectivities calculated. The membranes were then coated twice and the gas fluxes recorded after each coating cycles. Uncoated membranes showed poor selectivity, with the gas transport being governed by *Knudsen* diffusion. A pattern was identified, with the fluxes increasing with the increasing of the dope extrusion rate (and decreasing of the residence time in the forced convection chamber)

In general, the coating cycles did not yield improvements in the selectivities. Only one category of membranes presented selectivities above 2 ( $\Omega_{O_2/N_2} = 2.82 \pm 1.23$ ). For all the categories, the measured fluxes and selectivities showed large standard

deviations, thus showing the inconsistent gas permeation performance of individual membranes from the same batch.

The *Taguchi* method allowed to determine the best experimental conditions (within the range of conditions investigated) in order to achieve a target selectivity. The target selectivity chosen in this case was the average of the selectivities found in the literature for the pair oxygen/nitrogen for PVC flat sheet membranes ( $\Omega_{O_2/N_2}=5.1$ ). A spinning temperature of 50°C, a dope extrusion rate of 1 cm<sup>3</sup>/min and an external bath of 30°C were obtained as the best conditions. These conditions correspond to the membrane category number 4 and, because of this, a confirmation experiment was not needed.

An analysis of variance (*ANOVA*) was also performed to understand which of the parameters studied contributes the most for the variability of the selectivity results. The external bath temperature was the parameter that had the larger contribution to the results (50% comparing with 23% for the spinning temperature and 16% for the dope extrusion rate). These results highlight the importance of temperature as a crucial operating condition in different stages of spinning.

To get some insight about the structural characteristics of the prepared membranes, Scanning Electron Microscopy (SEM) technique was used. Cross section showed membranes with a circular shape, suggesting that no major flow instabilities occurred during the spinning. By determining the internal and external diameter of the prepared membranes it is possible to verify that there is a contraction in the dimensions of the fibres when compared with the dimensions of the *spinneret*, being this phenomena also found in the textile industry [177].

Surface imaging showed the presence of defects such as polymer aggregates and fractures in the prepared membranes, for all the categories. The existence of non-homogeneity domains, not visible at naked eye, in the starting polymer solution is suggested to be the reason for the polymer aggregates visible in the surface. The presence of fractures is attributed to stretching due to the weight of the extruded thread and/or to the mechanical damage due to the contact between the spinning equipment rollers and the membranes surface. Unfortunately, it was not possible to correlate structural properties with spinning conditions.

In order to predict the active layer thickness of the prepared membranes, two models were used - the mass transfer model and the resistance model. The mass

transfer model, based on the conditions in the forced convection chamber and on the most volatile solvent evaporation rate. If the region where laminar flow is present is considered as the region where the active layer is fully formed, the model predicts an increase in the active layer thickness with the increase in temperature and decrease in the dope extrusion rate. If the impingement zone is considered, thicker active layer thicknesses are predicted.

The resistance model, based on the experimental permeation data, allowed the calculation of the active layer thickness and also the surface porosity. Using this model, thick active layers were obtained with values of thickness of the same order of magnitude as the ones obtained in the mass transfer model considering the impingement zone. This suggests that the impingement zone has a big influence in the growth of the membrane active layer. Surface porosities predicted by the model were high. This result, coupled with the prediction of thick active layers, is suggested as the reason for the poor performance of the prepared membranes.

From the SEM micrographs, the fraction of surface area occupied by the mechanical defects (furrows) was determined to be of the order of  $10^{-4}$ . This is at least one order of magnitude greater than the surface porosity calculated by the resistance modelling. This results is encouraging as it indicates that the mechanical striations cannot be cracks all the way through the active layer (if they were, the resistance modelling surface porosities would be much larger). Thus the striations can simply be dismissed as aesthetic displeasing features. The high surface porosity is suggested to be due to the incomplete coalescence of the polymer nodules during the formation of the active layer in the forced convection chamber.

Although it was not possible to obtain membranes with good performance in terms of gas separation properties, this work allowed to have a deep insight on different aspects of the production of hollow fibre membranes such as phase inversion and rheological signature of solutions used to perform membrane spinning. The work developed in this thesis, together with the recommendations presented in the next section, can be used as a reference for further research in the production of hollow fibre membranes for other polymeric systems.



## Future Work

After the completion of this work, there are a number of recommendations that can be made in order to aid future research in hollow fibre membrane fabrication for gas separation applications.

The fabrication of hollow fibre membranes using the dry/wet forced convection spinning is a complex process that involves controlling a lot of parameters. The first recommendation is related with the control of the temperatures in the various points of the system (spinneret, forced convection chamber and external baths). As could be observed in this work, the rheological properties of the quaternary polymer solutions are highly dependent of the temperature. Also, the ternary phase diagrams are dependent of the temperature and consequently the phase inversion process. Because of this, a precise control of this parameter should be made in order to ensure that this variable is kept at the desired value at all the steps of the process. This can be achieved by using a experimental rig with "perfect" control of all experimental conditions, especially the careful environmental control of the temperatures of the different sections of the spinning installation. Analysing the permeation results obtained for the prepared membranes, it is possible to observe that no consistency within each batch was achieved, with big standard deviations obtained for membranes spinning in the same conditions. This reveals that a more rigorous control of the operational parameters is needed in order to achieve more reliable and consistent results.

The study of the phase inversion properties of the PVC quaternary solutions revealed some features related with the ternary phase diagram and the possible location of the binodal boundary. As mentioned before, the knowledge of the ternary diagram is of high importance in order to design the spinning experiment

in terms of starting dope composition and in terms of the pathway that should be followed in order to achieve spinodal decomposition. If the spinodal composition is achieved, it is likely that an asymmetric structure comprising a dense active layer supported by a porous structure is obtained by nodule coalescence and growth [81]. A recommendation for the future is the detailed study of the ternary (or pseudo-ternary) diagram for the polymer system being investigated. Parameters such as temperature and shear should be taken into account due to its influence in the phase diagrams and its relevancy to the spinning process [190, 191]. The determination of the boundaries such as the binodal curve can be done experimentally or using mathematical models such as the Flory-Huggins model. The latter also involves the experimental determination of the interaction parameters between the species in solution.

The determination of the relaxation time was made using angular frequency tests. However, for the solutions studied it was not possible to observe these times, it was only possible to suggest that these times were less than 10 seconds. This was due to the fact that the smaller frequency investigated was 0.01 rad/s. The use of smaller frequencies would lead to large experiment times that are not desirable when working with solutions that contain volatile solvents. A way to "predict" what happens at lower frequencies is by determining the master curves for these solutions accordingly with the time-temperature superposition principle [192]. These master curves are built doing angular frequency sweeps at different temperatures that are then put together to give the correspondent curve in terms of time (frequency).

Surface Electron Microscopy revealed the existence of tearing in the membrane surface that is suggested to be due to mechanical damage during the spinning process due to contact with the rollers that aid the membrane to move through the baths. This is an aspect that can be improved by reviewing the spinning equipment due to the big effect in the features of the prepared membranes that these defects can have.

The mass transfer model used, developed by *Shilton* [178], was pioneer in terms of describing what happens in the dry step, in the forced convection chamber.

However, effects such as shear, bore fluid influence or even phase inversion mechanisms are not taken into account in the models, giving room for improvement.

PVC is found as a cheap alternative for membrane fabrication. Its ozone resistance makes this material very interesting for applications such as oxygen/ozone separation. Its low permeability towards gases is the major drawback of this material, however, this problem can be surpassed if an asymmetric membrane containing a very thin active layer is achieved (thicknesses of active layers in the order of tens of nanometres, instead of hundreds or thousands of nanometres).

For the same application, there are other materials that can be explored. In the 70's an ozone resistant polymer blend composed by ethylene/propylene and conventional general purpose rubbers was patented [193]. Another good candidate polymer that is largely used in membrane fabrication is polycarbonate, although is not popular in hollow fibre fabrication [194, 195]. Polyethylene is also an ozone resistant polymer [196]. Apart from the ozone resistance capabilities, it is also necessary to investigate the solution properties of these materials in order to decide if they are suitable for membrane spinning.



# Bibliography

- [1] C. A. Jones, *Hollow Fiber Poly (vinyl chloride) (PVC) Gas Separation Membranes Prepared by Dry/Wet Spinning Production Methods*. PhD thesis, University of Strathclyde, 2015.
- [2] F. Okada, S. Tanaka, S. Tanaka, and K. Naya, “Electrochemical Production of 70wtppm Ozone Water,” *Electrochimica Acta*, vol. 153, pp. 210–216, jan 2015.
- [3] A. Zecchina and S. Califano, *The development of catalysis—a history of key processes and personas in catalytic science and technology*. Wiley, 2017.
- [4] T. Schettler, “Human exposure to phthalates via consumer products,” *International Journal of Andrology*, vol. 29, pp. 134–139, feb 2006.
- [5] S. Patrick, *Practical Guide to Polyvinyl Chloride*. Shawbury: iSmithers Rapra Publishing, 2005.
- [6] W. V. Titow, *PVC Technology*. Dordrecht: Springer Netherlands, 1984.
- [7] S. Alexander Stern, “Polymers for gas separations: the next decade,” *Journal of Membrane Science*, vol. 94, pp. 1–65, sep 1994.
- [8] C. Jones, S. Gordeyev, and S. Shilton, “Poly(vinyl chloride) (PVC) hollow fibre membranes for gas separation,” *Polymer*, vol. 52, no. 4, pp. 901–903, 2011.
- [9] K. Bierbrauer, M. López-González, E. Riande, and C. Mijangos, “Gas transport in fluorothiophenyl modified PVC membranes,” *Journal of Membrane Science*, vol. 362, pp. 164–171, oct 2010.

- [10] P. Tiemblo, J. Guzmán, E. Riande, C. Mijangos, and H. Reinecke, “The Gas Transport Properties of PVC Functionalized with Mercapto Pyridine Groups,” *Macromolecules*, vol. 35, no. 2, pp. 420–424, 2002.
- [11] P. Tiemblo, J. Guzman, E. Riande, C. Mijangos, M. Herrero, J. Espeso, and H. Reinecke, “Diffusion of small molecules through modified poly(vinyl chloride) membranes,” *Journal of Polymer Science Part B: Polymer Physics*, vol. 40, no. 10, pp. 964–971, 2002.
- [12] M. Sadeghi, M. Pourafshari Chenar, M. Rahimian, S. Moradi, and A. H. S. Dehaghani, “Gas permeation properties of polyvinylchloride/polyethyleneglycol blend membranes,” *Journal of Applied Polymer Science*, vol. 110, pp. 1093–1098, oct 2008.
- [13] M. Mohagheghian, M. Sadeghi, M. P. Chenar, and M. Naghsh, “Gas separation properties of polyvinylchloride (PVC)-silica nanocomposite membrane,” *Korean Journal of Chemical Engineering*, vol. 31, pp. 2041–2050, sep 2014.
- [14] M. Mulder, *Basic Principles of Membrane Technology*. Dordrecht: Springer Netherlands, 1996.
- [15] P. van de Witte, P. Dijkstra, J. van den Berg, and J. Feijen, “Phase separation processes in polymer solutions in relation to membrane formation,” *Journal of Membrane Science*, vol. 117, pp. 1–31, aug 1996.
- [16] M. Gilbert, “Crystallinity in Poly(vinyl Chloride),” *Journal of Macromolecular Science, Part C: Polymer Reviews*, sep 2006.
- [17] P.-D. Hong and J.-H. Chen, “Structure and properties of polyvinyl chloride physical gels,” *Polymer*, vol. 39, pp. 711–717, jan 1998.
- [18] J. Guenet, “The role of polymer-solvent compounds in thermoreversible gelation,” *Macromolecular Symposia*, vol. 114, pp. 97–108, feb 1997.
- [19] E. Pines and W. Prins, “Structure-Property Relations of Thermoreversible Macromolecular Hydrogels,” *Macromolecules*, vol. 6, pp. 888–895, nov 1973.
- [20] P. J. Flory, “Thermodynamics of High Polymer Solutions,” *The Journal of Chemical Physics*, vol. 10, pp. 51–61, jan 1942.

- [21] L. Z. Rogovina, V. G. Vasil'ev, and E. E. Braudo, "Definition of the concept of polymer gel," *Polymer Science Series C*, vol. 50, pp. 85–92, sep 2008.
- [22] L. Li and Y. Aoki, "Rheological Images of Poly(vinyl chloride) Gels. 3. Elasticity Evolution and the Scaling Law beyond the Sol Gel Transition," *Macromolecules*, vol. 31, pp. 740–745, feb 1998.
- [23] L. Li, H. Uchida, Y. Aoki, and M. L. Yao, "Rheological Images of Poly(vinyl chloride) Gels. 2. Divergence of Viscosity and the Scaling Law before the Sol Gel Transition," *Macromolecules*, vol. 30, pp. 7842–7848, dec 1997.
- [24] Y. Aoki, L. Li, H. Uchida, M. Kakiuchi, and H. Watanabe, "Rheological Images of Poly(vinyl chloride) Gels. 5. Effect of Molecular Weight Distribution," *Macromolecules*, vol. 31, pp. 7472–7478, oct 1998.
- [25] L. Li and Y. Aoki, "Rheological Images of Poly(vinyl chloride) Gels. 1. The Dependence of Sol Gel Transition on Concentration," *Macromolecules*, vol. 30, pp. 7835–7841, dec 1997.
- [26] S. J. Guerrero, A. Keller, P. L. Soni, and P. H. Geil, "Study of crystal texture in pvc gels by x-ray diffraction and infrared dichroism," *Journal of Polymer Science: Polymer Physics Edition*, vol. 18, pp. 1533–1559, jul 1980.
- [27] S. J. Guerrero, D. Meader, and A. Keller, "Structure changes in PVC at high temperatures as determined from X-ray diffractometer curves," *Journal of Macromolecular Science, Part B*, vol. 20, pp. 185–198, sep 1981.
- [28] S. J. Guerrero and A. Keller, "The gelation of PVC: Characterization and control," *Journal of Macromolecular Science, Part B*, vol. 20, pp. 167–184, sep 1981.
- [29] S. J. Guerrero, A. Keller, P. L. Soni, and P. H. Geil, "A study of texture in PVC gels by infrared dichroism and X-ray diffraction," *Journal of Macromolecular Science, Part B*, vol. 20, pp. 161–166, sep 1981.
- [30] H. Soenen and H. Berghmans, "Gelation and structure formation in solutions of poly(vinyl chloride)," *Journal of Polymer Science Part B: Polymer Physics*, vol. 34, pp. 241–247, jan 1996.

- [31] H. Tan, A. Moet, A. Hiltner, and E. Baer, "Thermoreversible gelation of atactic polystyrene solutions," *Macromolecules*, vol. 16, pp. 28–34, jan 1983.
- [32] H. M. Tan, B. H. Chang, E. Eaer, and A. Hiltner, "Relationship between crystallinity and thermoreversible gelation," *European Polymer Journal*, vol. 19, pp. 1021–1025, jan 1983.
- [33] Y. C. Yang and P. H. Geil, "Morphology and properties of PVC/solvent gels," *Journal of Macromolecular Science, Part B*, vol. 22, pp. 463–488, jan 1983.
- [34] K. Kawanishi, M. Komatsu, and T. Inoue, "Thermodynamic consideration of the sol-gel transition in polymer solutions," *Polymer*, vol. 28, pp. 980–984, may 1987.
- [35] A. Takahashi, M. Sakai, and T. Kato, "Melting Temperature of Thermally Reversible Gel. VI. Effect of Branching on the Sol–Gel Transition of Polyethylene Gels," *Polymer Journal*, vol. 12, pp. 335–341, may 1980.
- [36] M. Girolamo, A. Keller, K. Miyasaka, and N. Overbergh, "Gelation-crystallization in isotactic polystyrene solutions and its implications to crystal morphology, to the origin and structure of gels, and to the chemical homogeneity of polyolefins," *Journal of Polymer Science: Polymer Physics Edition*, vol. 14, pp. 39–61, jan 1976.
- [37] C. J. King, *Separation Processes*. Dover Publications Inc., 2nd ed., 2013.
- [38] J. L. Humphrey, *Separation Process Technology*. McGraw-Hill, 1997.
- [39] A. B. de Haan and H. Bosch, *Industrial Separation Processes: Fundamentals*. De Gruyter, 2013.
- [40] K. Vanherck, I. Vankelecom, and T. Verbiest, "Improving fluxes of polyimide membranes containing gold nanoparticles by photothermal heating," *Journal of Membrane Science*, vol. 373, pp. 5–13, may 2011.
- [41] H. A. Mannan, H. Mukhtar, T. Murugesan, R. Nasir, D. F. Mohshim, and A. Mushtaq, "Recent Applications of Polymer Blends in Gas Separation Membranes," *Chemical Engineering & Technology*, vol. 36, pp. 1838–1846, nov 2013.

- [42] R. W. Baker, "Overview of Membrane Science and Technology," in *Membrane Technology and Applications*, pp. 1–14, Chichester, UK: John Wiley & Sons, Ltd, jul 2012.
- [43] R. W. Baker, "Membrane Technology," in *Kirk-Othmer Encyclopedia of Chemical Technology*, Hoboken, NJ, USA: John Wiley & Sons, Inc., dec 2000.
- [44] P. Wu and M. Imai, "Novel Biopolymer Composite Membrane Involved with Selective Mass Transfer and Excellent Water Permeability," in *Advancing Desalination*, InTech, sep 2012.
- [45] K. Scott, *Handbook of Industrial Membranes*. Elsevier Science Publisher, 1995.
- [46] M. T. So, F. R. Eirich, H. Strathmann, and R. W. Baker, "Preparation of asymmetric loeb-sourirajan membranes," *Journal of Polymer Science: Polymer Letters Edition*, vol. 11, pp. 201–205, mar 1973.
- [47] J. Bouchilloux, A. Fabre, and A. Faure, "Anisotropic organosilicon polymer membrane," 1973.
- [48] S. Kimura, "Preparation of asymmetric polymer membranes," 1973.
- [49] O. T. Iorhemen, R. A. Hamza, and J. H. Tay, "Membrane Bioreactor (MBR) Technology for Wastewater Treatment and Reclamation: Membrane Fouling," *Membranes*, vol. 6, jun 2016.
- [50] P. Cornel and S. Krause, "Membrane bioreactors in industrial wastewater treatment—European experiences, examples and trends.," *Water science and technology : a journal of the International Association on Water Pollution Research*, vol. 53, no. 3, pp. 37–44, 2006.
- [51] C. Heath and G. Belfort, "Membranes and bioreactors," *International Journal of Biochemistry*, vol. 22, pp. 823–835, jan 1990.
- [52] M. Mänttari, J. Nuortila-Jokinen, and M. Nyström, "Evaluation of nanofiltration membranes for filtration of paper mill total effluent," *Filtration & Separation*, vol. 34, pp. 275–280, apr 1997.

- [53] A. Thormann, N. Teuscher, M. Pfannmöller, U. Rothe, and A. Heilmann, “Nanoporous Aluminum Oxide Membranes for Filtration and Biofunctionalization,” *Small*, vol. 3, pp. 1032–1040, jun 2007.
- [54] B. Winfield, “Cellulose acetate membranes for the reverse osmosis treatment of sewage effluents: Is long term performance a limiting factor?,” *Water Research*, vol. 16, no. 6, pp. 797–799, 1982.
- [55] A. P. Duarte, M. T. Cidade, and J. C. Bordado, “Cellulose acetate reverse osmosis membranes: Optimization of the composition,” *Journal of Applied Polymer Science*, vol. 100, pp. 4052–4058, jun 2006.
- [56] J. Balster, “Spiral Wound Membrane Module,” in *Encyclopedia of Membranes*, pp. 1–3, Berlin, Heidelberg: Springer Berlin Heidelberg, 2013.
- [57] H. I. Mahon, “Permeability separatory apparatus and process utilizing hollow fibers,” jan 1966.
- [58] C. Feng, K. Khulbe, T. Matsuura, and A. Ismail, “Recent progresses in polymeric hollow fiber membrane preparation, characterization and applications,” *Separation and Purification Technology*, vol. 111, pp. 43–71, jun 2013.
- [59] U. Balachandran, J. Dusek, R. Mieville, R. Poeppele, M. Kleefisch, S. Pei, T. Kobylinski, C. Udovich, and A. Bose, “Dense ceramic membranes for partial oxidation of methane to syngas,” *Applied Catalysis A: General*, vol. 133, pp. 19–29, dec 1995.
- [60] H. Bouwmeester and A. Burggraaf, “Dense ceramic membranes for oxygen separation,” *Membrane Science and Technology*, vol. 4, pp. 435–528, 1996.
- [61] H. J. Bouwmeester, “Dense ceramic membranes for methane conversion,” *Catalysis Today*, vol. 82, pp. 141–150, jul 2003.
- [62] S. Saufi and A. Ismail, “Fabrication of carbon membranes for gas separation—a review,” *Carbon*, vol. 42, no. 2, pp. 241–259, 2004.
- [63] J. Caro and M. Noack, “Zeolite membranes – Recent developments and progress,” *Microporous and Mesoporous Materials*, vol. 115, pp. 215–233, nov 2008.

- [64] Y. H. Ma, J. Catalano, F. Guazzone, Y. H. Ma, J. Catalano, and F. Guazzone, “Metallic Membranes for High Temperature Hydrogen Separation,” in *Encyclopedia of Membrane Science and Technology*, Hoboken, NJ, USA: John Wiley & Sons, Inc., apr 2013.
- [65] H. K. Lonsdale, “The growth of membrane technology,” *Journal of Membrane Science*, vol. 10, pp. 81–181, apr 1982.
- [66] W. Pusch and A. Walch, “Synthetic Membranes?Preparation, Structure, and Application,” *Angewandte Chemie International Edition in English*, vol. 21, pp. 660–685, sep 1982.
- [67] L. M. Robeson, “Correlation of separation factor versus permeability for polymeric membranes,” *Journal of Membrane Science*, vol. 62, pp. 165–185, oct 1991.
- [68] L. M. Robeson, “The upper bound revisited,” *Journal of Membrane Science*, vol. 320, pp. 390–400, 2008.
- [69] W. He, W. Lv, and J. Dickerson, *Gas Transport in Solid Oxide Fuel Cells*. SpringerBriefs in Energy, Cham: Springer International Publishing, 2014.
- [70] R. D. Noble and S. Stern, *Membrane Separations Technology: Principles and Applications*. Elsevier, 1995.
- [71] S. Shilton, G. Bell, and J. Ferguson, “The deduction of fine structural details of gas separation hollow fibre membranes using resistance modelling of gas permeation,” *Polymer*, vol. 37, pp. 485–492, feb 1996.
- [72] M. Mulder, T. Franken, and C. Smolders, “Preferential sorption versus preferential permeability in pervaporation,” *Journal of Membrane Science*, vol. 22, pp. 155–173, feb 1985.
- [73] N. Peng and T. S. Chung, “The effects of spinneret dimension and hollow fiber dimension on gas separation performance of ultra-thin defect-free Torlon hollow fiber membranes,” *Journal of Membrane Science*, vol. 310, pp. 455–465, mar 2008.

- [74] N. Widjojo, T.-S. Chung, D. Y. Arifin, M. Weber, and V. Warzelhan, "Elimination of die swell and instability in hollow fiber spinning process of hyperbranched polyethersulfone (HPES) via novel spinneret designs and precise spinning conditions," *Chemical Engineering Journal*, vol. 163, pp. 143–153, sep 2010.
- [75] S. Pesek and W. Koros, "Aqueous quenched asymmetric polysulfone membranes prepared by dry/wet phase separation," *Journal of Membrane Science*, vol. 81, pp. 71–88, jun 1993.
- [76] A. Idris, A. Ismail, M. Noorhayati, and S. Shilton, "Measurement of rheologically induced molecular orientation using attenuated total reflection infrared dichroism in reverse osmosis hollow fiber cellulose acetate membranes and influence on separation performance," *Journal of Membrane Science*, vol. 213, pp. 45–54, mar 2003.
- [77] A. Figoli, T. Marino, S. Simone, E. Di Nicolò, X.-M. Li, T. He, S. Tornaghi, and E. Drioli, "Towards non-toxic solvents for membrane preparation: a review," *Green Chemistry*, vol. 16, p. 4034, jul 2014.
- [78] N. Peng, N. Widjojo, P. Sukitpaneenit, M. M. Teoh, G. G. Lipscomb, T.-S. Chung, and J.-Y. Lai, "Evolution of polymeric hollow fibers as sustainable technologies: Past, present, and future," *Progress in Polymer Science*, vol. 37, pp. 1401–1424, oct 2012.
- [79] S.-G. Li, T. van den Boomgaard, C. A. Smolders, and H. Strathmann, "Physical Gelation of Amorphous Polymers in a Mixture of Solvent and Nonsolvent," *Macromolecules*, vol. 29, pp. 2053–2059, jan 1996.
- [80] D. R. Paul and Y. P. Yampolskii, *Polymeric gas separation membranes*. CRC Press, 1994.
- [81] I. Pinnau and W. J. Koros, "A qualitative skin layer formation mechanism for membranes made by dry/wet phase inversion," *Journal of Polymer Science Part B: Polymer Physics*, vol. 31, pp. 419–427, mar 1993.
- [82] J. W. Cahn, "Phase Separation by Spinodal Decomposition in Isotropic Systems," *The Journal of Chemical Physics*, vol. 42, pp. 93–99, jul 1965.

- [83] L. P. McMaster, “Aspects of Liquid-Liquid Phase Transition Phenomena in Multicomponent Polymeric Systems,” in *Copolymers, Polyblends, and Composites*, pp. 43–65, Advances in Chemistry, jun 1975.
- [84] R. E. Kesting, “The four tiers of structure in integrally skinned phase inversion membranes and their relevance to the various separation regimes,” *Journal of Applied Polymer Science*, vol. 41, no. 1112, pp. 2739–2752, 1990.
- [85] M. F. Butler and M. Heppenstall-Butler, ““Delayed” Phase Separation in a Gelatin/Dextran Mixture Studied by Small-Angle Light Scattering, Turbidity, Confocal Laser Scanning Microscopy, and Polarimetry,” *Biomacromolecules*, vol. 4, no. 4, pp. 928–36, 2003.
- [86] R. E. Kesting, “Concerning the microstructure of dry-RO membranes,” *Journal of Applied Polymer Science*, vol. 17, pp. 1771–1785, jun 1973.
- [87] G. L. Brown, “Formation of films from polymer dispersions,” *Journal of Polymer Science*, vol. 22, pp. 423–434, dec 1956.
- [88] L. Her and S. L. Nail, “Measurement of Glass Transition Temperatures of Freeze-Concentrated Solutes by Differential Scanning Calorimetry,” *Pharmaceutical Research*, vol. 11, no. 1, pp. 54–59, 1994.
- [89] T. G. Fox and P. J. Flory, “Second-Order Transition Temperatures and Related Properties of Polystyrene. I. Influence of Molecular Weight,” *Journal of Applied Physics*, vol. 21, pp. 581–591, jun 1950.
- [90] W. Burghardt, L. Yilmaz, and A. McHugh, “Glass transition, crystallization and thermoreversible gelation in ternary PPO solutions; relationship to asymmetric membrane formation,” *Polymer*, vol. 28, pp. 2085–2092, nov 1987.
- [91] G. Gaides and A. McHugh, “Gelation in an amorphous polymer: a discussion of its relation to membrane formation,” *Polymer*, vol. 30, pp. 2118–2123, nov 1989.
- [92] AZoM, “Polymer Basics: Structure and Properties,” tech. rep., Malvern Instruments Ltd, 2012.

- [93] A. J. Reuvers, *Membrane formation : diffusion induced demixing processes in ternary polymeric systems*. PhD thesis, Twente University of Technology, Netherlands, jan 1987.
- [94] M. Tan, G. He, Y. Dai, R. Wang, and W. Shi, "Calculation on phase diagrams of polyetherimide/N,N-dimethylacetamide/H<sub>2</sub>O-BuOH casting system and their relevance to membrane performances," *Frontiers of Chemical Science and Engineering*, vol. 8, pp. 312–319, oct 2014.
- [95] J. Y. Kim, H. K. Lee, K. J. Baik, and S. C. Kim, "Liquid-liquid phase separation in polysulfone/solvent/water systems," *Journal of Applied Polymer Science*, vol. 65, pp. 2643–2653, sep 1997.
- [96] R. M. Boom, H. W. Reinders, H. H. W. Rolevink, T. van den Boomgaard, and C. A. Smolders, "Equilibrium Thermodynamics of a Quaternary Membrane-Forming System with Two Polymers. 1. Calculations," *Macromolecules*, vol. 27, pp. 2034–2040, apr 1994.
- [97] C. C. Hsu and J. M. Prausnitz, "Thermodynamics of Polymer Compatibility in Ternary Systems," *Macromolecules*, vol. 7, pp. 320–324, may 1974.
- [98] J. A. Gonzalez-Leon and A. M. Mayes, "Phase Behavior Prediction of Ternary Polymer Mixtures," *Macromolecules*, vol. 36, pp. 2508–2515, apr 2003.
- [99] R. M. Boom, T. van den Boomgaard, and C. A. Smolders, "Equilibrium Thermodynamics of a Quaternary Membrane-Forming System with Two Polymers. 1. Calculations," *Macromolecules*, vol. 27, pp. 2034–2040, apr 1994.
- [100] K. Solc and R. Koningaveld, "Liquid-liquid phase separation in multicomponent polymer systems. 23. On the Gibbs criterion of the critical state," *The Journal of Physical Chemistry*, vol. 89, pp. 2237–2240, may 1985.
- [101] W. Kools, "Membrane formation by phase inversion in multicomponent polymer systems. Mechanisms and morphologies," feb 1998.
- [102] M. L. Huggins, "Solutions of Long Chain Compounds," *The Journal of Chemical Physics*, vol. 9, pp. 440–440, may 1941.

- [103] H. Tompa, "Phase relationships in polymer solutions," *Transactions of the Faraday Society*, vol. 45, p. 1142, jan 1949.
- [104] L. Zeman and G. Tkacik, "Thermodynamic analysis of a membrane-forming system water/N-methyl-2-pyrrolidone/polyethersulfone," *Journal of Membrane Science*, vol. 36, pp. 119–140, jan 1988.
- [105] L. Yilmaz and A. J. McHugh, "Analysis of nonsolvent–solvent–polymer phase diagrams and their relevance to membrane formation modeling," *Journal of Applied Polymer Science*, vol. 31, pp. 997–1018, mar 1986.
- [106] J. Wijmans, J. Kant, M. Mulder, and C. Smolders, "Phase separation phenomena in solutions of polysulfone in mixtures of a solvent and a nonsolvent: relationship with membrane formation," *Polymer*, vol. 26, pp. 1539–1545, sep 1985.
- [107] F. W. Altena and C. A. Smolders, "Calculation of liquid-liquid phase separation in a ternary system of a polymer in a mixture of a solvent and a nonsolvent," *Macromolecules*, vol. 15, pp. 1491–1497, nov 1982.
- [108] Z. Li and C. Jiang, "Determination of the nonsolvent–polymer interaction parameter  $\chi_{13}$  in the casting solutions," *Journal of Membrane Science*, vol. 174, pp. 87–96, jul 2000.
- [109] J. A. Emerson, D. T. W. Toolan, J. R. Howse, E. M. Furst, and T. H. Epps, "Determination of Solvent–Polymer and Polymer–Polymer Flory–Huggins Interaction Parameters for Poly(3-hexylthiophene) via Solvent Vapor Swelling," *Macromolecules*, vol. 46, pp. 6533–6540, aug 2013.
- [110] I. Bahar, H. Y. Erbil, B. M. Baysal, and B. Erman, "Determination of polymer-solvent interaction parameter from swelling of networks: the system poly(2-hydroxyethyl methacrylate)-diethylene glycol," *Macromolecules*, vol. 20, pp. 1353–1356, nov 1987.
- [111] M. Karimi, W. Albrecht, M. Heuchel, T. Weigel, and A. Lendlein, "Determination of solvent / polymer interaction parameters of moderately concentrated polymer solutions by vapor pressure osmometry," *Polymer*, vol. 49, no. 10, pp. 2587–2594, 2008.

- [112] T. G. Scholte, "Determination of thermodynamic parameters of polymer-solvent systems by light scattering," *European Polymer Journal*, vol. 6, pp. 1063–1074, aug 1970.
- [113] S. Shilton, G. Bell, and J. Ferguson, "The rheology of fibre spinning and the properties of hollow-fibre membranes for gas separation," *Polymer*, vol. 35, pp. 5327–5335, nov 1994.
- [114] I. Sharpe, A. Ismail, and S. Shilton, "A study of extrusion shear and forced convection residence time in the spinning of polysulfone hollow fiber membranes for gas separation," *Separation and Purification Technology*, vol. 17, pp. 101–109, oct 1999.
- [115] S. J. Shilton, "Flow profile induced in spinneret during hollow fiber membrane spinning," *Journal of Applied Polymer Science*, vol. 65, no. 7, pp. 1359–1362, 1997.
- [116] A. Ismail, S. Shilton, I. Dunkin, and S. Gallivan, "Direct measurement of rheologically induced molecular orientation in gas separation hollow fibre membranes and effects on selectivity," *Journal of Membrane Science*, vol. 126, no. 1, pp. 133–137, 1997.
- [117] A. Ismail, I. Dunkin, S. Gallivan, and S. Shilton, "Production of super selective polysulfone hollow fiber membranes for gas separation," *Polymer*, vol. 40, pp. 6499–6506, nov 1999.
- [118] B. A. Wolf, "Thermodynamic theory of flowing polymer solutions and its application to phase separation," *Macromolecules*, vol. 17, pp. 615–618, jul 1984.
- [119] B. A. Wolf, "Improvement of polymer solubility: influence of shear and of pressure," *Pure and Applied Chemistry*, vol. 69, pp. 929–934, jan 1997.
- [120] A. Ziabicki, *Fundamentals of fibre formation : the science of fibre spinning and drawing*. New York: Wiley, 1976.
- [121] J. D. Ferry, *Viscoelastic properties of polymers*. Wiley, 1980.
- [122] H. A. Barnes, *A handbook of elementary rheology*. University of Wales, Institute of Non-Newtonian Fluid Mechanics, 2000.

- [123] L. Sperling, “Polymer Viscoelasticity and Rheology,” in *Introduction to Physical Polymer Science*, pp. 507–556, Hoboken, NJ, USA: John Wiley & Sons, Inc., nov 2005.
- [124] T. G. Mezger, *The Rheology Handbook 4th Edition*. Vincentz Network, 2014.
- [125] T. Savvas, N. Markatos, and C. Papaspyrides, “On the flow of non-Newtonian polymer solutions,” *Applied Mathematical Modelling*, vol. 18, pp. 14–22, jan 1994.
- [126] H. A. Barnes, “Shear-Thickening (“Dilatancy”) in Suspensions of Nonaggregating Solid Particles Dispersed in Newtonian Liquids,” *Journal of Rheology*, vol. 33, pp. 329–366, feb 1989.
- [127] N. J. Wagner and J. F. Brady, “Shear thickening in colloidal dispersions,” *Physics Today*, vol. 62, pp. 27–32, oct 2009.
- [128] G. Lipscomb and M. Denn, “Flow of bingham fluids in complex geometries,” *Journal of Non-Newtonian Fluid Mechanics*, vol. 14, pp. 337–346, jan 1984.
- [129] H. A. Barnes, “Thixotropy—a review,” *Journal of Non-Newtonian Fluid Mechanics*, vol. 70, pp. 1–33, may 1997.
- [130] H. A. Barnes, “Thixotropy - a review,” *Journal of Non-Newtonian Fluid Mechanics*, vol. 70, pp. 1–33, may 1997.
- [131] J. M. Dealy and J. Wang, “Viscosity and Normal Stress Differences,” in *Melt Rheology and its Applications in the Plastics Industry*, pp. 19–47, Springer, 2013.
- [132] M. Reiner, “The Deborah Number,” *Physics Today*, vol. 17, pp. 62–62, jan 1964.
- [133] R. Lakes, *Viscoelastic Materials*. Cambridge: Cambridge University Press, 2009.
- [134] I. S. Sokolnikoff, *Mathematical theory of elasticity*. New York: McGraw-Hill, 2nd ed., 1956.

- [135] K. S. Fancey, "A Latch-Based Weibull Model for Polymeric Creep and Recovery," *Journal of Polymer Engineering*, vol. 21, pp. 489–510, jan 2001.
- [136] K. S. Fancey, "A mechanical model for creep, recovery and stress relaxation in polymeric materials," *Journal of Materials Science*, vol. 40, pp. 4827–4831, sep 2005.
- [137] Y. Aoki, L. Li, and M. Kakiuchi, "Rheological Images of Poly(vinyl chloride) Gels. 6. Effect of Temperature," *Macromolecules*, vol. 31, pp. 8117–8123, nov 1998.
- [138] H. Watanabe, T. Sato, K. Osaki, Y. Aoki, L. Li, M. Kakiuchi, and M.-L. Yao, "Rheological Images of Poly(Vinyl Chloride) Gels. 4. Nonlinear Behavior in a Critical Gel State," *Macromolecules*, vol. 31, pp. 4198–4204, jun 1998.
- [139] H. H. Winter, Winter, and H. Henning, "Gel Point," in *Encyclopedia of Polymer Science and Technology*, pp. 1–15, Hoboken, NJ, USA: John Wiley & Sons, Inc., feb 2016.
- [140] H. H. Winter, "Can the gel point of a cross linking polymer be detected by the G1 G2 crossover," *Polymer Engineering and Science*, vol. 27, pp. 1698–1702, dec 1987.
- [141] R. A. Wysk, B. W. Niebel, P. H. Cohen, and T. W. Simpson, *Manufacturing Processes: Integrated Product and Process Design*. New York, NY: McGraw Hill, 2000.
- [142] G. Taguchi, S. Chowdhury, and Y. Wu, *Taguchi's Quality Engineering Handbook*. Hoboken, NJ, USA: John Wiley & Sons, Inc., oct 2004.
- [143] T. Mohammadi and M. A. Safavi, "Application of Taguchi method in optimization of desalination by vacuum membrane distillation," *Desalination*, vol. 249, pp. 83–89, nov 2009.
- [144] S. Mohtada and T. Mohammadi, "Sea water desalination using electrodialysis," *Desalination*, vol. 221, pp. 440–447, mar 2008.
- [145] Z. B. Gönder, Y. Kaya, I. Vergili, and H. Barlas, "Optimization of filtration conditions for CIP wastewater treatment by nanofiltration process using

- Taguchi approach,” *Separation and Purification Technology*, vol. 70, no. 3, pp. 265–273, 2010.
- [146] H. Wu and H. Gu, “Analysis of operating parameters considering flow orientation for the performance of a proton exchange membrane fuel cell using the Taguchi method,” *Journal of Power Sources*, vol. 195, pp. 3621–3630, jun 2010.
- [147] M. G. Medeiros, R. R. Bessette, C. M. Deschenes, and D. W. Atwater, “Optimization of the magnesium-solution phase catholyte semi-fuel cell for long duration testing,” *Journal of Power Sources*, vol. 96, pp. 236–239, jun 2001.
- [148] S. Wu, S. Shiah, and W. Yub, “Parametric analysis of proton exchange membrane fuel cell performance by using the Taguchi method and a neural network,” *Renewable Energy*, vol. 34, pp. 135–144, jan 2009.
- [149] S. S. Madaeni and S. Koocheki, “Application of taguchi method in the optimization of wastewater treatment using spiral-wound reverse osmosis element,” *Chemical Engineering Journal*, vol. 119, pp. 37–44, jun 2006.
- [150] A. Idris, “Optimization of cellulose acetate hollow fiber reverse osmosis membrane production using Taguchi method,” *Journal of Membrane Science*, vol. 205, pp. 223–237, aug 2002.
- [151] M. Veronelli, M. Mauro, and S. Bresadola, “Influence of thermal dehydrochlorination on the photooxidation kinetics of PVC samples,” *Polymer Degradation and Stability*, vol. 66, pp. 349–357, dec 1999.
- [152] O. Starkova and A. Aniskevich, “Limits of linear viscoelastic behavior of polymers,” *Mechanics of Time-Dependent Materials*, vol. 11, pp. 111–126, nov 2007.
- [153] R. Durairaj, L. Wai, K. Chee, L. Jian, N. N., and L. Seow, “Rheological Characterisation of Diglycidylether of Bisphenol-A (DGEBA) and Polyurethane (PU) Based Isotropic Conductive Adhesives,” in *Rheology - New Concepts, Applications and Methods*, InTech, feb 2013.
- [154] P. Sunthar, “Polymer Rheology,” in *Rheology of Complex Fluids*, pp. 171–191, New York, NY: Springer New York, 2010.

- [155] X. J. Loh, ed., *In-Situ Gelling Polymers*. Series in BioEngineering, Singapore: Springer Singapore, 2015.
- [156] X. Liu, S. Zhang, X. Juan Xu, Z. Zhang, L. Zhou, and G. Zhang, “Study on the creep and recovery behaviors of UHMWPE/CNTs composite fiber,” *Fibers and Polymers*, vol. 14, pp. 1635–1640, oct 2013.
- [157] K. Golemanov, S. Tcholakova, N. Denkov, E. Pelan, and S. D. Stoyanov, “Remarkably high surface visco-elasticity of adsorption layers of triterpenoid saponins,” *Soft Matter*, vol. 9, p. 5738, may 2013.
- [158] P. L. Geiss, “Creep Load Conditions,” in *Handbook of Adhesion Technology*, pp. 875–902, Berlin, Heidelberg: Springer Berlin Heidelberg, 2011.
- [159] D. van Krevelen and K. te Nijenhuis, *Properties of Polymers: Their Correlation with Chemical Structure; their Numerical Estimation and Prediction from Additive Group Contributions*. Elsevier, 2009.
- [160] D. Nowicki, *An Investigation Into the Effect of the Jet-Stretch Ratio on the Performance of PVC Hollow Fibre Membranes*. PhD thesis, University of Strathclyde, 2014.
- [161] G. Kapantaidakis, G. Koops, and M. Wessling, “Effect of spinning conditions on the structure and the gas permeation properties of high flux polyethersulfone—polyimide blend hollow fibers,” *Desalination*, vol. 144, pp. 121–125, sep 2002.
- [162] S. A. McKelvey, D. T. Clausi, and W. J. Koros, “A guide to establishing hollow fiber macroscopic properties for membrane applications,” *Journal of Membrane Science*, vol. 124, pp. 223–232, feb 1997.
- [163] D. F. Li, T.-S. Chung, R. Wang, and Y. Liu, “Fabrication of fluoropolyimide/polyethersulfone (PES) dual-layer asymmetric hollow fiber membranes for gas separation,” *Journal of Membrane Science*, vol. 198, pp. 211–223, apr 2002.
- [164] S. Vinodh, S. Karthik Bharathi, and N. Gopi, “Parametric Optimization of Submerged Arc Welding Using Taguchi Method,” in *Design of Experiments in Production Engineering*, pp. 183–194, Springer, 2016.

- [165] B. Tylkowski and I. Tsibranska, “Overview of main techniques used for membrane characterisation,” *Journal of Chemical Technology and Metallurgy*, vol. 50, no. 1, pp. 3–12, 2015.
- [166] F. Cuperus, C. Smolders, C. Smolders, and C. Smolders, “Characterization of UF membranes,” *Advances in Colloid and Interface Science*, vol. 34, pp. 135–173, jan 1991.
- [167] I. Okazaki, H. Ohya, S. Semenova, S. Kikuchi, M. Aihara, and Y. Negishi, “Nanotechnological method to control the molecular weight cut-off and/or pore diameter of organic–inorganic composite membrane,” *Journal of Membrane Science*, vol. 141, pp. 65–74, apr 1998.
- [168] L. Wang and X. Wang, “Study of membrane morphology by microscopic image analysis and membrane structure parameter model,” *Journal of Membrane Science*, vol. 283, pp. 109–115, oct 2006.
- [169] B. Chakrabarty, A. K. Ghoshal, and M. Purkait, “SEM analysis and gas permeability test to characterize polysulfone membrane prepared with polyethylene glycol as additive,” *Journal of Colloid and Interface Science*, vol. 320, pp. 245–253, apr 2008.
- [170] X. Tan, S. Liu, and K. Li, “Preparation and characterization of inorganic hollow fiber membranes,” *Journal of Membrane Science*, vol. 188, pp. 87–95, jun 2001.
- [171] D. Wang, K. Li, and W. K. Teo, “Preparation and characterization of polyvinylidene fluoride (PVDF) hollow fiber membranes,” *Journal of Membrane Science*, vol. 163, pp. 211–220, nov 1999.
- [172] A. L. Carvalho, F. Maugeri, V. Silva, A. Hernández, L. Palacio, and P. Pradanos, “AFM analysis of the surface of nanoporous membranes: application to the nanofiltration of potassium clavulanate,” *Journal of Materials Science*, vol. 46, pp. 3356–3369, may 2011.
- [173] D. J. Johnson, N. Hilal, D. J. Johnson, and N. Hilal, “Membrane Characterization by Atomic Force Microscopy,” in *Encyclopedia of Membrane Science and Technology*, Hoboken, NJ, USA: John Wiley & Sons, Inc., sep 2013.

- [174] Y.-S. Lin and A. J. Burggraaf, "Preparation and Characterization of High-Temperature Thermally Stable Alumina Composite Membrane," *Journal of the American Ceramic Society*, vol. 74, pp. 219–224, jan 1991.
- [175] N. Nishiyama, D. H. Park, A. Koide, Y. Egashira, and K. Ueyama, "A mesoporous silica (MCM-48) membrane: preparation and characterization," *Journal of Membrane Science*, vol. 182, pp. 235–244, feb 2001.
- [176] S. J. Gregg, K. S. W. Sing, and H. W. Salzberg, "Adsorption Surface Area and Porosity," *Journal of The Electrochemical Society*, vol. 114, p. 279C, nov 1967.
- [177] R. Brun and M. Pages, "Selectively permeable membrane on hollow cord," 1974.
- [178] S. Shilton, "Forced convection spinning of hollow fibre membranes: Modelling of mass transfer in the dry gap, and prediction of active layer thickness and depth of orientation," *Separation and Purification Technology*, vol. 118, pp. 620–626, oct 2013.
- [179] S. Gordeyev and S. Shilton, "Forced convection spinning of gas separation hollow fibre membranes: some underlying factors, mechanisms and effects," *Journal of Membrane Science*, vol. 229, pp. 225–233, feb 2004.
- [180] C. Castellari, R. Francesconi, S. Ottani, F. Comelli, and G. Pezzin, "Latent skin in asymmetric loeb-type hollow fiber membrane," *Polymer Engineering and Science*, vol. 28, pp. 113–119, jan 1988.
- [181] T.-S. Chung, Z.-L. Xu, and W. Lin, "Fundamental understanding of the effect of air-gap distance on the fabrication of hollow fiber membranes," *Journal of Applied Polymer Science*, vol. 72, pp. 379–395, apr 1999.
- [182] W. H. Kohler and A. J. McHugh, "2D Modeling of high-speed fiber spinning with flow-enhanced crystallization," *Journal of Rheology*, vol. 51, pp. 721–733, jul 2007.
- [183] F. J. Blanco-Rodríguez and J. I. Ramos, "A simplified two-dimensional model of the melt spinning of semi-crystalline hollow compound fibers," *International Journal of Thermal Sciences*, vol. 58, pp. 102–112, aug 2012.

- [184] H. S. Wu and S. I. Sandler, "Vapor-liquid equilibria of tetrahydrofuran systems," *Journal of Chemical & Engineering Data*, vol. 33, pp. 157–162, apr 1988.
- [185] J. M. S. Henis and M. K. Tripodi, "Composite hollow fiber membranes for gas separation: the resistance model approach," *Journal of Membrane Science*, vol. 8, pp. 233–246, jan 1981.
- [186] J. M. S. Henis and M. K. Tripodi, "A Novel Approach to Gas Separations Using Composite Hollow Fiber Membranes," *Separation Science and Technology*, vol. 15, pp. 1059–1068, may 1980.
- [187] A. Fouda, Y. Chen, J. Bai, and T. Matsuura, "Wheatstone bridge model for the laminated polydimethylsiloxane/polyethersulfone membrane for gas separation," *Journal of Membrane Science*, vol. 64, pp. 263–271, dec 1991.
- [188] K. S. Houston, D. H. Weinkauff, and F. F. Stewart, "Gas transport characteristics of plasma treated poly(dimethylsiloxane) and polyphosphazene membrane materials," *Journal of Membrane Science*, vol. 205, pp. 103–112, aug 2002.
- [189] J. G. J. G. Crespo and K. W. K. W. Boddeker, *Membrane processes in separation and purification*. Springer, 1994.
- [190] A. Onuki, "Shear-Induced Phase Separation in Polymer Solutions," *Journal of the Physical Society of Japan*, vol. 59, pp. 3427–3430, oct 1990.
- [191] A. Onuki, D. Jou, J. Casas-Vázquez, G. Lebon, A. Onuki, and S. Yabunaka, "Phase transitions of fluids in shear flow," *J. Phys.: Condens. Matter*, vol. 9, no. 997, pp. 6119–6119, 1997.
- [192] C. D. Han and J. K. Kim, "On the use of time-temperature superposition in multicomponent/multiphase polymer systems," *Polymer*, vol. 34, pp. 2533–2539, jan 1993.
- [193] D. L. Turk, "Ozone resistant polymer blends," 1971.

- [194] M. Iqbal, Z. Man, H. Mukhtar, and B. K. Dutta, "Solvent effect on morphology and CO<sub>2</sub>/CH<sub>4</sub> separation performance of asymmetric polycarbonate membranes," *Journal of Membrane Science*, vol. 318, pp. 167–175, jun 2008.
- [195] P. Hacıoğlu, L. Toppare, and L. Yılmaz, "Effect of preparation parameters on performance of dense homogeneous polycarbonate gas separation membranes," *Journal of Applied Polymer Science*, vol. 90, pp. 776–785, oct 2003.
- [196] D. I. Cook, *Geosynthetics*. Rapra Technology Ltd, 2003.

# Appendix A: Rheology Measurements Errors

In this Appendix, the standard errors (standard deviations) obtained for the rheological data presented in Chapter 3 are presented. The errors presented are the average of the error of all the points in each curve. The errors are presented in percentage of the absolute value.

## A.1 Rheological Studies of PVC Solution Concentrations with Different Compositions

### A.1.1 Oscillatory Rheology

#### A.1.1.1 Amplitude Sweep Tests

In Table A.1 are presented the relative errors (%) obtained in the amplitude sweep tests (Figure 3.2 and 3.3).

TABLE A.1: Relative error (%) of the storage ( $G'$ ) and loss modulus ( $G''$ ) as function of strain (%) for different compositions at 20°C and 60°C.

Composition	20°C		60°C	
	$G'$	$G''$	$G'$	$G''$
<b>1</b>	3.8	1.2	8.2	3.7
<b>2</b>	2.8	1.3	12.0	3.4
<b>3</b>	5.7	8.2	9.7	8.6
<b>4</b>	5.7	1.6	13.5	1.9
<b>5</b>	2.9	1.7	10.8	6.2
<b>6</b>	4.1	6.6	13.9	10.9
<b>8</b>	7.7	4.6	17.2	7.5
<b>9</b>	1.5	0.4	9.3	5.4
<b>10</b>	0.5	0.3	1.2	2.9
<b>11</b>	14.4	8.9	10.5	12.3

#### A.1.1.2 Frequency Sweep Tests

In Table A.2 are presented the relative errors (%) obtained in the frequency sweep tests (Figure 3.5 and 3.6).

TABLE A.2: Relative error (%) of the storage ( $G'$ ) and loss modulus ( $G''$ ) as function of frequency for different compositions at 20°C.

Composition	$G'$	$G''$
<b>1</b>	2.3	2.5
<b>2</b>	1.8	3.5
<b>3</b>	5.6	5.2
<b>4</b>	7.5	8.4
<b>5</b>	2.2	2.9
<b>6</b>	1.9	1.2
<b>8</b>	6.3	6.8
<b>9</b>	2.2	2.1
<b>10</b>	1.1	3.0
<b>11</b>	6.3	5.2

### A.1.1.3 Temperature Sweep Tests

In Table A.3 are presented the relative errors (%) obtained in the temperature sweep tests at 10 rad/s (Figure 3.9 and 3.10).

TABLE A.3: Relative error (%) of the storage ( $G'$ ) and loss modulus ( $G''$ ) as function of temperature for different compositions at 10 rad/s.

<b>Composition</b>	<b><math>G'</math></b>	<b><math>G''</math></b>
<b>1</b>	1.6	1.8
<b>2</b>	2.3	3.2
<b>3</b>	6.3	5.9
<b>4</b>	1.9	3.2
<b>5</b>	3.4	5.9
<b>6</b>	4.9	5.2
<b>8</b>	5.3	6.3
<b>9</b>	6.3	1.2
<b>10</b>	2.3	6.4
<b>11</b>	9.5	8.9

In Table A.4 are presented the relative errors (%) obtained in the temperature sweep tests at different frequencies (Figure 3.12).

TABLE A.4: Relative error (%) of  $\tan \delta$  as function of temperature for different compositions at different frequencies.

Composition	Frequency (rad/s)	$\tan \delta$
<b>1</b>	<b>1</b>	2.3
	<b>10</b>	1.6
	<b>100</b>	3.2
<b>2</b>	<b>1</b>	3.4
	<b>10</b>	2.3
	<b>100</b>	3.4
<b>5</b>	<b>1</b>	2.5
	<b>10</b>	3.4
	<b>100</b>	5.1
<b>9</b>	<b>1</b>	1.9
	<b>10</b>	6.3
	<b>100</b>	4.2
<b>10</b>	<b>1</b>	5.5
	<b>10</b>	2.3
	<b>100</b>	1.8
<b>11</b>	<b>1</b>	2.9
	<b>10</b>	9.5
	<b>100</b>	2.6

#### A.1.1.4 Creep and Recovery Tests

In Table A.5 are presented the relative errors (%) obtained in the creep and recovery tests (strain) for different stresses at 20°C and 50°C (Figure 3.18).

TABLE A.5: Relative error (%) of strain (%) for different compositions at 20°C and 50°C.

Composition	20°C	50°C
	Strain (%)	
<b>1</b>	2.1	3.1
<b>2</b>	4.2	5.2
<b>3</b>	4.4	3.0
<b>4</b>	3.2	3.6
<b>5</b>	3.7	1.3
<b>6</b>	4.3	1.5
<b>8</b>	5.2	6.2
<b>9</b>	1.9	2.4
<b>10</b>	6.2	5.2
<b>11</b>	2.2	3.0

In Table A.6 are presented the relative errors (%) obtained in the creep tests (strain) fitted using the *Weibull* distribution at 20°C (Figure 3.27).

TABLE A.6: Relative error (%) of the creep parameters fitted using the *Weibull* distribution, at 20°C.

Composition	$\varepsilon_i$	$\varepsilon_c$	$\beta_c$	$\eta_c$
<b>1</b>	5.2	2.5	2.7	1.8
<b>2</b>	2.3	3.2	5.8	9.5
<b>3</b>	1.2	2.6	2.9	5.5
<b>4</b>	6.2	3.3	3.6	6.3
<b>5</b>	3.2	2.2	5.9	4.5
<b>6</b>	2.2	1.9	3.5	5.3
<b>8</b>	1.9	6.3	9.2	1.8
<b>9</b>	6.3	3.2	2.9	8.2
<b>10</b>	2.3	1.2	2.5	5.2
<b>11</b>	9.6	2.9	2.7	4.2

In Table A.7 are presented the relative errors (%) obtained in the creep tests (strain) fitted using the *Weibull* distribution at 50°C (Figure 3.28).

TABLE A.7: Relative error (%) of the creep parameters fitted using the *Weibull* distribution, at 50°C.

<b>Composition</b>	$\varepsilon_i$	$\varepsilon_c$	$\beta_c$	$\eta_c$
<b>2</b>	3.2	6.5	9.1	8.2
<b>3</b>	4.6	3.5	2.3	3.2
<b>5</b>	3.9	4.2	6.3	6.3
<b>6</b>	4.8	3.2	5.5	8.2
<b>10</b>	5.6	1.7	3.2	6.4

In Table A.8 are presented the relative errors (%) obtained in the recovery tests (strain) fitted using the *Weibull* distribution at 20°C (Figure 3.30).

TABLE A.8: Relative error (%) of the recovery parameters fitted using the *Weibull* distribution, at 20°C.

<b>Composition</b>	$\varepsilon_r$	$\eta_r$	$\beta_r$	$\varepsilon_f$
<b>1</b>	2.1	2.1	2.1	3.2
<b>2</b>	4.2	2.0	5.2	5.2
<b>3</b>	4.1	2.8	2.3	3.2
<b>4</b>	3.2	3.5	2.0	3.2
<b>5</b>	2.2	4.8	5.2	3.2
<b>6</b>	3.2	6.3	6.3	4.5
<b>8</b>	1.6	3.2	1.2	6.2
<b>9</b>	4.2	3.0	2.2	6.3
<b>10</b>	3.6	2.1	2.8	2.2
<b>11</b>	3.8	2.0	3.0	3.8

In Table A.9 are presented the relative errors (%) obtained in the recovery tests (strain) fitted using the *Weibull* distribution at 50°C (Figure 3.31).

TABLE A.9: Relative error (%) of the recovery parameters fitted using the *Weibull* distribution, at 50°C.

<b>Composition</b>	$\varepsilon_r$	$\eta_r$	$\beta_r$	$\varepsilon_f$
<b>2</b>	4.2	4.2	1.8	1.9
<b>3</b>	4.1	2.2	1.6	6.3
<b>5</b>	3.0	1.2	2.2	2.2
<b>6</b>	2.3	2.4	3.5	1.9
<b>10</b>	3.1	1.0	3.6	3.0

## A.1.2 Rheological Studies of a PVC Solution used for Membrane Spinning

### A.1.2.1 Flow Rheology

In Table A.10 are presented the relative errors (%) obtained in the flow tests (Figure 3.32).

TABLE A.10: Relative error (%) of viscosity as function of strain rate for different compositions at 20°C and 60°C.

<b>Temperature</b>	<b>Up Curve</b>	<b>Down Curve</b>
	<b>Shear rate (s<sup>-1</sup>)</b>	
<b>20°C</b>	7.8	8.6
<b>50°C</b>	9.6	10.2

### A.1.2.2 Frequency Tests

In Table A.11 are presented the relative errors (%) obtained in the frequency sweep tests at different temperatures (Figure 3.35).

TABLE A.11: Relative error (%) of the storage ( $G'$ ) and loss modulus ( $G''$ ) as function of frequency at 40°C, 50°C and 60°C.

Composition	$G'$	$G''$
40°C	3.8	1.2
50°C	2.8	1.3
60°C	5.7	8.2

### A.1.2.3 Creep and Recovery Tests

In Table A.12 are presented the relative errors (%) obtained in the creep and recovery tests (strain) for different temperatures (Figure 3.37).

TABLE A.12: Relative error (%) of strain (%) for different temperatures.

Temperature	Strain (%)
30°C	2.2
40°C	1.6
45°C	6.3
50°C	3.2
60°C	3.8

# Appendix B: Resistance Modelling Algorithm

This section shows the *Mathcad* algorithm used to solve the system of four equations with four unknowns obtained using the resistance modelling principles.

## Initial conditions:

Surface porosity/Active layer thickness ( $\text{cm}^{-1}$ )	$\text{APoverL} := 0.1$
Active layer thickness (cm)	$\text{L1} := 1 \cdot 10^{-4}$
Coating penetration depth (cm)	$\text{LL} := 1 \cdot 10^{-5}$
Surface porosity	$\text{AP} := 1 \cdot 10^{-5}$

## Experimental Data:

Pressure normalized flux for oxygen in uncoated membrane $\times 10^6$ (GPU)	$\text{PO2UN} := 41.51 \cdot 10^{-6}$
Pressure normalized flux for oxygen in coated membrane $\times 10^6$ (GPU)	$\text{PO2C} := 2.68 \cdot 10^{-6}$
Pressure normalized flux for nitrogen in uncoated membrane $\times 10^6$ (GPU)	$\text{PN2C} := 1.92 \cdot 10^{-6}$

Given

$$PO2UN = \frac{(0.0022035APoverL)}{[(32)^{0.5}]}$$

$$PO2C = \left[ \left( 620 \times 10^{-10} \cdot APoverL \cdot L1 - 0.0022APoverL \right) + \left[ (LL \cdot 0.0022APoverL) + \left[ 620 \times 10^{-10} \cdot APoverL \cdot L1 \cdot (32)^{0.5} \right] \right] \right]$$

$$PN2C = \left[ \left( 280 \times 10^{-10} \cdot APoverL \cdot L1 - 0.0022APoverL \right) + \left[ (LL \cdot 0.0022APoverL) + \left[ 280 \times 10^{-10} \cdot APoverL \cdot L1 \cdot (28)^{0.5} \right] \right] \right]$$

$$AP = (APoverL \cdot L1)$$

$$\text{Find}(APoverL, AP, L1, LL) = \begin{pmatrix} 0.107 \\ 9.479 \times 10^{-5} \\ 8.896 \times 10^{-4} \\ 1.856 \times 10^{-6} \end{pmatrix}$$

